Ollscoil na hÉireann, Corcaigh

National University of Ireland, Cork



Tinkering with Sn; One and Two Dimensional Tin Chalcogenide Nanostructures

Thesis presented by

Fionán Davitt, BSc. MSc.

for the degree of

Doctor of Philosophy

University College Cork

School of Chemistry

Head of School: Dr. Humphrey Moynihan

Supervisor: Professor Justin Holmes

2020

Table of Contents

Declaration ..... **v**

Abstract ..... **vi**

Common Abbreviations and Acronyms ..... **ix**

Acknowledgements ..... **xi**

1 1D Nanostructures from 2D Materials; a Review on the Growth and Analysis of One-Dimensional Tin Selenide **1**

1.1 Abstract 1

1.2 Introduction 2

1.2.1 Structural properties of SnSe 6

1.2.2 Potential applications of SnSe 9

1.3 One Dimensional SnSe 10

1.3.1 Solution phase methods for 1D SnSe 11

1.3.2 Ethylenediamine mediated 1D growth 11

1.3.3 Trisodium citrate directed synthesis in aqueous solution 14

1.3.4 Solution-Liquid-Solid mechanism for SnSe nanowires 16

1.3.5 Orientated attachment mechanism 17

1.3.6 Oleylamine and ethanolamine mediated methods 19

1.3.7 Microemulsion templated 1D SnSe 21

1.3.8 Cu doping induced structural transition 22

1.3.9 Application focused use of solution grown 1D SnSe 24

1.4 Vapour deposition methods for 1D SnSe 29

1.4.1 Application focused use of SnSe nanowires from vapour phase methods 35

1.5 Encapsulation and template assisted methods for 1D SnSe 38

1.6 Beyond Nanowires – Nanoribbons, Nanotubes and NanoNetworks 41

1.7 Conclusions and Outlook 46

1.8 Thesis Summary 46

1.9 References: 48

2 Crystallographically Controlled Synthesis of SnSe Nanowires: Potential in Resistive Memory Devices **60**

2.1 Abstract 62

2.2 Introduction 62

2.3 Experimental 65

2.4 Characterisation 66

2.5 Results and Discussion 67

2.6 Conclusions 85
2.7 References: 86
2.8 Appendix 93
2.8.1 Appendix Discussion 113
2.8.2 Appendix References 113
3 2D SnSe Nanonetworks; Growth and Evaluation for Li-ion Battery Applications 114
3.1 Abstract 115
3.2 Introduction 115
3.3 Experimental 118
3.4 Characterisation 119
3.5 Results and Discussion 120
3.6 Conclusions 136
3.7 References: 138
3.8 Appendix 144
3.8.1 Appendix References 149
4 Solution Phase Growth and Characterisation of Zigzag SnSe Nanoribbons 151
4.1 Abstract 153
4.2 Introduction 153
4.3 Experimental 156
4.3.1 Synthesis of $(Se)_m(PVP)_n$ nanoparticles 156
4.3.2 Synthesis of SnSe nanoribbons 156
4.4 Characterisation 157
4.5 Results and Discussion 158
4.6 Conclusions 169
4.7 References: 171
4.8 Appendix 176
5 Conclusions and Future Outlook 182
5.1 References 185
6 Appendix: Additional work 188
6.1 Electron beam induced exfoliation of <100> SnSe nanowires 188
6.2 Growth and Analysis of Core-Shell Ge-Sb_2Te_3 Nanoribbons 191
6.2.1 Abstract 193
6.2.2 Introduction 193
6.2.3 Experimental 195
6.2.4 Characterisation 195

6.2.5 Results and Discussion 196
6.2.6 Conclusions 203
6.2.7 References 203
6.2.8 Sub-appendix: Additional figures 208
7 Appendix: Publications and Conference presentations 213
7.1 Publications arising directly from this thesis 213
7.2 Co-authored publications 214
7.3 Conference Presentations 215

Declaration

This is to certify that the work I am submitting is my own and has not been submitted for another degree, either at University College Cork or elsewhere. All external references and sources are clearly acknowledged and identified within the contents. I have read and understood the regulations of University College Cork concerning plagiarism.

_____

Fionán Davitt

Abstract

2D layered chalcogenide materials have been subject to intense research interest in recent times, due to their unique physical properties and wide range of potential applications. Such layered materials adopt a bulk form consisting of Van der Waals bound 2D layers, and such a form readily lends itself to the formation of tailored nanostructures due to the easy cleavage of these layers along the van der Waals bound layers. SnSe is one such highly promising layered chalcogenide material which has been gathering a significant amount of interest over the last few years. SnSe exists in a layered material structure, with tightly bound in plane *b* and *c* atoms, and weakly bound *a* axis puckered layers. SnSe adopts a highly anisotropic crystal form, which yields significantly different surface energies and crystal growth speeds along different crystal facets, and thus lends itself ideally for the formation of tailored nanostructures. The effect of nanostructuring has long been shown to induce significant effects in the material properties, with beneficial effects such as better stability, cyclability and scalability being seen for nanostructured devices compared to bulk. 1D nanomaterials in particular are known to exhibit significant novel material properties, often resulting in improved performance for device applications. The properties of SnSe lend itself to utilisation in a wide range of technological applications, such as in Li-ion batteries, thermoelectric devices, memory devices, sensors and optoelectronic applications. This thesis aims to address the synthesis of novel SnSe chalcogenide nanostructures in 1D architectures.

Chapter 1 presents a review of 1D SnSe materials, highlighting in particular the synthesis methods involved in creating and tailoring such nanomaterials. The properties of SnSe as a material will be outlined, before exploring the synthesis of 1D SnSe in more detail. Such synthesis methods will be divided into three categories in this chapter, namely solution-phase methods, vapour-phase methods and methods which utilise a physical template. An overview of applications of 1D SnSe in the literature will also be outlined. Lastly the future directions

that 1D SnSe might take are examined, and novel 1D architectures such as branched nanowire networks, nanotubes and nanoribbons are discussed.

Chapter 2 details the tailored growth of SnSe nanowires and $SnSe_2$ flakes utilising a $[SnCl_4\{^nBuSe(CH_2)_3Se^nBu\}]$ single source diselenoether precursor under different CVD growth conditions. The SnSe nanowires can significantly be tailored to grow in either a <011> or <100> crystal growth direction, which is a step towards greater material control in the growth of 1D SnSe nanostructures. This tailored growth direction is of particular interest due to the highly anisotropic nature of the Pnma SnSe crystal, which could be expected to exhibit different properties for different crystal directions. The <011> oriented nanowires were shown to exhibit a bipolar resistive switching behaviour, different to the electrical properties previously seen for bulk and thin film SnSe.

Chapter 3 reports the growth of 2D SnSe nanonetworks. The novel form of these SnSe nanonetworks consists of networks of 1D nanowires, connected through single crystalline junctions. These networks all form in the same x-y plane, and were seen to join uniquely at either 86° or 93° to each other, representing network branches that grow in <011> and <01-1> directions. These SnSe nanonetworks were examined as an anode for Li-ion batteries, and were shown to exhibit enhanced performance compared to unstructured SnSe.

Chapter 4 details the solution phase synthesis of SnSe nanoribbons. These SnSe nanoribbons were grown in a stainless steel autoclave at 195 °C, with the assistance of PVP as a directing agent. The nanoribbons were seen to exhibit a thickness of ~11 - 13 nm, an average width of ~40 nm, and lengths of several hundreds of nanometres. Longer reaction times were seen to result in longer nanoribbon lengths. The SnSe nanoribbons were seen to grow uniquely along the <010> crystal direction, forming nanoribbons with a zigzag crystal structure, which has previously been theorised to show a semiconductor to metallic transition when confined to a

certain dimensional scale. Very thin SnSe nanoribbons such as these have not been seen experimentally until now, and open the door for the future exploration of the novel electronic properties which have previously been theorised for SnSe nanoribbons.

Chapter 5 presents the conclusions of the thesis, and offers a future outlook for further avenues of research which arise from the results detailed within.

Common Abbreviations and Acronyms

1D: One dimensional

2D: Two dimensional

BRS: Bipolar resistive switching

CVD: Chemical vapour deposition

EDX: Energy dispersive X-ray

EELS: Electron energy loss spectroscopy

FIB: Focused ion beam

HAADF: High-angle annular dark-field

HRS: High resistance state

HRTEM: High resolution transmission electron microscopy

Li-ion: Lithium ion

LRS: Low resistance state

PCRAM: Phase change random-access memory

PVP: Polyvinylpyrrolidone

RRAM: Resistive random-access memory

SAED: Selected area electron diffraction

SEM: Scanning electron microscopy

SLS: Solution liquid solid

STEM: Scanning transmission electron microscopy

TEM: Transmission electron microscopy

VLS: Vapour liquid solid

VS: Vapour solid

XPS: X-ray photoelectron spectroscopy

XRD: X-ray diffraction

Acknowledgements

First and foremost I would like to thank my supervisor Prof. Justin Holmes for giving me this chance to pursue a PhD in his group, and thank you for all the help and guidance along the way. Massive thanks are also greatly owed to Dr. Subhajit Biswas, for all his support and advice over the past few years.

Thank you to everyone in labs 115, 320 and 343, both past and present - Gillian, Karzan, Adria, Patrick, Debarati, Hazel, Éadaoin, Shane, Noel, Brenda, Mai, Russel, Ricky, John, Jessica, Darragh, Maart, Giuseppe, Sally, Colm, Dave, Alex, Tim, Elaine and Andres. Also a big thank you is due to Nikolay Petkov for his invaluable help and guidance with TEM and SEM. Thank you to Kamil for his expertise in solution phase synthesis, and for providing me with a wealth of samples to help me hone my microscopy skills.

Thank you to Prof. John Boland and his group in Trinity College Dublin, in particular Hugh Manning, Sahar Alialy and Michelle Gabriel.

Thank you to Prof. Gillian Reid, Samantha Hawken and Fred Robinson from the University of Southampton. This work would not have been possible without their assistance with CVD precursors.

Thank you to Dr. Maria Kolesnik-Gray and Prof. Vojislav Krstic from for the Friedrich–Alexander University Erlangen–Nürnberg for assistance with electrical measurements.

Thank you to Dr. Hugh Geaney, Prof. Kevin Ryan and Dr. Killian Stokes from the University of Limerick for their invaluable knowledge and expertise in Li-ion batteries.

Lastly, thank you also to all of the Irish fencing community, in particular the UCC fencing club, for both helping to alleviate (but sometimes add to…) some of the stressful times over the past few years.

Chapter 1

1D Nanostructures from 2D Materials; a Review on the Growth and Analysis of One-Dimensional Tin Selenide

1.1 Abstract

One-dimensional nanostructures of tin (II) selenide (SnSe) have attracted significant interest in recent years, due to the outstanding properties of SnSe coupled with the unique material properties induced by 1D nanostructuring. The controlled synthesis of 1D SnSe nanostructures is an exciting prospect, due to the highly anisotropic crystal structure of SnSe which can lead to directionally dependant properties. These unique properties can be exploited in a 1D structure with a well-defined crystal growth direction. This 1D morphology adds to the prospects of SnSe in device applications, where in general, SnSe has been garnering increasing research interest in recent times, as the wide spectrum of applications to which it finds use are further explored. As a relatively Earth abundant and non-toxic material, it is appealing as an alternative for many applications, where more toxic and scarce materials such as Pb and Te are often employed. The wide range of technological applications to which SnSe finds home includes batteries, solar cells, thermoelectric devices and nanoelectronic and optoelectronic devices, including memory devices, sensors and photodetectors. This chapter highlights the synthesis and potential applications of one dimensional SnSe, as well as some areas for future study.

1.2 Introduction

Tin (II) selenide (SnSe) as a material has seen a surge of research interest in recent years, prompted by its vast array of device applications, and the strong potential it has for advances in current device performance. SnSe sees applications in energy devices, such as batteries,[1,2] solar cells[3–5] and thermoelectric devices,[6–8] and also finds its home in the area of nanoelectronic and optoelectronic devices, including memory devices,[9–11] sensors[12–14] and photodetectors.[12,15] This exciting potential for SnSe is highlighted by the rapidly increasing growth in research publications in the area, owing to the many technological areas to which SnSe finds utilisation. This increase in research interest is clearly shown in Figure 1.1, where a record of 246 separate instances of "SnSe" appeared in the research literature in 2018, and this interest is continuing, with 157 instances of "SnSe" in the literature having appeared in the first three quarters of 2020 to date.

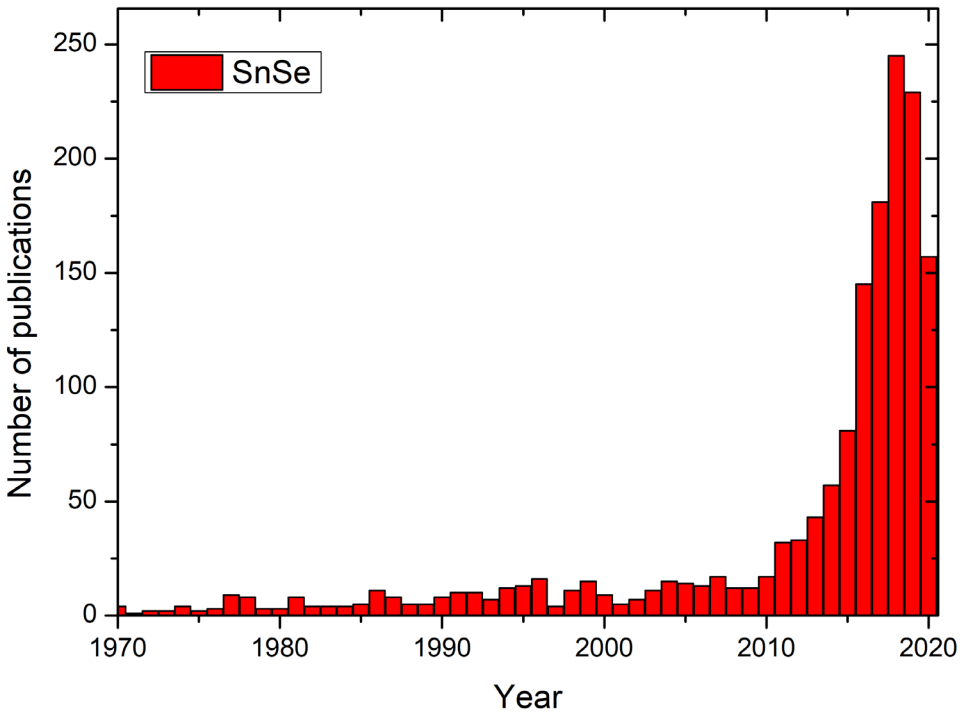


Figure 1.1: Web of science search results for "SnSe" from 1970 – 2020 (as of 01/09/2020).

Structuring materials in a 1D nanowire form has long been known to introduce novel features to the material properties.[16] The formation of a crystal along a single growth direction offers a unique advantage for a material such as that of Pnma SnSe; which exhibits a highly anisotropic structure, with different material properties along each crystal direction.[6,17] This 1D crystal growth direction can often be tuned, depending on the synthesis method used, theoretically meaning that different 1D SnSe structures could exhibit highly different properties, depending on what orientation the synthesis directs the crystal growth. As will be shown later, many different crystal growth directions have been reported for 1D SnSe nanostructures to date,

based on the synthesis method used. Although, detailed experimental knowledge of the effect of the change of growth direction on the physical and electrical properties for 1D SnSe nanostructures is at present lacking in the literature, offering score for future works in this area. Such growth methods are divided into three groups in this review; solution phase synthesis methods, vapour phase synthesis methods and growth methods using a physical 1D template. Synthesis of 1D SnSe through a combination of these methods has shown an uptake in recent years, in particular since 2018, as shown in Figure 1.2.

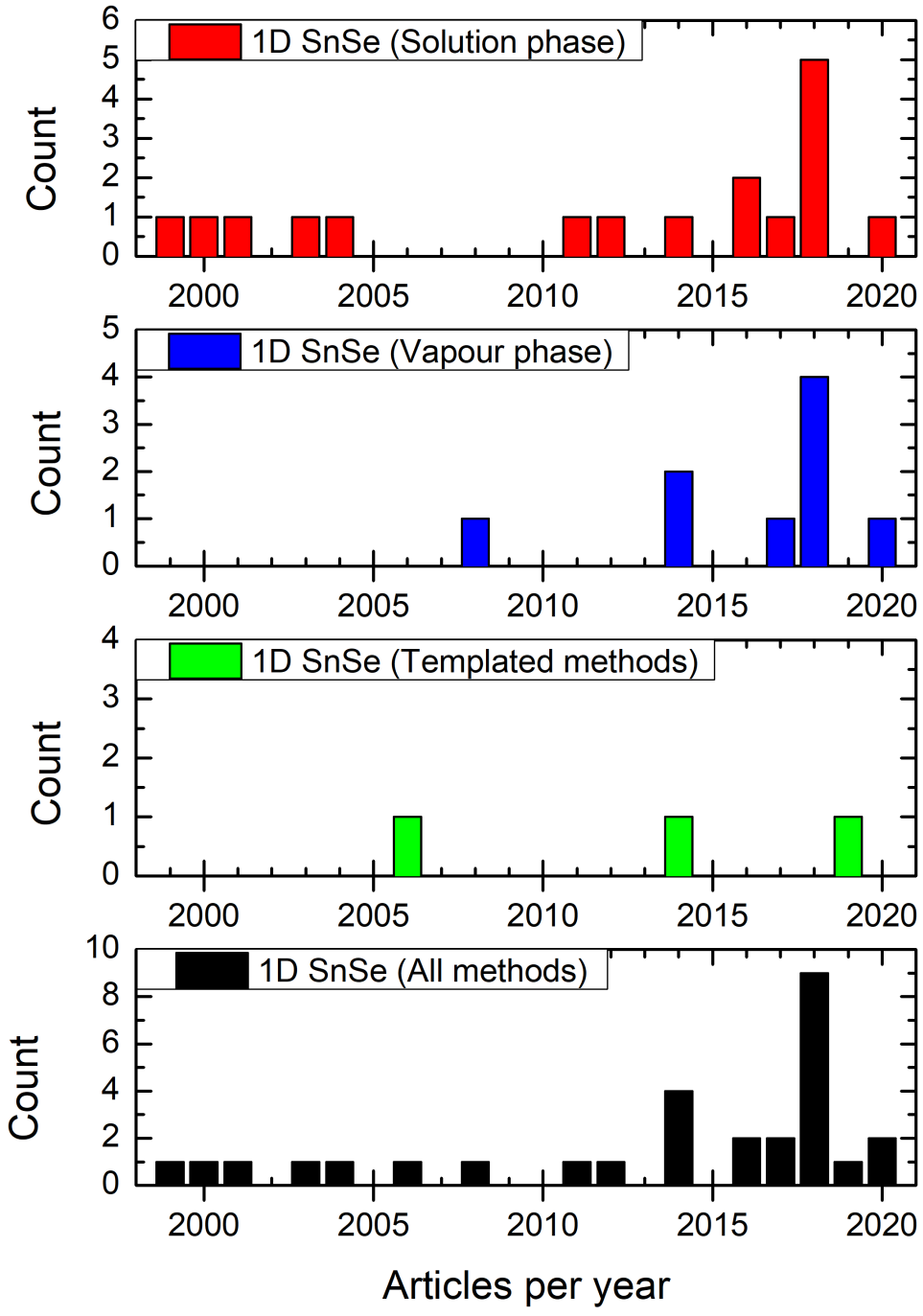


Figure 1.2: Counts of published articles on 1D SnSe, spanning the range from 1999 – 2020. The articles included in the plots are the articles cited in this chapter under the relevant sections.

For a general overview of SnSe growth, properties, and applications, the review by Weiran Shi *et. al.* in 2018 provides an overview up to this point.[18] This chapter will outline the nanostructured growth of 1D SnSe, detailing the different growth methods available for such, and the advantages and limitations of each. I will also briefly summarise the structural properties of SnSe, potential applications of SnSe and the influence of nanostructuring on such, before finally embarking on a more comprehensive review of growth methods for 1D SnSe in later sections.

1.2.1 Structural properties of SnSe

SnSe is known to crystallise in two orthorhombic forms and two cubic forms. SnSe exists as a layered material in its most common Pnma form, where it has strongly bound double layers of Sn and Se along the *b* and *c* axes, which are in turn separated by weakly bound Van der Waals bonds, as shown in Figure 1.3. In addition to this room temperature Pnma 62 space group, there exists a high temperature Cmcm 63 space group, a cubic $P2_13$ 198 space group and a cubic $Fm\bar{3}m$ form.[6,19–21] The orthorhombic forms exhibit lattice parameters of Pnma:[a=11.4976 Å, b=4.1533 Å and c=4.4400 Å – JCPDS 48-1224] and Cmcm:[a=4.3061 Å, b=11.7110 Å and c=4.3061 Å – JCPDS 89-0250]. The cubic $P2_13$ 198 form of SnSe has lattice parameters of a=11.9702(9) Å, and the $Fm\bar{3}m$ form has lattice parameters of a=5.99 Å.[20,22,23] Pnma SnSe resembles a highly anisotropic structure along all three crystal axes, with Cmcm being more isotropic along the *a*-axis and *c*-axis. Both orthorhombic structures adopt a layered structure along one crystal axis. These layers are weakly bound with Van der Waals interactions and is along the *a*-axis in Pnma SnSe and the *b*-axis in Cmcm SnSe. Cubic SnSe is isotropic along all directions. This is illustrated in Figure 1.3.

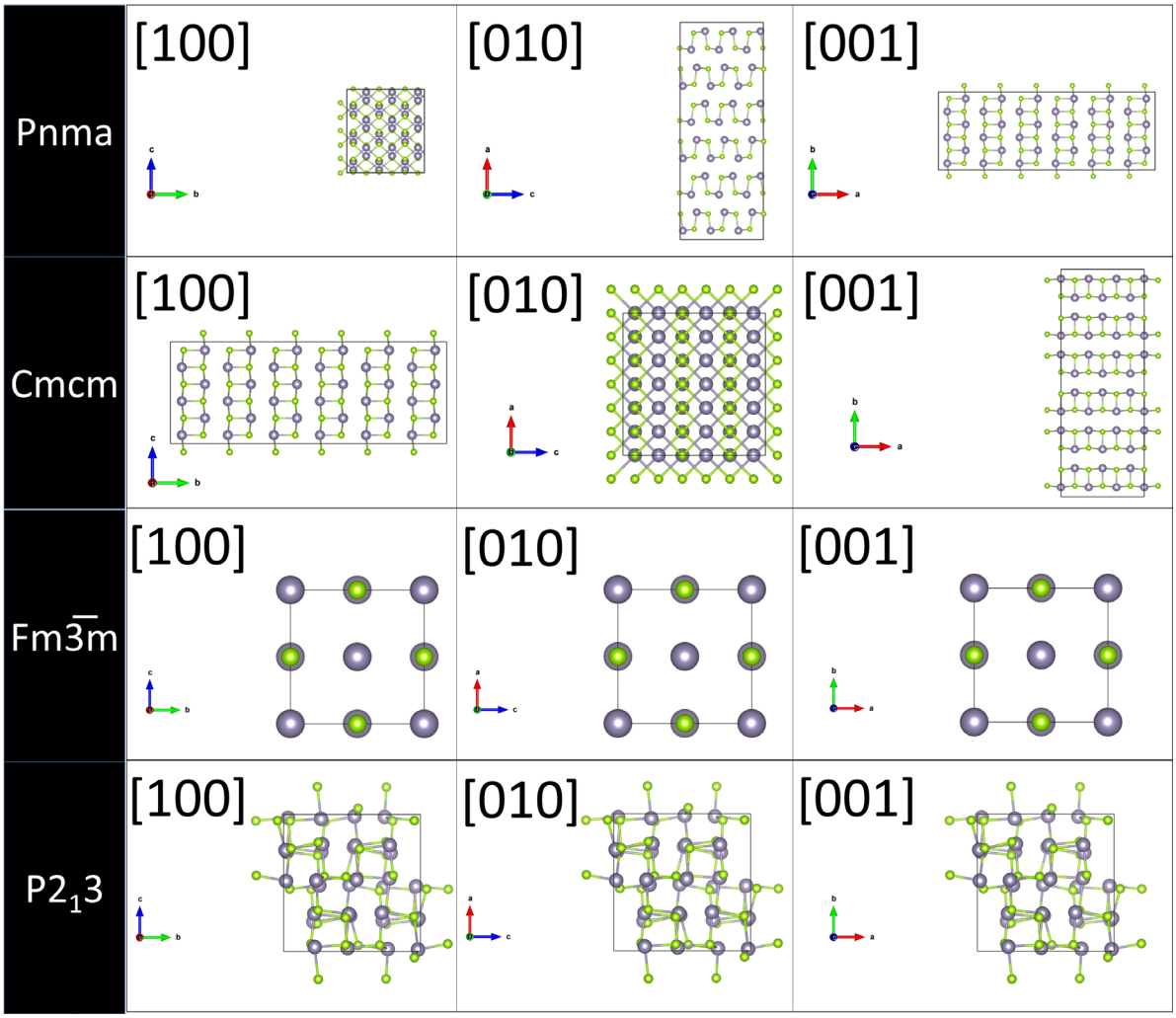


Figure 1.3: Schematic illustrating the crystal structure of Pnma 62, Cmcm 63, $Fm\bar{3}m$ and $P2_13$ SnSe down three major zone axes.

At room temperature and pressure, SnSe adopts an orthorhombic Pnma structure, and as this is the most studied form of 1D SnSe, and unless it is stated otherwise, is the form of SnSe referred to in this review. Pnma SnSe forms a highly anisotropic structure, with a long *a*-axis direction, upon which SnSe layers are stacked by weakly bonded Van der Waals forces. The *b* and *c* axis directions are again uniquely different in length to each other, but like one another in that they

are both much more tightly bound than the *a*-axis layers. Pnma SnSe forms in a zigzag like form along the *b*-axis, and an armchair like structure when directed along the *c*-axis. This highly isotropic nature also leads to very different surface plane energies, which lends itself to design strategies for controlled nanomaterial growth, as will be discussed later.[24]

Under either high temperature or high pressure conditions, SnSe is seen to adopt the Cmcm structure. This Cmcm structure is of a slightly less anisotropic form than the Pnma structure, with equal lengths along both the *a* and *c* axis, with a longer *b* axis; along which SnSe layers are bound by Van der Waals interactions. It has been known since the late 1970s that a higher symmetry Pnma to Cmcm transition in SnSe takes place at about 807 K,[25,26] as studied by Heribert Wiedemeier, Frank J. Csillag and Hans Georg von Schnering. A transition of this kind was also later seen for high pressure conditions, through computational studies[27] by Sebahaddin Alptekin *et. al.* and experimentally for bulk[28] and nanoscale[29] 2D SnSe by I Loa *et. al.* and Jian Zhang *et. al.* Most interestingly, this Cmcm phase has generated large amounts of interest due to its higher electrical conductivity compared to Pnma SnSe, contributing to its substantial thermoelectric properties.[6,30] This significant potential for thermoelectric applications has led to increasing amounts of study of this phase, including the investigation of alloying with secondary materials to induce this phase transition at lower temperatures.[31]

The cubic form of SnSe is less well studied, but offers interesting possibilities, nonetheless. A rocksalt form of SnSe was reported by A. Mariano and K. Chopra in 1967, and later in 2015 by Zhenyu Wang *et. al.*[22,23] This rocksalt form of SnSe with a lattice parameter of 5.99 Å is of interest as a topological crystalline insulator,[21,32] and additionally for thermoelectric devices.[33] A cubic structured SnSe, with a distinctly larger lattice parameter of ~11.97 Å was also reported by a number of groups in 2016-2017, revealing the potential of this form for solar cell and

thermoelectric devices.[20,34–36] As the Pnma form of SnSe is the room temperature stable form, it is in general the most reported on and studied version of SnSe. Additionally, in terms of nanowire synthesis to date, as will be seen later, very little research has been done to date on forms of SnSe beyond Pnma SnSe, leaving great scope for future work to explore the properties of the other phases of SnSe in a 1D form.

1.2.2 Potential applications of SnSe

SnSe is a highly attractive material for applications in energy storage, energy generation,[4–8] memory devices[9,10] and optoelectronic applications.[12,15] While we do not aim to fully cover the broad scope of the large amount of applications here, we will highlight a few notable examples. In the case of thermoelectric devices in particular, SnSe has been garnering intense interest in recent years.[37] An important example of this was in 2014, when Li-Dong Zhao *et. al.* investigated the thermoelectric properties of SnSe single crystals when room temperature *b*-axis oriented Pnma SnSe was heated above its phase transformation temperature to form Cmcm SnSe, displaying a very high ZT value of 2.62 at 923 K.[6] The ZT value represents the performance of a thermoelectric material, and is given by $ZT = \frac{\sigma S^2}{(\kappa_e + \kappa_l)} T$, where σ is the electrical conductivity, S is the Seebeck coefficient, T is the absolute temperature, and κ_e and κ_l represent the electronic and the lattice thermal conductivities respectively. This record high value fuelled significant further interest into the thermoelectric properties of SnSe. Detailed reviews by Zhi-Gan Chen *et. al.* and Xiao-Lei Shi have been published on SnSe thermoelectric materials in general.[7,8]

SnSe is also a highly attractive material for use in many energy applications beyond thermoelectric devices. SnSe for battery[1,38,47–51,39–46] and photovoltaic applications[1,3–5] are also highly active areas of study. The high theoretical capacity of 994 mAh g^{-1} possible for $Li_{4.4}Sn$

led to initial interest in Sn based chalcogenides for Li-ion battery applications, and experimental advances has led to a capacity of over 1000 mAh g^{-1} for SnSe based Li-ion anodes.[2,38–42,47,48] Such improvements in capacity have been attributed to the positive effect of forming a composite material with carbon,[38–42,47,48] as well as from the effect of nanostructuring of the material.[2] The optical properties of SnSe also make it interesting for photovoltaic applications, as it exhibits a bandgap in the range of 0.9 eV – 1.3 eV, which is within the optimum spectral region for solar cell light absorption. For a detailed perspective on the photovoltaic applications of SnSe, see the review article by Vasudeva Reddy Minnam Reddy et. al. on thin film based devices,[4] and the review articles on nanocrystalline SnSe in 2011, and later in 2017 by Priscilla D. Antunez *et. al.* and Babu Pejjai *et. al.*[3,5]

1.3 One Dimensional SnSe

Nanostructuring SnSe into a 1D structure has the potential to incorporate additional novel physics, as well as offering increased device performance for the many applications to which it finds use. Scaling down devices into one dimensional structures provides the advantages of reduced power requirements, increased stability and the ability to incorporate more devices per unit area from the smaller device footprint.[52–54] With SnSe being a layered material, it readily forms into 2D like structures[24,55–60] due to the slow growth rate of the *a*-axis compared to the *b* and *c* axes. However, 1D forms have been gathering increasing attention as shown in Figure 1.2, with 2018 showing a record number of publications for 1D SnSe. SnSe nanowires can be synthesised through a range of methods, which have been classified in this review into three broad categories that have been studied for 1D SnSe; solution phase methods, vapour phase methods and methods which involve the use of a physical templating agent. I will start firstly by reviewing the growth of 1D SnSe through solution phase methods, before progressing through the other different methods in turn.

1.3.1 Solution phase methods for 1D SnSe

Solution phase synthesis methods typically offer the advantage of high product quantity, lower temperature requirements, and the typically cheaper initial input costs for equipment, when compared with other techniques. However, as a trade-off, the crystal quality of the nanomaterials can sometimes be poor and quite often the precursors for these methods can consist of toxic organic compounds. Multiple such solution-based methods have been explored over the years for the production of 1D SnSe nanomaterials. In this section I will detail the main points of these different methods and review the progress that has been made over the years in developing these techniques. These methods range from techniques employing structural directing agents (oleylamine, ethylenediamine, ethanolamine, trisodium citrate, *etc*.), doping induced structural transitions, and metal catalysed solution-liquid-solid (SLS) reactions. At the end of this section an overview summary table of solution grown SnSe in the literature is presented.

1.3.2 Ethylenediamine mediated 1D growth

The solution phase synthesis of 1D SnSe began back in 1999, when Wenzhong Wang *et. al.* developed a method to produce nanocrystalline 1D SnSe in solution at room temperature.[61] This method consisted of sealing $SnCl_2$, KBH_4, elemental Se powder and ethylenediamine in a flask at about 20 °C for 4 hours. The dried products which were obtained resembled 1D nanowires of 30 nm in diameter and 1.5 μm in length (Figure 1.4(a)), with an orthorhombic Pnma SnSe crystal structure. The mechanism of this reaction was proposed to follow from the reduction of the elemental Se^0 powder to Se^{2-} from KBH_4, which then reacts with Sn^{2+} from the $SnCl_2$ source yielding SnSe. While $SnCl_2$ offers the potential to also reduce Se, forming Sn^{4+} in the process, no $SnSe_2$ formed from Sn^{4+} was detected in high enough quantities in this

report. Ethylenediamine was noted to play a significant role in the reaction, which will be discussed in more detail shortly. Unfortunately, in this early report very little material analysis beyond low resolution TEM and XRD was performed. Performing the reaction at elevated temperatures of 80 °C resulted in the formation of larger crystal grain sizes. This effect of a higher temperature is further evident in the solvothermal method developed in 2000 by Bin Li *et. al.* for the growth of SnSe.[62] This method used very similar precursors to the previous report, but involved higher temperatures and pressure, in which elemental Se powder, anhydrous $SnCl_2$ and ethylenediamine were placed into a sealed 50 ml Teflon lined autoclave at 180 °C for 7 days. However, the 1D SnSe which was produced thorough this method resembled very large microwire type structures, with diameters of 120 – 200 μm and lengths of about 0.8 – 1.5 cm. XRD analysis revealed intense 200, 400, 600 and 800 peaks, strongly suggesting that the crystal growth direction of the wires was perpendicular to the [100] direction. Investigation of a different Sn source with this same method, was investigated by Zhaohui Han in 2001, which involved placing ground stannous oxalate (SnC_2O_4) and elemental selenium into a stainless steel autoclave along with ethylenediamine.[63] The reaction temperature was also relativity high, and took place at 160 – 250 °C. Analysis of the products was relatively limited, but large microwires were seen through SEM analysis, similar to the previously mentioned report.

The limitations of the previous ethylenediamine-assisted routes, where only large microwires could be formed at high temperatures, was seemingly resolved in the ethylenediamine-assisted polyol solution phase method reported by Guozhen Shen *et. al.* in 2003.[64] The addition of diethylene glycol in this method led to small diameter nanowires being achieved at a temperature of up to 200 °C. The ability to use a higher temperature can aid in the crystallisation of the nanowire, yielding high quality single crystalline nanomaterials (Figure

1.4(b)). This route involved the use of elemental Se powder, diethylene glycol, ethylenediamine and $SnCl_2.2H_2O$. Notably, this synthesis was performed in air, and the $SnCl_2.2H_2O$ was not anhydrous as in previous reports, which increases the ease and reduces the cost in performing this reaction. The produced nanowires were single crystalline in nature, with mean diameters of 50 nm and lengths of up to 10 μm. However, the detailed crystal structure of the SnSe nanowires (growth direction *etc*.) was not explored in this report. As in previous reports, ethylenediamine was seen to be highly important in this method for the formation of phase pure SnSe nanowires. Ethylenediamine was proposed to both assist in the formation of Se^{2-} from the starting elemental Se, and also to play a major role in structuring the formed SnSe in a 1D morphology. The Sn^{2+} in the reaction was proposed to form a Sn^{2+}-ethylenediamine complex, to which the Se^{2-} ions coordinated to; assisting in the growth of the SnSe in a 1D manner.

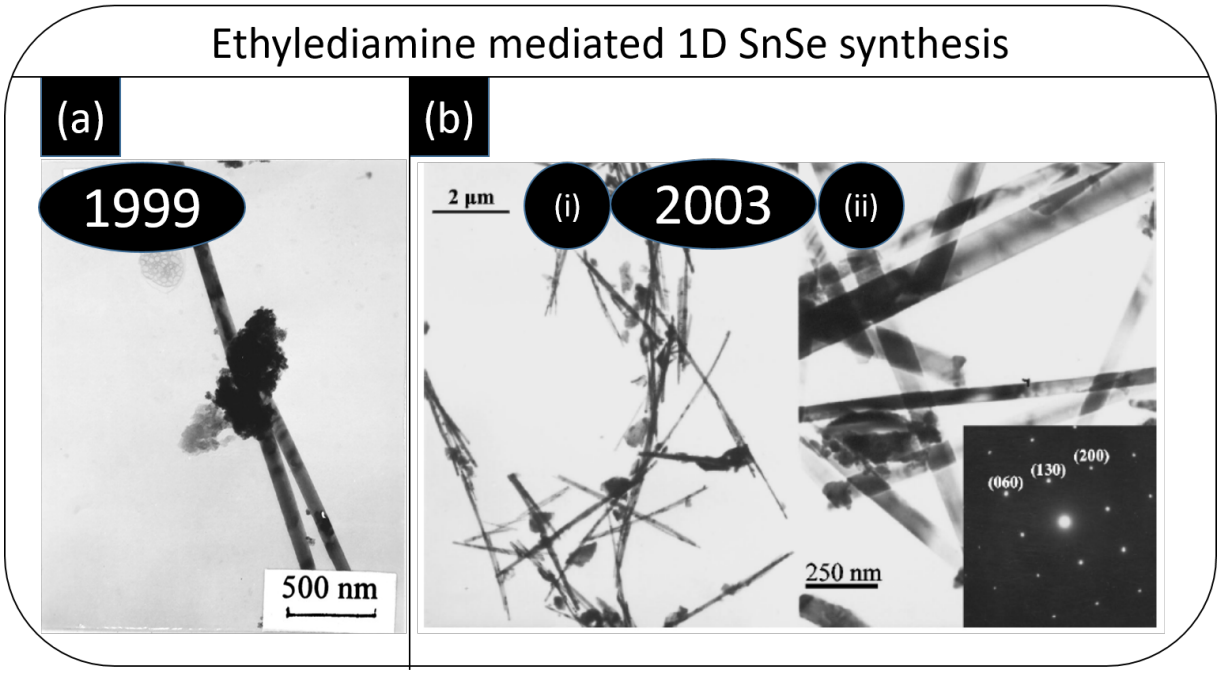


Figure 1.4: (a) SnSe nanowires synthesised through a room temperature ethylenediamine assisted route. Reprinted from Wang *et. al.* J. Am. Chem. Soc. 1999, 121, 4062–4063.[61] (b) SnSe nanowires produced through an ethylenediamine-assisted polyol method. (i) shows a low magnification TEM image, with a higher magnification shown in (ii). The inset of (ii) shows a single crystalline diffraction pattern. Reprinted from Shen *et. al.* Chem. Lett. **2003**, 32, 426–427.[64]

1.3.3 Trisodium citrate directed synthesis in aqueous solution

The first synthesis of 1D SnSe without the use of ethylenediamine occurred in 2004, brought about by the report of Qiaofeng Han *et. al.*, of the growth of SnSe nanorods in an aqueous solution (Figure 1.5).[65] This method involved dissolving elemental selenium in NaOH and water, to which a solution of $SnCl_2.2H_2O$, trisodium citrate (TSC) and NaOH in water was added. The trisodium citrate acts as a complexing agent in this reaction. TSC reacts with the Sn^{2+} in the reaction to form a $Sn(TSC)_2^{2-}$ complex, which facilitates the 1D growth of SnSe

when subsequently reacted with a source of Se^{2+} in a basic environment. TSC was shown to be highly important for the production of 1D SnSe through this method, and without any TSC, only bulk SnSe with an irregular morphology was formed. Reducing the concentration of TSC was seen to result in smaller diameter, but aggregated SnSe nanowires. Whereas an increase in the concentration of TSC resulted in slightly thicker SnSe nanorods. The reasoning for this was that the TSC affects the reaction rate, by reducing the concentration of free Sn^{2+} with increasing TSC. As the SnSe nucleation rate becomes slower, it then leads to larger diameter rods forming. The 1D nanorods obtained through this method were reported to have diameters of between 80 – 100 nm and lengths of up to 1 μm. The overall uniformity of the nanorods left room for improvement however, as many small aggregates were visible in the TEM analysis.

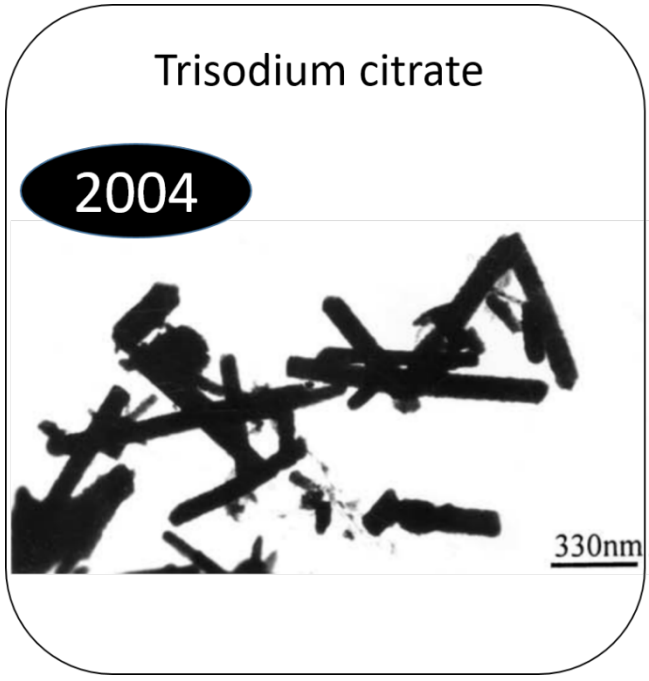


Figure 1.5: SnSe nanorods produced in an aqueous solution at room temperature, which used trisodium citrate to facilitate the 1D like growth. Reprinted from Han *et. al.* J. Mater. Sci. 2004, 39, 4643–4646.[65]

1.3.4 Solution-Liquid-Solid mechanism for SnSe nanowires

The solution-liquid-solid (SLS) mechanism for nanowire growth, which is a popular method for 1D growth of a wide variety of materials,[66] was first reported for the case of SnSe in 2011 by Sheng Liu et. al.[67] This mechanism involves the interaction of solution phase precursors with a liquid metal catalyst, resulting in the precipitation of a solid phase product. Ideal reagents for such reactions include high boiling point solvents, and low melting point metal catalysts, such as Bi or In. In this case, Bi nanoparticle catalysts were employed with oleylamine and tri-octylphosphine oxide as solvents. Electron microscopy revealed these nanowires to have relatively small diameters of 20.8 ± 2.2 nm, with lengths exceeding 10 μm. The diameters of the nanowires were seen to resemble that of the Bi nanoparticle catalyst seeds, and these seeds were clearly visible at the end of the nanowires; which is commonly seen for SLS growth techniques (Figure 1.6). XRD, HRTEM and electron diffraction measurements revealed that the nanowires were single crystalline orthorhombic Pnma SnSe, and oriented with a crystal growth direction along the <100> direction. This is more interesting, because of this growth orientation being the direction along which SnSe layers are stacked. These layers are bound through relatively weak van der Waals forces, and generally exhibit a slower growth rate to the other crystal directions.[24] This implies that the influence of the Bi particle driven SLS mechanism plays a significant role, and is enough to overcome the low growth rate that this crystal plane typically exhibits. These nanowires were examined by the authors with UV/Vis/NIR absorbance, cyclic voltammetry, and then fabricated into a solar cell device. The indirect and direct optical bandgaps of the SnSe nanowires were observed to be 1.12 and 1.55 eV, respectively, with both values larger than for bulk SnSe due to confinement effects exhibited by these very low diameter nanowires.

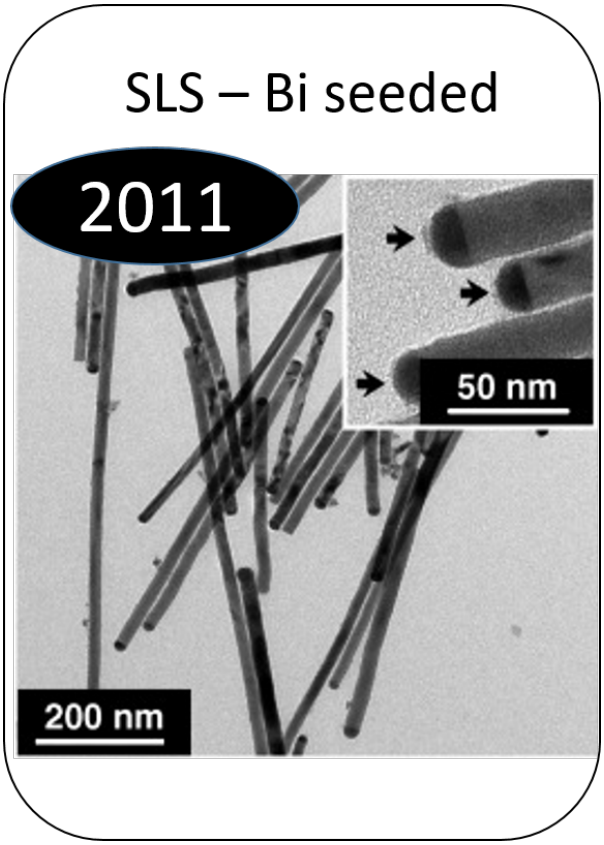


Figure 1.6: Bi seeded SnSe nanowires, grown through a SLS mechanism. Reprinted from Liu *et. al*. Angew. Chemie - Int. Ed. 2011, 50, 12050–12053.[67]

1.3.5 Orientated attachment mechanism

1D SnSe with a <100> crystal growth direction was additionally demonstrated by Kwonho Jang *et. al.* in 2012.[57] These 1D nanostructures were termed "nanocolumns" by the authors, due to their unique shape. The growth mechanism of these nanocolumns differed greatly to the previously reported SLS grown <100> oriented nanowires and involved an oriented attachment mechanism. This mechanism proceeded through firstly synthesising 2D like SnSe plates, which then attached together in a stack to form nanocolumns (Figure 1.7). The 2D SnSe plates were produced by reacting [$Me_2Si(N^tBu)_2Sn$:] with elemental Se powder to form a single source SnSe precursor. This precursor was then heated in oleylamine at 220 °C for between 20 – 60 minutes, yielding 2D like plates at the lower timescales, which then attached to form

1D like nanocolumns as the reaction time was increased to 60 minutes. These nanocolumns exhibited mean diameters of 810 ± 110 nm and lengths of about 10 μm. The individual plates which formed the nanocolumns were seen to have a thickness of 70 – 100 nm. Electron diffraction coupled with HRTEM imaging revealed the plates to be oriented with the (100) plane as its major facet, which is expected given its relatively slow growth rate, and the subsequent attachment of these flakes thus yields the <100> growth direction seen in the nanocolumns.

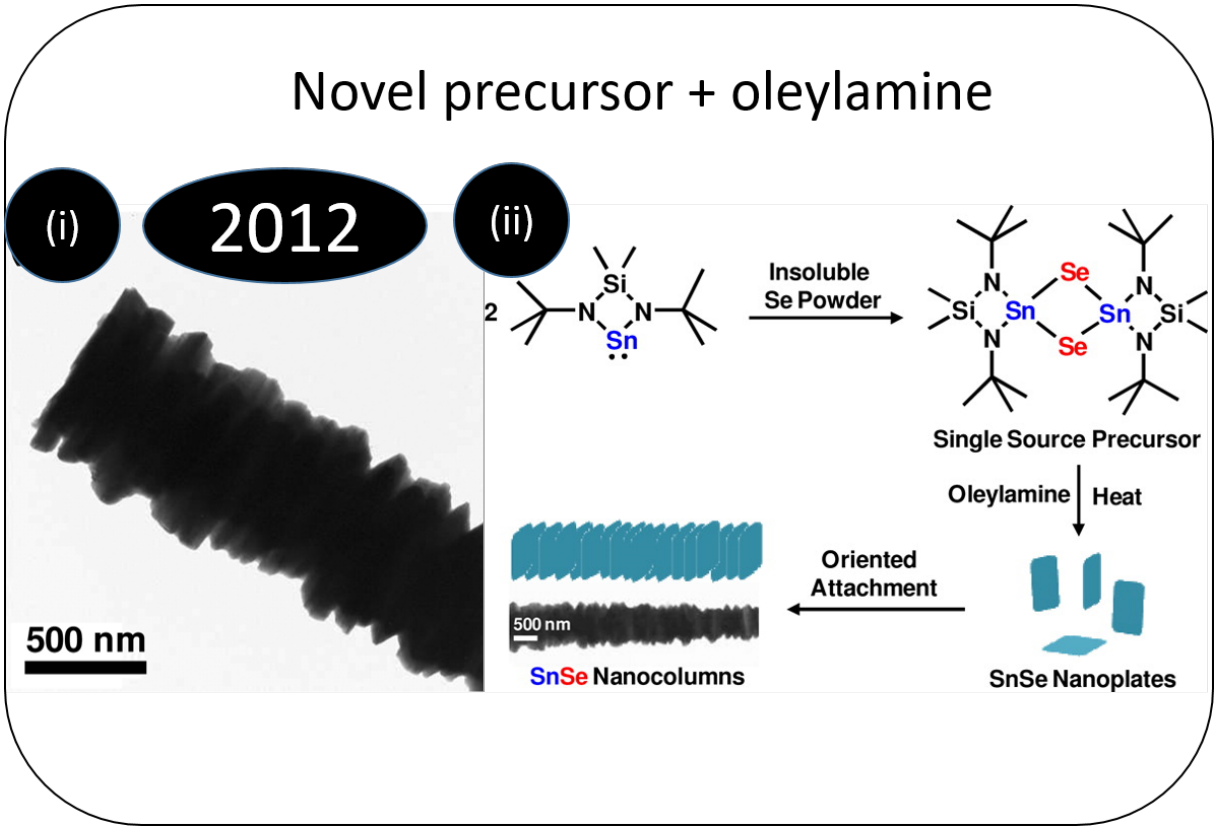


Figure 1.7: SnSe nanocolumns, synthesised through an orientated attachment mechanism. (i) TEM image of a SnSe nanocolumn. (ii) Schematic representation of the SnSe nanocolumns growth. Reprinted from Jang *et. al*. Cryst. Growth Des. 2012, 12, 3388–3391.[57]

1.3.6 Oleylamine and ethanolamine mediated methods

The use of oleylamine and ethanolamine to serve as structure-directing agents has also been employed in the growth of 1D SnSe.[12,68–70] Such a method using oleylamine as a solvent and structure-directing agent was examined by Rong Wang *et. al.* in 2014.[68] This synthesis route involved adding $SnCl_2.2H_2O$ to oleylamine at 80 °C, to form a tin-oleylamine complex. The Se source in the form of SeO_2 was then added at 175 °C, along with oleic acid, oleylamine and dodecanethiol. The reaction was relatively fast when compared to some other solution phase methods, taking a total reaction time of just over 2 hours long. Electron microscopy revealed the nanorods to have a mean width of 14 nm and length of 250 nm (Figure 1.8). Most interestingly, the nanorods exhibited a crystal growth direction along the <010> crystal direction, which up until this time had been unobserved. The authors however do not remark on the significance of this growth direction, which in addition to being unreported at the time, was also shown in the same year of 2014 to be the direction along which SnSe exhibits its greatest thermoelectric properties.[6] The mechanism proposed by the authors for the formation of these SnSe nanorods relies on the reduction of the SeO_2 by the dodecanethiol, which then reacts with the oleylamine (OLA) to form chain complexes of $(OLA)_m(Se)_n$. The Sn precursor then reacts with these chain complexes to form SnSe nanorods. Using elemental Se as a precursor source as a comparison yielded SnSe nanoparticles instead of nanorods, indicating that SeO_2 was highly important for this mechanism to proceed. Additionally, with the small 14 nm diameter of these nanorods confinement effects were seen to occur, with an increase in the direct band gap of the nanorods to 1.40 eV, from a value of 1.3 eV for bulk SnSe.

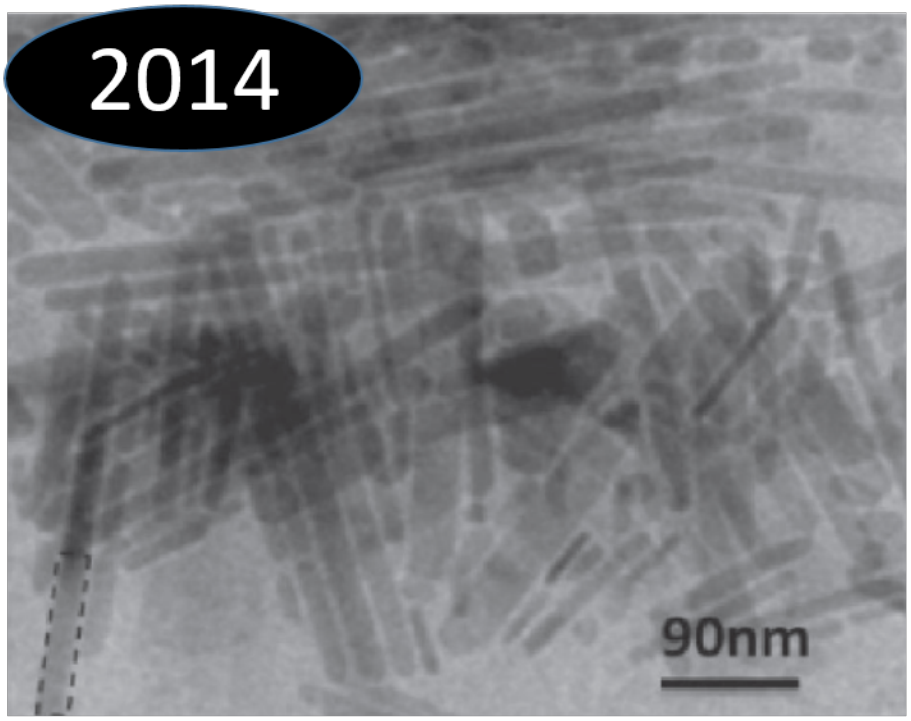


Figure 1.8: SnSe nanorods with a <010> crystal orientation, grown through an oleylamine mediated route and with SeO_2 as a Se source. Reprinted from Wang *et. al.* Chem. Lett. 2014, 43, 693–695.[68]

Ethanolamine also has been shown to enable the growth of <010> directed 1D SnSe, suggesting that it directs the growth of SnSe in a similar way to oleylamine.[69] Such an ethanolamine-based solvent approach was reported by Jing Guo *et. al.* in 2017, using elemental selenium powder, $SnCl_2.2H_2O$ and ethanolamine in a Teflon lined autoclave, to produce SnSe nanobelts with a <010> crystal growth direction (Figure 1.9). A temperature of 200 °C was required in this reaction for about 24 hours. The authors report that they have observed an organic-inorganic hybrid SnSe-(ethanolamine) compound that is involved in the formation process of the SnSe nanobelts, but however provide no further details on this in the report. Such a compound could play the role of the chain complexes predicted in previous 1D SnSe reports.

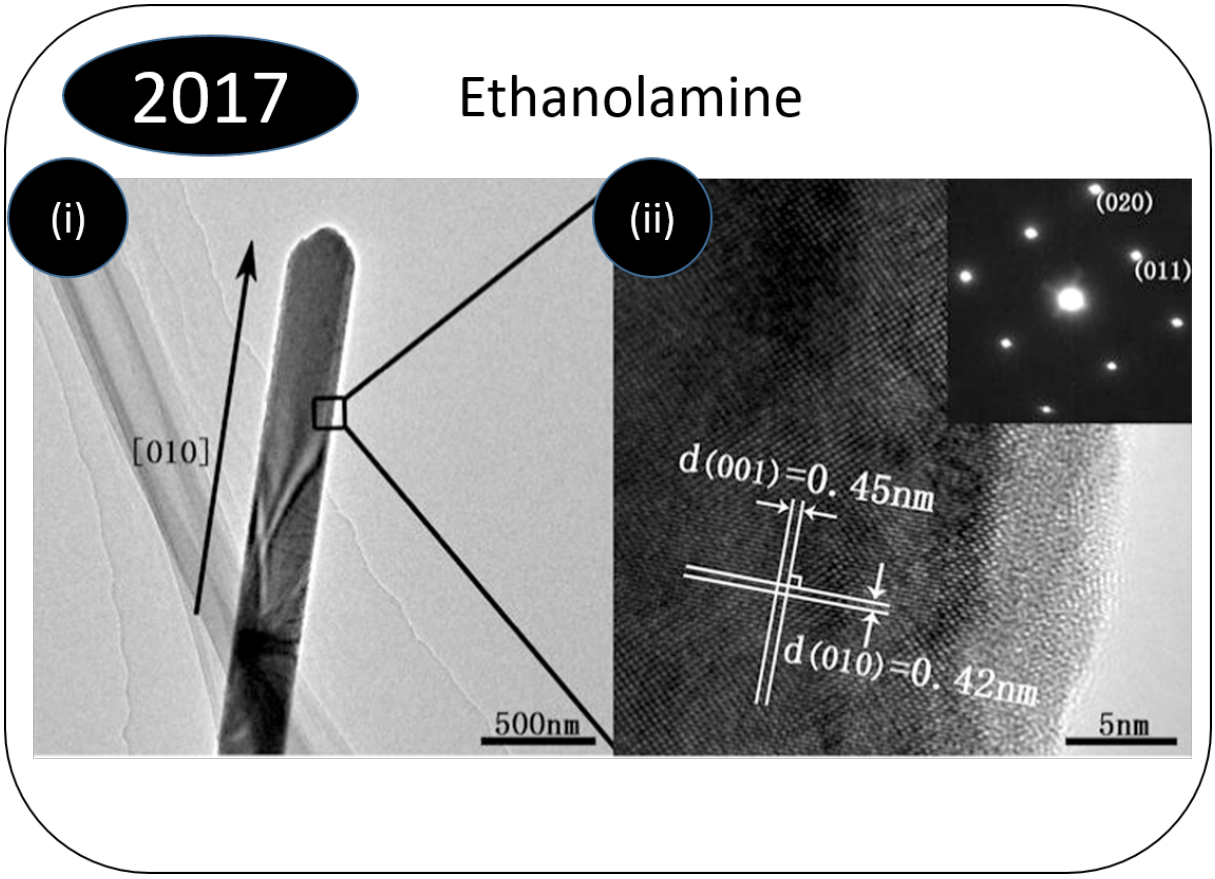


Figure 1.9: SnSe nanobelts with a <010> crystal growth direction, grown through an ethanolamine assisted route. (i) low magnification TEM image of a SnSe nanobelt. (ii) HRTEM image of a SnSe nanobelt, with SAED pattern in the inset. Reprinted from Guo *et. al*. Nano Energy 2017, 38, 569–575.[69]

1.3.7 Microemulsion templated 1D SnSe

A ternary water-in-oil microemulsion system for the synthesis of SnSe nanorods was developed by Laboni Das *et. al.* in 2018.[71] This involved the use of sodium bis(2-ethylhexyl) sulfosuccinate (known also as Aerosol-OT or AOT) as a templating agent, as well as $SnCl_2.2H_2O$, Se powder, $NaBH_4$, HCl and iso-octane. The mole ratio of water to surfactant was defined as $W_0 = [H_2O]/[AOT]$, and variation of this value through adjustment of the amount of water in the microemulsion led to the ability to tailor the nanorod dimensions (Figure 1.10). For example, a W_0 value of 5 led to the formation of nanorods with lengths of 1700 ±

300 nm and diameters of 60 ± 10 nm. TEM analysis of these nanorods revealed them to be polycrystalline in nature. The formation of nanorod structures at a low W_0 value was reasoned to be due to the low level of water content, causing the surfactants to orient themselves into cylinder or rod shapes, in order to achieve maximum contact with the aqueous polar phase. Whereas at higher levels of water concentration, the surfactant takes a spherical shape, resulting in the formation of SnSe nanoparticles. This is illustrated in Figure 1.10.

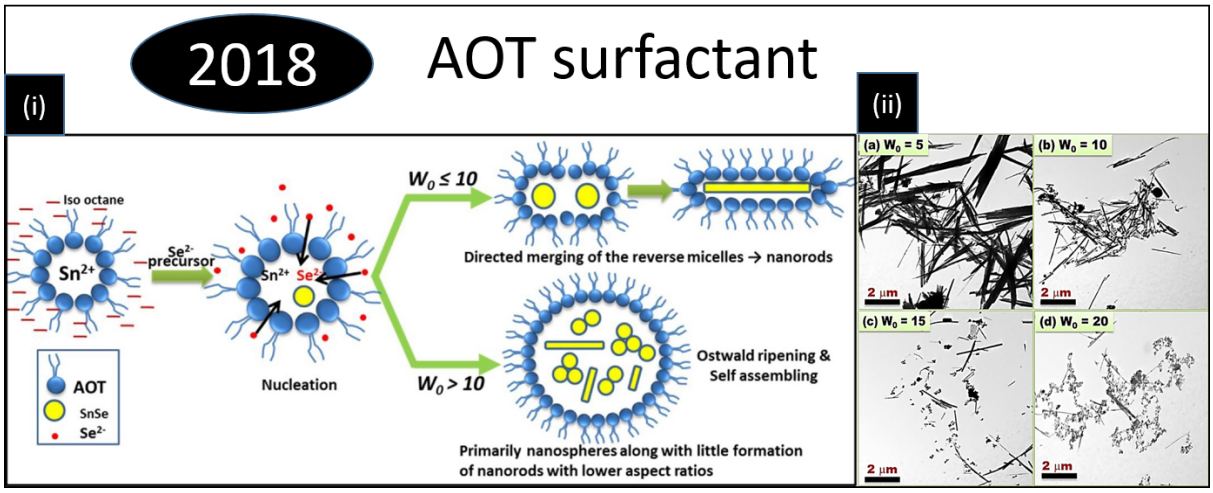


Figure 1.10: (i) Schematic illustrating the formation of 1D SnSe through an AOT based microemulsion approach. The different W_0 values represent the mole ratio of water to surfactant. (ii) shows the nanostructures formed with different W_0 values. Reprinted from Das *et. al*. Colloids Surfaces A Physicochem. Eng. Asp. 2018, 555, 781–786.[71]

1.3.8 Cu doping induced structural transition

In 2018, Xiaolei Shi *et. al.* investigated the effect of doping Cu in SnSe, with the aim of boosting its thermoelectric performance.[72] However, on addition of Cu, the observation of a structural change from 2D like microplates to 1D like microbelts with increasing Cu content was seen. This method employed a solvothermal approach, using Na_2SeO_3, $SnCl_2.2H_2O$,

$CuCl_2$, anhydrous ethylene glycol and NaOH. This reaction progressed in a polytetrafluoroethylene lined stainless steel autoclave at 230 °C for 36 hours. NaOH provided a basic environment, while ethylene glycol played the role of reducing agent. With a molar percentage of >20 % of $CuCl_2$ to $SnCl_2.2H_2O$ in the solution, a maximum solubility of 11.8 % was reached in the SnSe system and the product material resembled almost single-phase $Sn_{0.882}Cu_{0.118}Se$ microbelts (Figure 1.11). These Cu doped microbelts were shown to exhibit excellent thermoelectric properties, with a high ZT value of ~1.41 being obtained at 550 °C.

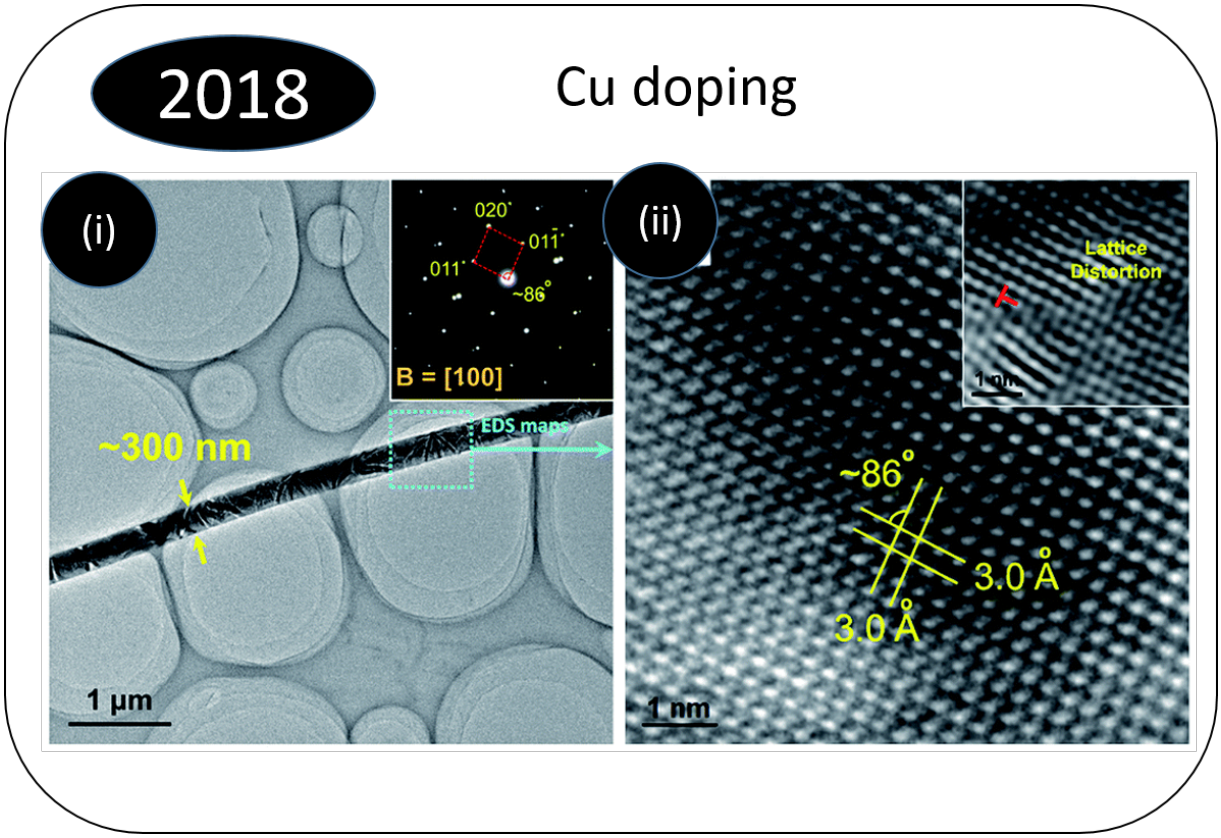


Figure 1.11: SnSe microbelts, which exhibited a 2D to 1D morphological change when doped with Cu. (i) low magnification TEM image of a SnSe microbelt, with SAED pattern in the inset. (ii) HRTEM image of a SnSe microbelt, with a second HRTEM revealing the presence of Cu induced defects in the inset. Reprinted from Shi *et. al.* Chem. Sci. 2018, 9, 7376–7389.[72]

As 1D SnSe is a highly promising material for future thermoelectric devices, Arixin Bo *et. al.* set out to study the thermostability of SnSe nanowires under localised heating from an electron beam in a TEM.[73] The synthesis of these nanowires followed a solvothermal route, which dissolved $SnCl_2.2H_2O$, Na_2SeO_3, $CuCl_2$ and NaOH in ethylene glycol. The solution was placed into a polytetrafluoroethylene-lined stainless steel autoclave and heated to ~ 230 °C for 36 hours. While it is not explicitly noted in the paper, this method appears to be the same method as used by Xiaolei Shi *et. al.* in 2018, where SnSe microbelts were doped with Cu.[72] In particular, $CuCl_2$ is also used in this paper, and therefore it is natural to assume that the SnSe nanowires used in this later report are also doped with Cu; as $CuCl_2$ was the source of the Cu doping in the previous report. If the SnSe nanowires are indeed Cu doped, it is possible that the inclusion of Cu in the nanowires may affect the conclusions reached about the thermostability measurements of the Cu doped SnSe nanowires when compared to phase pure SnSe nanowires. Nonetheless, it is a highly interesting study, which reveals that certain facets of the SnSe nanowires exhibit pronounced melting relative to other facets. In particular, the (210), (211), and (002) facets were shown to exhibit pronounced melting in that particular order.

1.3.9 Application focused use of solution grown 1D SnSe

Solution phase grown 1D SnSe has been studied for use in sensors,[12] thermoelectric devices,[69,72,74] Li-ion batteries,[41,75] solar cells,[67] optoelectronic devices[12,57] and for biomedical applications.[70] A major advantage of such solution phase grown 1D SnSe is the potential it offers for large volumes of product material when compared to other synthesis methods, and the successful scaling up of these reactions to sufficiently high quantities needs to be realised if 1D SnSe nanostructures are ever to be successfully integrated into large scale devices.

Subrata Kundu *et. al.* made progress with such a task in 2018, with the scaling up of the production of SnSe nanorods to gram-scale quantities, using a hydrothermal method.[74] Se powder, $NaBH_4$, sodium ascorbate and $SnCl_2.2H_2O$ were used as the precursor materials, and deionised water was used as the solvent for this method. Whilst the rods formed were relatively short, with mean lengths of ~370 nm, over a gram of product material was obtained from a single reaction after 24 hrs. Sodium ascorbate is claimed by the authors to be responsible for surface capping the SnSe to form a 1D structure, and appears to result in shorter lengths of the 1D structures when compared to previous methods.[12,64,65,68,69] The effect of a longer reaction time beyond 24 hrs could be investigated to see if this results in a greater 1D aspect ratio. Forming the SnSe nanorods into a pellet for thermoelectric measurements requires a reasonable amount of material, and the authors demonstrated the capability of their method for such purposes.

The large quantities of product material that can be obtained from solution phase methods also makes them highly desirable for Li-ion batteries or solar cells, where large quantities of material are required to ensure significant coverage and uniformity in the device. The high utility of solution grown 1D SnSe for Li-ion battery applications was demonstrated by Danfeng Wang *et. al.* in 2016, where SnSe nanorods produced using an ethylenediamine-assisted polyol method were wrapped in graphene oxide and yielded improved performance for Li-ion battery applications,[41] and again in 2018 where SnSe nanorods were incorporated into a SnO_x@CNF membrane by Haocheng Yuan *et. al.*, yielding significant improvement in its performance as a Li-ion battery anode.[75] SnSe nanowires for solar cell applications was demonstrated by Sheng Liu *et. al.* in 2011.[67] Additionally, solution grown SnSe nanorods, using $SnCl_2.2H_2O$, SeO_2 powder and oleylamine yielded 1D SnSe with diameters of about 100 nm and lengths of up to

a few micrometres, and these were demonstrated as both a humidity sensor and as a photodetector by Amit S. Pawbake *et. al.* in 2016.[12]

1D SnSe also finds use for biomedical applications, as shown by Zhongmin Tang *et. al.* in 2018, where they investigated SnSe nanorods functionalised with polyvinylpyrrolidone (PVP) on the surface for tumour photoacoustic imaging and photothermal therapy (PTT) accompanied by pyroelectric dynamic therapy (PEDT).[70] The synthesis of these SnSe-PVP nanorods was carried out in two steps; firstly the SnSe nanorods were synthesised through a solution method, using $SnCl_2.2H_2O$, oleic acid, oleylamine, Se powder, octadecene and dodecanethiol, and then subsequently surface treated with PVP. PVP is a non-toxic and biocompatible material which opens a route for the further study of 1D SnSe-PVP for biomedical applications.

SnSe Nanowires	***Solution phase growth methods***	Reaction mechanism	Growth direction	Application	Year	Reference number
1	*Room temperature + ambient pressure*	*Ethylenediamine assisted*	*Unreported*	*N/A*	1999	61
2	*Solvothermal rods + plates*	*Ethylenediamine assisted*	*Perpendicular to [100] direction*	*N/A*	2000	62
3	*Organic solution method*	*Ethylenediamine assisted*	*Unreported*	*N/A*	2001	63
4	*Solution method – diethylene glycol + ethylenediamine*	*Ethylenediamine assisted*	*Unreported – Single crystalline*	*N/A*	2003	64
5	*Growth in aqueous solution*	*Trisodium citrate*	*Unreported*	*N/A*	2004	65
6	*Bi seed seeded growth*	*SLS – Bi seed*	*<100>*	*Solar cells*	2011	67
7	*Orientated attachment of flakes into 1D columns*	*Novel precursor + oleylamine*	*<100>*	*Photodetector*	2012	57
8	*SnSe nanorods – SeO_2 - Oleylamine*	*SeO_2 + oleylamine, oleic acid, dodecanethiol*	*<010>*	*N/A*	2014	68
9	*SnSe nanorods – wrapped in graphene oxide*	*Ethylenediamine assisted*	*Unreported*	*Li-ion batteries*	2016	41
10	*Solvothermal*	*SeO_2 + oleylamine*	*Unreported*	*Humidity sensor and photodetector*	2016	12
11	*Solvothermal - nanobelts*	*Ethanolamine*	*<010>*	*Thermoelectric measurements*	2017	69

12	*Cu doped SnSe – Microbelts + microplates*	*Cu doping*	*<001>**	*Thermoelectric measurements*	2018	72
13	*Microemulsion based solution method*	*AOT surfactant*	*Polycrystalline*	*N/A*	2018	71
14	*SnSe-PVP nanorods*	*Oleylamine and dodecanethiol -Surface treated with PVP after growth*	*Unreported*	*Photothermal and pyroelectric dynamic therapy*	2018	70
15	*Electrospinning of SnSe nanorods in SnO_x@CNFs membranes*	*SnSe nanorods were formed in solution. Electrospun to combine them with SnO_x@CNFs*	*Unreported*	*Li-ion batteries*	2018	75
16	*Gram-scale Synthesis*	*L-ascorbic acid/sodium ascorbate*	*Unreported*	*Thermoelectric measurements*	2018	74
17	*TEM – Facet-Dependent melting*	*Cu doping***	*<001>****		2020	73

Table 1.1: Solution phase methods for 1D SnSe. * Suspected to be <001> from the analysis provided in the report, but no detail in the text of the paper. ** Solvothermal – possible Cu doping due to the presence of $CuCl_2$. *** A growth direction of <001> is reported, and this growth method is identical to that of the suspected <001> oriented nanowires in (*).

1.4 Vapour deposition methods for 1D SnSe

The utility of vapour phase synthesis methods for nanowire production is commonly known, with such methods offering the capability for significant control of the nanostructures produced, such as controlled crystal growth directions, controlled levels of doping and control in the orientation of nanowires to the underlying substrate.[76,77] Such vapour phase methods most commonly follow either a vapour-solid (VS) or vapour-liquid-solid (VLS) mechanism, where the precursor vapour directly condenses to the solid nanostructure in the former case and indirectly through an interaction with a liquid metal catalyst in the latter case. Vapour phase synthesis methods for 1D SnSe were explored back as early as 2008, with multiple subsequent reports and advances in the techniques existing in the literature. The first report of vapour phase grown 1D SnSe nanostructures consisted of the formation of SnSe-C core shell nanorods. These were grown by Vilas G. Pol *et. al.* in 2008.[78] This method consisted of the thermal decomposition of tetramethyltin and Se in a sealed chamber, which was heated to 700 °C in a tube furnace under an inert atmosphere. The structural analysis of the SnSe-C nanorods in this report did not go beyond low resolution SEM analysis; from which it is hard to obtain a comprehensive understanding of the nanostructures produced. The SnSe-C core shell structure could offer advantages for applications such as Li-ion batteries, where SnSe-C nanocomposites have been shown to offer improved performance and capacity retention compared to bare SnSe.[38,41,48] However, the visual quality and uniformity of the 1D SnSe nanostructures resulting from this synthesis appeared relativity poor, with many large aggregates apparent in the SEM analysis (See Figure 1.12(a)). Advances in the uniformity of vapour produced 1D SnSe was achieved in the later report by F. K. Butt *et. al.*[79] on the CVD synthesis of SnSe nanowires (Figure 1.12(b)), which was investigated simultaneously in 2014 with the report of CVD grown SnSe nanorod arrays (Figure 1.12(c)) by J. Cao *et. al.*[80] Both methods employed the use of metal catalyst seeds to initiate a VLS type mechanism, as well as either a mixture of

Sn and Se powders, or SnSe powder as a precursor source. The SnSe nanorods were grown using a Bi catalyst and the SnSe nanowires using a Au catalyst. The Bi seed induced growth in the <100> direction, as seen for Bi-seeded solution grown SnSe nanowires.[67] The use of Au as a seed for the nanowire growth was reported by the authors to result in growth along the <001> crystal direction. However, as the value for the (001) plane is expected to be 4.44 Å (JCPDS 48-1224), this is inconsistent with the value for the interplanar distance reported by the authors of 0.3 nm. An alternative crystal growth direction that could be assigned to this value is the (011) plane, with a value of 3.033 Å (JCPDS 48-1224). Additionally, growth along the <001> direction in theory should be unfavourable, due to the exposure of higher surface energy planes than for <011> growth.[24] This <011> growth direction would then be in agreement with the 2017 report of ultralong CVD grown SnSe nanowires by J. Liu *et. al.*[81] This 2017 report details the growth of SnSe nanowires though a CVD method, without the use of any external metal catalyst (Figure 1.12(d)). A VS type mechanism is proposed, where vapour phase SnSe condenses onto the substrate, forming small SnSe nucleation sites. Further SnSe vapour then adds to these SnSe nuclei preferentially along the (011) plane, yielding <011> orientated SnSe nanowires. These nanowires were seen to be longer than in any previous reports, with a length of up to 1 mm and a mean diameter of about ~270 nm.

Typically SnSe nanowires are grown using Sn and Se, or SnSe powders in a CVD setup, but the potential to use metalorganic precursors exists, and could offer advantages such as lower decomposition temperatures and easier tuning of elemental compositions through the use of single-source precursors.[59,82] Malik Dilshad Khan *et. al.* developed a single source Bis(selenobenzoato)dibutyltin(IV) precursor, and reported its utility for the CVD growth of both SnSe nanowires as well as SnSe flakes in 2018.[83] These nanowires were seen to exhibit diameters of between 400 – 500 nm, with lengths greater than 10 μm (Figure 1.12(e)). The

cross section of these wires could be seen through SEM images and exhibited a square shape. Detailed TEM analysis of the SnSe nanowires was not performed, making it hard to determine the crystal parameters such as the growth direction of the nanowires. The Raman spectrum reported by the authors exhibits a peak at 185 cm^{-1}, which is known to correspond to $SnSe_2$.[84,85] SnSe has been shown previously to decay to $SnSe_2$ under intense laser irradiation,[11] and coupled with the authors report of a slight Se deficiency, with an EDX Sn/Se ratio of 1.24, suggests that a partial SnSe-$SnSe_2$ conversion could be the cause of this. However, not enough additional material analysis is available to conclude this with certainty from the report. The authors additionally investigated SnSe as a suitable electrode material for both the oxygen and hydrogen evolution reaction.

Jinyang Liu *et. al.* developed a synthesis method for the production of SnSe pyramids in 2018.[86] These SnSe pyramids formed a pseudo-1D type structure, resembling that of a highly tapered wire (Figure 1.12(f)). The pyramids had lateral sizes of several micrometres at the bottom, but this then tapered off to a few hundred nanometres at the uppermost region. A Sn nanoparticle was clearly visible at the top most and thinnest region of the tapered 1D structures, which led credence to the growth mechanism of the pyramids being through a VLS like mechanism, where an initial in-situ formed Sn nanoparticle seeded the 1D like growth. SnSe powder was used as the precursor source, at a temperature of 750 °C, with the SiO_2/Si substrate placed in such a way as a location gradient was created across it, resulting in a gradient distribution of the precursor vapour density during the CVD reaction. The 1D growth direction of the pyramids is along the *a*-axis, yielding a <100> growth direction. One reasoning for this growth direction could be that the Sn nanoparticle initiates a VLS like 1D growth, whereas the lateral growth is due to a VS like nature. Thus, the bottom layer of the pyramid is larger, due to forming first, and having a longer time for precursor vapour to adsorb and lead to additional

growth. The <100> growth direction should present a much slower growth rate than the other crystal facets in SnSe, and the Sn seed would induce a VLS like growth to compensate and aid the growth rate in this direction. Raman analysis was also shown by the authors to be highly effective for determining the orientation of the 1D structures, by revealing significant differences in the Raman spectra from differently oriented SnSe pyramids.

Such ability to determine the orientation of 1D structures is important and a recent report by our group also revealed differences in the Raman spectra between differently orientated 1D SnSe nanostructures.[11] In our report, 1D nanostructures with either a <011> or <100> growth direction could be controllably synthesised by variation of the growth temperature (Figure 1.12(g)). Such control over the growth orientation presents great potential for a highly anisotropic crystal such as SnSe, that for example, exhibits different thermoelectric properties along its different crystal axes.[6] The <011> oriented SnSe nanowires were also shown to exhibit a polarity dependant resistive switching behaviour, demonstrating their potential for future SnSe nanowire based memory devices.

Accurate control of the orientation of the 1D structures is highly important, and to date, synthesis methods for the controlled production of <011> and <100> orientated 1D SnSe have been developed. Compared to solution phase methods, a smaller catalogue of 1D growth directions exist at present for vapour phase methods. However, a major advantage that vapour phase nanowire growth offers to solution phase methods, is the possibility of epitaxial growth of nanowires with aligned orientation relative to the substrate, facilitating easier incorporation into devices. The reports of CVD grown SnSe nanorod arrays by J. Cao *et. al.* and the SnSe pyramids by Jinyang Liu *et. al.* demonstrate the potential for this with <100> oriented 1D structures.[80,86] These aligned structures offer room for improvement in terms of surface and

diameter uniformity along their length. However, to date no successful achievement of such an aligned growth process like this has yet been reported for <011> oriented SnSe nanowires.

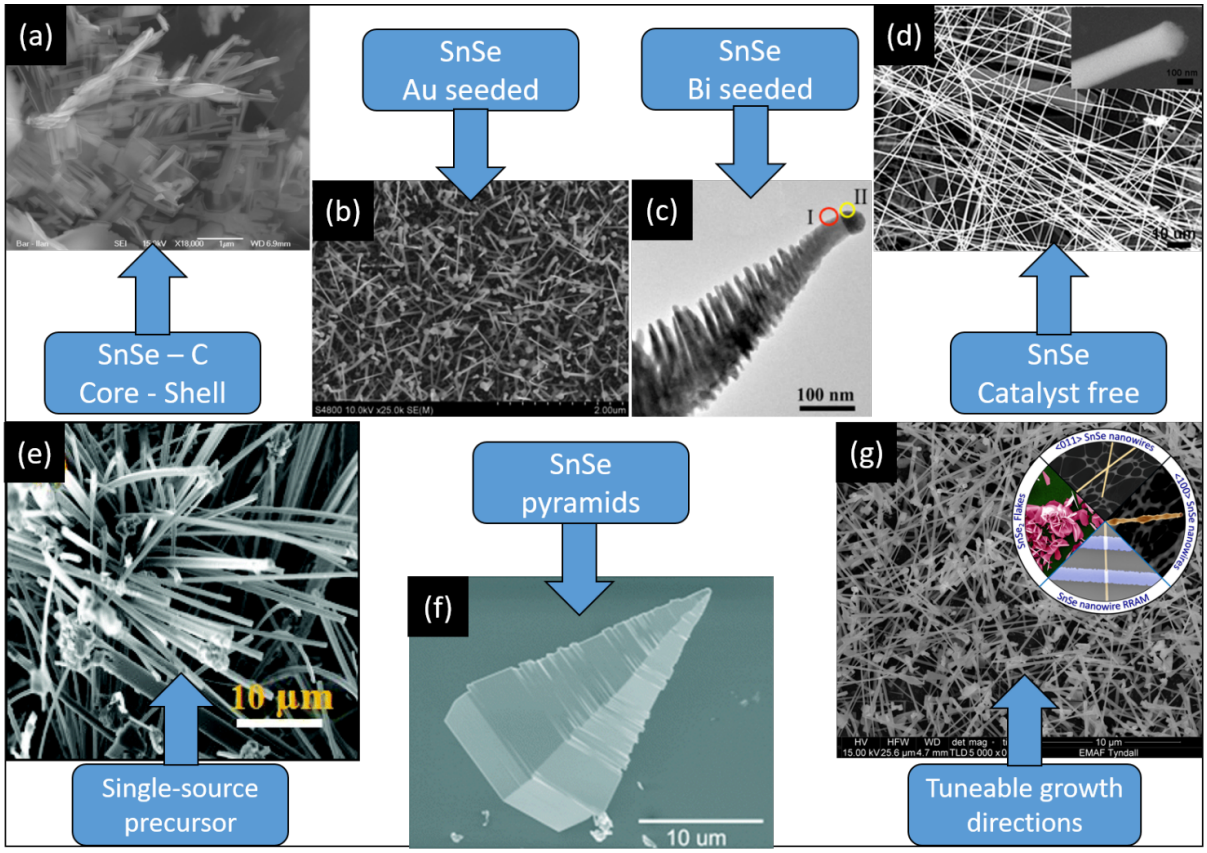


Figure 1.12: Illustration of the various 1D like SnSe nanostructures reported in the literature, synthesised through vapour deposition methods. (a) SnSe-C core shell structures, which includes 1D structures and mixed aggregates. Reprinted from Pol *et. al*. Langmuir 2008, 24, 5135–5139.[78] (b) CVD grown SnSe nanowires, using a Au seed. Reprinted from Butt *et. al*. CrystEngComm 2014, 16, 3470.[79] (c) CVD grown SnSe nanorod arrays, using a Bi seed. Reprinted from Cao *et. al.* Nanotechnology 2014, 25, 105705.[80] (d) Catalyst free CVD grown SnSe nanowires. Reprinted from Liu *et. al.* Cryst. Growth Des. 2017, 17, 6163–6168.[81] (e) Square cross section SnSe nanowires, grown through a CVD method, using a single-source Bis(selenobenzoato)dibutyltin(iv) precursor. Reprinted from Khan *et. al.* Dalt. Trans. 2018, 47, 5465–5473.[83] (f) SnSe pyramids, resembling a highly tapered 1D structure. Reprinted from Liu *et. al.* CrystEngComm 2018, 20, 1037–1041.[86] (g) SnSe nanowires grown via a CVD method, which allowed a temperature mediated tuning of the 1D crystal growth direction. Reprinted from Davitt *et. al.* Adv. Mater. Interfaces 2020, 2000474.[11]

1.4.1 Application focused use of SnSe nanowires from vapour phase methods

Vapour phase SnSe nanowires produced based on previously reported growth methods have been incorporated for use in many device focused reports. Vapour phase grown 1D SnSe has typically found use for investigation for single nanostructure studies, where for example a single nanowire would be contacted with two or more electrical probes. 2018 reports by J. A. Hermandez *et. al.*[87] and D. Zheng *et. al.*[15] follow a similar Au seeded CVD synthesis of SnSe nanowires to the 2014 report mentioned previously,[79] with crystal growth directions of 2.95 Å and 2.9 Å respectively. The authors assign these planes to the (111) and (100) planes respectively, but as per my argument for the previous reports of SnSe nanowires, I believe that these planes are likely to be in fact the (011) plane in both cases. These two reports focus on the thermoelectric and optoelectronic properties of the SnSe nanowires, with the SnSe devices explored by the authors depicted in Figure 1.13. The thermoelectric properties of SnSe nanowires were investigated for diameter ranges between 130 nm and 1.15 μm, as shown in Figure 1.13 (a). The nanowire diameter variation resulted in significant changes in the thermoelectric ZT value over the temperature range studied, highlighting that forming SnSe in 1D architectures is a valid method for tailoring of the thermoelectric performance. SnSe nanowires have also been manufactured into photodetector devices showing excellent performance, exhibiting high responsivities over a wide range from visible to near-infrared wavelengths (Figure 1.13 (b)). A high photoconductive gain of 1.5×10^4, responsivity of 1.0×10^4 A W^{-1}, with a detectivity value of 3.3×10^{12} Jones under near-infrared illumination was observed for these 1D SnSe nanowires, demonstrating their value as excellent low dimensional devices for such applications.

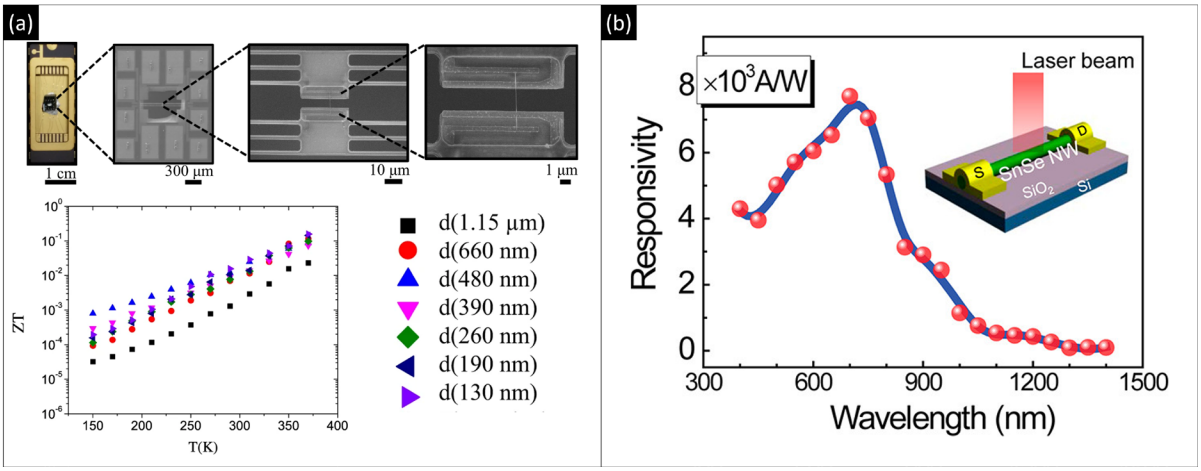


Figure 1.13: Applications of vapour phase produced SnSe nanowires in the literature. (a) depicts a micro-thermometry device, with a SnSe nanowire attached. The ZT value of the SnSe nanowire was seen to vary as a function of nanowire diameter. Reprinted from Hernandez *et. al.* Sci. Rep. 2018, 8, 1–8.[87] (b) shows a near-infrared photodetector based on a SnSe nanowire. Reprinted from Zheng *et. al.* ACS Nano 2018, 12, 7239–7245.[15]

SnSe nanowires	**Vapour phase growth methods**	Applications investigated	Growth direction	Year	Reference number
1	*Closed cell reaction – Core-shell SnSe-C nanorods*	*N/A*	*Polycrystalline*	2008	78
2	*Powder CVD – Au seed*	*Optoelectronic properties*	*<011> **	2014	79
3	*SnSe Nanorods – Powder CVD – Bi seed*	*Thermistor and photoresistor*	*<100>*	2014	80
4	*Powder CVD – No seed*	*Optoelectronic properties*	*<011>*	2017	81
5	*Bis(selenobenzoato)dibutyltin(IV) precursor - Square cross section nanowires + SnSe flakes*	*Water splitting*	*Unreported*	2018	83
6	*SnSe pyramids*	*N/A*	*<100>***	2018	86
7	*Powder CVD – Au seed*	*Thermoelectric properties*	*<011> ****	2018	87
8	*Powder CVD – Au seed*	*Photodetectors*	*<011> *****	2018	15
9	*$[SnCl_4\{^nBuSe(CH_2)_3Se^nBu\}]$ precursor – Au seed*	*Memory device*	*<011> and <100>*	2020	11

Table 1.2: Vapour phase synthesis methods for 1D SnSe. * Unclear growth direction – Paper reports 0.3 nm, which could correspond to <011>. Paper claims 0.3 nm corresponds to the <001> direction, but their SAED pattern shows <011>. ** Pyramids are stacked layer by layer. *** Paper reports 0.29501 nm and claims this to be the <111> direction, but <011> is more reasonable. **** Paper reports a lattice distance of 0.29 nm along the growth direction. This value could be attributed to the <011> direction.

1.5 Encapsulation and template assisted methods for 1D SnSe

Templated and encapsulation methods offer a simple and robust way to form 1D structures by physically constraining the growth material during the synthesis process. Such a method for the formation of SnSe nanowires, using porous alumina templates to confine the growth in a 1D manner, was reported by Lili Zhao *et. al.* in 2006.[88] $Sn(SePh)_4$ was melted to infiltrate the precursor into the pores in the alumina template, and subsequently annealed at 350°C for 36 hours. The alumina template was then selectively etched with potassium hydroxide to release the SnSe nanowires. These nanowires exhibited diameters of about 25 nm and lengths of several hundreds of nanometres. However, the crystal quality of the nanowires remained poor, displaying a highly polycrystalline nature. When alumina pore sizes of 25 nm diameter were used, nanowires such as these were seen to form, however, on changing the diameter of the pore size in the alumina template to a larger value of 180 nm, polycrystalline SnSe nanotubes were formed instead of nanowires. Figures 1.14(a) and (b) illustrates examples of these nanostructures.

Encapsulation of SnSe inside single-walled carbon nanotubes (SWNTs) is another variation of such a method and was investigated by Robin Carter *et. al.* in 2014.[89] SWNTs were filled using a molten-phase capillarity technique, which consisted of grinding the SWNTs with SnSe and heating the mixture to ~960 °C under vacuum. Encapsulation in SWNTs <1.4 nm diameter was seen to yield bilayer 2 × 2 SnSe nanocrystals with a $Fm\bar{3}m$ rocksalt form (Figure 1.14 (c)). Significantly, this $Fm\bar{3}m$ form is a metastable form, and only remained relatively stable when the SWNTs were <1.4 nm in diameter. Increasing the diameter of the SWNT to accommodate larger diameter SnSe led to instabilities that were predicted to be due to a competition between the formation of $Fm\bar{3}m$ and Pnma SnSe at larger sizes. The effect of this encapsulation was calculated to lead to a vast expansion of the band gap, from 0.68 eV for bulk $Fm\bar{3}m$ SnSe to

1.41 eV for a small $Fm\bar{3}m$ SnSe nanorod. Notably, this was the first report of a phase of SnSe other than Pnma for 1D SnSe systems.

Additional forms of encapsulated SnSe inside SWNTs of ~0.7 – 1.3 nm diameter were later seen by Charlotte A. Slade *et. al.* in 2019.[90] These SWNTs were filled using a vapour phase transport method, from sublimation of SnSe under vacuum. Five unique forms of 1D SnSe were observed inside the SWNTs after encapsulation, as shown in Figure 1.14(d). 1×1 and zigzag chains of SnSe, as well as 2×1 and 2×2 forms were seen. Most interestingly however, a new form of 1D SnSe was observed, with a structure similar to that seen previously for 1D MX (M = Mo, W; X= S, Se) nanowires, but never before for SnSe. This opens an avenue for the realisation and further study of novel 1D SnSe architectures.

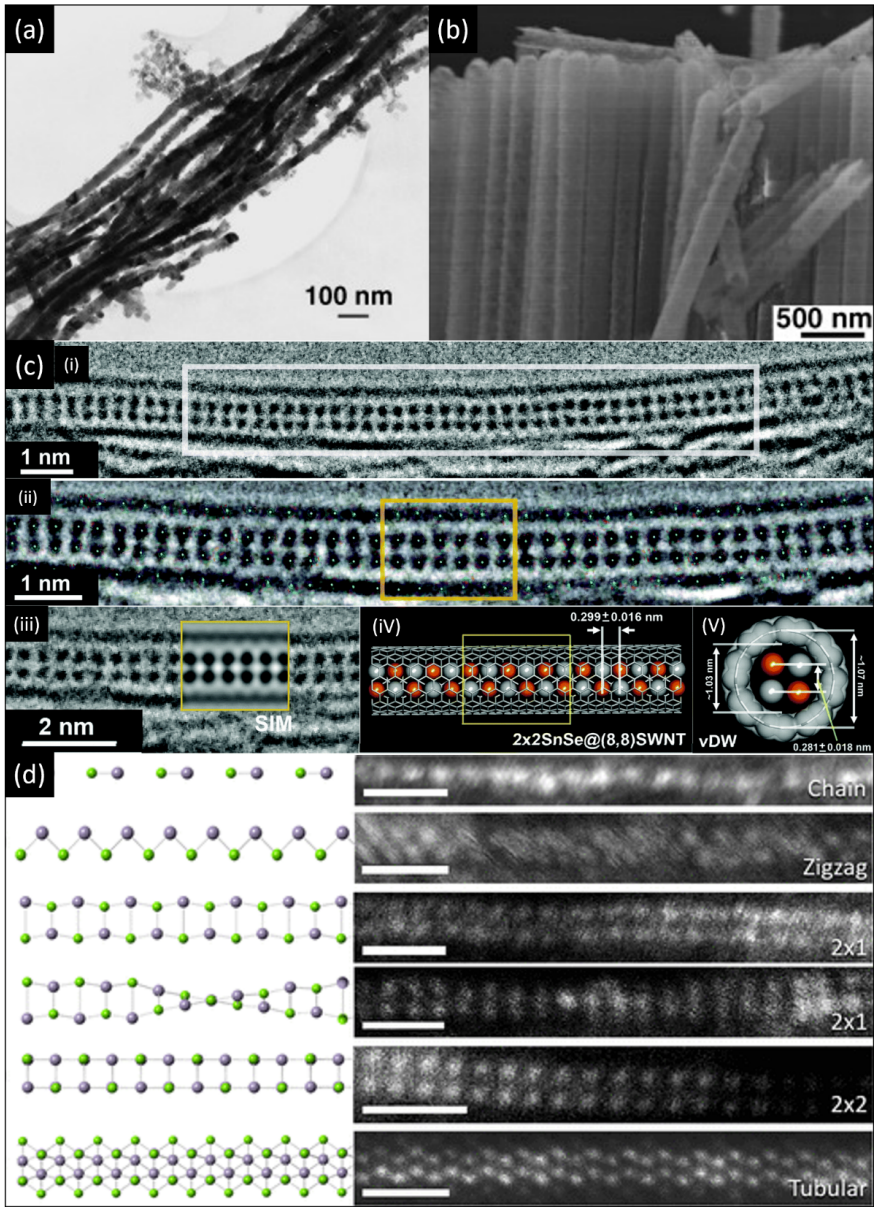


Figure 1.14: 1D SnSe formed from templated processes. (a) shows a bundle of SnSe nanowires, formed from a porous alumina templated method, and (b) shows the formation of SnSe nanotubes using by using larger diameter pores through the same method. Reprinted from Zhao *et. al.* Angew. Chemie Int. Ed. 2006, 45, 311–315.[88] (c) shows the encapsulation of SnSe inside a SWNT, forming a 2x2 $Fm\bar{3}m$ SnSe form. (i-v) shows TEM images and corresponding simulated images of the SnSe nanorod encapsulated in the SWNT. Reprinted from Carter *et. al.* Dalt. Trans. 2014, 43, 7391–7399.[89] (d) shows 6 STEM images, resembling 5 unique SnSe forms encapsulated within SWNTs. Chain, zigzag, 2x1, 2x2 and tubular forms can be seen. Reprinted from Slade *et. al.* Nano Lett. 2019, 19, 2979–2984.[90]

1D SnSe - *Encapsulation and template assisted methods*	*Growth direction*	Year	Reference number
Infiltration of $Sn(SePh)_4$ into porous alumina templates	*Polycrystalline*	2006	88
Molten-phase capillarity technique (SWNTs)	*<100> - $Fm\bar{3}m$*	2014	89
Vapour phase transport via sublimation (SWNTs)	*N/A*	2019	90

Table 1.3: Encapsulation and template assisted methods for 1D SnSe.

1.6 Beyond Nanowires – Nanoribbons, Nanotubes and NanoNetworks

Research into the further advancement of dimensionally confined nanostructures is ongoing. Avenues for further research exist in exotic morphologies such as complex branched structures, heterostructures and nanoribbon type structures for example. Morphologies such as these have been explored for a range of other layered materials, highlighting the novel physics and material properties induced in these exotic nanostructures.[91–95] In terms of SnSe, studies on these types of complex nanostructures are still in the early days of development.

For an example of current studies of these systems for SnSe, we have recently achieved the development of networked 1D structures of SnSe, formed from a 2D network of SnSe nanowires,[2] as shown in Figure 1.15. Different to single 1D nanostructures, these nanonetworks consist of many nanowires, connected throughout by single crystalline junctions. Such complex networked structures offer advantages beyond single nanowires structures, such as increased mechanical stability whilst retaining the beneficial properties of 1D nanostructures. For example, in our report we demonstrate the increased stability of the SnSe

nanonetworks compared to SnSe alone, revealing a greater % of retained capacity after repeated cycles as a Li-ion battery anode.

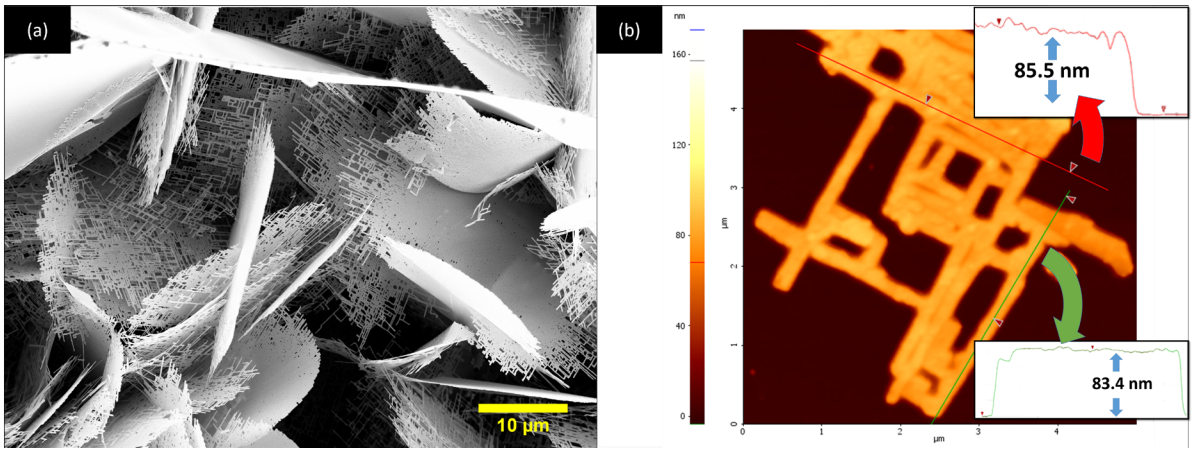


Figure 1.15: 2D SnSe nanonetworks. (a) SEM image of the SnSe nanonetworks. (b) AFM image of the SnSe nanonetworks, with the nanonetwork thickness shown in the insets. Reprinted from Davitt *et. al.* ACS Appl. Energy Mater. 2020, 3, 6602–6610.[2]

These SnSe nanonetworks were shown to have a thickness in the range of 89 ± 9 nm, with an example shown in Figure 1.15(b). Due to the layered nature of SnSe, if these structures could be shrunk to smaller thicknesses, more exotic properties could potentially be realised. SnSe nanoribbons, which are defined as a form of 1D SnSe with extremely small thickness, are predicted to present vastly different properties to any other form of SnSe. Yucheng Huang *et. al.* demonstrated, by using density functional theory, that such exotic electronic properties should be realised in SnSe nanoribbons.[96] Their study found that the structure of the edge shape of the SnSe nanoribbons drastically altered their electronic properties, when formed from a single layer of 1D SnSe with a very small nanoribbon width. Depending on the 1D growth direction, SnSe nanoribbons can exhibit either a zigzag structure, or an armchair structure, as shown in Figure 1.16. Pristine SnSe nanoribbons with a zigzag structure, *i.e.* with a <010> growth direction, displayed metallic behaviour. However, if any distortion to the Sn-Se bonds was introduced (from tensile strain *etc*.) then a metal to semiconductor transition was induced

in the material. The width parameter N_Z (zigzag) or N_A (armchair), was used to define the width of the nanoribbons, as shown in Figure 1.16. Increasing the width parameter of the zigzag nanoribbons beyond $N_Z = 8$ was also seen to induce this metal to semiconductor change. If the nanoribbons were structured with an armchair terminated edge, *i.e.* a <001> growth direction, then only semiconductor type properties were displayed by the SnSe nanoribbons.[97] Yang Yang *et. al.* have additionally demonstrated that the band gap of armchair SnSe nanoribbons varies with ribbon width, and shows an indirect-to-direct transition which is dependent on the ribbon width.[97]

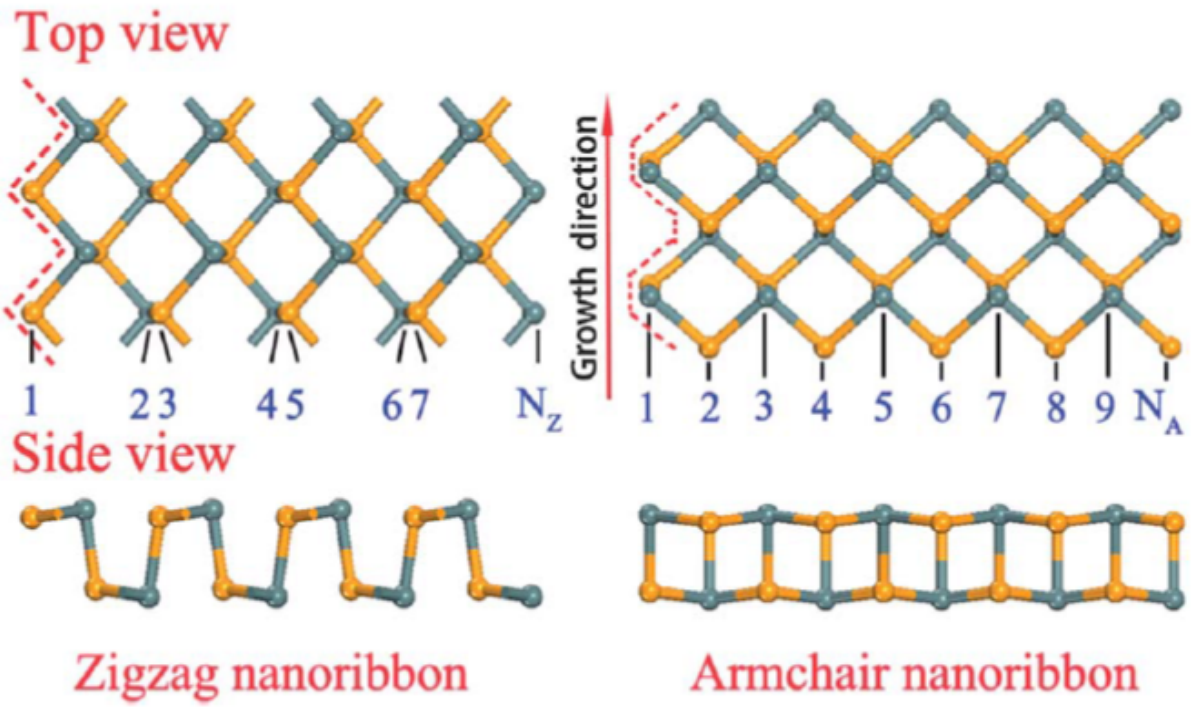


Figure 1.16: Zigzag and armchair SnSe nanoribbons. Reprinted from Huang *et. al*. RSC Adv. 2014, 4, 6933–6938.[96]

As discussed previously in section 1.5, SnSe nanotubes with a diameter of ~180 nm have been synthesised before through the use of a porous alumina template in 2006.[88] However, in 2017 Chensheng Lin *et. al.* showed through first principles simulations that reducing the diameter of SnSe nanotubes, to form low dimension (12,0) star-like zigzag SnSe nanotubes would give rise to exceptional thermoelectric properties.[98] Such a predicted star-like nanotube structure is shown in Figure 1.17. These nanotubes could potentially yield a very high ZT value of up to 3.5 – 4.6, vastly greater than the values of 0.6 – 2.6 that currently exist for crystalline SnSe. Such values are obtained for an optimal doping concentration of 6.3×10^{20} cm^{-3}, and thus both the synthesis and the doping of the nanotube are two challenges that remain to be addressed if these high values are to be realised experimentally.

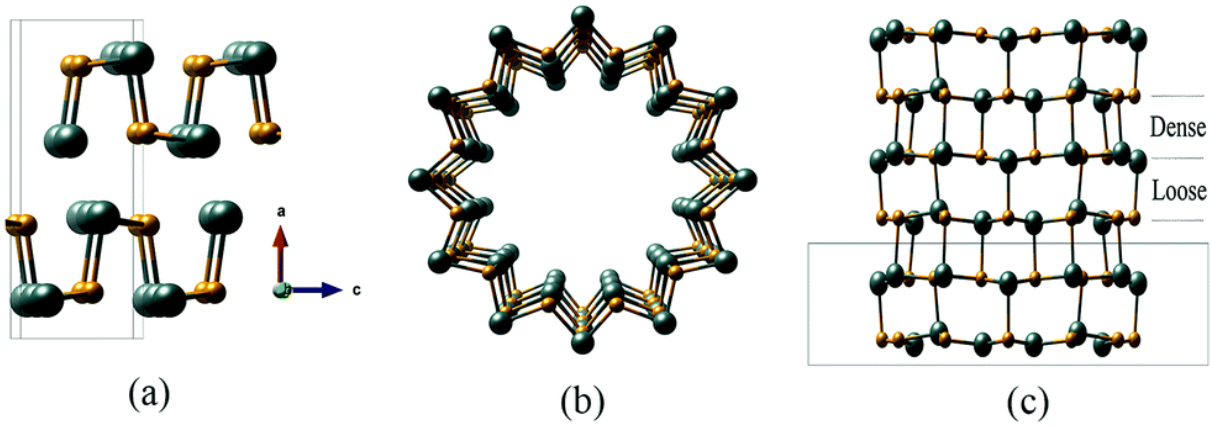


Figure 1.17: Star-like (12,0) SnSe nanotubes. (a) Pnma SnSe structure. (b) Cross section of a (12,0) SnSe nanotube. (c) Side view of the same nanotube. Reprinted from Lin *et. al.* Phys. Chem. Chem. Phys. 2017, 19, 23247–23253.[98]

Beyond nanowires – Complex 1D SnSe structures	*Structure*	*Theory/experimental*	Year	Reference number
Semiconductor-metal transition in SnSe nanoribbons	*Nanoribbon*	*Theory*	2014	96
Thermoelectric properties of SnSe nanoribbons	*Nanoribbon*	*Theory*	2016	99
Star-like ultra-low diameter SnSe nanotubes	*Nanotube*	*Theory*	2017	98
Electronic structure of SnS-SnSe nanoribbon heterostructures	*Nanoribbon*	*Theory*	2019	97
SnSe nanowire networks	*Nanonetwork*	*Experimental*	2020	2

Table 1.4: Beyond nanowires – Complex 1D SnSe structures.

1.7 Conclusions and Outlook

1D SnSe constituents a highly interesting materials system, offering a platform to fully exploit the highly anisotropic structure and directional dependent properties of SnSe. I have highlighted the wide variety of synthesis methods that exist for the formation of 1D SnSe, including solution phase, vapour phase, and physical templated methods. Diameter control, length control, and tailoring of the nanowire crystal growth orientation can be achieved based on the growth method that is chosen. 1D SnSe has been shown to demonstrate promising potential for applications in thermoelectric devices, sensors, battery devices, memory devices, photodetectors, photoelectrochemical devices, solar cells and recently for biomedical applications. A large amount of further scope exists for the exploration of novel 1D SnSe architectures even still; with room to explore phases beyond the Pnma form of SnSe, as well as novel morphologies such as nanoribbons, nanotubes and nanonetworks offering an exciting future for 1D SnSe.

1.8 Thesis Summary

With the increasing research interest in SnSe materials, this thesis will highlight my contributions to the developing field of 1D SnSe nanostructures. Chapter 2 details the growth of SnSe nanowires, utilising a liquid injection CVD method in combination with a single source diselenother precursor. From this method two forms of SnSe nanowires were produced by tailoring of the growth temperature. <011> growth direction nanowires were formed at lower temperatures, with <100> growth direction nanowires seen as the temperature was increased. The <011> nanowires were additionally shown to exhibit a bipolar resistive switching effect, revealing their possible potential for future SnSe RRAM devices.

In Chapter 3 further control of the SnSe nanostructures which were seen in Chapter 2 is demonstrated. By further modification of the CVD growth parameters interconnected 2D

networks of SnSe nanowires were formed. The relatively high surface area and mechanical stability of this novel SnSe nanonetwork morphology was seen to offer improved performance and cyclability as a Li-ion battery anode material.

Chapter 4 reports on the solution-phase synthesis of pseudo 1D SnSe nanoribbons. PVP was used to selectively passivate the {100} and {001} facets, leading to growth primarily along the <010> crystal direction. These nanoribbons were seen to have thicknesses of ~11 – 13 nm, mean widths of ~40 nm and lengths of several hundreds of nanometres. Nanoribbons of a similarly layered chalcogenide material of Sb_2Te_3 are demonstrated through a CVD method in "Appendix: Additional work" at the end of this thesis.

Chapter 5 provides the conclusions of this thesis, and highlights future avenues of research that could arise from this work.

1.9 References:

(1) Gao, M. R.; Xu, Y. F.; Jiang, J.; Yu, S. H. Nanostructured Metal Chalcogenides: Synthesis, Modification, and Applications in Energy Conversion and Storage Devices. *Chem. Soc. Rev.* **2013**, *42*, 2986–3017.

(2) Davitt, F.; Stokes, K.; Collins, T. W.; Roldan-gutierrez, M.; Robinson, F.; Geaney, H.; Biswas, S.; Chang, S. L. Y.; Ryan, K. M.; Reid, G.; et al. 2D SnSe Nanonetworks; Growth and Evaluation for Li-Ion Battery Applications. *ACS Appl. Energy Mater.* **2020**, *3*, 6602–6610.

(3) Antunez, P. D.; Buckley, J. J.; Brutchey, R. L. Tin and Germanium Monochalcogenide IV–VI Semiconductor Nanocrystals for Use in Solar Cells. *Nanoscale* **2011**, *3*, 2399–2411.

(4) Minnam Reddy, V. R.; Gedi, S.; Pejjai, B.; Park, C. Perspectives on SnSe-Based Thin Film Solar Cells: A Comprehensive Review. *J. Mater. Sci. Mater. Electron.* **2016**, *27*, 5491–5508.

(5) Pejjai, B.; Minnam Reddy, V. R.; Gedi, S.; Park, C. Status Review on Earth-Abundant and Environmentally Green Sn-X (X = Se, S) Nanoparticle Synthesis by Solution Methods for Photovoltaic Applications. *Int. J. Hydrogen Energy* **2017**, *42*, 2790–2831.

(6) Zhao, L.-D.; Lo, S.-H.; Zhang, Y.; Sun, H.; Tan, G.; Uher, C.; Wolverton, C.; Dravid, V. P.; Kanatzidis, M. G. Ultralow Thermal Conductivity and High Thermoelectric Figure of Merit in SnSe Crystals. *Nature* **2014**, *508*, 373–377.

(7) Chen, Z. G.; Shi, X.; Zhao, L. D.; Zou, J. High-Performance SnSe Thermoelectric Materials: Progress and Future Challenge. *Prog. Mater. Sci.* **2018**, *97*, 283–346.

(8) Shi, X. L.; Tao, X.; Zou, J.; Chen, Z. G. High-Performance Thermoelectric SnSe: Aqueous Synthesis, Innovations, and Challenges. *Adv. Sci.* **2020**, *1902923*.

(9) Chun, D.; Walser, R. M.; Bené, R. W.; Courtney, T. H. Polarity-Dependent Memory

Switching in Devices with SnSe and $SnSe_2$ crystals. *Appl. Phys. Lett.* **1974**, *24*, 479–481.

(10) Tian, H.; Wang, X. F.; Mohammad, M. A.; Gou, G. Y.; Wu, F.; Yang, Y.; Ren, T. L. A Hardware Markov Chain Algorithm Realized in a Single Device for Machine Learning. *Nat. Commun.* **2018**, *9*, 1–11.

(11) Davitt, F.; Manning, H. G.; Robinson, F.; Hawken, S. L.; Biswas, S.; Petkov, N.; Druenen, M.; Boland, J. J.; Reid, G.; Holmes, J. D. Crystallographically Controlled Synthesis of SnSe Nanowires: Potential in Resistive Memory Devices. *Adv. Mater. Interfaces* **2020**, 2000474.

(12) Pawbake, A. S.; Jadkar, S. R.; Late, D. J. High Performance Humidity Sensor and Photodetector Based on SnSe Nanorods. *Mater. Res. Express* **2016**, *3*.

(13) Hun, X.; Wang, S.; Mei, S.; Qin, H.; Zhang, H.; Luo, X. Photoelectrochemical Dopamine Sensor Based on a Gold Electrode Modified with SnSe Nanosheets. *Microchim. Acta* **2017**, *184*, 3333–3338.

(14) Wang, J.; Yang, G. F.; Xue, J. J.; Lei, J. M.; Chen, D. J.; Lu, H.; Zhang, R.; Zheng, Y. D. A Reusable and High Sensitivity Nitrogen Dioxide Sensor Based on Monolayer SnSe. *IEEE Electron Device Lett.* **2018**, *39*, 599–602.

(15) Zheng, D.; Fang, H.; Long, M.; Wu, F.; Wang, P.; Gong, F.; Wu, X.; Ho, J. C.; Liao, L.; Hu, W. High-Performance Near-Infrared Photodetectors Based on p-Type SnX (X = S, Se) Nanowires Grown via Chemical Vapor Deposition. *ACS Nano* **2018**, *12*, 7239–7245.

(16) Hu, J.; Odom, T. W.; Lieber, C. M. Chemistry and Physics in One Dimension: Synthesis and Properties of Nanowires and Nanotubes. *Acc. Chem. Res.* **1999**, *32*, 435–445.

(17) Xu, X.; Song, Q.; Wang, H.; Li, P.; Zhang, K.; Wang, Y.; Yuan, K.; Yang, Z.; Ye, Y.; Dai, L. In-Plane Anisotropies of Polarized Raman Response and Electrical Conductivity in Layered Tin Selenide. *ACS Appl. Mater. Interfaces* **2017**, *9*, 12601–12607.

(18) Shi, W.; Gao, M.; Wei, J.; Gao, J.; Fan, C.; Ashalley, E.; Li, H.; Wang, Z. Tin Selenide (SnSe): Growth, Properties, and Applications. *Adv. Sci.* **2018**, *5*.

(19) Chattopadhyay, T.; Pannetier, J.; Von Schnering, H. G. Neutron Diffraction Study of the Structural Phase Transition in SnS and SnSe. *J. Phys. Chem. Solids* **1986**, *47*, 879–885.

(20) Abutbul, R. E.; Segev, E.; Samuha, S.; Zeiri, L.; Ezersky, V.; Makov, G.; Golan, Y. A New Nanocrystalline Binary Phase: Synthesis and Properties of Cubic Tin Monoselenide. *CrystEngComm* **2016**, *18*, 1918–1923.

(21) Sun, Y.; Zhong, Z.; Shirakawa, T.; Franchini, C.; Li, D.; Li, Y.; Yunoki, S.; Chen, X. Q. Rocksalt SnS and SnSe: Native Topological Crystalline Insulators. *Phys. Rev. B - Condens. Matter Mater. Phys.* **2013**, *88*, 1–6.

(22) Mariano, A. N.; Chopra, K. L. Polymorphism in some IV-VI Compounds Induced by High Pressure and Thin-Film Epitaxial growth. *Appl. Phys. Lett.* **1967**, *10*, 282–284.

(23) Wang, Z.; Wang, J.; Zang, Y.; Zhang, Q.; Shi, J. A.; Jiang, T.; Gong, Y.; Song, C. L.; Ji, S. H.; Wang, L. L.; et al. Molecular Beam Epitaxy-Grown SnSe in the Rock-Salt Structure: An Artificial Topological Crystalline Insulator Material. *Adv. Mater.* **2015**, *27*, 4150–4154.

(24) Ma, X. H.; Cho, K. H.; Sung, Y. M. Growth Mechanism of Vertically Aligned SnSe Nanosheets via Physical Vapour Deposition. *CrystEngComm* **2014**, *16*, 5080–5086.

(25) Wiedemeier, H.; Csillag, F. J. The Thermal Expansion and High Temperature Transformation of SnS and SnSe. *Zeitschrift für Krist. - Cryst. Mater.* **1979**, *149*, 17–29.

(26) Schnering, H. G. von; Wiedemeier, H. The High Temperature Structure of β-SnS and β-SnSe and the B16-to-B33 Type λ-Transition Path. *Zeitschrift für Krist. - Cryst. Mater.* **1981**, *156*, 143–150.

(27) Alptekin, S. Structural Phase Transition of SnSe under Uniaxial Stress and Hydrostatic Pressure: An Ab Initio Study. *J. Mol. Model.* **2011**, *17*, 2989–2994.

(28) Loa, I.; Husband, R. J.; Downie, R. A.; Popuri, S. R.; Bos, J. W. G. Structural Changes in Thermoelectric SnSe at High Pressures. *J. Phys. Condens. Matter* **2015**, *27*, 72202.

(29) Jian, Z.; Zhu, H.; Wu, X.; Cui, H.; Li, D.; Jiang, J.; Gao, C.; Wang, Q.; Cui, Q. Plasma-Assisted Synthesis and Pressure-Induced Structural Transition of Single-Crystalline SnSe Nanosheets. *Nanoscale* **2015**, *7*, 10807–10816.

(30) Yu, H.; Dai, S.; Chen, Y. Enhanced Power Factor via the Control of Structural Phase Transition in SnSe. *Sci. Rep.* **2016**, *6*, 1–12.

(31) Lee, Y. K.; Ahn, K.; Cha, J.; Zhou, C.; Kim, H. S.; Choi, G.; Chae, S. I.; Park, J. H.; Cho, S. P.; Park, S. H.; et al. Enhancing P-Type Thermoelectric Performances of Polycrystalline SnSe via Tuning Phase Transition Temperature. *J. Am. Chem. Soc.* **2017**, *139*, 10887–10896.

(32) Jin, W.; Vishwanath, S.; Liu, J.; Kong, L.; Lou, R.; Dai, Z.; Sadowski, J. T.; Liu, X.; Lien, H. H.; Chaney, A.; et al. Electronic Structure of the Metastable Epitaxial Rock-Salt SnSe {111} Topological Crystalline Insulator. *Phys. Rev. X* **2017**, *7*, 1–9.

(33) Xie, Y.; Zhou, Y.; Gong, X. G. The Intrinsic Low Lattice Thermal Conductivity in the Rock Salt SnSe. *Comput. Mater. Sci.* **2018**, *148*, 54–59.

(34) Barrios-Salgado, E.; Rodríguez-Guadarrama, L. A.; Garcia-Angelmo, A. R.; Campos Álvarez, J.; Nair, M. T. S.; Nair, P. K. Large Cubic Tin Sulfide–Tin Selenide Thin Film Stacks for Energy Conversion. *Thin Solid Films* **2016**, *615*, 415–422.

(35) Nair, P. K.; Barrios-Salgado, E.; Nair, M. T. S. Cubic-Structured Tin Selenide Thin Film as a Novel Solar Cell Absorber. *Phys. Status Solidi Appl. Mater. Sci.* **2016**, *213*, 2229–2236.

(36) Butt, F. K.; Ul Haq, B.; ur Rehman, S.; Ahmed, R.; Cao, C.; AlFaifi, S. Investigation of

Thermoelectric Properties of Novel Cubic Phase SnSe: A Promising Material for Thermoelectric Applications. *J. Alloys Compd.* **2017**, *715*, 438–444.

(37) Zhao, L. D.; Chang, C.; Tan, G.; Kanatzidis, M. G. SnSe: A Remarkable New Thermoelectric Material. *Energy Environ. Sci.* **2016**, *9*, 3044–3060.

(38) Zhang, L.; Lu, L.; Zhang, D.; Hu, W.; Wang, N.; Xu, B.; Li, Y.; Zeng, H. Dual-Buffered SnSe@CNFs as Negative Electrode with Outstanding Lithium Storage Performance. *Electrochim. Acta* **2016**, *209*, 423–429.

(39) Gurung, A.; Naderi, R.; Vaagensmith, B.; Varnekar, G.; Zhou, Z.; Elbohy, H.; Qiao, Q. Tin Selenide – Multi-Walled Carbon Nanotubes Hybrid Anodes for High Performance Lithium-Ion Batteries. *Electrochim. Acta* **2016**, *211*, 720–725.

(40) Wang, X.; Liu, B.; Xiang, Q.; Wang, Q.; Hou, X.; Chen, D.; Shen, G. Spray-Painted Binder-Free SnSe Electrodes for High-Performance Energy-Storage Devices. *ChemSusChem* **2014**, *7*, 308–313.

(41) Wang, D.; Zhang, K.; Zhu, Y.; Lan, Y.; Hu, L.; Lin, N.; Zhou, J.; Qian, Y. A Novel Strategy to Prepare Graphene Oxide-Wrapped Nanocrystals Composite for High-Performance Lithium Storage. *Mater. Lett.* **2016**, *175*, 32–35.

(42) Kang, S. Z.; Jia, L.; Li, X.; Yin, Y.; Li, L.; Guo, Y. G.; Mu, J. Amine-Free Preparation of SnSe Nanosheets with High Crystallinity and Their Lithium Storage Properties. *Colloids Surfaces A Physicochem. Eng. Asp.* **2012**, *406*, 1–5.

(43) Yuan, S.; Zhu, Y. H.; Li, W.; Wang, S.; Xu, D.; Li, L.; Zhang, Y.; Zhang, X. B. Surfactant-Free Aqueous Synthesis of Pure Single-Crystalline SnSe Nanosheet Clusters as Anode for High Energy- and Power-Density Sodium-Ion Batteries. *Adv. Mater.* **2017**, *29*, 1–6.

(44) Park, G. D.; Lee, J. H.; Kang, Y. C. Superior Na-Ion Storage Properties of High Aspect Ratio SnSe Nanoplates Prepared by a Spray Pyrolysis Process. *Nanoscale* **2016**, *8*,

11889–11896.

(45) Xue, M. Z.; Yao, J.; Cheng, S. C.; Fu, Z. W. Lithium Electrochemistry of a Novel SnSe Thin-Film Anode. *J. Electrochem. Soc.* **2006**, *153*, 270–274.

(46) Wang, W.; Li, P.; Zheng, H.; Liu, Q.; Lv, F.; Wu, J.; Wang, H.; Guo, S. Ultrathin Layered SnSe Nanoplates for Low Voltage, High-Rate, and Long-Life Alkali–Ion Batteries. *Small* **2017**, *13*, 1–7.

(47) Cheng, Y.; Huang, J.; Li, J.; Cao, L.; Xu, Z.; Luo, X.; Qi, H.; Guo, P. SnSe/r-GO Composite with Enhanced Pseudocapacitance as a High-Performance Anode for Li-Ion Batteries. *ACS Sustain. Chem. Eng.* **2019**, *7*, 8637–8646.

(48) Zhang, Z.; Zhao, X.; Li, J. SnSe/Carbon Nanocomposite Synthesized by High Energy Ball Milling as an Anode Material for Sodium-Ion and Lithium-Ion Batteries. *Electrochim. Acta* **2015**, *176*, 1296–1301.

(49) Im, H. S.; Lim, Y. R.; Cho, Y. J.; Park, J.; Cha, E. H.; Kang, H. S. Germanium and Tin Selenide Nanocrystals for High-Capacity Lithium Ion Batteries: Comparative Phase Conversion of Germanium and Tin. *J. Phys. Chem. C* **2014**, *118*, 21884–21888.

(50) Kim, Y.; Kim, Y.; Park, Y.; Jo, Y. N.; Kim, Y.-J.; Choi, N.-S.; Lee, K. T. SnSe Alloy as a Promising Anode Material for Na-Ion Batteries. *Chem. Commun.* **2015**, *51*, 50–53.

(51) Lee, D.-H.; Park, C.-M. Tin Selenides with Layered Crystal Structures for Li-Ion Batteries: Interesting Phase Change Mechanisms and Outstanding Electrochemical Behaviors. *ACS Appl. Mater. Interfaces* **2017**, *9*, 15439–15448.

(52) Lee, S.-H.; Jung, Y.; Agarwal, R. Highly Scalable Non-Volatile and Ultra-Low-Power Phase-Change Nanowire Memory. *Nat. Nanotechnol.* **2007**, *2*, 626–630.

(53) Chan, C. K.; Peng, H.; Liu, G.; McIlwrath, K.; Zhang, X. F.; Huggins, R. A.; Cui, Y. High-Performance Lithium Battery Anodes Using Silicon Nanowires. *Nat. Nanotechnol.* **2008**, *3*, 31–35.

(54) Hochbaum, A. I.; Chen, R.; Delgado, R. D.; Liang, W.; Garnett, E. C.; Najarian, M.; Majumdar, A.; Yang, P. Enhanced Thermoelectric Performance of Rough Silicon Nanowires. *Nature* **2008**, *451*, 163–167.

(55) Vaughn, D. D.; In, S. Il; Schaak, R. E. A Precursor-Limited Nanoparticle Coalescence Pathway for Tuning the Thickness of Laterally-Uniform Colloidal Nanosheets: The Case of SnSe. *ACS Nano* **2011**, *5*, 8852–8860.

(56) Li, L.; Chen, Z.; Hu, Y.; Wang, X.; Zhang, T.; Chen, W.; Wang, Q. Single-Layer Single-Crystalline SnSe Nanosheets. *J. Am. Chem. Soc.* **2013**, *135*, 1213–1216.

(57) Jang, K.; Lee, I. Y.; Xu, J.; Choi, J.; Jin, J.; Park, J. H.; Kim, H. J.; Kim, G. H.; Son, S. U. Colloidal Synthesis of SnSe Nanocolumns through Tin Precursor Chemistry and Their Optoelectrical Properties. *Cryst. Growth Des.* **2012**, *12*, 3388–3391.

(58) Boscher, N. D.; Carmalt, C. J.; Palgrave, R. G.; Parkin, I. P. Atmospheric Pressure Chemical Vapour Deposition of SnSe and $SnSe_2$ Thin Films on Glass. *Thin Solid Films* **2008**, *516*, 4750–4757.

(59) De Groot, C. H.; Gurnani, C.; Hector, A. L.; Huang, R.; Jura, M.; Levason, W.; Reid, G. Highly Selective Chemical Vapor Deposition of Tin Diselenide Thin Films onto Patterned Substrates via Single Source Diselenoether Precursors. *Chem. Mater.* **2012**, *24*, 4442–4449.

(60) Zhao, S.; Wang, H.; Zhou, Y.; Liao, L.; Jiang, Y.; Yang, X.; Chen, G.; Lin, M.; Wang, Y.; Peng, H.; et al. Controlled Synthesis of Single-Crystal SnSe Nanoplates. *Nano Res.* **2015**, *8*, 288–295.

(61) Wang, W.; Geng, Y.; Yan, P.; Liu, F.; Xie, Y.; Qian, Y. A Novel Mild Route to Nanocrystalline Selenides at Room Temperature. *J. Am. Chem. Soc.* **1999**, *121*, 4062–4063.

(62) Li, B.; Xie, Y.; Huang, J.; Qian, Y. Solvothermal Route to Tin Monoselenide Bulk

Single Crystal with Different Morphologies. *Inorg. Chem.* **2000**, *39*, 2061–2064.

(63) Han, Z.; Li, Y.; Yu, S.; Zhong, C.; Chen, X.; Zhao, H.; Qian, Y. An Organic Solution Method for Crystal Growth of Tin Chalcogenides with Special Morphologies. *J. Cryst. Growth* **2001**, *223*, 1–5.

(64) Shen, G.; Chen, D.; Jiang, X.; Tang, K.; Liu, Y.; Qian, Y. Rapid Synthesis of SnSe Nanowires via an Ethylenediamine-Assisted Polyol Route. *Chem. Lett.* **2003**, *32*, 426–427.

(65) Han, Q.; Zhu, Y.; Wang, X.; Ding, W. Room Temperature Growth of SnSe Nanorods from Aqueous Solution. *J. Mater. Sci.* **2004**, *39*, 4643–4646.

(66) Wang, F.; Dong, A.; Sun, J.; Tang, R.; Yu, H.; Buhro, W. E. Solution-Liquid-Solid Growth of Semiconductor Nanowires. *Inorg. Chem.* **2006**, *45*, 7511–7521.

(67) Liu, S.; Guo, X.; Li, M.; Zhang, W. H.; Liu, X.; Li, C. Solution-Phase Synthesis and Characterization of Single-Crystalline SnSe Nanowires. *Angew. Chemie - Int. Ed.* **2011**, *50*, 12050–12053.

(68) Wang, R.; Wei, M.; Jiang, G.; Liu, W.; Zhu, C. Study of the Preperation of Snse Nanorods with Selenium Dioxide as Source. *Chem. Lett.* **2014**, *43*, 693–695.

(69) Guo, J.; Jian, J.; Liu, J.; Cao, B.; Lei, R.; Zhang, Z.; Song, B.; Zhao, H. Synthesis of SnSe Nanobelts and the Enhanced Thermoelectric Performance in Its Hot-Pressed Bulk Composite. *Nano Energy* **2017**, *38*, 569–575.

(70) Tang, Z.; Zhao, P.; Ni, D.; Liu, Y.; Zhang, M.; Wang, H.; Zhang, H.; Gao, H.; Yao, Z.; Bu, W. Pyroelectric Nanoplatform for NIR-II-Triggered Photothermal Therapy with Simultaneous Pyroelectric Dynamic Therapy. *Mater. Horizons* **2018**, *5*, 946–952.

(71) Das, L.; Guleria, A.; Neogy, S.; Adhikari, S. Tuning of the Aspect Ratio of SnSe Nanorods: A Rapid and Facile Microemulsion Templated Approach. *Colloids Surfaces A Physicochem. Eng. Asp.* **2018**, *555*, 781–786.

(72) Shi, X.; Zheng, K.; Hong, M.; Liu, W.; Moshwan, R.; Wang, Y.; Qu, X.; Chen, Z. G.; Zou, J. Boosting the Thermoelectric Performance of P-Type Heavily Cu-Doped Polycrystalline SnSe: Via Inducing Intensive Crystal Imperfections and Defect Phonon Scattering. *Chem. Sci.* **2018**, *9*, 7376–7389.

(73) Bo, A.; Liu, Q.; Zhan, H.; Shi, X.; Chen, Z. G.; Gu, Y. Atomic Investigation on the Facet-Dependent Melting of Ceramic Nanostructures via In Situ Electron Irradiation. *Adv. Mater. Interfaces* **2020**, *2000288*, 1–9.

(74) Kundu, S.; Yi, S. I.; Yu, C. Gram-Scale Solution-Based Synthesis of SnSe Thermoelectric Nanomaterials. *Appl. Surf. Sci.* **2018**, *459*, 376–384.

(75) Yuan, H.; Jin, Y.; Lan, J.; Liu, Y.; Yu, Y.; Yang, X. In Situ Synthesized SnSe Nanorods in a SnO x @CNF Membrane toward High-Performance Freestanding and Binder-Free Lithium-Ion Batteries. *Inorg. Chem. Front.* **2018**, *5*, 932–938.

(76) Fortuna, S. A.; Li, X. Metal-Catalyzed Semiconductor Nanowires: A Review on the Control of Growth Directions. *Semicond. Sci. Technol.* **2010**, *25*.

(77) Güniat, L.; Caroff, P.; Fontcuberta I Morral, A. Vapor Phase Growth of Semiconductor Nanowires: Key Developments and Open Questions. *Chem. Rev.* **2019**, *119*, 8958–8971.

(78) Pol, V. G.; Pol, S. V.; Gedanken, A. Core-Shell Nanorods of SnS-C and SnSe-C: Synthesis and Characterization. *Langmuir* **2008**, *24*, 5135–5139.

(79) Butt, F. K.; Mirza, M.; Cao, C.; Idrees, F.; Tahir, M.; Safdar, M.; Ali, Z.; Tanveer, M.; Aslam, I. Synthesis of Mid-Infrared SnSe Nanowires and Their Optoelectronic Properties. *CrystEngComm* **2014**, *16*, 3470.

(80) Cao, J.; Wang, Z.; Zhan, X.; Wang, Q.; Safdar, M.; Wang, Y.; He, J. Vertical SnSe Nanorod Arrays: From Controlled Synthesis and Growth Mechanism to Thermistor and Photoresistor. *Nanotechnology* **2014**, *25*, 105705.

(81) Liu, J.; Jian, J.; Yu, Z.; Zhang, Z.; Cao, B.; Du, B. Catalyst-Free Vapor Phase Growth

of Ultralong SnSe Single-Crystalline Nanowires. *Cryst. Growth Des.* **2017**, *17*, 6163–6168.

(82) Gurnani, C.; Hawken, S. L.; Hector, A. L.; Huang, R.; Jura, M.; Levason, W.; Perkins, J.; Reid, G.; Stenning, G. B. G. Tin(IV) Chalcogenoether Complexes as Single Source Precursors for the Chemical Vapour Deposition of SnE_2 and SnE (E = S, Se) Thin Films. *Dalt. Trans.* **2018**, *47*, 2628–2637.

(83) Khan, M. D.; Aamir, M.; Sohail, M.; Sher, M.; Baig, N.; Akhtar, J.; Malik, M. A.; Revaprasadu, N. Bis(Selenobenzoato)Dibutyltin(IV) as a Single Source Precursor for the Synthesis of SnSe Nanosheets and Their Photo-Electrochemical Study for Water Splitting. *Dalt. Trans.* **2018**, *47*, 5465–5473.

(84) Smith, A. J.; Meek, P. E.; Liang, W. Y. Raman Scattering Studies of SnS_2 and $SnSe_2$. *J. Phys. C Solid State Phys.* **1977**, *10*, 1321–1323.

(85) Fernandes, P. A.; Sousa, M. G.; Salomé, P. M. P.; Leitão, J. P.; da Cunha, A. F. Thermodynamic Pathway for the Formation of SnSe and $SnSe_2$ Polycrystalline Thin Films by Selenization of Metal Precursors. *CrystEngComm* **2013**, *15*, 10278.

(86) Liu, J.; Zhou, Y.; Liang, Y.; Liu, M.; Huang, Z.; Lin, L.; Zheng, W.; Lai, F. Large Scale SnSe Pyramid Structure Grown by Gradient Vapor Deposition Method. *CrystEngComm* **2018**, *20*, 1037–1041.

(87) Hernandez, J. A.; Ruiz, A.; Fonseca, L. F.; Pettes, M. T.; Jose-Yacaman, M.; Benitez, A. Thermoelectric Properties of SnSe Nanowires with Different Diameters. *Sci. Rep.* **2018**, *8*, 1–8.

(88) Zhao, L.; Yosef, M.; Steinhart, M.; Göring, P.; Hofmeister, H.; Gösele, U.; Schlecht, S. Porous Silicon and Alumina as Chemically Reactive Templates for the Synthesis of Tubes and Wires of SnSe, Sn, and SnO_2. *Angew. Chemie Int. Ed.* **2006**, *45*, 311–315.

(89) Carter, R.; Suyetin, M.; Lister, S.; Dyson, M. A.; Trewhitt, H.; Goel, S.; Liu, Z.;

Suenaga, K.; Giusca, C.; Kashtiban, R. J.; et al. Band Gap Expansion, Shear Inversion Phase Change Behaviour and Low-Voltage Induced Crystal Oscillation in Low-Dimensional Tin Selenide Crystals. *Dalt. Trans.* **2014**, *43*, 7391–7399.

(90) Slade, C. A.; Sanchez, A. M.; Sloan, J. Unprecedented New Crystalline Forms of SnSe in Narrow to Medium Diameter Carbon Nanotubes. *Nano Lett.* **2019**, *19*, 2979–2984.

(91) Han, M. Y.; Özyilmaz, B.; Zhang, Y.; Kim, P. Energy Band-Gap Engineering of Graphene Nanoribbons. *Phys. Rev. Lett.* **2007**, *98*, 1–4.

(92) Li, S.; Lin, Y.; Zhao, W.; Wu, J.; Wang, Z.; Hu, Z.; Shen, Y.; Tang, D.; Wang, J.; Zhang, Q.; et al. Vapour–Liquid–Solid Growth of Monolayer MoS_2 Nanoribbons. *Nat. Mater.* **2018**, 17, 535-542.

(93) Deng, Z.; Cao, D.; He, J.; Lin, S.; Lindsay, S. M.; Liu, Y. Solution Synthesis of Ultrathin Single-Crystalline SnS Nanoribbons for Photodetectors via Phase Transition and Surface Processing. *ACS Nano* **2012**, *6*, 6197–6207.

(94) Liu, X.; Lin, Y.; Zhou, S.; Sheehan, S.; Wang, D. Complex Nanostructures: Synthesis and Energetic Applications. *Energies* **2010**, *3*, 285–300.

(95) Cheng, C.; Fan, H. J. Branched Nanowires: Synthesis and Energy Applications. *Nano Today* **2012**, *7*, 327–343.

(96) Huang, Y.; Ling, C.; Liu, H.; Wang, S. Edge-, Width- and Strain-Dependent Semiconductor-Metal Transition in SnSe Nanoribbons. *RSC Adv.* **2014**, *4*, 6933–6938.

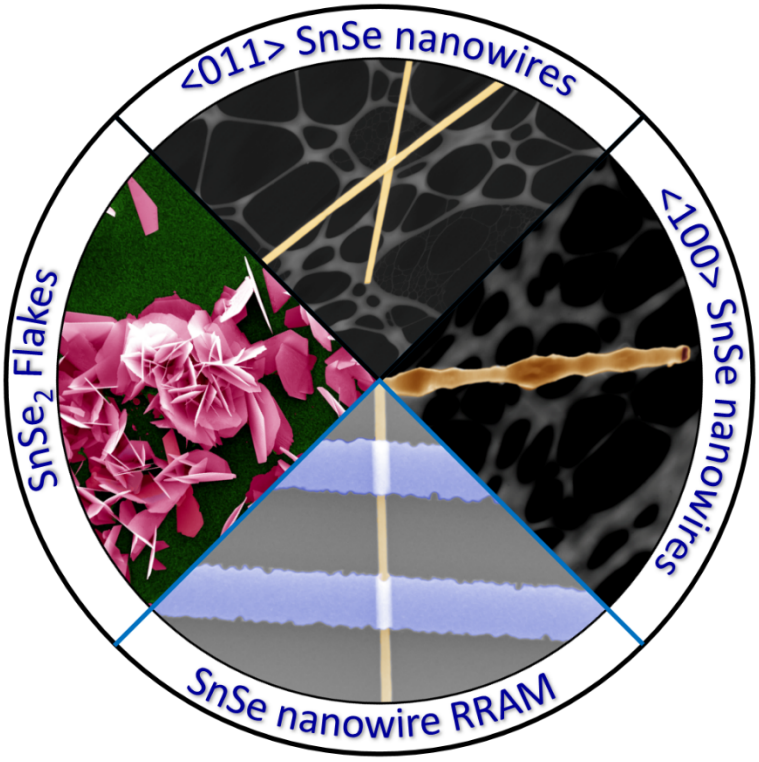
(97) Yang, Y.; Zhou, Y.; Luo, Z.; Guo, Y.; Rao, D.; Yan, X. Electronic Structures and Transport Properties of SnS-SnSe Nanoribbon Lateral Heterostructures. *Phys. Chem. Chem. Phys.* **2019**, *21*, 9296–9301.

(98) Lin, C.; Cheng, W.; Guo, Z.; Chai, G.; Zhang, H. Exceptional Thermoelectric Performance of a “Star-like” SnSe Nanotube with Ultra-Low Thermal Conductivity and a High Power Factor. *Phys. Chem. Chem. Phys.* **2017**, *19*, 23247–23253.

(99) Tyagi, K.; Waters, K.; Wang, G.; Gahtori, B.; Haranath, D.; Pandey, R. Thermoelectric Properties of SnSe Nanoribbons: A Theoretical Aspect. *Mater. Res. Express* **2016**, *3*.

Chapter 2

Crystallographically Controlled Synthesis of SnSe Nanowires: Potential in Resistive Memory Devices



Nanomaterial growth and analysis was performed by myself; including all CVD reactions, SEM, EDX, TEM, electron diffraction, XRD and Raman analysis.

Fred Robinson and Samantha L. Hawken provided the starting precursor for the CVD experiments.

Hugh G. Manning and John J. Boland performed electrical measurements based on the SnSe nanowires.

Nikolay Petkov prepared FIB cross sections of the SnSe nanowires.

Maart van Druenen preformed the XPS analysis.

I co-wrote this paper with Subhajit Biswas, Hugh G. Manning and Justin D. Holmes.

Davitt, F., Manning, H. G., Robinson, F., Hawken, S. L., Biswas, S., Petkov, N., van Druenen, M., Boland, J. J., Reid, G., Holmes, J. D., *Crystallographically Controlled Synthesis of SnSe Nanowires: Potential in Resistive Memory Devices*. Adv. Mater. Interfaces 2020, 7, 2000474. https://doi.org/10.1002/admi.202000474

2.1 Abstract

Here the controlled growth of SnSe nanowires by a liquid injection chemical vapor deposition (CVD) method employing a distorted octahedral [$SnCl_4\{^nBuSe(CH_2)_3Se^nBu\}$] single source diselenoether precursor is reported. CVD with this single source precursor allows morphological and compositional control of the $SnSe_x$ nanostructures formed, including the transformation of $SnSe_2$ nanoflakes into SnSe nanowires and again to SnSe nanoflakes with increasing growth temperature. Significantly, highly crystalline SnSe nanowires with an orthorhombic Pnma 62 crystal structure could be controllably synthesized in two growth directions, either <011> or <100>. The ability to tune the growth direction of SnSe will have important implications for devices constructed using these nanocrystals. The SnSe nanowires with a <011> growth direction display a reversible polarity dependent memory switching ability, not previously reported for nanoscale SnSe. A resistive switching on/off ratio of 10^3 without the use of a current compliance limit was seen, illustrating the potential use of SnSe nanowires for low power non-volatile memory applications.

2.2 Introduction

The drive to further advance energy technologies,[1,2] optoelectronic[3–6] devices and nanoelectronic[7–13] applications, such as memory[14–16] devices, has led to great interest in layered metal chalcogenide materials, which exhibit strong in-plane chemical bonds, but weak out-of-plane van der Waals bonds. This group of layered materials have been comprehensively studied, both theoretically and experimentally, particularly the exfoliation and synthesis of few-layer two dimensional (2D) structures of these materials.[17–19] In general, 2D materials possess highly interesting electrical, optical, electrochemical and mechanical properties, such as layer dependent bandgaps, leading to tuneable optical and electrical properties.[20–23] Whilst 2D variants of layered chalcogenides have developed a firm grounding in the literature, one

dimensional (1D) forms of these metal chalcogenides have recently begun to garner interest due to their potential for scalable device architectures, larger surface areas and lower active device volumes due to the small diameter of the nanowire. Due to the lower active volumes, limiting the region where any electronic, heating or chemical interaction will take place, scaling the dimensions of devices down to nanowire form is appealing for increased stability[24] and also reduced device power requirements.[25] Confining 2D materials into a 1D morphology would constitute the basis for further developing 1D nano/opto-electronics, where some of the novel physics of 2D ultra-thin lattices can be incorporated into 1D materials. Current reports of 1D metal chalcogenide layered materials are mostly centred on transition metal dichalcogenides (TMDCs) such as MoS_2.[26,27]

Recently IV-VI monochalcogenide layered materials have been proposed as promising candidates for sustainable electronic and photonic devices.[28] Among these materials, SnSe with a layered puckered crystal structure, has the advantage of being relatively Earth abundant and non-toxic compared to other popular materials for energy and memory device applications, such as Bi_2Te_3 and GeTe. SnSe is an indirect bandgap semiconductor, with a small difference between the indirect and direct band gaps (bulk indirect band gap of 0.90 eV and a direct band gap of 1.30 eV),[29] giving opportunities for an indirect to direct bandgap crossover with external perturbation such as strain. An advanced study of 1D SnSe is also of importance for many technological areas of interest, with SnSe having great potential for applications in non-volatile memory devices,[15,16] field effect transistors,[30] sensors[31,32] and photodetectors.[31,33] Engineering these materials in nanowire form is particularly appealing for device scaling and integration, as well as potentially lower power consumption, particularly in relation to nanoscale memory devices, such as phase change random-access memory (PCRAM) and resistive random-access memory (RRAM) devices.[25,34–36] SnSe has recently presented interest for use in RRAM

devices, with SnO_x/SnSe/SnO_x layered devices shown to exhibit unipolar resistive switching.[37] Structuring the RRAM device in a nanowire form can offer added benefits such as controlled orientation of the SnSe crystal. For memory applications, control over the morphology of the nanowire is important as this can drastically affect the optical and electronic properties of the material. Additionally, 1D nanostructures provide an excellent route to facilitate the construction of devices with tailored crystal direction. This is more important for SnSe as it is a highly anisotropic material, and has been shown, for example, to exhibit vastly different thermoelectric figures of merit along its different crystal orientations.[38]

Nanowires of tin monoselenide (SnSe) have been sparsely reported previously, through both high-temperature CVD and solution based methods containing toxic catalyst metals and solvents.[39–41] But the tailored growth of 1D SnSe nanowires has not been explored in great detail to date, with different growth methods producing nanowires with varying crystal growth directions, e.g. <011> growth by CVD[40] and <100> growth using a Bi-seeded solution phase approach.[41] Importantly, the previous reports on SnSe nanowires lack details on the effect of growth constraints on the structure, composition and morphology of the nanocrystals formed,[39–41] which is essential for the future development for this technologically relevant material. In this regard, as precursor decomposition kinetics can play a major role in CVD growth methods, by influencing the partial pressure of the vapour source, the use of a customized single source CVD precursor has advantages over using multi-precursor, elemental or powder sources. Single source precursors can have a single decomposition temperature, and can thus supply reaction species with pre-formed bonds, Sn-Se in the case of SnSe, leading to uniform control of the deposited material's composition.[42] The use of single source precursors also leads to controlled adsorption and deposition at the growth interfaces, which results in improved control over the morphology.[43–45]

Herein we report the controlled growth of SnSe nanowires via an atmospheric pressure CVD reaction from a single source diselenother precursor, [$SnCl_4${$^nBuSe(CH_2)_3Se^nBu$}]. The critical growth parameters for nanowire growth, as well as their crystal structure, were explored in detail. The diselenother precursor also allows morphology, phase and crystal orientation controlled synthesis of nanowire and 2D sheets of SnSe and $SnSe_2$ through manipulation of the CVD growth parameters. Due to the relatively low decomposition temperature of this precursor, the thermal budget required for the growth of these SnSe nanowires has also been significantly reduced from 850 – 950 °C to 500 – 550 °C, compared to previous reports of CVD grown SnSe nanowires.[40] We present electrical data from SnSe nanowires with a <011> growth direction, which are shown to undergo electrically stimulated bipolar resistive switching, illustrating the potential use of these SnSe nanowires in non-volatile memory applications.

2.3 Experimental

$SnSe_x$ nanostructures were synthesized using a liquid-injection CVD method, utilizing [$SnCl_4${$^nBuSe(CH_2)_3Se^nBu$}] as a customized single source diselenoether precursor. This precursor was prepared as described in the previous report[46] by a reaction of $SnCl_4$ with the selenoether ligand in anhydrous CH_2Cl_2.[46] This precursor was dissolved at a concentration of 7.5 mg ml^{-1} in anhydrous toluene, inside a nitrogen filled glovebox, before being loaded into a Hamilton sample-lock Gastight syringe.

$SnSe_2$ and SnSe nanostructures were grown on silicon (100) substrates with a native oxide. The substrates were cleaned in acetone and isopropyl alcohol (IPA), before being dried with nitrogen and heated in a vacuum oven at 70 °C overnight, to ensure thorough removal of

residual moisture. Using a Quorum Q150R S sputter coater, the Si wafers were coated with a 3 nm thick Au film and transferred to the CVD chamber with a 6 mm inside diameter quartz tube lining. The Si substrate was placed approximately 5 cm downstream from the centre of the tube furnace. Prior to precursor injection, the chamber was dried under vacuum and purged with high purity argon gas. The reaction chamber was heated to the desired temperature, with a constant set flow of 1.1 sccm of argon gas. Injection of the precursor was then initiated and maintained at a constant rate of 1.5 ml h^{-1} using a KDS series 100 single-syringe pump until the desired injection volume was achieved. Nanowire growth was investigated over the temperature range between 450 - 550 °C.

2.4 Characterisation

After removal from the CVD chamber, the synthesized nanomaterials were analysed using a Helios Nanolab 600i scanning electron microscope (SEM) and a Zeiss Supra 40 SEM. Raman scattering spectroscopy was performed with a Renishaw InVia Raman spectrometer equipped with a 2400 lines/mm grating using a 514 nm laser. Spectra were collected using a RenCam CCD camera, with the beam focused onto the samples using a 50× objective lens. Measurements were undertaken at 1 % of the total 1.9 mW laser power. The crystal structure of the product was confirmed by X-ray diffraction (XRD) using a Philips X'pert Pro MPD equipped with a Panalytical Empyrean Cu X-ray tube and a Philips X'celerator detector. X-ray photoelectron spectroscopy (XPS) analysis was completed on an Oxford Applied Research Escabase XPS system with a base pressure of 5 x 10^{-10} mbar and a nonmonochromated Al K_α X-ray source at 200 W. Survey spectra were recorded at 0 - 1000 eV at a step size of 0.7 eV, a dwell time of 0.3 s and a pass energy of 100 eV. Core levels scans were acquired at a step size of 0.1 eV, a dwell time of 0.1 s and a pass energy of 20 eV. CasaXPS software was used for spectra processing with peaks corrected to a Shirley background and fitted to Voigt profiles.

Charge correction was based on the C 1s peak at 285 eV. The products were mechanically removed from the Si growth substrate for (scanning) transmission electron microscopy ((S)TEM) and energy dispersive X-ray (EDX) analysis. Removal of the nanomaterial was easily achieved through a quick sonication of the growth substrate in an ultrasonic bath, using a small amount of IPA. The resulting solution was then drop-cast onto a carbon coated TEM grid. TEM and STEM analysis was performed on a FEI Titan electron microscope operating at 300 kV, equipped with HAADF detectors and EDX. Cross-sections of SnSe nanowires were prepared using a Helios Nanolab 600i focused ion beam (FIB) and the STEM mode was used on the same instrument for EDX elemental mapping at 30kV. The Vesta software was used for the illustration of crystal structures.[47] For electrical device fabrication, SnSe nanowires were transferred from the growth substrate into solution by sonicating the substrate in an IPA solution at a frequency of 37 kHz and a power of 175 W for 30 s. The SnSe solution was drop-cast onto a clean Si substrate (1 μm thermal oxide) with optical lithography-defined contact pads and alignment marks of Ti/Au (5/25 nm). Single SnSe nanowires were contacted by electron beam lithography (EBL) using contacts of Ti-Al-Au (5-170-10 nm) deposited by thermal evaporation. Electrical measurements were carried out at room temperature using a Keithley 4200-SCS.

2.5 Results and Discussion

$SnSe_x$ nanostructures were synthesised using a liquid-injection CVD method, utilising $[SnCl_4\{^nBuSe(CH_2)_3Se^nBu\}]$ as a customised single source diselenoether precursor.[46] Nanowires were grown on silicon (100) substrates with Au catalyst via a conventional vapour-liquid-solid (VLS) growth (see appendix Figure A.2.1 for a typical VLS growth schematic). Nanowire growth was investigated over the temperature range between 450 - 550 °C under a

flowing Ar (1.1 sccm) atmosphere (see the Experimental and Characterisation sections for more detail).

The morphology of the nanostructures grown on Si substrates at different CVD growth temperatures (450 - 550 °C) are shown in the SEM images of Figure 2.1. At the lowest growth temperature of 450 °C, a material with a flower-like morphology was produced (Figure 2.1(a)). These flowers were several tens of microns in size, in the range of 10 - 40 μm and consisted of many individual flakes growing in a vertical manner from the underlying silicon substrate, as commonly seen for other layered materials.[48] The "petals" of these flowers were easily separated by sonication in isopropyl alcohol (IPA) to obtain individual flake structures (see appendix Figure A.2.2). These flakes had lengths and widths between 1 - 5 μm and thicknesses between 20 - 100 nm (inset of Figure 2.1(a)). At this low growth temperature, *i.e.* 450 °C, whilst the Au film does melt to form droplets (see appendix Figure A.2.3) on the Si surface, no indication of vapour-liquid-solid (VLS) growth, and the subsequent growth of 1D nanostructures was observed at this temperature. This suggests that the temperature of 450 °C is not high enough to form a liquid eutectic alloy with the Sn and Se to instigate VLS growth. Instead, the condensation of the $SnSe_2$ vapour leads to the vapour-solid (VS) growth of the flake structures, similar to previous studies using this precursor.[46] The growth of tin selenide materials in a flake structure is readily observed in the literature.[49,50] This predisposition for the formation of flake-like structures is attributed to the slower growth rate along the <100> van der Waals bonding direction. The slower growth rate is ascribed to the much larger lattice spacing in this direction, and the subsequently increased difficulty of atomic addition to this plane, resulting in the radial growth of the flakes being more energetically favourable than the addition of <100> directional layers to the flakes.

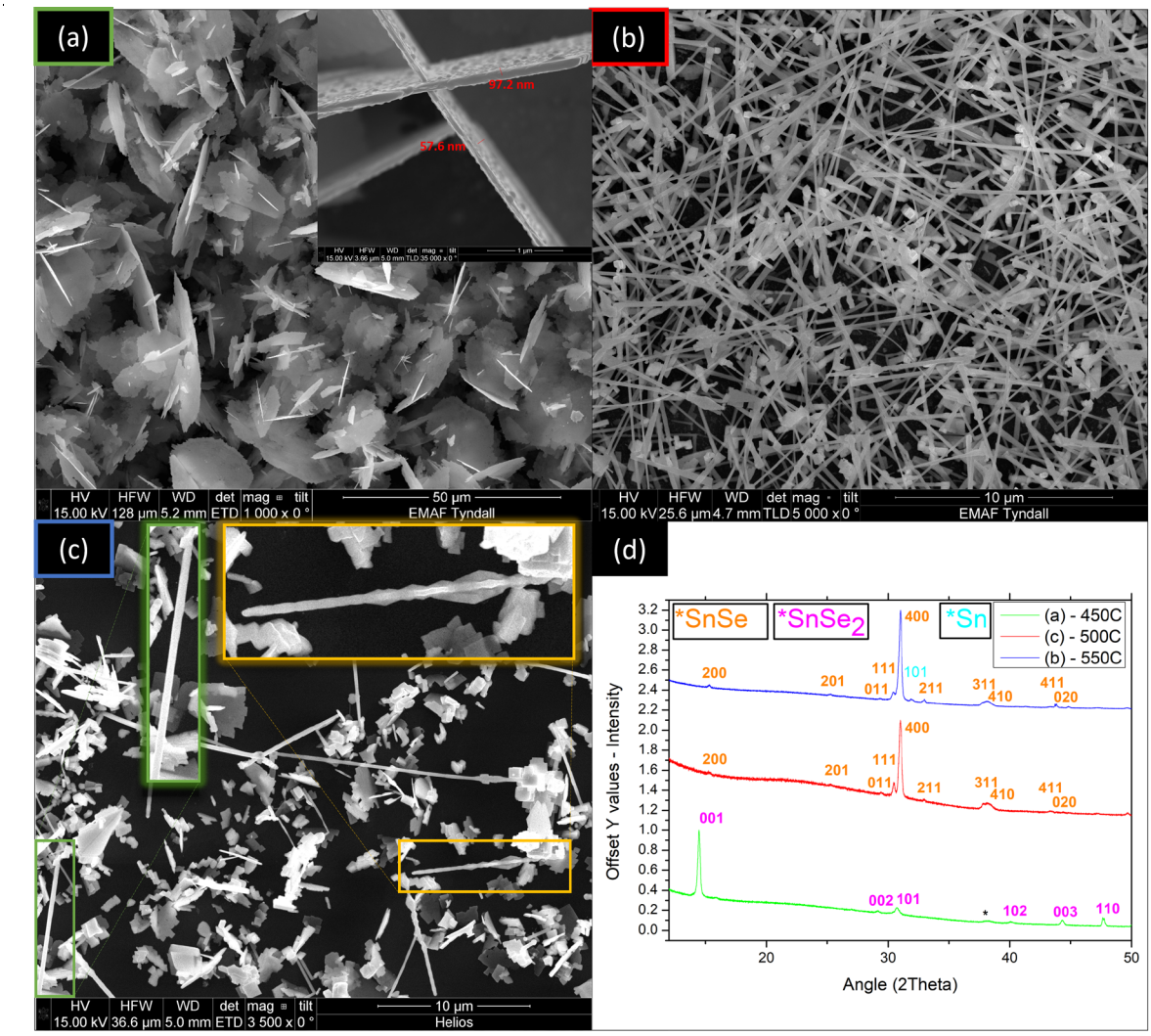


Figure 2.1: SEM images showing the evolution of the $SnSe_x$ nanostructures with respect to the growth temperature: (a) large flakes with diameters of several microns grown at 450 °C, with a thickness of ~ 60 nm shown in the inset, (b) high yield of nanowire growth at 500 °C. (c) A growth temperature of 550 °C leads a further change in the morphology, with the formation of both 2D flakes and 1D wires. The insets show the wires formed at this temperature, which consist of two visually different types. A "type A" nanowire is shown in the green border inset, and a "type B" nanowire is shown in the yellow bordered inset. (d) XRD analysis of the samples shown in (a), (b) and (c), which are assigned to P-3m1 164 hexagonal $SnSe_2$ (JCPDS 23-0602) [Magenta] and Pnma 62 orthorhombic SnSe (JCPDS 48-1224) [Orange]. Also present is a very small peak indexed to 111 Au (marked by *), and trace quantities of Sn [141/amd 141 tetragonal (JCPDS 04-0673)] [Blue] at higher temperatures.

An increase of the growth temperature to 500 °C resulted in the prominent growth of nanowires on the Si substrate, which is shown in the SEM image in Figure 2.1(b). These nanowires were tens of microns long (on average 10-20 μm), with a mean diameter of 115 ± 42 nm (see appendix for diameter distribution, Figure A.2.4). Along with the predominant growth of the nanowires on the Si wafer, negligible amounts of flake-like structures were also observed at this temperature (Figure 2.1(b)). Although this growth temperature (500 °C) favours the VLS growth of nanowires, the negligible growth of flakes is also produced from a competitive VS growth process at this growth temperature. At a higher growth temperature of 550 °C (Figure 2.1(c)), the relative yield of these homogeneously nucleated flakes increased greatly, with a roughly tenfold reduction of the amount of nanowires compared to the nanostructures grown at 500 °C growth temperature. However, upon further investigation of the nanowires formed under this growth temperature, two distinct types of nanowire were seen to exist (inset of Figure 2.1(c)). The first type (Type A) of nanowires is similar to those formed at the lower temperature of 500 °C (shown in the green bordered inset). These wires were relatively uniform in diameter along their length; with similar lengths and diameters to the nanowires grown at 500 °C. The second type of nanowire (Type B; shown in yellow bordered inset) however showed a different nanowire morphology, with a larger diameter of ~200 nm (see appendix for diameter measurement of a type B SnSe nanowire, Figure A.2.5). These nanowires were very visually different, and less uniform in diameter along their length. The ratio of type A to type B nanowires was roughly 5:1 under these growth conditions.

The crystal structure and phase purity of the as-grown nanostructures were verified through XRD analysis. Figure 2.1(d) displays the XRD patterns of the flakes and nanowires, produced at 450 °C, 500 °C and 550 °C. The flakes grown at the growth temperature of 450 °C can be

indexed to hexagonal $SnSe_2$ (P-3m1 (164) space group, JCPDS 23-0602), with the strongest reflection corresponding to the (001) plane. SEM analysis revealed that the flakes appeared to grow in a perpendicular manner to the silicon substrate (Figure 2.1(a)), and high resolution TEM (HRTEM) analysis confirmed that the flakes were stacked along the (001) plane (see appendix Figure A.2.6). This preferred orientation of the flakes contributes to the strongest (001) reflection in the XRD pattern from the $SnSe_2$ flake sample (Figure 2.1(d)). Raman analysis (Figure A.2.7 in appendix) further confirmed the growth of $SnSe_2$ at 450 °C with clearly visible E_g and A_{1g} Raman modes corresponding to $SnSe_2$. At 500 °C a phase evolution of the nanomaterial was observed, with the XRD pattern from the sample indexed to orthorhombic SnSe (Pnma (62) space group, JCPDS 48-1224), with no visible $SnSe_2$ peaks present. At the higher growth temperature of 550 °C the orthorhombic SnSe phase of the sample was maintained, with the XRD pattern (Figure 2.1(d)) showing reflections corresponding to orthorhombic SnSe.

At a growth temperature of 450 °C, the VS growth of $SnSe_2$ flakes prevails, whereas at an increased temperature of 500 °C, the VLS growth of SnSe nanowires dominates. This is in agreement with the Sn-Se phase diagram, where at higher temperatures, SnSe is expected to predominate over $SnSe_2$,[51] and similar to previous studies using this precursor under low pressure CVD conditions, where $SnSe_2$ was achieved for deposition temperatures of 480-500 °C[46] and SnSe was seen at a deposition temperature of 588 °C.[45]. This phase transformation is proposed to rely on the depletion of Se in the $SnSe_2$ atmosphere at relatively high growth temperatures. The high temperatures promote further dissociation of $SnSe_2$, either through a complete dissociation reaction of $SnSe_2$ followed by SnSe formation, or by a direct formation of SnSe from $SnSe_2$ with loss of the Se to the carrier gas.[52,53] This then leads to the predominant formation of SnSe in the CVD reactor. Precise knowledge of the decomposition

mechanism of the precursor is hard to elucidate, thus a fully detailed reaction formula is not included.

This SnSe vapour interacts with the Au catalyst in a VLS-type growth, as indicated in the energy dispersive X-ray (EDX) map (Figure 2.2(a)) by the presence of the Au seed at the nanowire tip, leading to the 1D growth of SnSe. The self-seeded growth of SnSe nanowires has previously been reported,[40] but in our case the growth without any Au film results in the formation of only SnSe flake like structures (see appendix Figure A.2.8). The EDX map of Figure 2.2(a) further confirms the uniformity in the distribution of Sn and Se in the nanowires, with no segregation or clustering of Sn or Se observed on the surface or in the bulk of the nanowires. For this particular nanowire an atomic ratio of 50.6:49.4 of Sn:Se was measured, which confirms the stoichiometric formation of the SnSe nanowires (see appendix for EDX spectrum, Figure A.2.9). Also, of importance is the clear observation of a spherical Au seed at the tip of the nanowires. Point EDX analysis was performed on the tip of a nanowire (see appendix Figure A.2.10), which showed a high amount of both Sn and Se in the Au seed at the tip of a nanowire (21 % Se, 14 % Sn, and 65 % Au). This significant incorporation of both Sn and Se in the Au particle is an indication of a VLS growth mechanism. Figure 2.2(b) shows a room temperature Raman spectrum of an individual SnSe nanowire grown at 500 °C. All Raman measurements were carefully undertaken at a very low laser power to avoid laser induced heating (see appendix Figure A.2.11 for the effect of laser power on phase and morphology of SnSe flake). The B_{3g} vibrational mode of SnSe can be clearly seen at ~110 cm^{-1}, with modes corresponding to the SnSe A^2_g and A^3_g modes also seen at ~132 cm^{-1} and ~152 cm^{-1} respectively in the Raman spectrum.[54,55]

The EDX map in Figure 2.2(c) shows the elemental distribution of Sn, Se and Au in a Type B nanowire formed at 550 °C. Similar to the nanowires formed at the lower temperatures, Sn and Se are seen to exist uniformly throughout the body of the nanowire grown at 550 °C. The clear presence of a semi-spherical Au tip was observed, with minimal Au contamination in the nanowire body. Notably, this semi-spherical Au seed is different to the spherical Au seed seen for the nanowires grown at 500 °C, indicating that there is a change in the nature of the VLS growth. A differently shaped metallic catalyst at the nanowire tip could infer a different eutectic composition for the metastable alloy during VLS growth which may influence the interfacial shape during nanowire growth, further influencing the morphology of the 1D crystal, resulting in a different variant of SnSe nanowires being formed. At this growth temperature additional VS growth of SnSe flakes also become more prominent than at 500°C, as seen in Figures 2.1(b) and (c), indicating that VS-type deposition is further enhanced under these reaction conditions. This additional competitive VS type growth is also observed in the less uniform nanowire diameter of the Type B nanowires, where additional nanowire sidewall growth is proposed to occur through a VS type process. The observation of Au seeds in both types of nanowires confirms the essential role of Au in 1D nanowire formation. Figure 2.2(d) shows a room temperature Raman spectrum of an individual Type B SnSe nanowire grown at 550 °C. The B_{3g} vibrational mode of SnSe can be clearly seen at ~105 cm^{-1}, with the SnSe A^2_g mode also detected at ~129 cm^{-1}.[54,55] A clear red shift of about 5 cm^{-1} of the Raman modes was observed for the Type B nanowires, compared to the Raman modes for those grown at 500 °C (Type A) shown in Figure 2.2(b) (See inset of Figure 2.2(d)), indicating a clear difference in phonon dynamics between the two nanowire types; possibly due to the different crystal growth directions of the two variants of SnSe nanowires.[56]

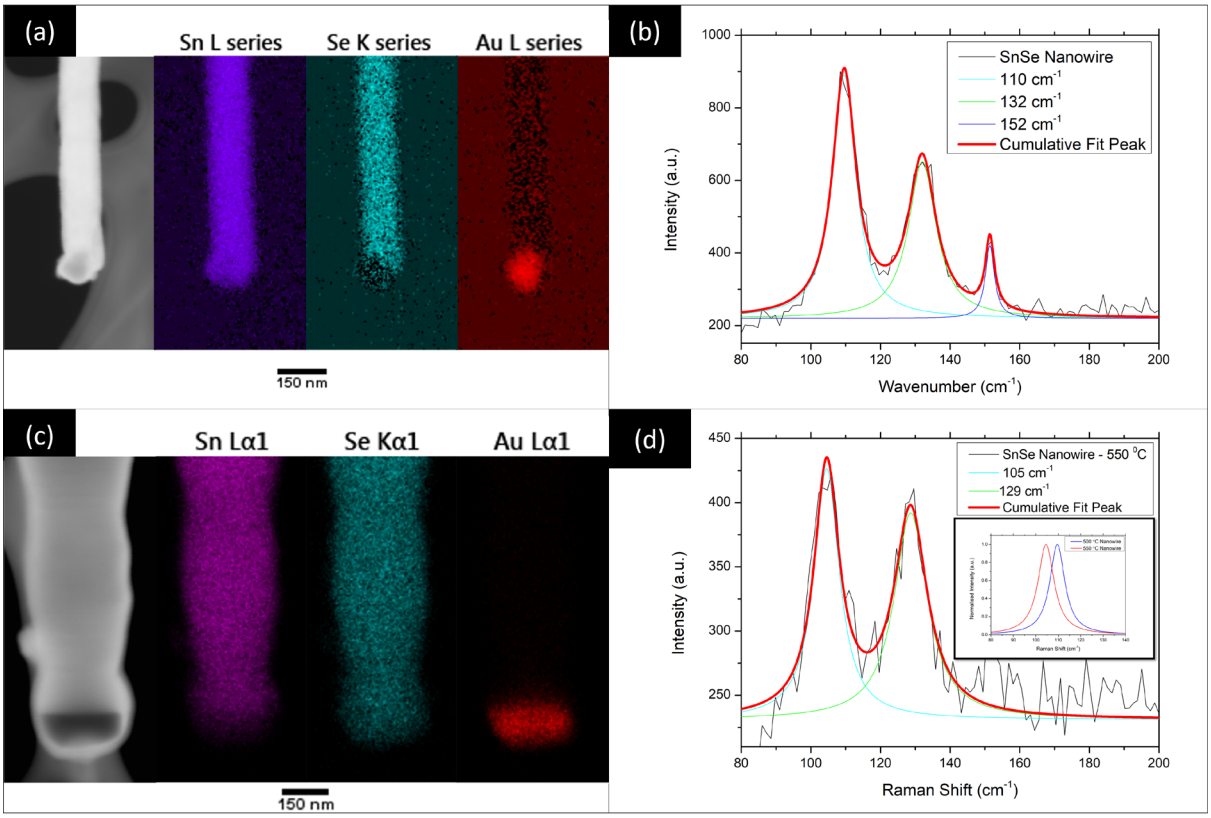


Figure 2.2: Individual nanowire elemental analysis: (a) STEM EDX mapping of a SnSe nanowire grown at 500 °C (referred to as type A in this report). The uniform distribution of Sn and Se in the wire is clearly evident. (b) Raman spectrum of an individual 500 °C nanowire, showing peaks at ~110 cm^{-1}, ~132 cm^{-1} and 152 cm^{-1}, corresponding to the B_{3g}, A^2_g and A^3_g SnSe Raman modes respectively (514 nm laser excitation, peaks fitted with a Lorentzian function). (c) STEM EDX mapping of a SnSe nanowire grown at 550 °C (referred to as type B in this report). The presence of a Au tip is clearly shown. (d) Raman spectrum of an individual nanowire grown at 550 °C, showing peaks at ~105 cm^{-1} and ~129 cm^{-1}, corresponding to the B_{3g} and A^2_g SnSe Raman modes. Inset shows the relative shift of the fitted B_{3g} mode between nanowires grown at 500 and 550 °C (514 nm laser excitation, peaks fitted with a Lorentzian function).

The crystal structure and the structural quality of the SnSe nanowires grown at 500 °C was further examined through HRTEM and selected area electron diffraction (SAED) (Figure 2.3). Accurate knowledge of the crystal quality and structure of the grown nanostructures is imperative for device implementation, including memory devices such as PCRAM and RRAM. Figure 2.3(a) shows a TEM image of a single SnSe nanowire orientated down the [-100] zone axis, revealing its single crystalline nature with no apparent crystal defects, such as stacking faults or twin boundaries. SnSe is expected to form a surface oxide after being exposed to ambient air.[37] This oxide (Figure 2.3), determined to be SnO_2 by XPS analysis (see Figure A.2.12 in the appendix), forms within minutes, and after this the SnSe nanowires then remain further stable for many weeks. The thickness of this amorphous SnO_2 layer is generally uniform, as determined from HRTEM analysis, regardless of nanowire diameter (Figure A.2.13 in the appendix). The magnified HRTEM image and SAED pattern at the top right inset of Figure 2.3(a) confirmed the crystal structure of the type A nanowires grown at 550 °C, revealing d-spacing of 0.308 nm along the nanowire growth axis, corresponding to a <011> growth direction. This <011> growth direction is perpendicular to the <100> direction; *i.e.* the direction along which the SnSe layers are stacked. Given the expected slower growth rate along the van der Waals bond direction, *i.e.* <100>, for SnSe layered crystals, a direction perpendicular to this should be a favourable direction for nanowire growth to occur. This growth direction is in agreement with previous reports of SnSe nanowires, which have been shown to grow along the <011> direction for orthorhombic SnSe.[40] To explore the SnSe crystal structure in more detail, TEM investigations were undertaken for SnSe nanowires orientated down different zone axes. Figure 2.3(b) shows a SnSe nanowire orientated down the [01-1] zone axis, with a HRTEM image in the top right corner, and an SAED pattern in the bottom right hand corner. A <011> growth direction was seen for this nanowire, in agreement with the previous observation for the SnSe nanowire viewed down the [-100] zone axis (Figure

2.3(a)). Figure 2.3(c) shows a TEM image of a cross section, taken from one of the SnSe nanowires. The cross section of the nanowire is seen to clearly exhibit a rectangular shape with a width of ~60 nm and a height of ~40 nm (~70 SnSe layers). This rectangular nanowire cross section explains the large standard deviation seen for the nanowire diameter distribution of these wires, and the presence of two apparent peaks in the data at 71.66 ± 2.86 nm and 119.47 ± 9.60 nm, indicating average thicknesses and widths respectively (appendix Figure A.2.4). The zone axis of this TEM cross section is assigned to the [0-1-1] direction, in agreement with the growth directions of <011> seen for the nanowires shown in Figures 2.3(a) and (b). The right insets show a fast Fourier transform (FFT) and two HRTEM images of this nanowire cross section, revealing clearly the (400) and (01-1) lattice planes. Figure 2.3(d) shows an illustration of the nanowire structure with a <011> growth direction, based on the TEM data from Figures 2.3(a), (b) and (c). The planes labelled (a), (b) and (c) indicate the viewing directions of the wires in Figures 2.3(a), (b) and (c).

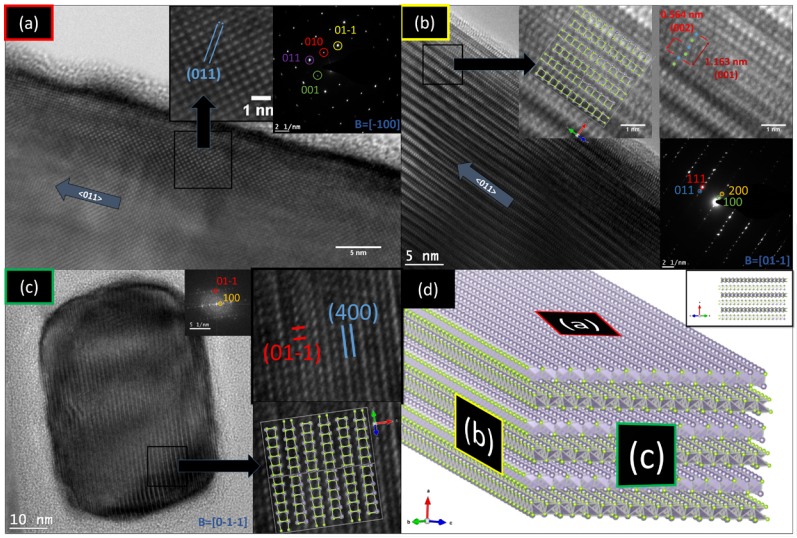


Figure 2.3: (a) TEM image of an individual nanowire. A thin-oxide shell is visible on the surface edge of the wire. Top middle inset is a HRTEM image of the nanowire, with an SAED pattern in the top right inset. The nanowire was observed to be oriented down the [-100] zone axis, and a nanowire growth direction d-spacing of 0.308 nm was measured, corresponding to the <011> growth direction. (b) TEM image of a single SnSe nanowire oriented down the [01-1] zone axis. Top middle and top right insets are HRTEM images of this wire, with a schematic of the SnSe crystal structure, viewed down the [01-1] zone axis overlaid on the HRTEM image. Bottom right inset is an SAED pattern of this nanowire. A growth direction d-spacing value of 0.308 nm was measured, assigned to the <011> growth direction. (c) TEM image of a cross section of a single SnSe nanowire aligned down the [0-1-1] direction. A visible surface oxide was observed surrounding the body of the wire. Insets show a fast Fourier transform (FFT) of the nanowire cross-section, HRTEM images and the overlaid SnSe crystal structure viewed down the [0-1-1] direction. (d) Schematic of the SnSe nanowire crystal structure with a <011> growth direction. The planes labelled (a), (b) and (c) indicate the viewing directions of the wire in Figures 2.3 (a), (b) and (c). The inset shows the nanowire structure viewed down the [0-1-1] direction. The arrows in the bottom left corner indicate the directions of the a, b and c lattice directions. Red arrow: a-axis, green arrow: b-axis, blue arrow: c-axis.

Figure 2.4 shows TEM analysis of type B nanowires formed at a growth temperature of 550 °C. Figure 2.4(a) shows a low magnification TEM image of one of these SnSe nanowires. The dark contrasted hemispherical shaped Au seed can be seen at the tip of the nanowire. The top right inset shows an SAED pattern of this nanowire, which can be indexed to the [0-10] zone axis. Most significantly, in contrast to the SnSe nanowires grown at 500 °C, the type B nanowires grown at 550 °C are seen to grow along the <100> crystal direction. This growth direction is along the SnSe van der Waals bound layer direction, which for high quality SnSe nanowires has only been seen before for very small diameter Bi seeded growth.[41] Higher temperatures have been shown to play a major role in the growth orientation of other layered materials, such as with MoS_2 flakes,[48] and this higher temperature used here clearly alters the growth rate along the <100> direction. The different shapes of the Au seeds between these type A and type B nanowires (see Figures 2.2 (a) and (c)) indicate that the nature of the VLS growth of the SnSe nanowires is also affected, and this difference in the VLS growth properties could play a role in the growth of the nanowire in a different crystal growth direction. This change in the nanowire crystal direction between the two nanowire types offers a potential explanation for the red shift observed in the Raman spectra for type B compared to type A nanowires (inset in Figure 2.2(d)). Similarly, changes in Raman spectra have previously been assigned to localised polarisation effects from an anisotropic crystal lattice.[56]

At a growth temperature of 550 °C additional crystal growth was also observed on the sidewall of the nanowires which effects on their morphology, as is seen in the TEM image of Figure 2.4(b). The nanowire morphology (dark contrasted region of the TEM image) is guided through a VLS process whereas the irregular jutted sidewall growth is triggered via the vaporisation and condensation of growth species on the nanowire sidewalls, *i.e.* VS-type growth. These large bulges are seen for many of the SnSe nanowires produced at this temperature. Figure A.2.14 shows the growth of these large bulb structures without any Au seed, and without any nanowires being produced. To explore this sidewall growth further, cross sectional TEM was taken of one of these nanowires (Figure 2.4(c)). A "cross-like" shape is clearly seen, with three branches sprouting from the centre nanowire body. The top right inset shows an SAED pattern of this nanowire cross section, assigned to the [-100] zone axis. From this information, the overlaid red box can be seen as the [-100] viewed SnSe unit cell, corresponding to the nanowire body, with the sidewall growth indicated by the blue arrows in the <011> equivalent directions. The VLS-guided nanowire body is faceted by high surface energy (010) and (001) sidewalls, which lends to favourable VS addition to these planes, forming low surface energy (011) facetted surfaces. No obvious crystal defects are seen in these nanowires, and the small number of additional satellite spots that are seen in the SAED pattern of this cross-section in Figure 2.4(c) are expected to be induced from the cross-sectioning process, as a fully single crystalline SAED pattern is seen for the as-grown pristine nanowire in Figure 2.4(a). Figure 2.4(d) shows a schematic representation of the type B nanowires with a <100> growth direction, with the SnSe layers stacked along this direction. The insets show the SnSe structure down three major zone axes.

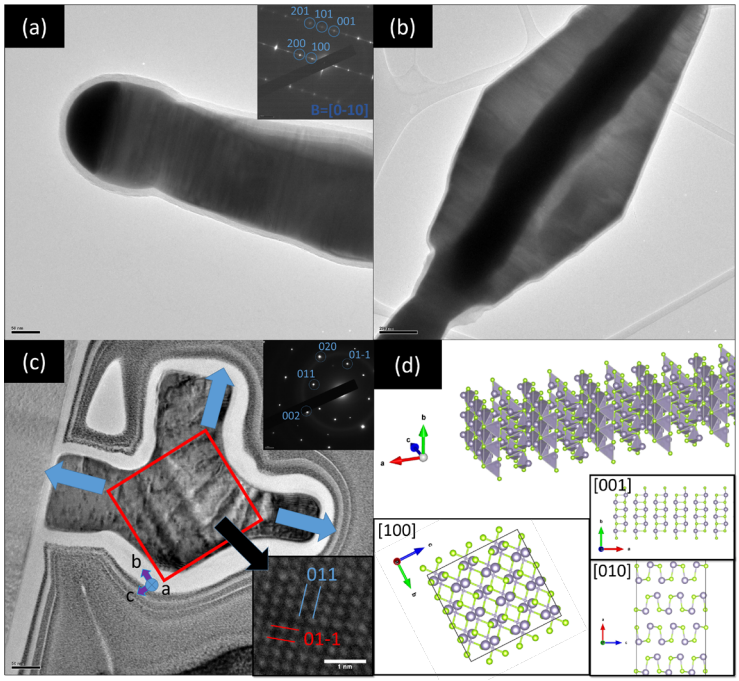


Figure 2.4: TEM analysis of the nanowires formed at 550 °C. (a) Low magnification TEM image showing the body of one of these nanowires. The dark contrast at the tip of the wire is indicative of the Au seed. Inset is an SAED pattern recorded from the bulk of the nanowire, indexed to orthorhombic Pmna SnSe viewed down the [0-10] zone axis. A growth direction of <100> was observed, which is perpendicular to the SnSe interlayer direction. (b) TEM image of a nanowire similar to that shown in image (a), with some additional sidewall growth. The dark contrast is due to the thickness of the layer from additional growth in this area. (c) Cross-sectional TEM image taken from a nanowire similar to that shown in image (b). A T-shaped nanowire cross section is clearly observed. The top right inset shows the SAED pattern, indexed down the [100] zone axis. The red box overlaid on the image represents the orthorhombic Pnma 62 SnSe unit cell, with the blue arrows indicating the [011] equivalent growth directions. (d) Schematic of the crystal structure of a SnSe nanowire grown at a temperature of 550 °C. The top left image shows the simulated general structure of the nanowire, with a <100> growth direction. The bottom right shows the SnSe Pmna 62 structure down [100], [010] and [001] zone axes. The coloured arrows indicate the directions of the a, b and c lattice directions. Red arrow: a-axis, green arrow: b-axis, blue arrow: c-axis.

The electrical behaviour of the SnSe nanowires was studied using two terminal electrical contacts, as shown in the inset of Figure 2.5(a). Due to the high yield, and regular morphology of the SnSe nanowires produced at 500 °C (type A), this set of nanowires were chosen for electrical testing. For electrical device fabrication, SnSe nanowires were mechanically transferred from the growth substrate onto a clean Si substrate (1 μm thermal oxide) with optical lithography-defined contact pads. Single SnSe nanowires were contacted by electron beam lithography (EBL) using Ti-Al-Au contacts (for details of the device fabrication see the Characterisation section). The channel length of the electrodes was ~ 1 μm and the thickness was determined by the nanowire diameter. Figure 2.5(a) shows an *I-V* curve (first sweep) from a pristine, individual SnSe nanowire (black curve). The extremely low current levels under a low voltage (*V*) bias show that the device is initially in a high resistance state (HRS) due to the presence of a thin but insulating oxide surrounding the nanowire. This amorphous oxide layer of a few nanometres thick can be observed surrounding the nanowire in the HRTEM image in Figure 2.3(a) and confirmed to be SnO_2 by XPS analysis (Figure A.2.12 in the appendix). At ~ 4 V the current level suddenly increases and the device switches to a low resistance state (LRS). This change from a HRS to a LRS is referred to as the SET event, with the reverse, a change of the LRS to a HRS describing the RESET event. Subsequent measurement, shown by the red curve, indicates that the LRS is sustained after the SET event. Figure 2.5(b) shows the resistance of the LRS, measured at 1 V, fluctuating slightly over time before spontaneously decaying to the HRS at just under 1000 s. Figure 2.5(c) displays the bipolar resistive switching (BRS) behaviour as the voltage is swept from a positive to a negative bias. At ~ 4 V, the device experiences a SET event, transitioning from the HRS to the LRS, the large resistance of the device means that no current limiting compliance was necessary to operate between memory states, which is a desirable feature as current-limiting transistors bring additional complexity

to memory circuitry. Under a sufficient negative bias, ~ -4 V, the measured current suddenly drops as the device returns to the HRS (RESET event). This voltage range is similar to previous reports of nanowire RRAM devices.[57]

The polarity dependent memory switching describes the bipolar process whereby a conducting filament (CF) must bridge the crystalline core of the wire and the metal contact through the insulating oxide shell. Unipolar resistive switching; where the SET and RESET events are controlled by the magnitude of current flow through the device, has been reported for SnO_x/SnSe/SnO_x layered nanoscale devices.[37] The RRAM measurement presents preliminary evidence that nanowire SnSe devices exhibit vastly different resistive switching properties to that of planar SnSe layer devices. The previous report on SnO_x/SnSe/SnO_x layered device[37] proposes a mechanism based on the formation of a CF composed of O vacancies through the SnO_x layer. Formation of an O vacancy CF is a highly likely mechanism for the BRS we observe, given the SnO_2 layer on the surface of the nanowire. The decay back to the HRS seen in Figure 2.5(b) is proposed to be due to the decay of the CF or a build-up of oxygen at the electrodes as described in previous reports on SnO_x/SnSe/SnO_x planar devices.[37] A BRS mechanism based on the formation of a CF has been reported in large SnSe and $SnSe_2$ crystals,[16] however BRS has not been previously reported for SnSe nanowires. During application of a voltage bias, electrochemical oxidation may also occur at the anode, leading to the evolution of molecular O, injecting O vacancies into the oxide layer where they move towards and accumulate at the cathode, bridging the conductive nanowire core and the electrode through the formation of a CF.[58] The attracting and repelling of the O vacancies establishes the core-process of the BRS observed in these devices. O vacancies can give rise to both unipolar, and bipolar resistive switching behaviours, and is highly dependent on oxide structure, forming current and device area.[59] Through repetition of the bipolar *I-V* sweep the

SnSe nanowire devices could be repeatedly switched between the HRS and the LRS. The difference between the HRS and the LRS for four such switching cycles (with each cycle plotted individually in the appendix; see Figure A.2.15-A, a second device is also shown in Figure A.2.15-B) is shown in Figure 2.5(d). The level of the LRS was measured in the MΩ range with the HRS almost three orders of magnitude higher. The significant resistance difference between the LRS and the HRS indicates the potential for future memory devices based on this material.

To get an insight to the conduction mechanism at various points of the resistive switching cycle, resistive switching data for two devices were analysed in log scale (Figure A.2.16-A, A.2.16-B). The results indicate a space-charge-limited current (SCLC) mechanism with trapped SCLC behaviour ($I \propto V^{>2}$) when the voltage is below the SET threshold. The formation of the CF causes a rapid rise in current flow and SETs the device into the LRS. In the LRS, ohmic ($I \propto V$) and trap-free behaviour are identified, whereby, the current is dominated by charge carriers injected from the contacts and the *I-V* characteristics becomes quadratic in what is termed the Child's square law region ($I \propto V^2$).[60] This is similar to stacked SnO_x/SnSe/SnO_x devices, where the conduction mechanism was interpreted to follow the shallow trap-associated theory. Memory device studies on oxide coated II-VI semiconductor nanowire materials have also shown trapping of electrons by O vacancies to be the responsible mechanism.[57] SCLC conduction has been observed in a wide range of materials, it is commonly accepted that the defect-related traps, e.g., O vacancies contribute to the SCLC conduction.[61] Other conduction mechanisms such as Schottky and Poole-Frenkel (PF) emission were also investigated through plots of log(I/V) versus √V and log(I) versus √V (Figure A.2.17-A, A.2.17-B). The linear relationship determining PF conduction is poor across both devices, however, regions of Schottky conduction can be observed in the high bias portions (Figure A.2.17-B (b, d)). From

this we can conclude that both trap-controlled SCLC and Schottky conduction mechanisms play a role in the device behaviour (detailed discussion in appendix 2.8.1).

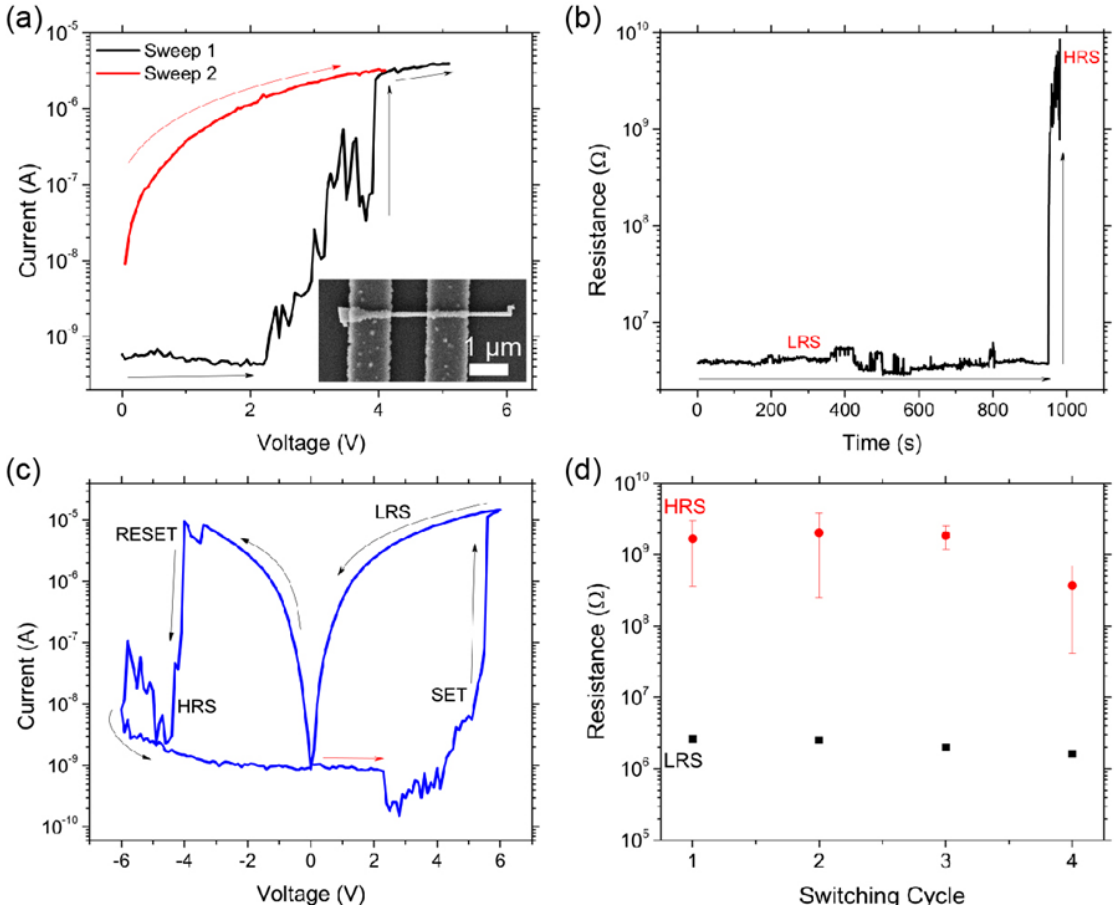


Figure 2.5: (a) First and second *I-V* sweeps of a single SnSe nanowire device. The inset shows a SEM image of a SnSe nanowire between 2 electrical contacts with a separation of 1 μm. The black curve details the initial sweep, where the device was initially in the high resistance state (HRS), at 4 V there is a sudden increase of current and the device resistively switches to a low resistance state (LRS). The second sweep shows that the device remains in the LRS. (b) The LRS remains for 1000 s before spontaneously decaying to the HRS. The read voltage during this experiment was 1 V. (c) Polarity dependent resistive switching is demonstrated through the positive SET event to the LRS, and the RESET event which returns the device to the HRS under application of a sufficient negative bias. (d) The single SnSe nanowire could be repeatedly switched between the LRS and the HRS with an on/off ratio of ~10^3.

2.6 Conclusions

Highly crystalline, defect free SnSe nanowires have been grown via a CVD method, utilising a single source diselenoether precursor and Au catalyst. The morphologies, phase and the crystal structure of the nanostructures produced have been tuned from $SnSe_2$ to SnSe flakes and to two uniquely different types of SnSe nanowires. The growth direction for the SnSe nanowires can be engineered from <011> to <100> by simply varying the nanowire growth temperature from 500 to 550 °C. The tailoring of the SnSe nanowire crystal structure and growth orientation has important consequences for future device engineering including thermoelectric devices, as SnSe crystals tend to show prominent anisotropic behaviour. The control over directionality of the 1D crystals also expands the scope of obtaining hierarchical nanostructures from this set of materials. The knowledge obtained on the growth and crystal structure of differently oriented nanowires will cater to the future objective; which is to synthesise high yields of uniform nanowire morphology of chalcogenide materials with different crystal orientations for large scale applications. Electrical results from two-terminal <011> oriented SnSe nanowires showed polarity dependent resistive switching, without the use of a current compliance limit, and an on/off ratio of 10^3. Compared to previous studies on layered SnSe based planar RRAM devices, these nanowire devices show bipolar switching behaviour as opposed to unipolar switching, and such a nanowire form presents greater capacity for efficient scaling down of SnSe RRAM devices. These results could form a route for more in-depth memory studies, such as temperature dependent and stability measurements. Also, the electrical behaviour of SnSe nanowires shown in this chapter could pave the way to explore anisotropically tailored SnSe nanowire devices with different crystal orientations, materials geometry, and device architectures (e.g. nanowire arrays, vertical devices).

2.7 References:

(1) Gao, M. R.; Xu, Y. F.; Jiang, J.; Yu, S. H. Nanostructured Metal Chalcogenides: Synthesis, Modification, and Applications in Energy Conversion and Storage Devices. *Chem. Soc. Rev.* **2013**, *42*, 2986–3017.

(2) Lee, D.-H.; Park, C.-M. Tin Selenides with Layered Crystal Structures for Li-Ion Batteries: Interesting Phase Change Mechanisms and Outstanding Electrochemical Behaviors. *ACS Appl. Mater. Interfaces* **2017**, *9*, 15439–15448.

(3) Yu, P.; Yu, X.; Lu, W.; Lin, H.; Sun, L.; Du, K.; Liu, F.; Fu, W.; Zeng, Q.; Shen, Z.; Jin, C.; Wang, Q. J.; Liu, Z. Fast Photoresponse from 1T Tin Diselenide Atomic Layers. *Adv. Funct. Mater.* **2016**, *26*, 137–145.

(4) Choi, W.; Cho, M. Y.; Konar, A.; Lee, J. H.; Cha, G. B.; Hong, S. C.; Kim, S.; Kim, J.; Jena, D.; Joo, J.; Kim, S. High-Detectivity Multilayer MoS_2 Phototransistors with Spectral Response from Ultraviolet to Infrared. *Adv. Mater.* **2012**, *24*, 5832–5836.

(5) Mukhokosi, E. P.; Krupanidhi, S. B.; Nanda, K. K. Band Gap Engineering of Hexagonal $SnSe_2$ Nanostructured Thin Films for Infra-Red Photodetection. *Sci. Rep.* **2017**, *7*, 15215.

(6) Chang, Y.-H.; Zhang, W.; Zhu, Y.; Han, Y.; Pu, J.; Chang, J.-K.; Hsu, W.-T.; Huang, J.-K.; Hsu, C.-L.; Chiu, M.-H.; Takenobu, T.; Li, H.; Wu, C.-I.; Chang, W.-H.; Wee, A. T. S.; Li, L.-J. Monolayer $MoSe_2$ Grown by Chemical Vapor Deposition for Fast Photodetection. *ACS Nano* **2014**, *8*, 8582–8590.

(7) Radisavljevic, B.; Radenovic, A.; Brivio, J.; Giacometti, V.; Kis, A. Single-Layer MoS2transistors. *Nat. Nanotechnol.* **2011**, *6*, 147–150.

(8) Wang, H.; Yu, L.; Lee, Y. H.; Shi, Y.; Hsu, A.; Chin, M. L.; Li, L. J.; Dubey, M.; Kong, J.; Palacios, T. Integrated Circuits Based on Bilayer MoS_2 Transistors. *Nano Lett.* **2012**, *12*, 4674–4680.

(9) Desai, S. B.; Madhvapathy, S. R.; Sachid, A. B.; Llinas, J. P.; Wang, Q.; Ahn, H.; Pitner, G.; Kim, M. J.; Bokor, J.; Hu, C.; Wong, H.-S. P.; Javey, A. MoS_2 Transistors with 1-Nanometer Gate Lengths. *Science,* **2016**, *354*, 99–102.

(10) Pradhan, N. R.; Rhodes, D.; Feng, S.; Xin, Y.; Memaran, S.; Moon, B. H.; Terrones, H.; Terrones, M.; Balicas, L. Field-Effect Transistors Based on Few-Layered α-$MoTe_2$. *ACS Nano* **2014**, *8*, 5911–5920.

(11) Zhou, X.; Wu, L.; Song, Z.; Rao, F.; Ren, K.; Peng, C.; Song, S.; Liu, B.; Xu, L.; Feng, S. Phase Transition Characteristics of Al-Sb Phase Change Materials for Phase Change Memory Application. *Appl. Phys. Lett.* **2013**, *103*.

(12) Podzorov, V.; Gershenson, M. E.; Kloc, C.; Zeis, R.; Bucher, E. High-Mobility Field-Effect Transistors Based on Transition Metal Dichalcogenides. *Appl. Phys. Lett.* **2004**, *84*, 3301–3303.

(13) Larentis, S.; Fallahazad, B.; Tutuc, E. Field-Effect Transistors and Intrinsic Mobility in Ultra-Thin $MoSe_2$ layers. *Appl. Phys. Lett.* **2012**, *101*.

(14) Wang, R. Y.; Caldwell, M. A.; Jeyasingh, R. G. D.; Aloni, S.; Shelby, R. M.; Wong, H. S. P.; Milliron, D. J. Electronic and Optical Switching of Solution-Phase Deposited $SnSe_2$ Phase Change Memory Material. *J. Appl. Phys.* **2011**, *109*.

(15) Chung, K.-M.; Wamwangi, D.; Woda, M.; Wuttig, M.; Bensch, W. Investigation of SnSe, SnSe2, and Sn2Se3 Alloys for Phase Change Memory Applications. *J. Appl. Phys.* **2008**, *103*, 083523.

(16) Chun, D.; Walser, R. M.; Bené, R. W.; Courtney, T. H. Polarity-Dependent Memory Switching in Devices with SnSe and $SnSe_2$ crystals. *Appl. Phys. Lett.* **1974**, *24*, 479–481.

(17) Khotkevich, V. V.; Novoselov, K. S.; Booth, T. J.; Jiang, D.; Geim, A. K.; Morozov, S. V.; Schedin, F. Two-Dimensional Atomic Crystals. *Proc. Natl. Acad. Sci.* **2005**, *102*,

10451–10453.

(18) Nicolosi, V.; Chhowalla, M.; Kanatzidis, M. G.; Strano, M. S.; Coleman, J. N. Liquid Exfoliation of Layered Materials. *Science* **2013**, *340*, 1226419–1226419.

(19) Miró, P.; Audiffred, M.; Heine, T. An Atlas of Two-Dimensional Materials. *Chem. Soc. Rev.* **2014**, *43*, 6537–6554.

(20) Pawar, M.; Kadam, S.; Late, D. J. High-Performance Sensing Behavior Using Electronic Ink of 2D $SnSe_2$ Nanosheets. *ChemistrySelect* **2017**, *2*, 4068–4075.

(21) Li, L.; Kim, J.; Jin, C.; Ye, G. J.; Qiu, D. Y.; da Jornada, F. H.; Shi, Z.; Chen, L.; Zhang, Z.; Yang, F.; Watanabe, K.; Taniguchi, T.; Ren, W.; Louie, S. G.; Chen, X. H.; Zhang, Y.; Wang, F. Direct Observation of the Layer-Dependent Electronic Structure in Phosphorene. *Nat. Nanotechnol.* **2017**, *12*, 21–25.

(22) Zhang, W.; Qin, J.; Huang, Z.; Zhang, W. The Mechanism of Layer Number and Strain Dependent Bandgap of 2D Crystal $PtSe_2$. *J. Appl. Phys.* **2017**, *122*, 205701.

(23) Kang, J.; Zhang, L.; Wei, S. H. A Unified Understanding of the Thickness-Dependent Bandgap Transition in Hexagonal Two-Dimensional Semiconductors. *J. Phys. Chem. Lett.* **2016**, *7*, 597–602.

(24) Raoux, S.; Xiong, F.; Wuttig, M.; Pop, E. Phase Change Materials and Phase Change Memory. *MRS Bull.* **2014**, *39*, 703–710.

(25) Lee, S.-H.; Jung, Y.; Agarwal, R. Highly Scalable Non-Volatile and Ultra-Low-Power Phase-Change Nanowire Memory. *Nat. Nanotechnol.* **2007**, *2*, 626–630.

(26) Han, S.; Yuan, C.; Luo, X.; Cao, Y.; Yu, T.; Yang, Y.; Li, Q.; Ye, S. Horizontal Growth of MoS_2 Nanowires by Chemical Vapour Deposition. *RSC Adv.* **2015**, *5*, 68283–68286.

(27) Kumar, R.; Goel, N.; Kumar, M. High Performance NO_2 Sensor Using MoS_2 Nanowires Network. *Appl. Phys. Lett.* **2018**, *112*, 053502.

(28) Zhou, X.; Zhang, Q.; Gan, L.; Li, H.; Xiong, J.; Zhai, T. Booming Development of

Group IV–VI Semiconductors: Fresh Blood of 2D Family. *Adv. Sci.* **2016***, 3, 1600177.*

(29) Huang, Y.; Li, L.; Lin, Y.; Nan, C.-W. Liquid Exfoliation Few-Layer SnSe Nanosheets with Tunable Band Gap. *J. Phys. Chem. C* **2017**, 121, 32, 17530-17537.

(30) Cho, S. H.; Cho, K.; Park, N. W.; Park, S.; Koh, J. H.; Lee, S. K. Multi-Layer SnSe Nanoflake Field-Effect Transistors with Low-Resistance Au Ohmic Contacts. *Nanoscale Res. Lett.* **2017**, *12*, 2–7.

(31) Pawbake, A. S.; Jadkar, S. R.; Late, D. J. High Performance Humidity Sensor and Photodetector Based on SnSe Nanorods. *Mater. Res. Express* **2016**, *3*.

(32) Wang, J.; Yang, G. F.; Xue, J. J.; Lei, J. M.; Chen, D. J.; Lu, H.; Zhang, R.; Zheng, Y. D. A Reusable and High Sensitivity Nitrogen Dioxide Sensor Based on Monolayer SnSe. *IEEE Electron Device Lett.* **2018**, *39*, 599–602.

(33) Zhao, S.; Wang, H.; Zhou, Y.; Liao, L.; Jiang, Y.; Yang, X.; Chen, G.; Lin, M.; Wang, Y.; Peng, H.; Liu, Z. Controlled Synthesis of Single-Crystal SnSe Nanoplates. *Nano Res.* **2015**, *8*, 288–295.

(34) Braga, S.; Cabrini, A.; Torelli, G. Impact of Technology Scaling on Phase-Change Memory Performance. In *Advances in Solid State Circuit Technologies*; InTech, 2010; p 450.

(35) Xu, W.; Lee, Y.; Min, S. Y.; Park, C.; Lee, T. W. Simple, Inexpensive, and Rapid Approach to Fabricate Cross-Shaped Memristors Using an Inorganic-Nanowire-Digital-Alignment Technique and a One-Step Reduction Process. *Adv. Mater.* **2016**, *28*, 527–532.

(36) Nukala, P.; Agarwal, R.; Qian, X.; Jang, M. H.; Dhara, S.; Kumar, K.; Johnson, A. T. C.; Li, J.; Agarwal, R. Direct Observation of Metal-Insulator Transition in Single-Crystalline Germanium Telluride Nanowire Memory Devices Prior to Amorphization. *Nano Lett.* **2014**, *14*, 2201–2209.

(37) Tian, H.; Wang, X. F.; Mohammad, M. A.; Gou, G. Y.; Wu, F.; Yang, Y.; Ren, T. L. A Hardware Markov Chain Algorithm Realized in a Single Device for Machine Learning. *Nat. Commun.* **2018**, *9*, 1–11.

(38) Zhao, L.-D.; Lo, S.-H.; Zhang, Y.; Sun, H.; Tan, G.; Uher, C.; Wolverton, C.; Dravid, V. P.; Kanatzidis, M. G. Ultralow Thermal Conductivity and High Thermoelectric Figure of Merit in SnSe Crystals. *Nature* **2014**, *508*, 373–377.

(39) Butt, F. K.; Mirza, M.; Cao, C.; Idrees, F.; Tahir, M.; Safdar, M.; Ali, Z.; Tanveer, M.; Aslam, I. Synthesis of Mid-Infrared SnSe Nanowires and Their Optoelectronic Properties. *CrystEngComm* **2014**, *16*, 3470.

(40) Liu, J.; Jian, J.; Yu, Z.; Zhang, Z.; Cao, B.; Du, B. Catalyst-Free Vapor Phase Growth of Ultralong SnSe Single-Crystalline Nanowires. *Cryst. Growth Des.* **2017**, *17*, 6163–6168.

(41) Liu, S.; Guo, X.; Li, M.; Zhang, W. H.; Liu, X.; Li, C. Solution-Phase Synthesis and Characterization of Single-Crystalline SnSe Nanowires. *Angew. Chemie - Int. Ed.* **2011**, *50*, 12050–12053.

(42) Boadi, N. O.; Malik, M. A.; O'Brien, P.; Awudza, J. A. M. Single Source Molecular Precursor Routes to Lead Chalcogenides. *Dalt. Trans.* **2012**, *41*, 10497.

(43) Cowley, A. H.; Jones, R. A. Single-Source III/V Precursors: A New Approach to Gallium Arsenide and Related Semiconductors. *Angew. Chemie Int. Ed. English* **1989**, *28*, 1208–1215.

(44) Barrelet, C. J.; Wu, Y.; Bell, D. C.; Lieber, C. M. Synthesis of CdS and ZnS Nanowires Using Single-Source Molecular Precursors. *J. Am. Chem. Soc.* **2003**, *125*, 11498–11499.

(45) Gurnani, C.; Hawken, S. L.; Hector, A. L.; Huang, R.; Jura, M.; Levason, W.; Perkins, J.; Reid, G.; Stenning, G. B. G. Tin(IV) Chalcogenoether Complexes as Single Source Precursors for the Chemical Vapour Deposition of SnE_2 and SnE (E = S, Se) Thin Films.

Dalt. Trans. **2018**, *47*, 2628–2637.

(46) De Groot, C. H.; Gurnani, C.; Hector, A. L.; Huang, R.; Jura, M.; Levason, W.; Reid, G. Highly Selective Chemical Vapor Deposition of Tin Diselenide Thin Films onto Patterned Substrates via Single Source Diselenoether Precursors. *Chem. Mater.* **2012**, *24*, 4442–4449.

(47) Momma, K.; Izumi, F. VESTA 3 for Three-Dimensional Visualization of Crystal, Volumetric and Morphology Data. *J. Appl. Crystallogr.* **2011**, *44*, 1272–1276.

(48) Fei, L.; Lei, S.; Zhang, W. B.; Lu, W.; Lin, Z.; Lam, C. H.; Chai, Y.; Wang, Y. Direct TEM Observations of Growth Mechanisms of Two-Dimensional MoS_2 Flakes. *Nat. Commun.* **2016**, *7*, 1–7.

(49) Ma, X. H.; Cho, K. H.; Sung, Y. M. Growth Mechanism of Vertically Aligned SnSe Nanosheets via Physical Vapour Deposition. *CrystEngComm* **2014**, *16*, 5080–5086.

(50) Boscher, N. D.; Carmalt, C. J.; Palgrave, R. G.; Parkin, I. P. Atmospheric Pressure Chemical Vapour Deposition of SnSe and $SnSe_2$ Thin Films on Glass. *Thin Solid Films* **2008**, *516*, 4750–4757.

(51) Bletskan, D. I. Phase Equilibrium in Binary Systems $A^{IV}B^{VI}$ – Part. III Systems Sn-Chalchogenides. *J. Ovonic Res.* **2005**, *1*, 61–69.

(52) Fernandes, P. A.; Sousa, M. G.; Salomé, P. M. P.; Leitão, J. P.; da Cunha, A. F. Thermodynamic Pathway for the Formation of SnSe and $SnSe_2$ Polycrystalline Thin Films by Selenization of Metal Precursors. *CrystEngComm* **2013**, *15*, 10278.

(53) Huang, Y.; Xu, K.; Wang, Z.; Shifa, T. A.; Wang, Q.; Wang, F.; Jiang, C.; He, J. Designing the Shape Evolution of $SnSe_2$ Nanosheets and Their Optoelectronic Properties. *Nanoscale* **2015**, *7*, 17375–17380.

(54) Chandrasekhar, H. R.; Humphreys, R. G.; Zwick, U.; Cardona, M. Infrared and Raman Spectra of the IV-VI Compounds SnS and SnSe. *Phys. Rev. B* **1977**, *15*, 2177–2183.

(55) Luo, S.; Qi, X.; Yao, H.; Ren, X.; Chen, Q.; Zhong, J. Temperature-Dependent Raman Responses of the Vapor-Deposited Tin Selenide Ultrathin Flakes. *J. Phys. Chem. C* **2017**, *121*, 4674–4679.

(56) Xia, J.; Li, X. Z.; Huang, X.; Mao, N.; Zhu, D. D.; Wang, L.; Xu, H.; Meng, X. M. Physical Vapor Deposition Synthesis of Two-Dimensional Orthorhombic SnS Flakes with Strong Angle/Temperature-Dependent Raman Responses. *Nanoscale* **2016**, *8*, 2063–2070.

(57) Xie, C.; Nie, B.; Zhu, L.; Zeng, L. H.; Yu, Y. Q.; Wang, X. H.; Fang, Q. L.; Luo, L. B.; Wu, Y. C. High-Performance Nonvolatile Al/AlO_x/CdTe:Sb Nanowire Memory Device. *Nanotechnology* **2013**, *24*.

(58) Waser, R.; Dittmann, R.; Staikov, C.; Szot, K. Redox-Based Resistive Switching Memories Nanoionic Mechanisms, Prospects, and Challenges. *Adv. Mater.* **2009**, *21*, 2632–2663.

(59) Yanagida, T.; Nagashima, K.; Oka, K.; Kanai, M.; Klamchuen, A.; Park, B. H.; Kawai, T. Scaling Effect on Unipolar and Bipolar Resistive Switching of Metal Oxides. *Sci. Rep.* **2013**, *3*, 1–6.

(60) Wong, H. S. P.; Lee, H. Y.; Yu, S.; Chen, Y. S.; Wu, Y.; Chen, P. S.; Lee, B.; Chen, F. T.; Tsai, M. J. Metal-Oxide RRAM. *Proc. IEEE* **2012**, *100*, 1951–1970.

(61) Lim, E. W.; Ismail, R. Conduction Mechanism of Valence Change Resistive Switching Memory: A Survey. *Electron.* **2015**, *4*, 586–613.

2.8 Appendix

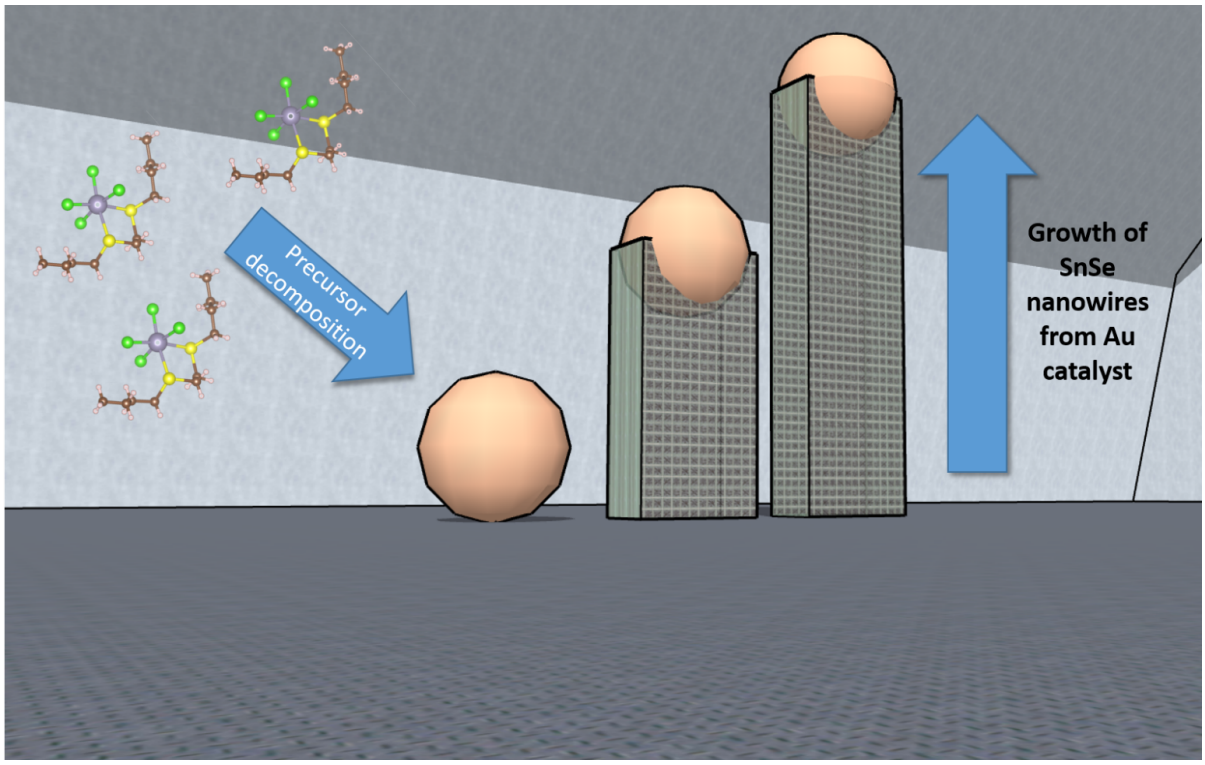


Figure A.2.1: Schematic of a VLS growth mechanism for SnSe nanowire growth.

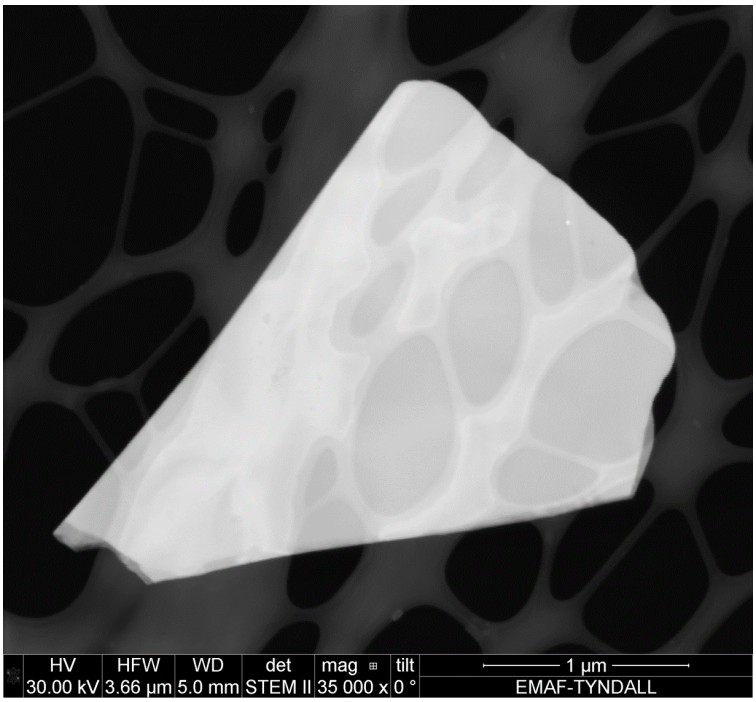


Figure A.2.2: STEM image of a drop cast $SnSe_2$ flake, showing that the flakes can be easily separated out from the flower like structures.

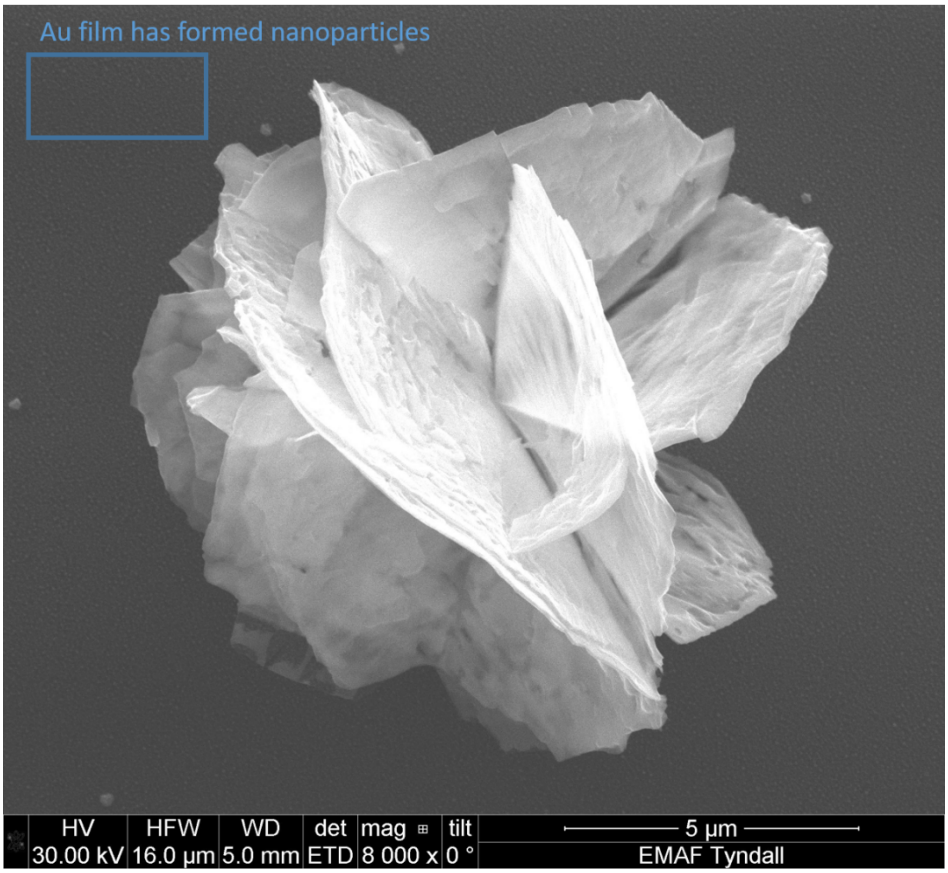


Figure A.2.3: SEM image of $SnSe_2$ flakes, showing that the gold film has melted to form particles on the surface at a temperature of 450 °C.

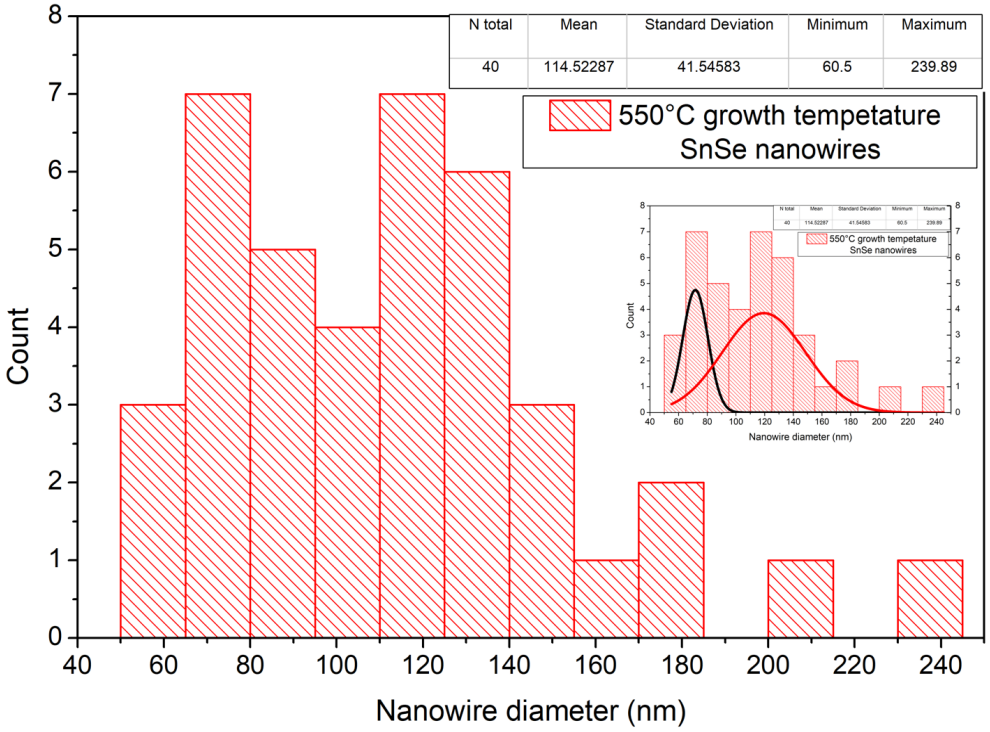


Figure A.2.4: Histogram of the diameter distribution of SnSe nanowires grown at a temperature of 500 °C. The inset shows two fitted peaks to the data, centred at 71.66 ± 2.86 nm and 119.47 ± 9.60 nm.

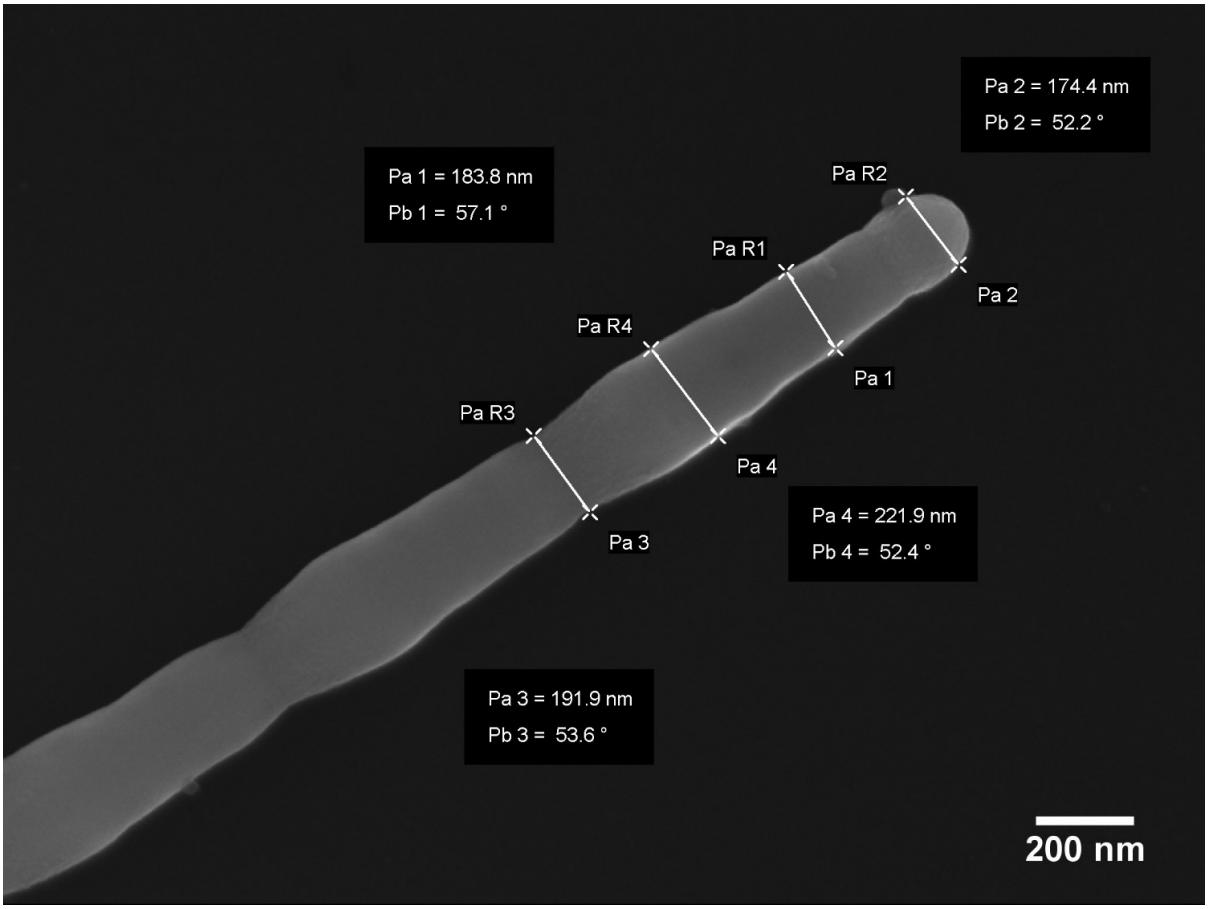


Figure A.2.5: Diameter measurements of a SnSe nanowire grown at 550 °C, showing a mean diameter around ~200 nm.

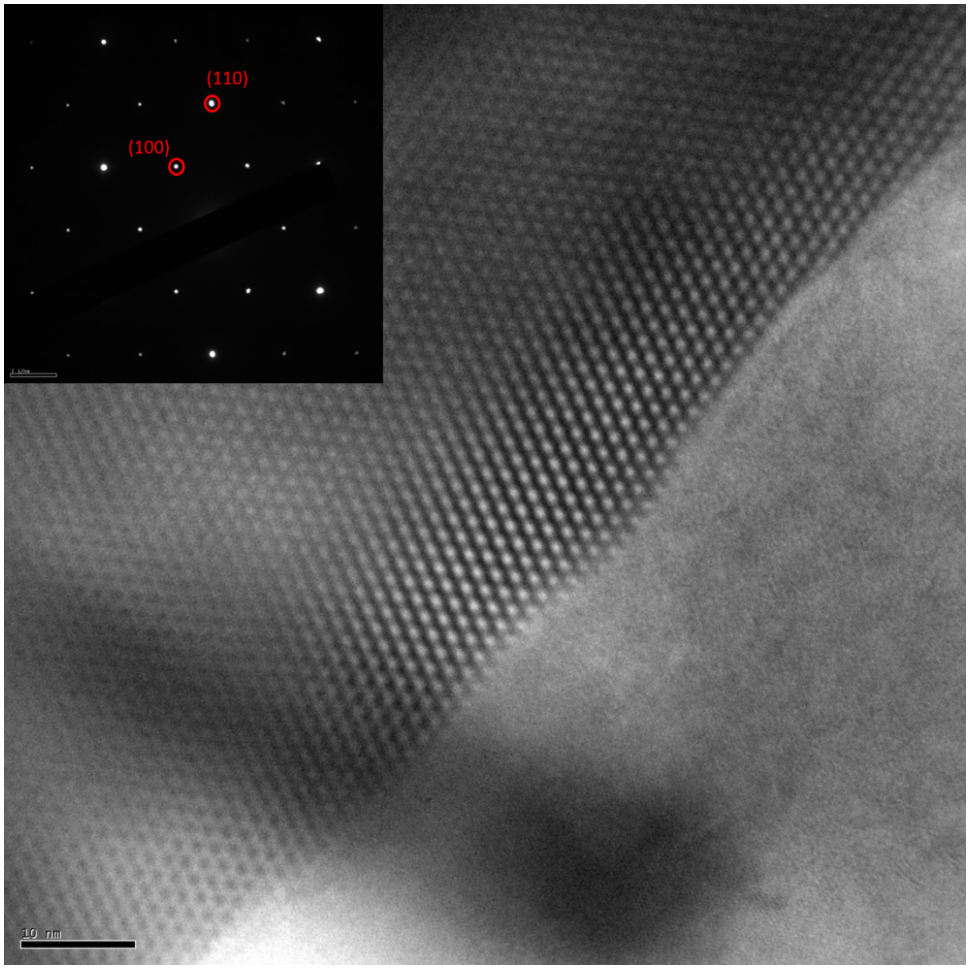


Figure A.2.6: TEM image of a $SnSe_2$ flake grown at a temperature of 450 °C viewed down the [001] zone axis. Inset: SAED pattern indexed to hexagonal $SnSe_2$ (P-3m1 (164) space group, JCPDS 23-0602).

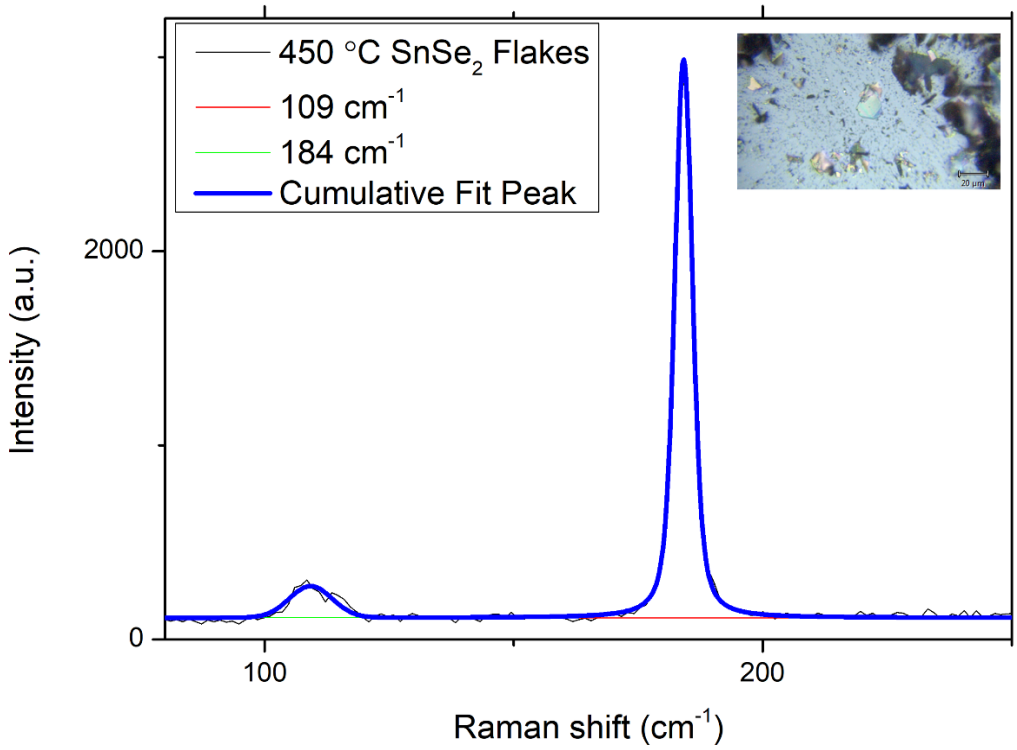


Figure A.2.7: Raman spectrum of a $SnSe_2$ flake (inset), showing the E_g (109 cm^{-1}, 12 FWHM) and A_{1g} (184 cm^{-1}, 5 FWHM) modes corresponding to $SnSe_2$ (514 nm excitation laser, peaks fitted using a Voigt function).

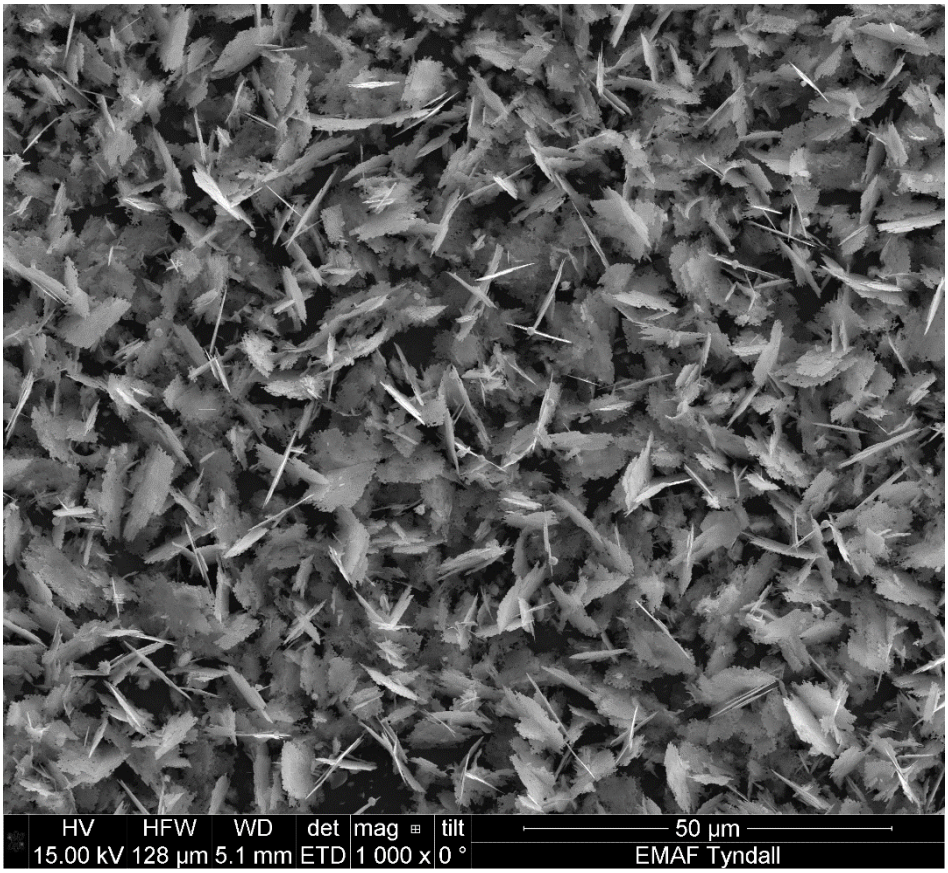


Figure A.2.8: SEM image of the growth substrate at temperature of 500 °C without the use of a Au film. Only large flakes are seen.

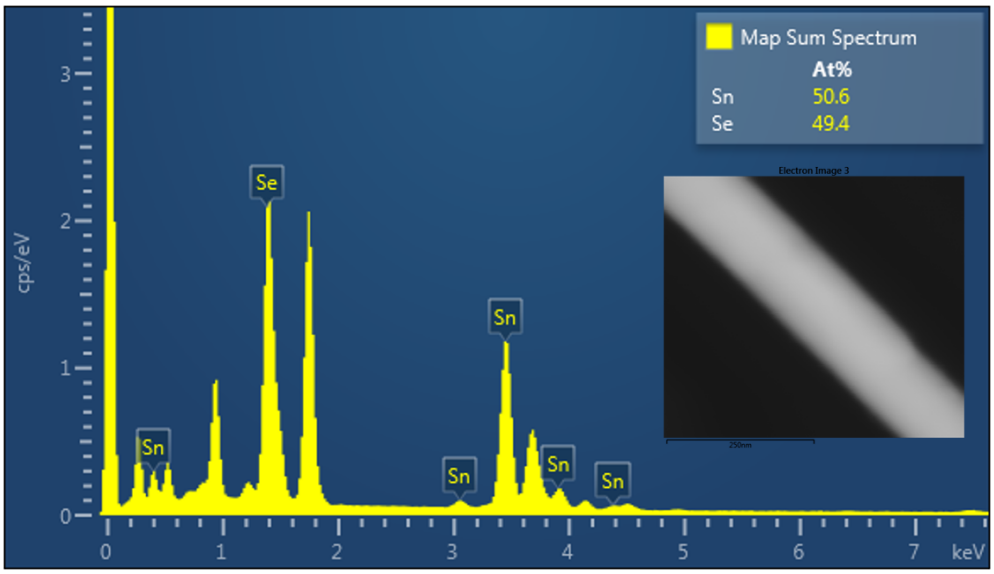


Figure A.2.9: EDX spectrum of a SnSe nanowire grown at 500 °C, showing the roughly 1:1 ratio of Sn:Se in the nanowire.

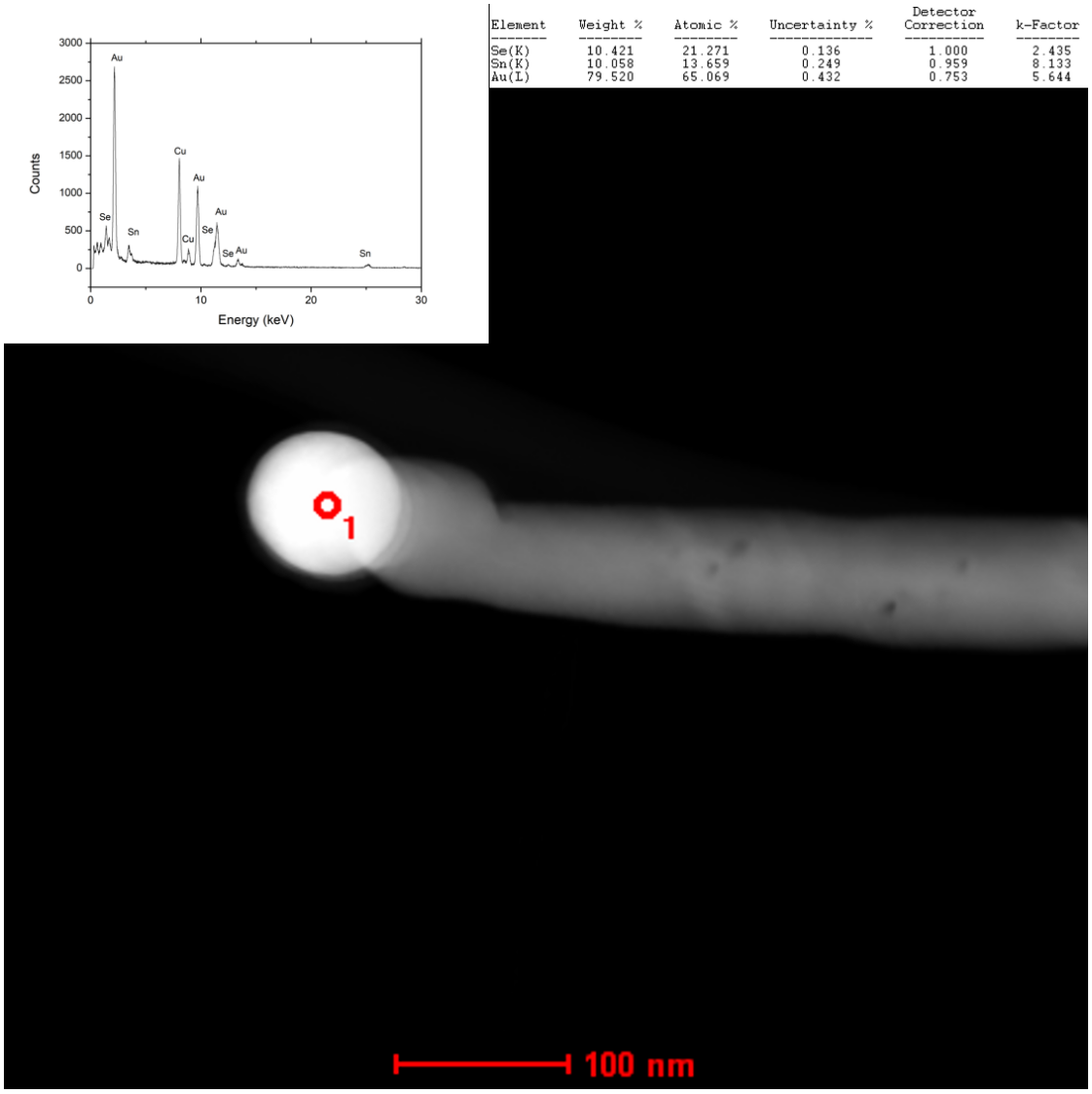


Figure A.2.10: STEM image of a SnSe nanowire grown at a temperature of 500 °C, showing the presence of a Au seed at the tip, which is confirmed by EDX analysis (inset).

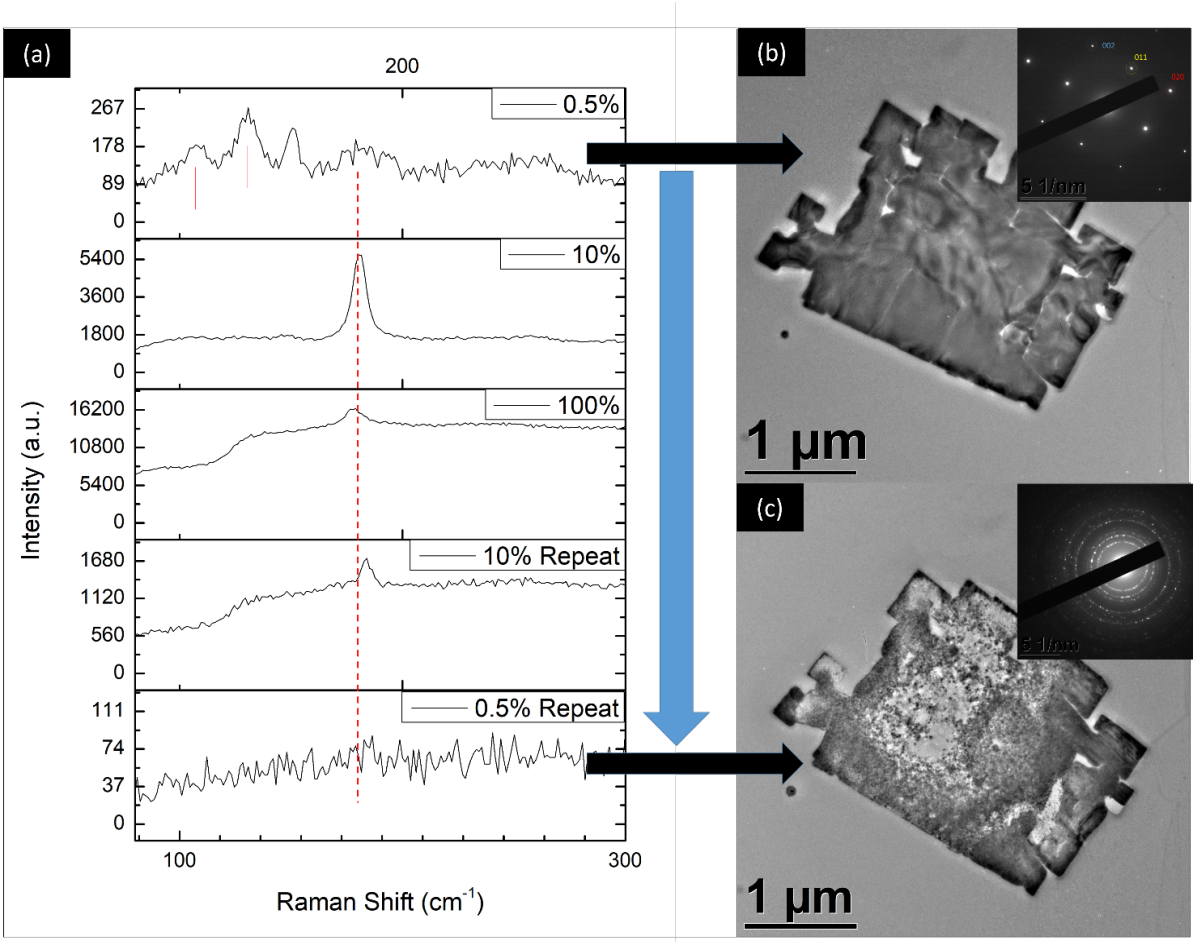


Figure A.2.11: (a) Sample damage from Raman analysis on a single SnSe flake. Raman analysis is shown with increasing power from top to bottom. The power is raised from 0.5 % to 10 %, and then to 100 % - and then back down to 10 % and then 0.5 % again. The modes for SnSe are seen at the initial 0.5 %, but after irradiation at 10 % laser power the ~180 cm^{-1} $SnSe_2$ Raman mode becomes highly prominent. This peak then becomes fainter as the power is increased above 10 %. (b) shows the flake before any Raman measurements are performed. The SAED shows single crystalline SnSe. (c) shows the flake after the Raman measurements are performed. The flake is now heavily damaged where the beam was incident on the flake, and the SAED pattern shows that the flake now exhibits a highly polycrystalline structure.

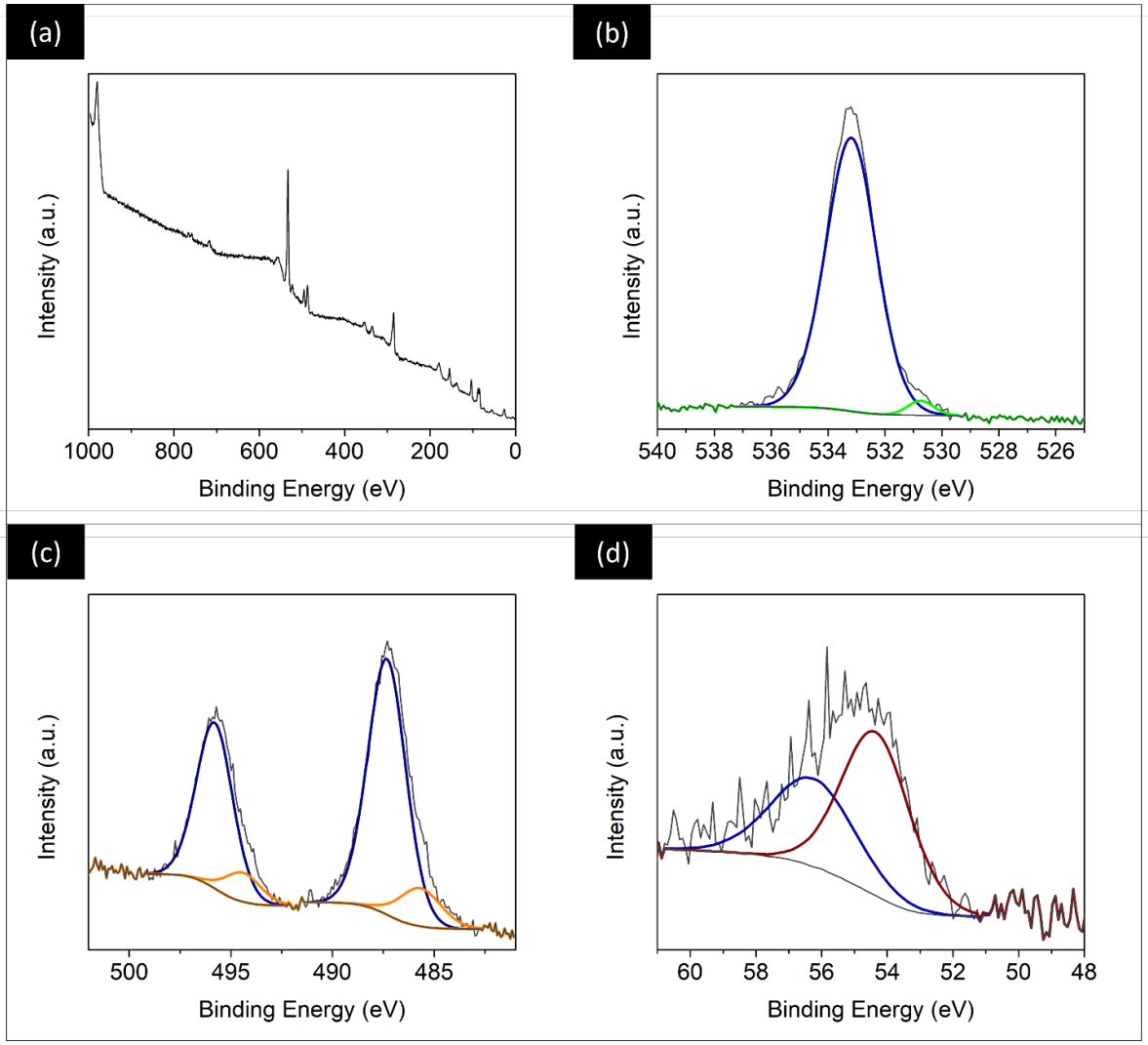


Figure A.2.12: XPS analysis of the nanowires formed at a growth temperature of 500 °C. (a) Survey spectrum indicating the presence of both Sn and Se. (b) shows the O 1s peak, assigned to ambient contamination and other oxide forms, *e.g.* surface hydroxide groups. Also shown in this spectrum however is the presence of a SnO_2 component at 530.8 eV. (c) shows the Sn 3d peak, with the presence of oxide peaks. Sn 3d5/2 is shown at 485.7 eV with an oxide component at 487.3 eV and the Sn 3d3/2 is shown at 494.4 eV with an oxide component at 495.8 eV. (d) The Se 3d peak, with the Se 3d/2 at 56.26 eV, and the Se 3d5/2 at 54.36 eV.

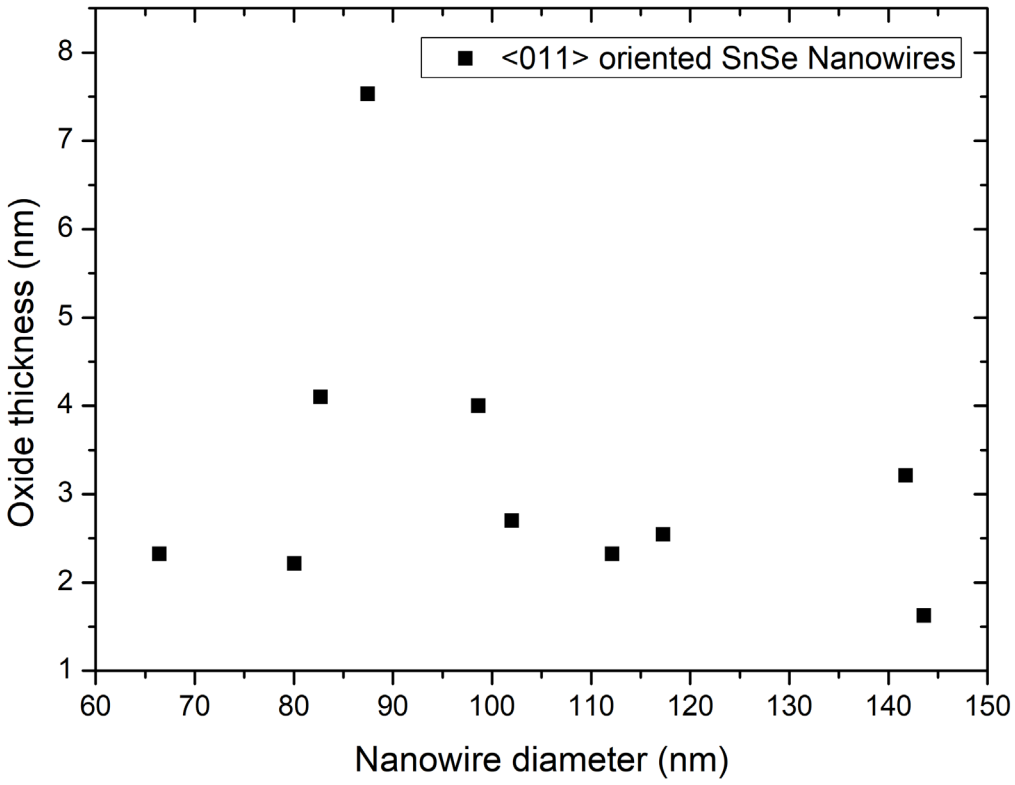


Figure A.2.13: Measured oxide thickness vs. nanowire diameter from TEM analysis, for a sample of nanowires which were grown at 550 °C.

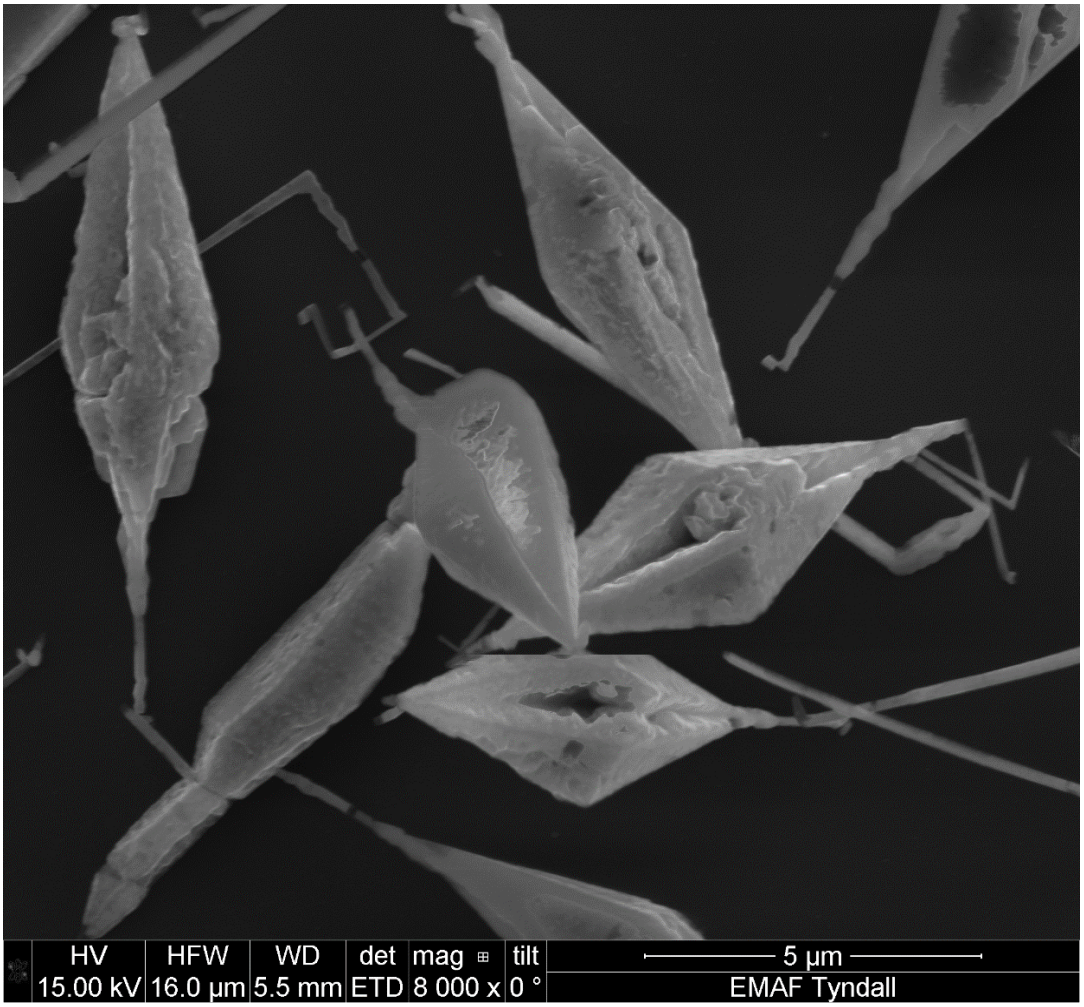


Figure A.2.14: SEM image of structures grown on a Si wafer in the absence of a Au film, by CVD at a temperature of 550 °C. Large bulb-like objects and large microwires are seen to form under these conditions.

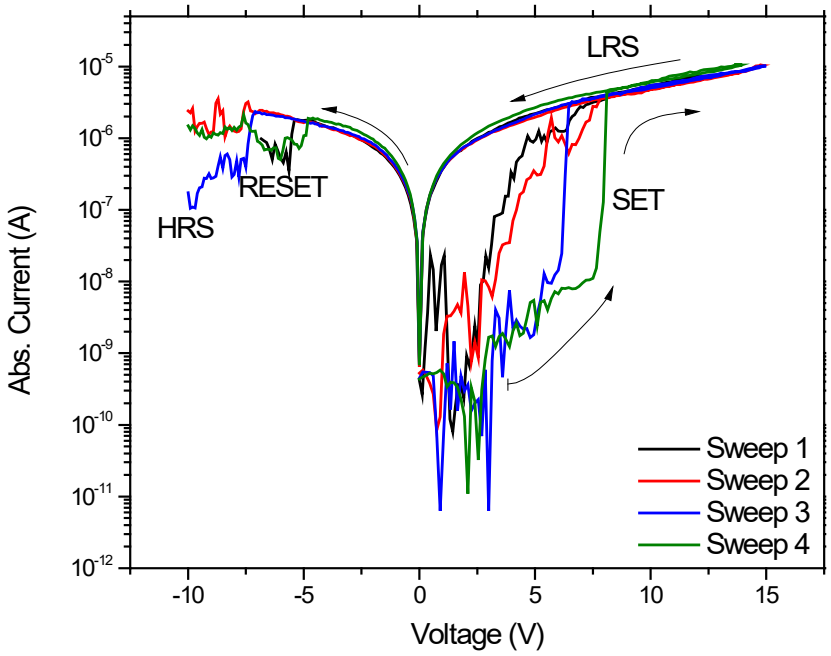


Figure A.2.15-A: Four stacked I-V curves (black arrows indicate the voltage sweep direction) demonstrating the consecutive polarity-dependent resistive switching shown in Figure 2.5(d). Sweep 1 was set to a maximum positive voltage of 12 V while sweeps 2 - 4 had a maximum of 15 V. Each experiment was ended after the device experienced a RESET event, which was between -5 V and -7.5 V.

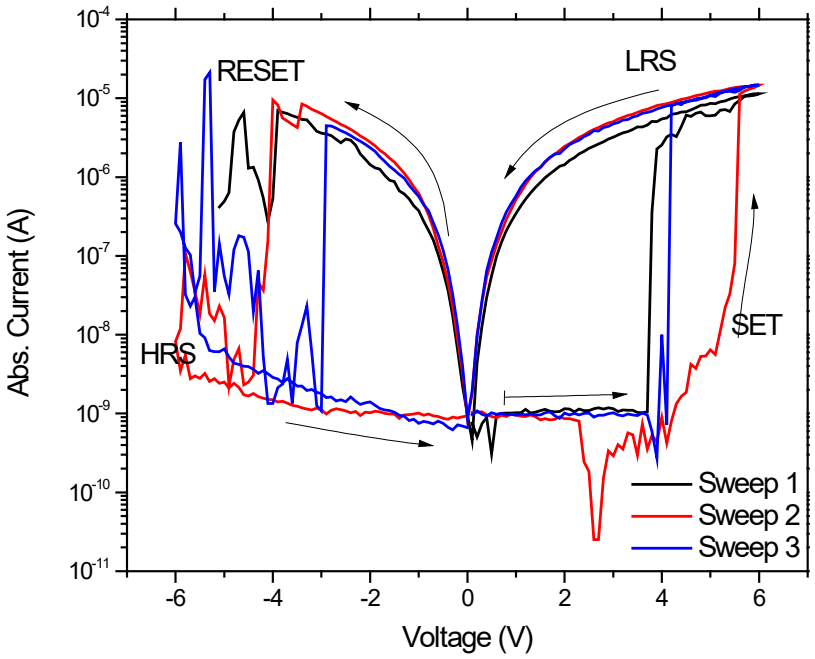


Figure A.2.15-B: Three stacked I-V curves (black arrows indicate the voltage sweep direction) of a device which demonstrated three consecutive SET/RESET cycles.

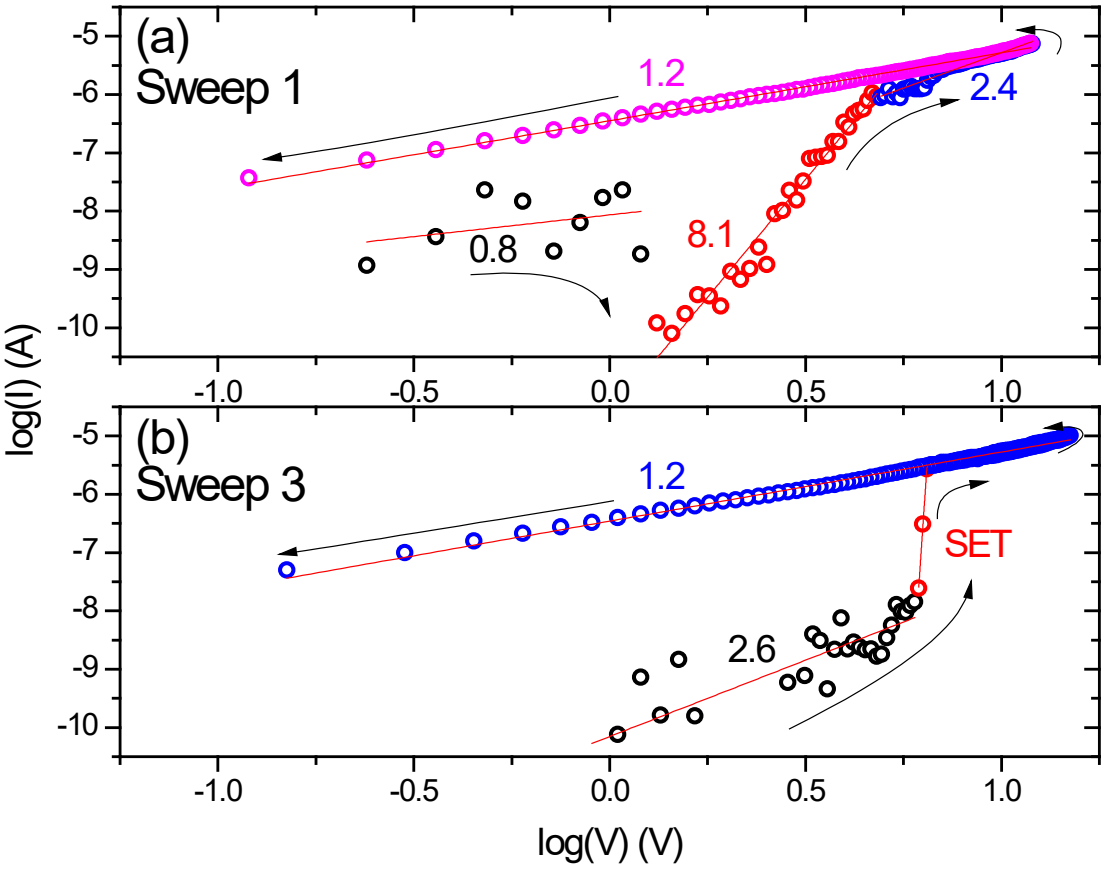


Figure A.2.16-A: The resistive switching behaviour of a SnSe nanowire device (Figure A.2.15-A, sweep 1 and 3) plotted as a log of current versus voltage. Black arrows indicate the sweep direction. The slope values of straight-line fits to regions of the data have been marked on the curves.

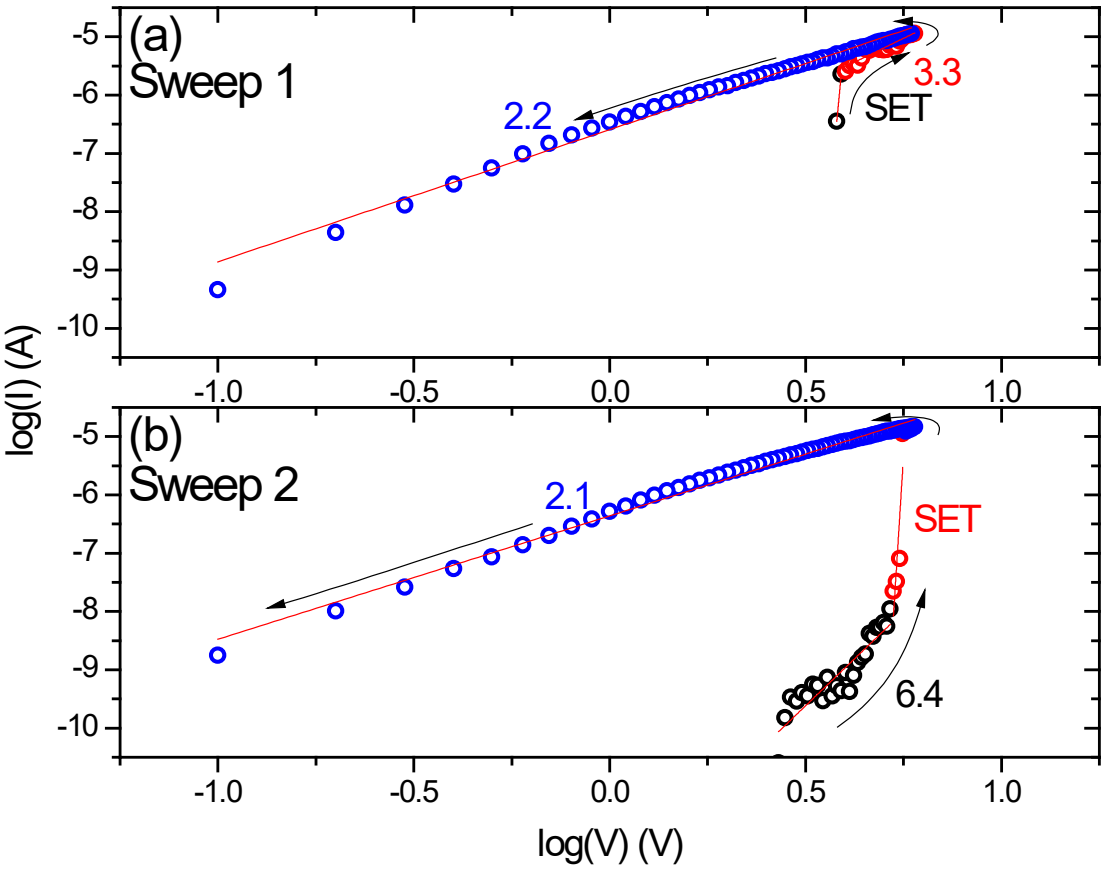


Figure A.2.16-B: log of current versus voltage data for a SnSe nanowire device (Figure A.2.15-B, sweep 1 and 2). Black arrows indicate the voltage sweep direction. Distinct regions have been marked on the graphs with straight line fits and slope values. Current data from the low bias regions of the experiment were recorded as negative values (noise) and could not be plotted.

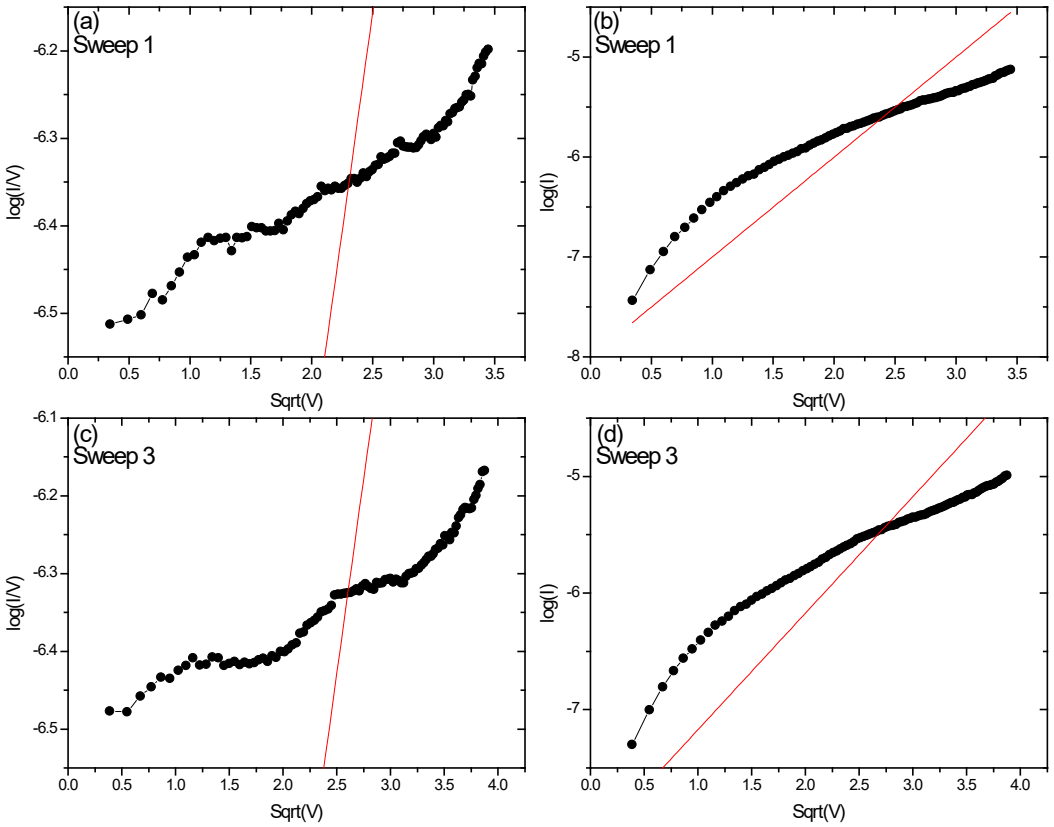


Figure A.2.17-A: Electrical data for Figure A.2.15-A (sweep 1, 3) plotted as log(I/V) versus √V (a, b) and log(I) versus √V (c, d) for the LRS in order to identify Poole-Frenkel and Schottky emission conduction mechanisms. The red line, with slope = 1 is a guide to the eye, representing a linear relationship between the plotted data.

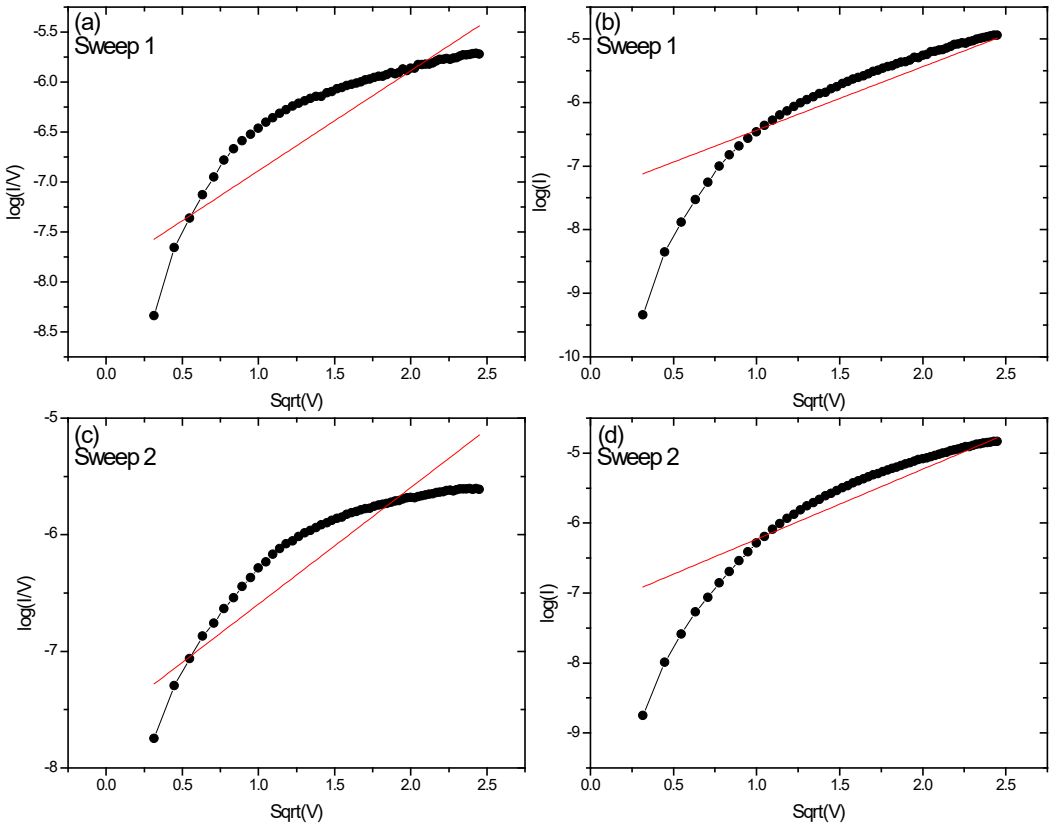


Figure A.2.17-B: Electrical data for Figure A.2.15-B (sweep 1, 2) plotted as log(I/V) versus √V (a, b) and log(I) versus √V (c, d) for the LRS in order to identify Poole-Frenkel and Schottky emission conduction mechanisms. The red line, with slope = 1 is a guide to the eye, representing a linear relationship between the plotted data. The current data from the low bias regions of the experiment were recorded as negative values (noise) and could not be plotted.

2.8.1 Appendix Discussion

Figures A.2.16-A and A.2.16-B show the resistive switching behaviour of two two-terminal SnSe nanowire devices plotted in log-log format. The slopes of the linear fit regions can be described by the space-charge-limited current (SCLC) theory. In the case of Figure A.2.16-A, in the LRS the behaviour is Ohmic-like, as the current-voltage relationship is observed to be close to linear. While in Figure A.2.16-B the LRS region follows the Child's square law ($I \propto V^2$) similar to stacked $SnO_x/SnSe/SnO_x$ devices, where the conduction mechanism was interpreted to follow the shallow trap-associated theory.[1]

The resistive switching data is plotted is Figures A.2.17-A and A.2.17-B to investigate the presence of Poole-Frenkel (PF) (a, c) and Schottky (b, d) conduction mechanisms.[2] The linear relationship determining PF conduction is poor across both devices, however, regions of Schottky conduction can be observed in the high bias portions of the of the data plotted in Figure A.2.17-B (b, d). From this we can conclude that both trap-controlled SCLC and Schottky conduction mechanisms play a role in the device behaviour.

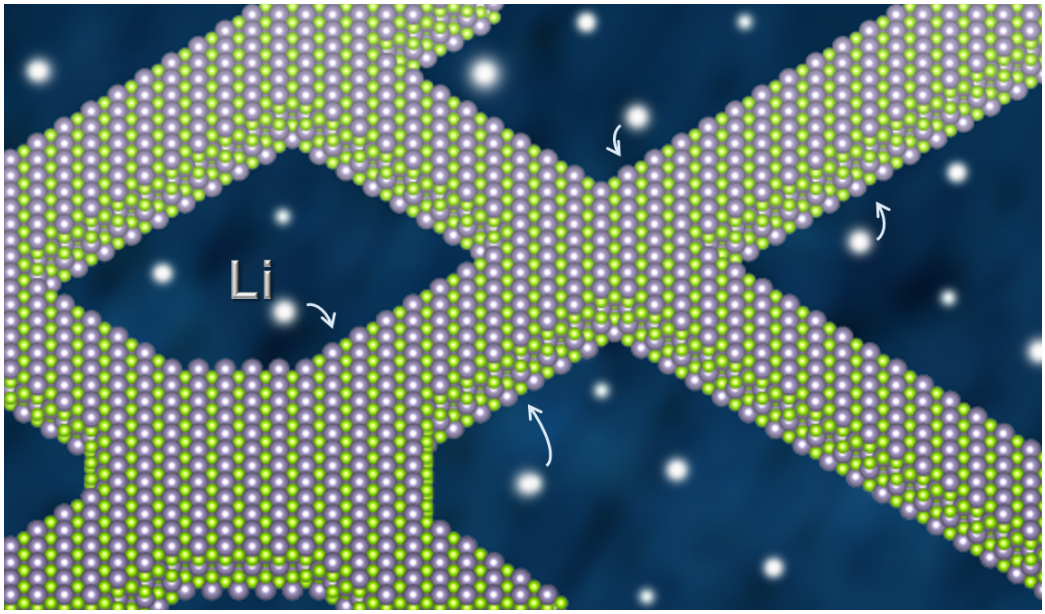
2.8.2 Appendix References

(1) Tian, H.; Wang, X. F.; Mohammad, M. A.; Gou, G. Y.; Wu, F.; Yang, Y.; Ren, T. L. A Hardware Markov Chain Algorithm Realized in a Single Device for Machine Learning. *Nat. Commun.* **2018**, *9*, 1–11.

(2) Lim, E. W.; Ismail, R. Conduction Mechanism of Valence Change Resistive Switching Memory: A Survey. *Electron.* **2015**, *4*, 586–613.

Chapter 3

2D SnSe Nanonetworks; Growth and Evaluation for Li-ion Battery Applications



Nanomaterial growth and analysis was performed by myself; including CVD reactions, SEM, EDX, TEM, electron diffraction, XRD and Raman analysis.

Killian Stokes, Hugh Geaney and Kevin M. Ryan undertook the electrochemical testing of the SnSe nanonetworks.

Timothy W. Collins performed the AFM measurements and assisted in producing the samples for electrochemical testing.

Fred Robinson and Gillian Reid provided the starting precursor for the CVD experiments.

Manuel Roldan-Gutierrez and Shery L. Y. Chang performed high resolution STEM and EELS measurements

I co-wrote this paper with Subhajit Biswas and Justin D. Holmes.

Davitt, F., Stokes, K., Collins, T. W., Roldan-Gutierrez, M., Robinson, F., Geaney, H., Biswas, S., Chang, S. L.Y., Ryan K. M., Reid, G., Holmes, J. D., Two-Dimensional SnSe Nanonetworks: Growth and Evaluation for Li-Ion Battery Applications. ACS Applied Energy Materials 2020, 3 (7), 6602-6610, https://doi.org/10.1021/acsaem.0c00776

3.1 Abstract

Engineered two-dimensional (2D) layered materials possess unique physical properties, with the potential to improve the performance and endurance of future electronic and energy devices. Here we report the growth of complex 2D nanonetworks of crystalline tin selenide (SnSe) via liquid injection chemical vapour deposition using a single source diselenoether precursor. Potential applications of SnSe span a wide range of technological areas, particularly in energy devices. The synthesized SnSe networks were composed of high surface area interconnected junctions of one dimensional (1D) nanowires in a 2D plane; such complex SnSe nanonetwork structures have not previously been reported. The SnSe networks possessed an orthorhombic Pnma 62 crystal structure throughout, with the individual network branches uniformly orientated along the <011> and <01-1> directions. The width of the individual interconnected nanowire branches ranged from 120 – 250 nm, with lengths ranging from 1 to 4 μm. The networks of 1D nanowires had a layer thickness of 88 ± 10 nm. A growth mechanism for the formation of these networks is proposed based on the minimisation of high surface energy planes. We also highlight the potential of SnSe nanonetworks as anode material for Li-ion batteries, with galvanostatic testing showing an initial discharge capacity in excess of 1000 mAh g^{-1}, with a 92 % capacity retention after 50 cycles at a specific current of 100 mA g^{-1}.

3.2 Introduction

The increasing demand on the Earths' resources, and the surge in interest in green technology, is fuelling research into new materials and new morphological design for efficient energy generation and storage devices. Metal chalcogenide materials, typically in the form of varying stoichiometries of MX [M=Pb, Cd, Zn, Ag, Sb, Sn, etc.; X=S, Se, Te] have shown great prospects for energy device applications.[1] Materials such as PbTe and Bi_2Te_3 have historically

been popular in the field of thermoelectric materials,[2] however, avoiding scarce and environmentally toxic materials such as Pb, Bi and Te, is of great importance for such applications if they are to be sustainable. Similarly for photovoltaic applications, materials such as Pb and Cd based chalcogenides have been widely studied.[3] In comparison to these, other chalcogenide materials, such as SnSe, a relatively Earth abundant and non-toxic material, is an attractive option for sustainable energy device applications.[1] Indeed, SnSe has shown great promise for thermoelectric devices[4–7] and for solar cells[8–10] and has been reported to have a record high thermoelectric ZT value of 2.6 along its crystal b-axis.[11] In addition to these promising energy harvesting capabilities, SnSe also has great promise for applications in Li-ion batteries.[12–15] Commercial Li-ion batteries typically use graphite as an anode; possessing a capacity of ~372 mAh g^{-1}.[16] SnSe, however, is a very attractive material for improvement of Li-ion batteries due to the high theoretical capacity of $Li_{4.4}Sn$ of 994 mAh g^{-1}, which sparked initial interest into thin film SnSe as an anode material.[17] Early results, however, showed a reduced capacity for SnSe based anodes of 400 mAh g^{-1} after 40 cycles, with improvements made in recent studies to as high as 1003 mAh g^{-1}.[16] Therefore there is a strong motivation to study SnSe as a promising alternative to other scarce and toxic chalcogenide materials for energy applications.[1]

SnSe is a layered metal chalcogenide material, formed from tightly bound chemical bonds across the *b* and *c* crystal axes, and weak van der Waals bonds across the longer *a*-axis direction. This weakly bound *a*-axis direction contributes to SnSe forming readily in 2D plate structures,[18] due to the slower crystal growth rate along this direction, and easier cleavage along this plane.[19] SnSe has also been shown to form as 1D nanowire structures.[20,21] Engineering the morphology of nanomaterials, such as in a 2D sheet or 1D nanowire form, is an ideal way to tune their material properties, as well as the scalability for device implementation.[22]

The controlled growth and structural engineering of nanomaterials has the potential to offer an untold impact on technology. Engineering materials in a nanostructure form allows incredible potential for device scaling to smaller dimensions, as well as presenting unique electrical, optical and mechanical properties, distinct from the bulk material.[23–25] 2D materials in particular are being heavily pursued for battery applications, with the 2D form offering many advantages over the bulk structure.[26,27] Further engineering of the material structure can lead to even more exotic nanostructures,[28] such as complex branched nanonetworks. These nanonetworks are formed from large groups of intersecting nanowires with single crystalline junctions, and have been shown to exhibit novel electrical, chemical and mechanical properties compared to their bulk counterparts.[29–31] In particular, nanonetworks with high porosity are an ideal energy harvesting platform (e.g. thermoelectric, photovoltaic, etc.), as the thermal conductivity is drastically reduced in such structures due to a combination of the high porosity with increased backscattering at the nodes and enhanced light absorption due to high surface area.[32] In addition, a seamless network made of nanowires is also an ideal material for energy storage applications; combining the improved cyclability associated with nanowire battery materials[33] with stronger mechanical strength and continuous electron transport pathways, while also maintaining a large exposed surface area to enhance electrolyte infiltration.[30]

Complex branched nanostructures exist for many technologically-important materials, such as Si[34] and III-V materials like GaN,[34] GaP[35] and GaSb.[36] Branched chalcogenide nanomaterials such as MoS_2[37] and CdTe[38] have been produced through solution methods, and branched PbS[39] and PbSe[40] nanostructures have been grown though various bottom-up CVD growth methods. SnSe has been shown to form in both 2D plate structures[18,41,42] and 1D nanowire structures[20,21] via chemical vapour deposition (CVD) methods, but engineering the nanowires in a seamless

2D network structure of SnSe has thus far proved elusive. The 2D nature of the layered SnSe material can act as a constraint in one direction to confine the network to a 2D plane. Further controlled reaction mechanics, such as energetically preferred crystal growth directions or selective surface passivation, then act to restrict the lateral growth into a nanowire-like form along the 2D plane, resulting in a 2D network of nanowires, which grow in the same x-y plane. $TiSi_2$, which crystallises in a similar layered structure to SnSe, has been shown to form in a branched 2D nanonetwork where the branched nanowires all lie within the same plane.[43,44]

Herein we report for the first time the growth of single crystalline 2D networks of SnSe nanowires, forming large complex branched structures. These networks are grown through the use of an atmospheric pressure CVD method, using a single source $[SnCl_4\{^nBuSe(CH_2)_3Se^nBu\}]$ precursor[45] without any growth catalysts. The growth of these networked SnSe nanowires instead relies on the nucleation of localised high surface energy sites, and the subsequent surface energy minimisation of these sites, which leads to the growth of nanowire networks with low surface energy faceted planes. We report electrochemical data from these SnSe nanonetworks, presenting them as a promising material for future high performance Li-ion battery applications.

3.3 Experimental

SnSe nanonetworks were synthesised using a liquid-injection CVD method, utilising $[SnCl_4\{^nBuSe(CH_2)_3Se^nBu\}]$ as a single source precursor.[45] This precursor was prepared in the same manner as described in the previous report by de Groot *et. al.*[45] This precursor was dissolved to a concentration of 7.5 mg ml^{-1} in anhydrous toluene, inside a nitrogen filled glovebox, before being loaded in a Hamilton sample-lock Gastight syringe.

The growth of the SnSe nanonetworks was performed on Si (100) substrates without removing the native oxide. For electrochemical testing the samples were grown on stainless steel substrates. Both types of substrates were cleaned in acetone and iso-propyl alcohol (IPA), before being dried with nitrogen and heated in a vacuum oven at 70 °C overnight, to ensure thorough removal of residual moisture. The substrates were then transferred to the CVD chamber with a 6 mm inner diameter quartz tube lining. The growth substrate was placed at the centre of the tube furnace. Prior to precursor injection the chamber was dried under vacuum and purged with high purity argon gas. The reaction chamber was heated to 550 °C, with a constant flow of 1.1 SCCM of argon gas. Injection of the precursor was then initiated and maintained at a constant rate of 1.5 ml h^{-1} using a KDS series 100 single-syringe pump until the desired injection volume was achieved.

3.4 Characterisation

After removal from the CVD chamber, the synthesised nanomaterials were analysed using a Zeiss Supra 40 scanning electron microscope (SEM) and a Helios Nanolab 600i SEM. Raman scattering spectroscopy was performed with a Renishaw InVia Raman spectrometer equipped with a 2400 lines/mm grating using a 514 nm laser. Spectra were collected using a RenCam CCD camera, with the beam focused onto the samples using a 50× objective lens. Measurements were undertaken at 1% of the total 1.9 mW laser power. The crystal structure of the product was confirmed by X-ray diffraction (XRD) using a Philips X'pert Pro MPD equipped with a Panalytical Empyrean Cu X-ray tube and a Philips X'celerator detector. The products were mechanically removed from the Si growth substrate for (scanning) transmission electron microscopy ((S)TEM) and energy dispersive X-ray (EDX) analysis. Removal of the nanomaterial was easily achieved through a quick sonication of the growth substrate in an ultrasonic bath, using a small amount of IPA. The resulting solution was then drop-cast onto

a carbon-coated TEM grid. TEM analysis was performed on a JEOL 2100 electron microscope operating at 200 kV and an FEI Titan electron microscope operating at 300 kV. STEM and EDX analysis were performed on an FEI Titan electron microscope operating at 300 kV. High annular dark field (HAADF) and bright field (BF) STEM imaging, EDX mapping and Electron energy loss spectroscopy (EELS) was performed on a Probe Corrected JEOL ARM TEM operating at 200 kV.

Electrochemical testing was carried out galvanostatically using a Biologic MPG-2. The two electrode Swagelok type half-cells were assembled within an Ar filled glovebox with H_2O and O_2 levels below 1 ppm. The SnSe samples were directly grown on stainless steel current collectors and tested as the working electrode versus a Li metal counter/reference electrode. Typical areal loadings for the samples were ~0.2 mg/cm^2. All potentials mentioned are quoted relative to Li/Li$^+$. Celgard separators impregnated with a carbonate based electrolyte (1.0 M lithium hexafluorophosphate ($LiPF_6$) solution in ethylene carbonate and diethyl carbonate, battery grade Aldrich) with 3 wt% vinylene carbonate (97 % purity, Aldrich) were used. A specific current of ± 100 mAh g^{-1} was applied for testing within a cycling window of 3.0 - 0.011 V (vs. Li/Li$^+$) to fully include the alloying and conversion processes. The mass of the SnSe active material was determined through careful measurement using a Sartorius Ultra-Microbalance SE2 (repeatability ± 0.25 μg). Thorough accurate weighing at each stage in electrode preparation ensured accurate mass loadings which were used to calculate the C rate and galvanostatic capacities.

3.5 Results and Discussion

SnSe nanonetworks were synthesised (see Experimental section 3.3 for the detailed experimental method) using a liquid-injection CVD method at 550 °C, injecting

[$SnCl_4\{^nBuSe(CH_2)_3Se^nBu\}$] as a single source precursor[45] (precursor concentration of 7.5 mg ml^{-1}) at a constant rate of 1.5 ml h^{-1} under a constant flow of 1.1 SCCM of argon gas. The nanonetworks were grown on a Si substrate, which was placed at the centre of the furnace. The morphology, structural and chemical composition of the nanonetworks synthesised at 550 °C is shown in Figure 3.1. Figure 3.1(a) shows an SEM image of the networks, with an AFM topography image shown in Figure 3.1(b), highlighting large 2D plate-like structures, 30 – 40 μm in dimension and around 88 ± 10 nm thick (see Appendix Figure A.3.1 for additional AFM measurements and average thickness value), that are composed of many interconnected nanowire-like branches, approximately 120 nm wide. The lengths of the individual branches in the network vary from a few hundred nanometres to up to ~4 μm. This branched nature of the networks presents a greatly increased surface to volume area as compared to a uniform flake (appendix Figure A.3.2). Figure 3.1(c) shows an XRD pattern taken from the network sample shown in Figure 3.1(a) and can be assigned to phase pure orthorhombic SnSe (Pnma 62 orthorhombic, JCPDS 48-1224). The most intense peak in the XRD pattern is seen to be the 400 peak, demonstrating significant ordering of the 2D nanonetworks on the Si substrate. The (400) plane corresponds to the plane along which SnSe layers are stacked, and the observation of a relatively strong 400 XRD peak is commonly seen for 2D SnSe.[46] Figure 3.1(d) shows a TEM image of a section of these network branches after removal from the growth substrate. The networks are 2D in nature and are seen to lie flat on the TEM grid, with the nanowire branches all lying within the same plane, in a perpendicular manner to each other. The structural nature of these 2D nanonetworks closely resembles that of previously reported $TiSi_2$ nanonetworks.[43,44] The inset shows an EDX spectrum taken from the area highlighted in blue, showing an atomic percent ratio of 53:47 Sn:Se in the wire branches, presenting further evidence for the formation of stoichiometric SnSe. Raman analysis on these nanonetworks is shown in Figure 3.1(e), and exhibits the B_g vibrational mode of SnSe at ~107 cm^{-1}, and also

the modes corresponding to the SnSe A^2_g and A^3_g modes at 129 cm^{-1} and 151 cm^{-1}, respectively.[47] These values are in agreement with previously reported values for ultrathin SnSe flakes.[48]

The detailed crystal structure of the individual branches was analysed using high resolution TEM (HRTEM), as shown in Figure 3.1(f). The HRTEM image was taken from a junction area of the network, and this particular junction is highlighted in red in the low resolution TEM image of the nanonetwork structure shown in Figure 3.1(d). The bottom right inset of Figure 3.1(f) shows a magnified HRTEM image of an area of the branch, with a measured d-spacing of 0.299 nm which corresponds to the (011) and (0-11) lattice planes of Pnma 62 orthorhombic SnSe (JCPDS 48-1224). The top right inset shows a selected area electron diffraction (SAED) pattern taken from the area highlighted in purple in Figure 3.1(d). Diffraction spots in this SAED are assigned to Pnma 62 orthorhombic SnSe (JCPDS 48-1224) viewed down the [100] zone axis. The individual nanowire branches of these networks are seen to exhibit a growth direction in either the <011> or <0-11> directions (Figure 3.1(f)). The angles between the 011 and 0-11 diffraction spots were found to be ~93°, with the angle between the 011 and 01-1 spots being ~87°. These are low surface energy planes for orthorhombic SnSe,[49,50] making these network structures energetically favourable due to the maximum exposure of these low energy surface planes. Previous reports on single SnSe nanowires have shown that these planes are also prevalent growth directions for simple 1D SnSe geometries.[20] The (001) and (010) planes are however expected to be higher surface energy planes and should exhibit an initially higher growth rate. From the TEM image of Figure 3.1(d), it is apparent that the network branches are not fully uniform in roughness along their length, and many expanded sites on the edges of the branches are seen in the low resolution TEM image (green circle in Figure 3.1(d)). These irregularly expanded surface regions are proposed to be initiated from growth along the

(001) and (010) planes. These surface edge sites are thought to act as nucleation sites for further branching. If the reaction was allowed to continue, it is proposed that these (001) and (010) planes would then be subsequently supressed by lower surface energy planes, leading to further branch formation along the (011) and (01-1) planes. This will be discussed in detail while discussing the growth mechanism of the nanonetworks.

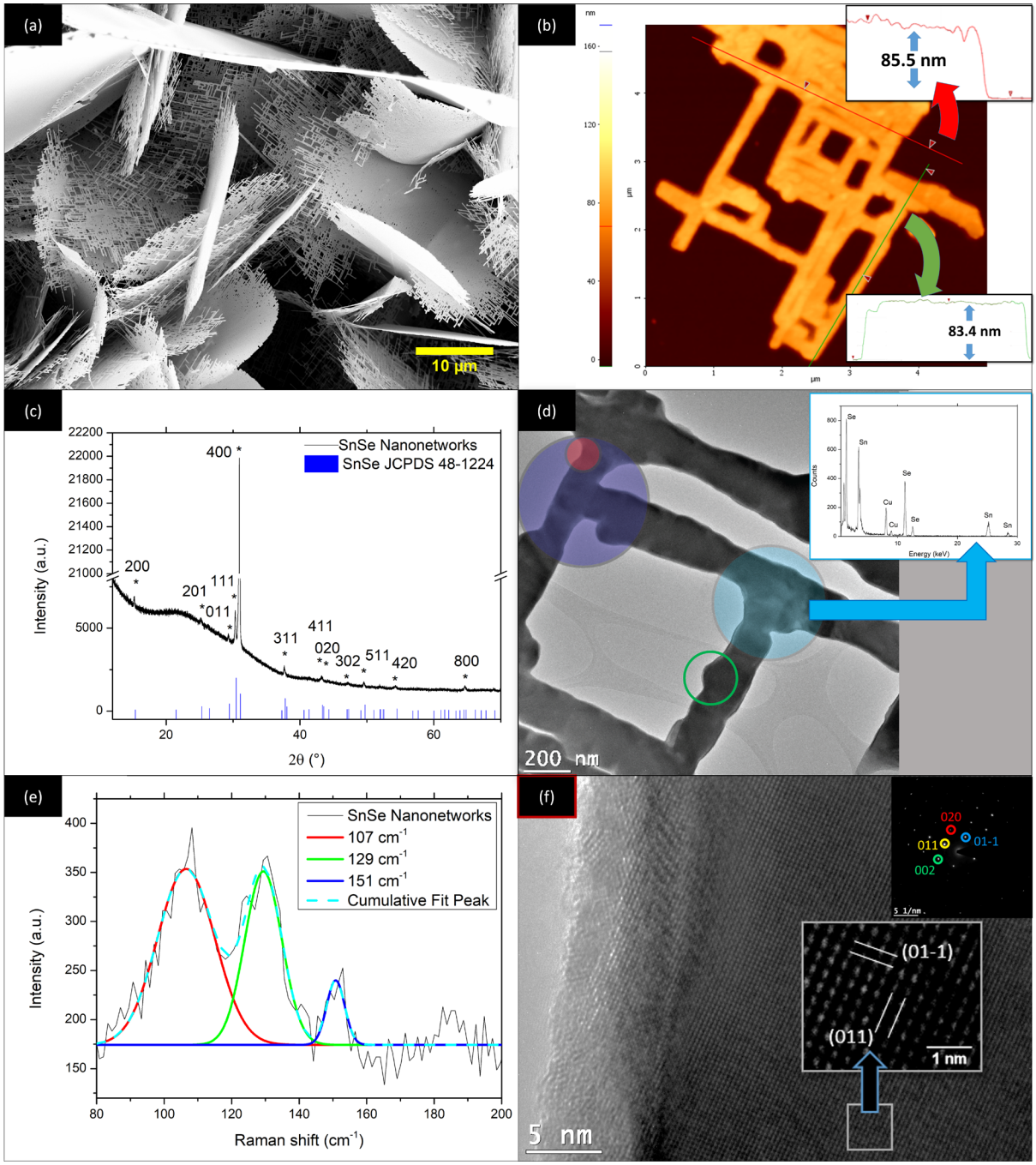


Figure 3.1: Analysis of the structure and composition of the nanonetworks. (a) SEM image of the SnSe nanonetworks, showing a large amount of interconnected nanowires growing from 2D plate structures. (b) AFM analysis of the SnSe nanonetworks, after dropcasting onto a Si wafer. Thickness profiles are shown in the two insets. (c) XRD analysis of the sample shown in **(a)**, indexed to Pnma 62 orthorhombic SnSe (JCPDS 48-1224). The broad peak in the region of ~22° is due to the glass slide upon which the sample was placed for the XRD measurement. (d) Low magnification TEM image of a section of a SnSe nanonetwork. The inset shows an

EDX spectrum of the area highlighted in blue, showing an atomic percent ratio of Sn:Se of 53:47. (e) Raman analysis of the SnSe nanonetworks. The peaks seen correspond to the B_g vibrational mode of SnSe at ~107 cm^{-1}, and the SnSe A^2_g and A^3_g modes at 129 cm^{-1} and 151 cm^{-1}, respectively.[47] (f) HRTEM image of the area highlighted in (d) in red, showing the high-quality single crystal structure of the SnSe networks. The measured lattice spacing confirms that the growth direction of the branches are along the <011> and <0-11> directions. This area is also at the interface of two meeting branches, and importantly shows no significant crystal defects at this intersection. The inset shows an SAED pattern of the area highlighted in purple in (d), showing a crystal structure indexed to Pnma 62 orthorhombic SnSe (JCPDS 48-1224). This also indicates that the growth direction of the branches is along the <011> and <0-11> directions.

The participation of a surface energy minimisation mechanism in the growth of the SnSe networks was further investigated through detailed TEM analysis. Figure 3.2(a) shows a low magnification TEM image of a SnSe nanonetwork. The network shows a highly uniform nature, with the angles between all the interconnected nanowires in the network visually appearing to form in a perpendicular manner to each other. From the SAED pattern shown in Figure 3.1(d) it is expected that these branches should be formed along the <011> and <0-11> directions, which for a Pnma SnSe crystal (JCPDS 48-1224) makes an angle of 93.822° between the (011) and (0-11) planes and 86.178° between the (011) and (01-1) planes. Measuring the angles between the branches in Figure 3.2(a) reveals angles of 93° and 87° between the wires in the nanonetwork, in close agreement with the calculated values. This provides further evidence for the uniform growth of the branches along these particular directions. Outside of these regular branches marked in red, a small amount of additional growth is also seen, particularly between the junctions of two meeting branches (Figure 3.2(a)).

The intersection of multiple branches is highlighted in the different coloured boxes with corresponding arrows. Figure 3.2(b) shows a schematic of the SnSe crystal structure in the proposed network form, viewed down the [100] direction. The branches are assigned to the <011> equivalent directions. Additional growth along the <010> and <001> directions at the branch intersections, as shown in the schematic of Figure 3.2(b), results in a simulated structure strongly resembling the TEM image of Figure 3.2(a), indicating that additional growth has occurred along these directions. The intersecting nanonetwork junction highlighted by the purple circle in Figure 3.2(a) is shown in detail in Figure 3.2(c), with a webbed structure seen between the two branches (white box). This webbed structure indicates growth along the <001> direction. Figure 3.2(d) shows a lattice resolved HAADF STEM image of a junction region, revealing a highly ordered single crystalline structure. This clearly shows the branches as <011> and <01-1> growth, with the additional inter-junction growth along the <001> direction. The thin amorphous layer seen at the surface of the network is composed of SnO_x (see EELS and EDX maps in the appendix, Figures A.3.3, A.3.4 and A.3.5), which is expected to have formed after exposure to atmospheric conditions, on removal from the CVD chamber, as seen before for previous reports on SnSe.[51]

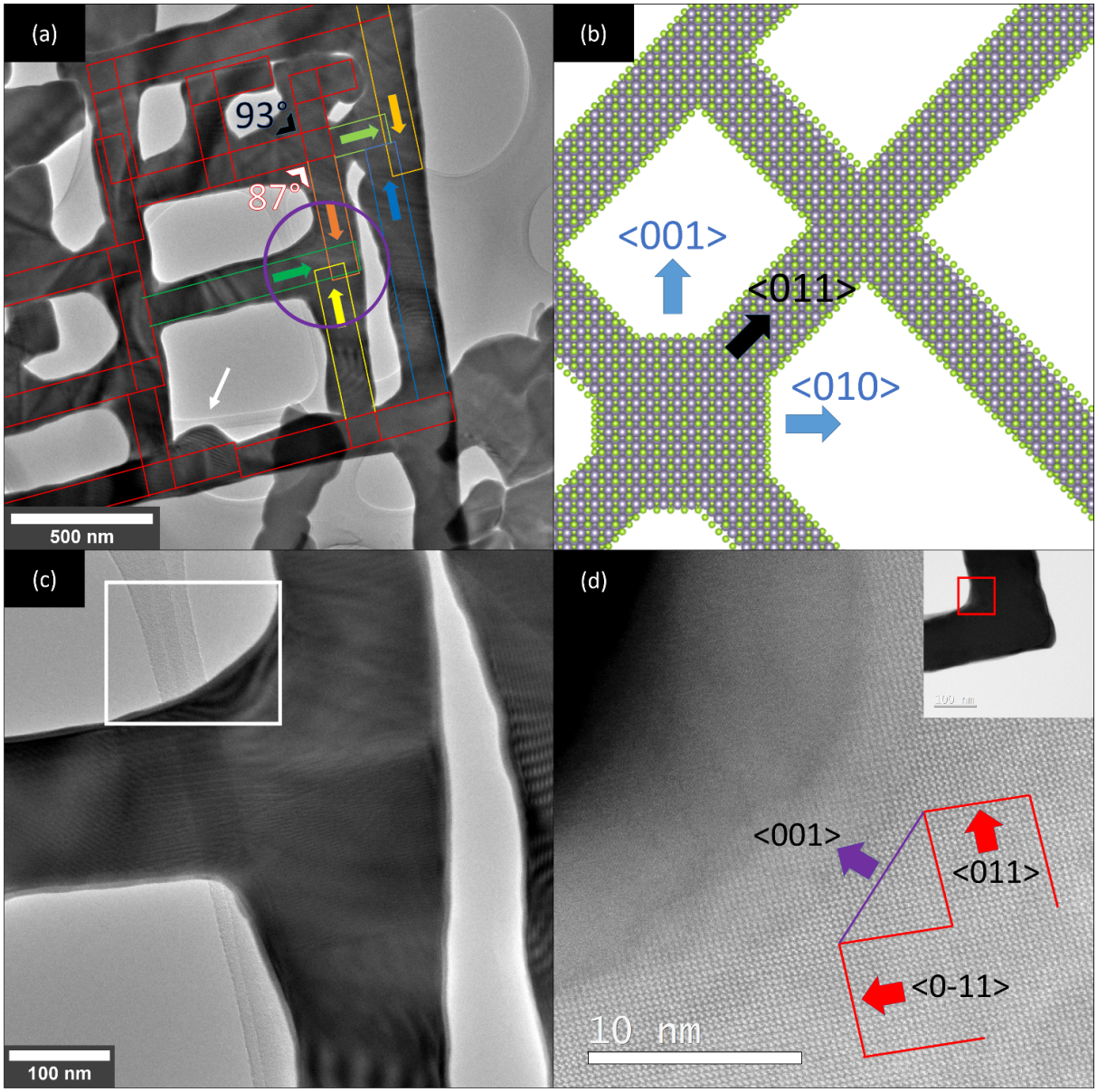


Figure 3.2: Analysis of the structure of the individual nanowire branches in a network: (a) Low magnification TEM image of a section of a nanonetwork. All of the branches are seen to form in a regular manner to each other, at angles of 93° and 87° to each branch. (b) Illustration of the predicted SnSe structure, based on the crystal data inferred from Figure 3.1, showing the growth direction of the branches along the <011> and <0-11> directions. (c) TEM image of the SnSe network junction within the purple circle in **(a)**. (d) High resolution STEM image of a single crystalline junction, with the branches assigned as growth in the <011> and <0-11> directions. Additional growth along the <001> direction at the junction interface is observed. Inset shows the junction region that the high resolution image is taken from.

A growth model; borrowing knowledge from the TEM and HRTEM observations; explaining the growth of SnSe nanonetworks is proposed in Figure 3.3. The (010) and (001) planes have previously been calculated to be high energy surface planes for an orthorhombic SnSe structure,[50] which should exhibit an initially high growth rate. The growth rate of these planes is expected to decrease as the reaction progresses, as the crystal system tries to minimise its surface energy by forming lower energy surface planes. Based on this, the growth is predicted to start with the nucleation of small (010) and (001) faceted SnSe flakes, as shown in Figure 3.3(a). As the growth continues, surface energy minimisation results in the appearance of the lower surface energy (011) and (0-11) planes as is shown in Figure 3.3(b), with these low surface energy planes eventually dominating the growth (Figure 3.3(c)). However, changes in the favoured growth planes could be induced through small changes in reaction equilibrium, such as temperature or gas flow fluctuations (leading to precursor vapour pressure variations). Changes in such reaction conditions have previously been shown to alter the preferred growth planes in $TiSi_2$ nanonetworks.[44] These changes in reaction equilibrium could lead to the reappearance of a small number of (010) and (001) surface planes, as shown in Figure 3.3(d). Defects induced by the interaction between the meeting of two <011> nanowire branches could also lead to a change in locally favoured growth planes (additional <010> and <001> growth is seen at the meeting of three branches in Figure 3.2(c). These planes would then grow until the growth along these planes again became unfavourable, and the low-energy (011) and (01-1) plane growth would begin to dominate once again (Figure 3.3(e)). Maximisation of these low surface energy planes would then continue, with the growth progressing predominantly in the <011> and <01-1> directions, leading to a protruded edge site on the wire structure (Figure 3.3(e)). The white arrow in figure 3.2(a) indicates an example of this in the nanonetwork. This edge site would then act as a nucleation site for the branch growth, with continuation of growth

along the <011> and <01-1> directions then leading to the network structure as shown in Figure 3.3(f). Notably the webbed-like structure between the junctions of the nanowire branches, which is seen in Figure 3.3(f), is also seen in the TEM image in Figure 3.2(c) (white box).

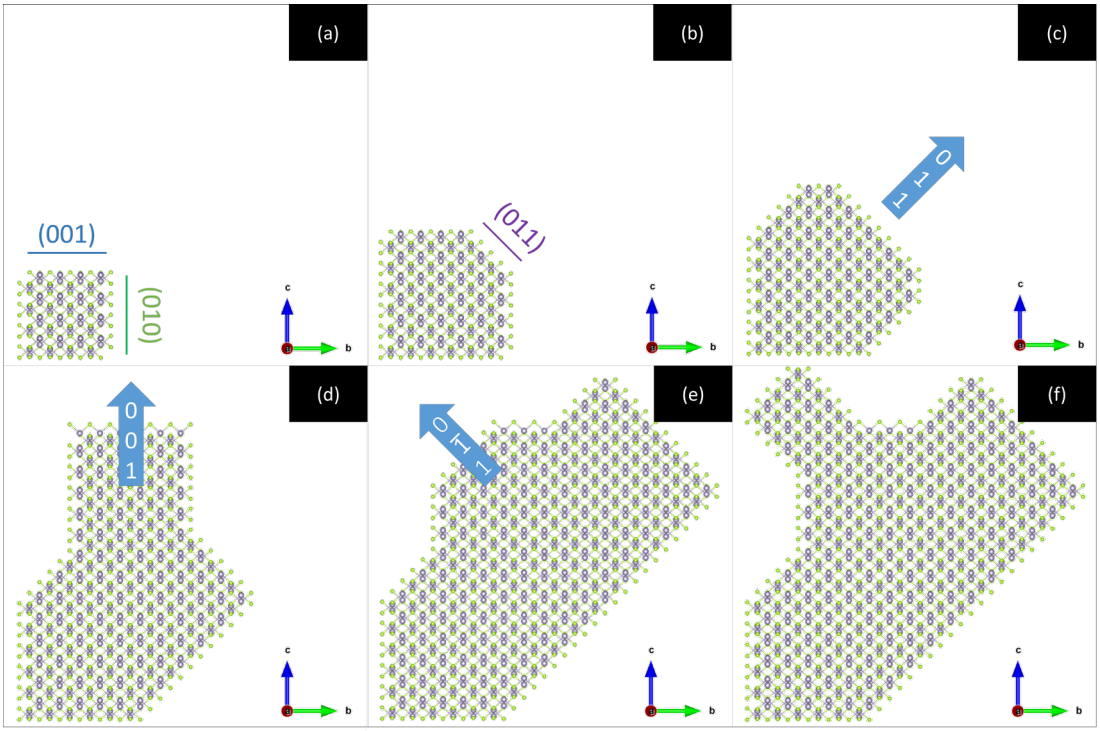


Figure 3.3: Proposed growth mechanism of the SnSe nanonetworks. (a) Initial {010} and {001} faceted SnSe flake is formed. (b) From this initial nucleation site, the flake continues to grow, with the gradual appearance of the lower surface energy {011} planes. (c) As the growth progresses, the high surface energy {010} and {001} planes are replaced with the lower surface energy {011} and {0-11} planes. (d) Small disturbances in the reaction equilibrium as the growth progresses results in the sporadic reappearance of a small number of {010} and {001} planes. (e) Surface energy minimisation results in the repression of these high surface energy planes with {011} equivalent planes, leading to these {010} and {001} planes acting as nucleation sites for additional <011> directed branches. (f) The growth continues along these <011> planes, leading to the networked SnSe structure.

Many factors can contribute to the nucleation and growth rate of crystal facets in CVD reactions, such as growth temperature, precursor concentration, chamber pressure, etc. In an attempt to further control the growth of these SnSe nanonetworks, the reaction was performed at a higher temperature (Figure 3.4) and then also at varying initial precursor concentrations (Figure 3.5). SEM images in Figure 3.4 show the comparison in network morphology for the growth at 550 and 600 ºC. A higher growth temperature is expected to yield a greater preference for high energy surface planes.[52] This is seen by increased growth of the less stable (001) and (010) planes, leading to increased density in branching with the branches that form being highly uneven along their length (see Figure 3.4, which shows the networks formed as a function of temperature). This increased density in branching resulted in a less porous 2D network nanostructure at 600 ºC compared to the growth at 550 ºC (Figure 3.4).

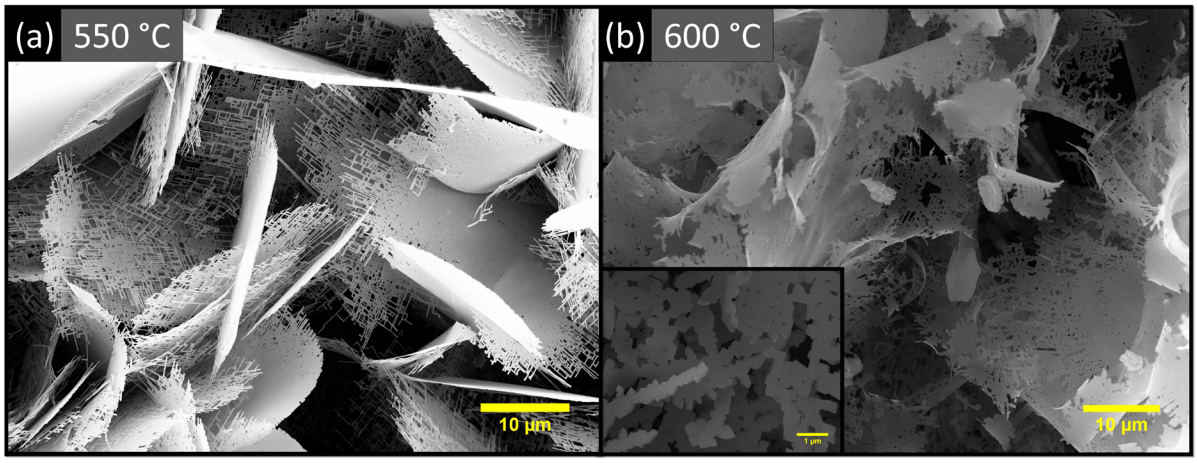


Figure 3.4: Growth of the SnSe structures as a function of growth temperature. (a) was performed at a furnace temperature of 550 °C and (b) at 600 °C.

Preforming the growth at a fixed temperature (550 ºC), whilst varying the initial precursor concentration (3.75 mg/ml, 7.5 mg/ml and 15 mg/ml), was also examined to observe the effect of limiting and increasing the precursor vapour influx to the crystal surface. However, this was seen to have very little influence on the structure of the final product in terms of dimension and branching density (Figure 3.5).

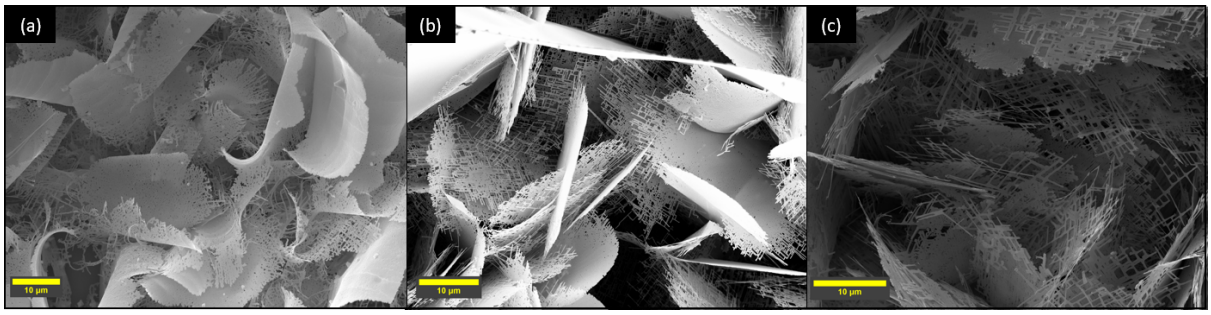


Figure 3.5: Growth of the SnSe structures as a function of initial precursor concentration at 550 ºC. Part (a), (b) and (c) shows growth with 3.75 mg/ml, 7.5 mg/ml and 15 mg/ml respectively.

Galvanostatic testing was carried out to assess the use of the SnSe nanonetworks as a potential anode material for Li-ion battery applications. To facilitate these tests, SnSe nanonetworks were grown directly on stainless steel current collectors. For electrochemical testing, SnSe nanonetworks were achieved at a growth temperature of 550 °C with 7.5 mg/ml precursor concentration. This growth condition was selected for electrochemical testing as previous growth at 550 °C produced a network structure with highest porosity and uniformity (Figure 3.4), whereas changing precursor concertation had minimal effect on the network morphology (Figure 3.5). Small changes in the morphology of the 2D network structures were observed in the networks grown on stainless steel compared to that grown on a silicon substrate, such as branch width and length, etc. (Figure 3.5(b) and appendix Figure A.3.6). The initial discharge capacity was in excess of 1000 mAh g^{-1} and showed a 92 % capacity retention after 50 cycles

at a specific current of 100 mA g^{-1} (Figure 3.6(a)), which compares favourably with previously reported SnSe anodes (appendix Table A.3.1 shows comparison with published SnSe electrochemical data). This capacity retention is drastically improved compared to other pure (i.e. not formed from a nanocomposite material) SnSe morphologies, where capacity retention is typically <35 % at this point.[12,16] Reduction of the volume of battery anode materials through nanostructuring has been shown to have a positive impact on the capacity retention of the device,[33] and we ascribe this improvement of the SnSe nanonetworks compared to non-structured SnSe to the better ability of the networks to accommodate the volume changes typically associated with Li insertion and removal. The voltage profiles shown in Figure 3.6(b) are consistent with the occurrence of conversion reactions at higher potentials (i.e. between ~1 V and 3 V) and Li alloying below ~1 V.

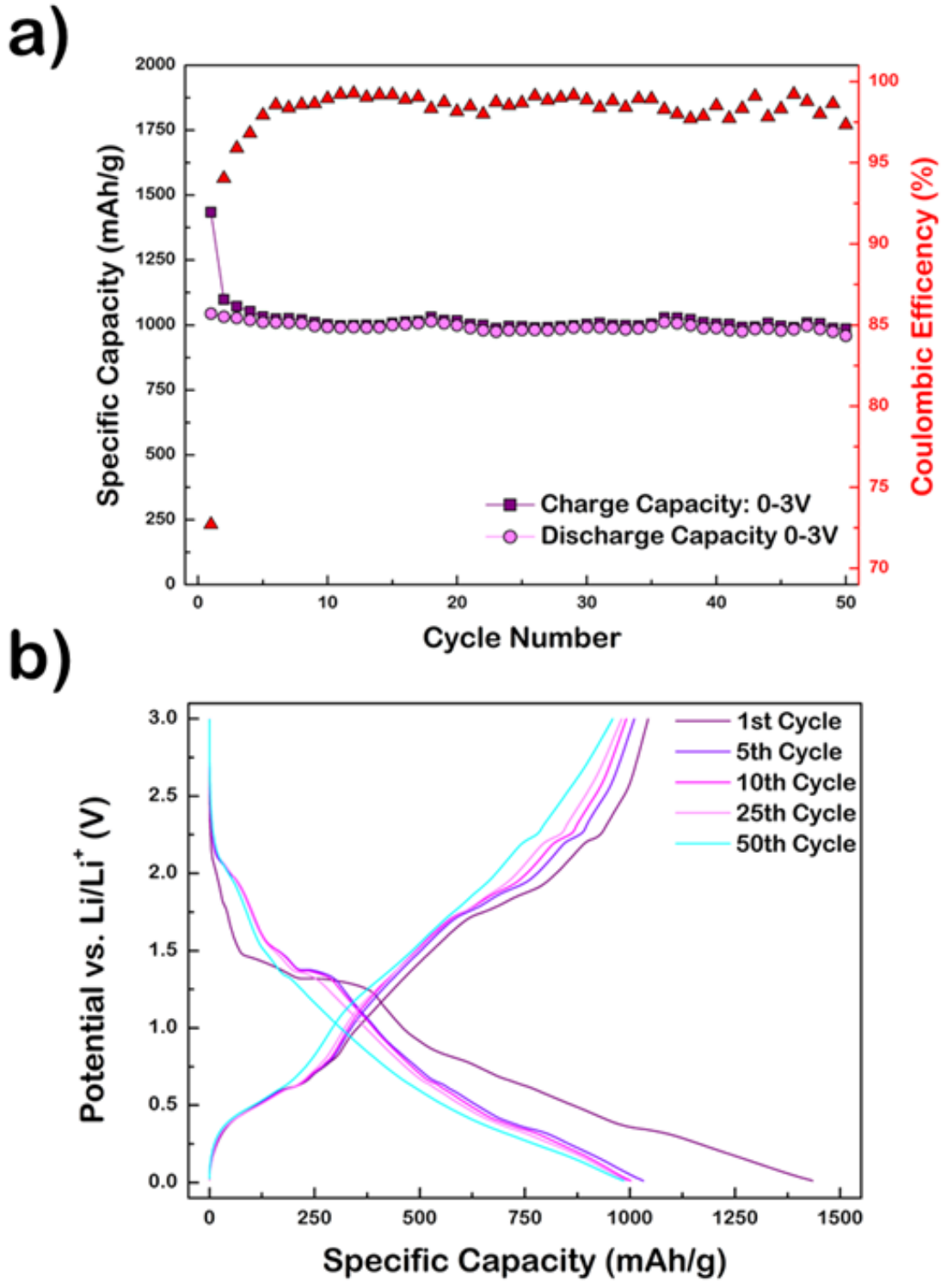


Figure 3.6: (a) Capacity retention summary for the SnSe nanonetworks tested at a specific current of 100 mA/g and (b) corresponding voltage profiles for the 1st, 5th, 10th, 25th and 50th cycle.

Examination of the differential capacity plots, shown in Figure 3.7, shows clear peaks that match extremely well with the peak locations presented by Lee *et al.*[12] during their combination of ex-situ XRD and DQ/DV analysis. The peak locations from the DQ/DV analysis are consistent with the transformation of the SnSe nano-networks to Sn and Li_2Se during the lithiation down to ~1 V, followed by lithiation of the Sn via an alloying process. The reverse processes are identified for delithiation with the persistent peaks above 1 V for the 50 cycles, suggesting excellent reversibility for Se related conversion reactions.

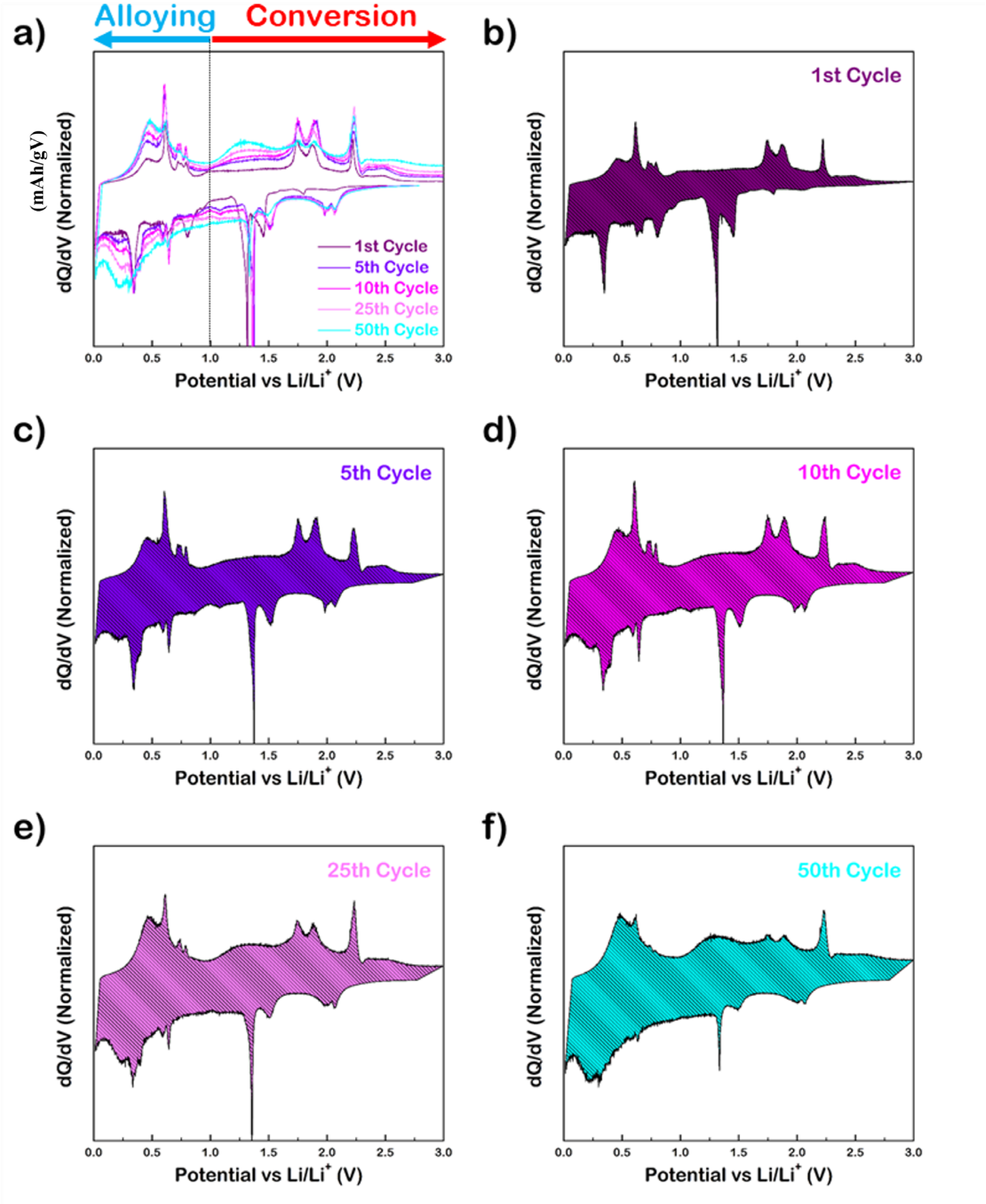


Figure 3.7: (a) Combined differential capacity plot for the 1st, 5th, 10th, 25th and 50th cycle for the galvanostatic test shown in Figure 3.6. Individual plots of the differential capacity for the 1st (b), 5th (c), 10th (d), 25th (e) and 50th (f) cycle.

3.6 Conclusions

Previously unexplored complex 2D SnSe nanonetwork structures have been grown via an atmospheric pressure CVD method, utilising a single source [$SnCl_4\{^nBuSe(CH_2)_3Se^nBu\}$] precursor, without the presence of an external catalysing agent. These 2D networks were seen to consist of many interconnected nanowires, with a nanowire width of about ~120 nm and thickness of ~88 nm. The lengths of these wires within the network were between 100 nm and 4 μm long. These nanowires were seen to join at regular uniform junctions at an angle of either 87° or 93° to one another, attributed to every wire having either a <011> or <0-11> growth direction throughout the network. Minimisation of the surface energy of the crystal planes was proposed to be the driving force behind the formation of these porous network structures, consistent with the prevalence of the (011) and (0-11) SnSe planes in the final structure. Owing to the porosity induced by the internal nanowire substructure that is present in complex 2D SnSe nanonetworks such as these, a correspondingly higher surface area to volume ratio is justified compared to an equivalent uniform 2D SnSe flake. These SnSe nanonetworks show great promise for for Li-ion battery devices, exhibiting a high initial discharge capacity, in excess of 1000 mAh g^{-1}, and maintaining a 92 % capacity retention after 50 cycles at a specific current of 100 mA g^{-1}. These values show a significant enhancement compared to previously reported values for pure SnSe nanocrystals, and this is attributed to the combination of the SnSe network morphology and the correspondingly higher surface area. Further control in the nucleation of the branch sites through future experimental design changes (high vacuum set-ups, etc.), could lead to even greater manipulation of the porosity of the network, and hence further potential control of the surface area and the material properties. The results demonstrated here on the growth of SnSe nanonetworks and their energy storage device application, presents motivation for the continued research into the electrochemical potential of this material system. For example, a future study could aim at complete electrochemical

analysis of the SnSe network nanomaterial within different voltage windows, *e.g.,* isolating alloying, conversion, and finding a 'sweet spot' between the two to obtain the optimal cycling parameters for the SnSe network electrodes. This research also instigates future potential for engineered hierarchical networked structures (e.g. 2D network with different porosity, branching orientation, thickness, diameter or even 3D network structure) of energy relevant materials for energy storage (Li-ion battery) and energy harvesting (thermoelectric, photovoltaic, etc.) applications.

3.7 References:

(1) Gao, M. R.; Xu, Y. F.; Jiang, J.; Yu, S. H. Nanostructured Metal Chalcogenides: Synthesis, Modification, and Applications in Energy Conversion and Storage Devices. Chem. Soc. Rev. **2013**, 42, 2986–3017.

(2) Twaha, S.; Zhu, J.; Yan, Y.; Li, B. A Comprehensive Review of Thermoelectric Technology: Materials, Applications, Modelling and Performance Improvement. Renew. Sustain. Energy Rev. **2016**, 65, 698–726.

(3) Zhang, G.; Finefrock, S.; Liang, D.; Yadav, G. G.; Yang, H.; Fang, H.; Wu, Y. Semiconductor Nanostructure-Based Photovoltaic Solar Cells. Nanoscale **2011**, 3, 2430–2443.

(4) Hernandez, J. A.; Ruiz, A.; Fonseca, L. F.; Pettes, M. T.; Jose-Yacaman, M.; Benitez, A. Thermoelectric Properties of SnSe Nanowires with Different Diameters. Sci. Rep. **2018**, 8, 1–8.

(5) Chen, Z. G.; Shi, X.; Zhao, L. D.; Zou, J. High-Performance SnSe Thermoelectric Materials: Progress and Future Challenge. Prog. Mater. Sci. **2018**, 97, 283–346.

(6) Chandra, S.; Banik, A.; Biswas, K. N -Type Ultrathin Few-Layer Nanosheets of Bi-Doped SnSe: Synthesis and Thermoelectric Properties. ACS Energy Lett. **2018**, 3, 1153–1158.

(7) Chandra, S.; Biswas, K. Realization of High Thermoelectric Figure of Merit in Solution Synthesized 2D SnSe Nanoplates via Ge Alloying. J. Am. Chem. Soc. **2019**, 141, 6141–6145.

(8) Franzman, M. A.; Schlenker, C. W.; Thompson, M. E.; Brutchey, R. L. Solution-Phase Synthesis of SnSe Nanocrystals for Use in Solar Cells. J. Am. Chem. Soc. **2010**, 132, 4060–4061.

(9) Liu, S.; Guo, X.; Li, M.; Zhang, W. H.; Liu, X.; Li, C. Solution-Phase Synthesis and

Characterization of Single-Crystalline SnSe Nanowires. Angew. Chemie - Int. Ed. **2011**, 50, 12050–12053.

(10) Minnam Reddy, V. R.; Gedi, S.; Pejjai, B.; Park, C. Perspectives on SnSe-Based Thin Film Solar Cells: A Comprehensive Review. J. Mater. Sci. Mater. Electron. **2016**, 27, 5491–5508.

(11) Zhao, L.-D.; Lo, S.-H.; Zhang, Y.; Sun, H.; Tan, G.; Uher, C.; Wolverton, C.; Dravid, V. P.; Kanatzidis, M. G. Ultralow Thermal Conductivity and High Thermoelectric Figure of Merit in SnSe Crystals. Nature **2014**, 508, 373–377.

(12) Lee, D.-H.; Park, C.-M. Tin Selenides with Layered Crystal Structures for Li-Ion Batteries: Interesting Phase Change Mechanisms and Outstanding Electrochemical Behaviors. ACS Appl. Mater. Interfaces **2017**, 9, 15439–15448.

(13) Zhang, Z.; Zhao, X.; Li, J. SnSe/Carbon Nanocomposite Synthesized by High Energy Ball Milling as an Anode Material for Sodium-Ion and Lithium-Ion Batteries. Electrochim. Acta **2015**, 176, 1296–1301.

(14) Im, H. S.; Lim, Y. R.; Cho, Y. J.; Park, J.; Cha, E. H.; Kang, H. S. Germanium and Tin Selenide Nanocrystals for High-Capacity Lithium Ion Batteries: Comparative Phase Conversion of Germanium and Tin. J. Phys. Chem. C **2014**, 118, 21884–21888.

(15) Wang, W.; Li, P.; Zheng, H.; Liu, Q.; Lv, F.; Wu, J.; Wang, H.; Guo, S. Ultrathin Layered SnSe Nanoplates for Low Voltage, High-Rate, and Long-Life Alkali–Ion Batteries. Small **2017**, 13, 1–7.

(16) Cheng, Y.; Huang, J.; Li, J.; Cao, L.; Xu, Z.; Luo, X.; Qi, H.; Guo, P. SnSe/r-GO Composite with Enhanced Pseudocapacitance as a High-Performance Anode for Li-Ion Batteries. ACS Sustain. Chem. Eng. **2019**, 7, 8637–8646.

(17) Xue, M. Z.; Yao, J.; Cheng, S. C.; Fu, Z. W. Lithium Electrochemistry of a Novel SnSe Thin-Film Anode. J. Electrochem. Soc. **2006**, 153, 270–274.

(18) Huang, Y.; Li, L.; Lin, Y. H.; Nan, C. W. Liquid Exfoliation Few-Layer SnSe Nanosheets with Tunable Band Gap. J. Phys. Chem. C **2017**, 121, 17530–17537.

(19) Nicolosi, V.; Chhowalla, M.; Kanatzidis, M. G.; Strano, M. S.; Coleman, J. N. Liquid Exfoliation of Layered Materials. Science **2013**, 340, 1226419–1226419.

(20) Liu, J.; Jian, J.; Yu, Z.; Zhang, Z.; Cao, B.; Du, B. Catalyst-Free Vapor Phase Growth of Ultralong SnSe Single-Crystalline Nanowires. Cryst. Growth Des. **2017**, 17, 6163–6168.

(21) Butt, F. K.; Mirza, M.; Cao, C.; Idrees, F.; Tahir, M.; Safdar, M.; Ali, Z.; Tanveer, M.; Aslam, I. Synthesis of Mid-Infrared SnSe Nanowires and Their Optoelectronic Properties. CrystEngComm **2014**, 16, 3470.

(22) Hu, J.; Odom, T. W.; Lieber, C. M. Chemistry and Physics in One Dimension: Synthesis and Properties of Nanowires and Nanotubes. Acc. Chem. Res. **1999**, 32, 435–445.

(23) Gao, H.; Ji, B.; Jäger, I. L.; Arzt, E.; Fratzl, P. Materials Become Insensitive to Flaws at Nanoscale: Lessons from Nature. Proc. Natl. Acad. Sci. U. S. A. **2003**, 100, 5597–5600.

(24) Goldstein, A. N.; Echer, C. M.; Alivisatos, A. P. Melting in Semiconductor Nanocrystals. Science **1992**, 256, 1425–1427.

(25) Wang, J.; Duan, H. L.; Huang, Z. P.; Karihaloo, B. L. A Scaling Law for Properties of Nano-Structured Materials. Proc. R. Soc. A Math. Phys. Eng. Sci. **2006**, 462, 1355–1363.

(26) Shi, L.; Zhao, T. Recent Advances in Inorganic 2D Materials and Their Applications in Lithium and Sodium Batteries. J. Mater. Chem. A **2017**, 5, 3735–3758.

(27) Rojaee, R.; Shahbazian-Yassar, R. Two-Dimensional Materials to Address the Lithium Battery Challenges. ACS Nano **2020**, 14, 2628–2658.

(28) Manna, L.; Milliron, D. J.; Meisel, A.; Scher, E. C.; Alivisatos, A. P. Controlled Growth of Tetrapod-Branched Inorganic Nanocrystals. Nat. Mater. **2003**, 2, 382–385.

(29) Liu, X.; Lin, Y.; Zhou, S.; Sheehan, S.; Wang, D. Complex Nanostructures: Synthesis and Energetic Applications. Energies **2010**, 3, 285–300.

(30) Cheng, C.; Fan, H. J. Branched Nanowires: Synthesis and Energy Applications. Nano Today **2012**, 7, 327–343.

(31) Bierman, M. J.; Jin, S. Potential Applications of Hierarchical Branching Nanowires in Solar Energy Conversion. Energy Environ. Sci. **2009**, 2, 1050–1059.

(32) Verdier, M.; Lacroix, D.; Termentzidis, K. Thermal Transport in Two- and Three-Dimensional Nanowire Networks. Phys. Rev. B **2018**, 94, 1–7.

(33) Chan, C. K.; Peng, H.; Liu, G.; McIlwrath, K.; Zhang, X. F.; Huggins, R. A.; Cui, Y. High-Performance Lithium Battery Anodes Using Silicon Nanowires. Nat. Nanotechnol. **2008**, 3, 31–35.

(34) Wang, D.; Qian, F.; Yang, C.; Zhong, Z.; Lieber, C. M. Rational Growth of Branched and Hyperbranched Nanowire Structures. Nano Lett. **2004**, 4, 871–874.

(35) Dick, K. A.; Deppert, K.; Larsson, M. W.; Mårtensson, T.; Seifert, W.; Wallenberg, L. R.; Samuelson, L. Synthesis of Branched "nanotrees" by Controlled Seeding of Multiple Branching Events. Nat. Mater. **2004**, 3, 380–384.

(36) Yan, C.; Li, X.; Zhou, K.; Pan, A.; Werner, P.; Mensah, S. L.; Vogel, A. T.; Schmidt, V. Heteroepitaxial Growth of GaSb Nanotrees with an Ultra-Low Reflectivity in a Broad Spectral Range. Nano Lett. **2012**, 12, 1799–1805.

(37) Jia, Y.; Ma, Y.; Lin, Y.; Tang, J.; Shi, W. Facile Synthesis of Branched MoS_2 Nanowires. Chem. Phys. **2018**, 513, 209–212.

(38) Kuno, M.; Ahmad, O.; Protasenko, V.; Bacinello, D.; Kosel, T. H. Solution-Based Straight and Branched CdTe Nanowires. Chem. Mater. **2006**, 18, 5722–5732.

(39) Bierman, M. J.; Lau, Y. K. A.; Kvit, A. V.; Schmitt, A. L.; Jin, S. Dislocation-Driven Nanowire Growth and Eshelby Twist. Science **2008**, 320, 1060–1063.

(40) Zhu, J.; Peng, H.; Marshall, A. F.; Barnett, D. M.; Nix, W. D.; Cui, Y. Formation of Chiral Branched Nanowires by the Eshelby Twist. Nat. Nanotechnol. **2008**, 3, 477–481.

(41) Boscher, N. D.; Carmalt, C. J.; Palgrave, R. G.; Parkin, I. P. Atmospheric Pressure Chemical Vapour Deposition of SnSe and $SnSe_2$ Thin Films on Glass. Thin Solid Films **2008**, 516, 4750–4757.

(42) Gurnani, C.; Hawken, S. L.; Hector, A. L.; Huang, R.; Jura, M.; Levason, W.; Perkins, J.; Reid, G.; Stenning, G. B. G. Tin(IV) Chalcogenoether Complexes as Single Source Precursors for the Chemical Vapour Deposition of SnE_2 and SnE (E = S, Se) Thin Films. Dalt. Trans. **2018**, 47, 2628–2637.

(43) Zhou, S.; Liu, X.; Lin, Y.; Wang, D. Spontaneous Growth of Highly Conductive Two-Dimensional Single-Crystalline $TiSi_2$ nanonets. Angew. Chemie - Int. Ed. **2008**, 47, 7681–7684.

(44) Zhou, S.; Liu, X.; Lin, Y.; Wang, D. Rational Synthesis and Structural Characterizations of Complex $TiSi_2$ Nanostructures. Chem. Mater. **2009**, 21, 1023–1027.

(45) De Groot, C. H.; Gurnani, C.; Hector, A. L.; Huang, R.; Jura, M.; Levason, W.; Reid, G. Highly Selective Chemical Vapor Deposition of Tin Diselenide Thin Films onto Patterned Substrates via Single Source Diselenoether Precursors. Chem. Mater. **2012**, 24, 4442–4449.

(46) Vaughn, D. D.; In, S. Il; Schaak, R. E. A Precursor-Limited Nanoparticle Coalescence Pathway for Tuning the Thickness of Laterally-Uniform Colloidal Nanosheets: The Case of SnSe. ACS Nano **2011**, 5, 8852–8860.

(47) Chandrasekhar, H. R.; Humphreys, R. G.; Zwick, U.; Cardona, M. Infrared and Raman Spectra of the IV-VI Compounds SnS and SnSe. Phys. Rev. B **1977**, 15, 2177–2183.

(48) Luo, S.; Qi, X.; Yao, H.; Ren, X.; Chen, Q.; Zhong, J. Temperature-Dependent Raman Responses of the Vapor-Deposited Tin Selenide Ultrathin Flakes. J. Phys. Chem. C

2017, 121, 4674–4679.

(49) Han, G.; Popuri, S. R.; Greer, H. F.; Bos, J. W. G.; Zhou, W.; Knox, A. R.; Montecucco, A.; Siviter, J.; Man, E. A.; MacAuley, M.; Paul, D. J.; Li, W. G.; Paul, M. C.; Gao, M.; Sweet, T.; Freer, R.; Azough, F.; Baig, H.; Sellami, N.; Mallick, T. K.; Gregory, D. H. Facile Surfactant-Free Synthesis of p-Type Snse Nanoplates with Exceptional Thermoelectric Power Factors. Angew. Chemie - Int. Ed. **2016**, 55, 6433–6437.

(50) Ma, X. H.; Cho, K. H.; Sung, Y. M. Growth Mechanism of Vertically Aligned SnSe Nanosheets via Physical Vapour Deposition. CrystEngComm **2014**, 16, 5080–5086.

(51) Tian, H.; Wang, X. F.; Mohammad, M. A.; Gou, G. Y.; Wu, F.; Yang, Y.; Ren, T. L. A Hardware Markov Chain Algorithm Realized in a Single Device for Machine Learning. Nat. Commun. **2018**, 9, 1–11.

(52) Hu, Z.; Zheng, D.; Tu, R.; Yang, M.; Li, Q.; Han, M.; Zhang, S.; Zhang, L.; Goto, T. Structural Controlling of Highly-Oriented Polycrystal 3C-SiC Bulks via Halide CVD. Materials (Basel). **2019**, 12, 1–10.

3.8 Appendix

Author (Year)	Material	Number of Cycles	Initial Discharge Capacity (mAh/g)	Final Discharge Capacity (mAh/g)	Capacity retention (%)
Xue, M.-Z.; et al. (2006)[2]	SnSe Thinfilm	60	681	>100	15
Ning, J.; et al. (2011)[3]	SnSe/carbon black/poly-vinylidenefluoride	30	353	~200	~56.7
Kang, S. Z.; et al. (2012)[4]	SnSe nanosheets/ poly(vinylidene fluoride)/carbon black	20	1009	73	7.2
Wang, X; et al. (2014)[5]	SnSe nanocrystal/carbon fabric	80	1216	676	55.6
Im, H.S.; et al. (2014)[6]	SnSe, $SnSe_2$, GeSe, $GeSe_2$	70	867 (SnSe), 647 ($SnSe_2$), 1232 (GeSe), 1099 ($GeSe_2$)	510 (SnSe), 412 ($SnSe_2$), 771 (GeSe), 514 ($GeSe_2$)	58.8 (SnSe), 63.7 ($SnSe_2$), 62.6 (GeSe), 46.8 ($GeSe_2$)
Zhang, Z.; et al. (2015)[7]	SnSe/carbon nanocomposite	100	1097.6	633.1	57.7
Gurung, A; et al. (2016)[8]	SnSe/multi-walled carbon nanotubes	50	1241	651	52.5
Zhang, L; et al. (2016)[9]	SnSe/carbon composite	100	1148	840	73.2
Wang, D; et al. (2016)[10]	SnSe nanorods/graphene oxide	100	1362	764	56
Wang, W.; et al. (2017)[11]	Layered SnSe Nanoplates	300	~1190	787.9	66.2
Lee, D.-H.; et al. (2017)[12]	SnSe/C	200	726	626	86.2
Cheng, Y.; et al. (2019)[13]	SnSe, SnSe/r-GO Composite	150 (SnSe) 200 (SnSe/r-GO)	1302 (SnSe) 1049 (SnSe/r-GO)	<300 (SnSe) 1002 (SnSe/r-GO)	<23 (SnSe) 95.5 (SnSe/r-GO)
This Work	SnSe nanonetworks	50	1043	959	92

Table A.3.1: Comparison of the performance for previously published SnSe anodes

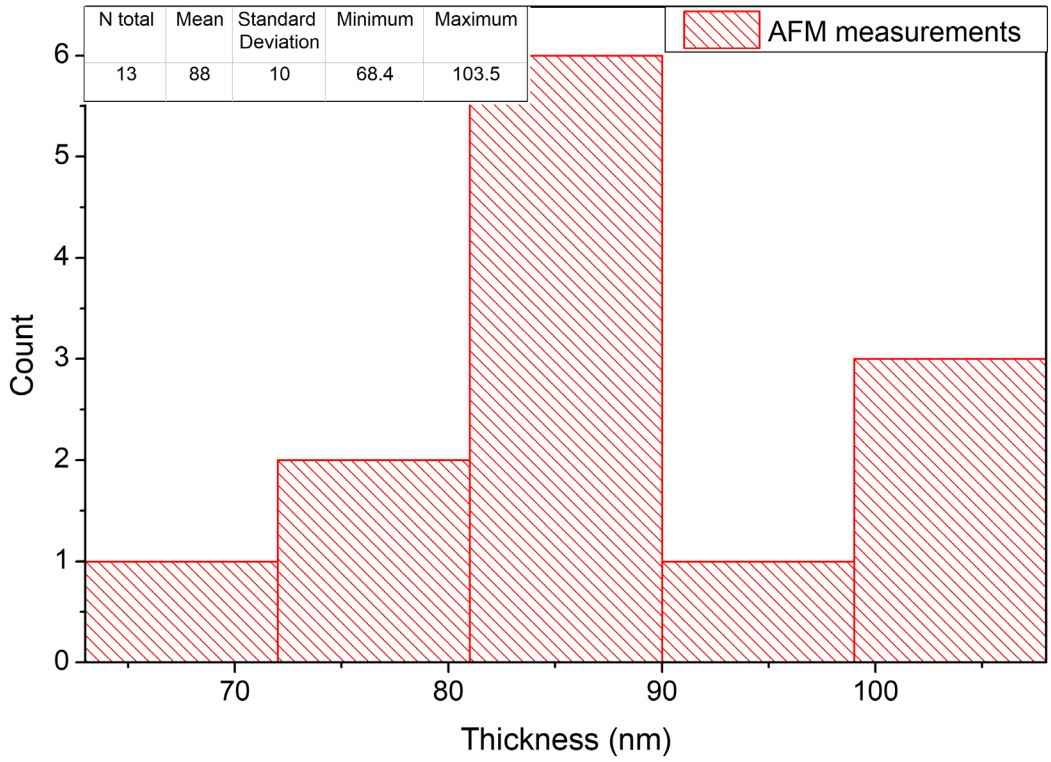


Figure A.3.1: Histogram of AFM thickness measurements at various points of the SnSe nanonetworks.

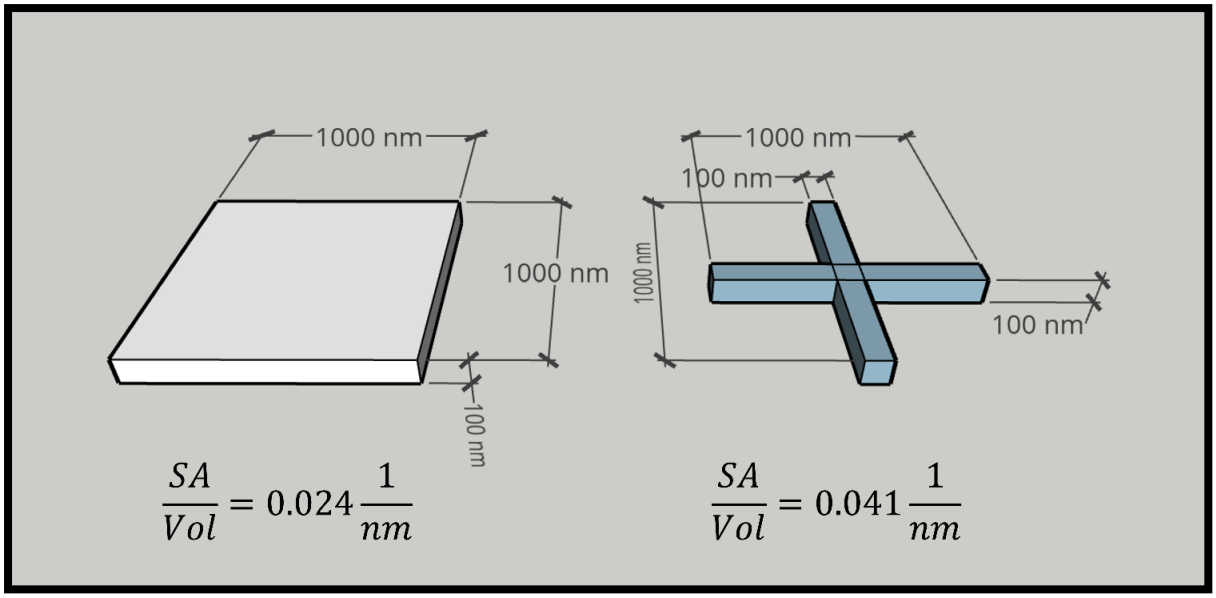


Figure A.3.2: Surface area to volume ratio comparison for a uniform flake structure compared to a networked structure. Network structures present a higher surface area to volume ratio.

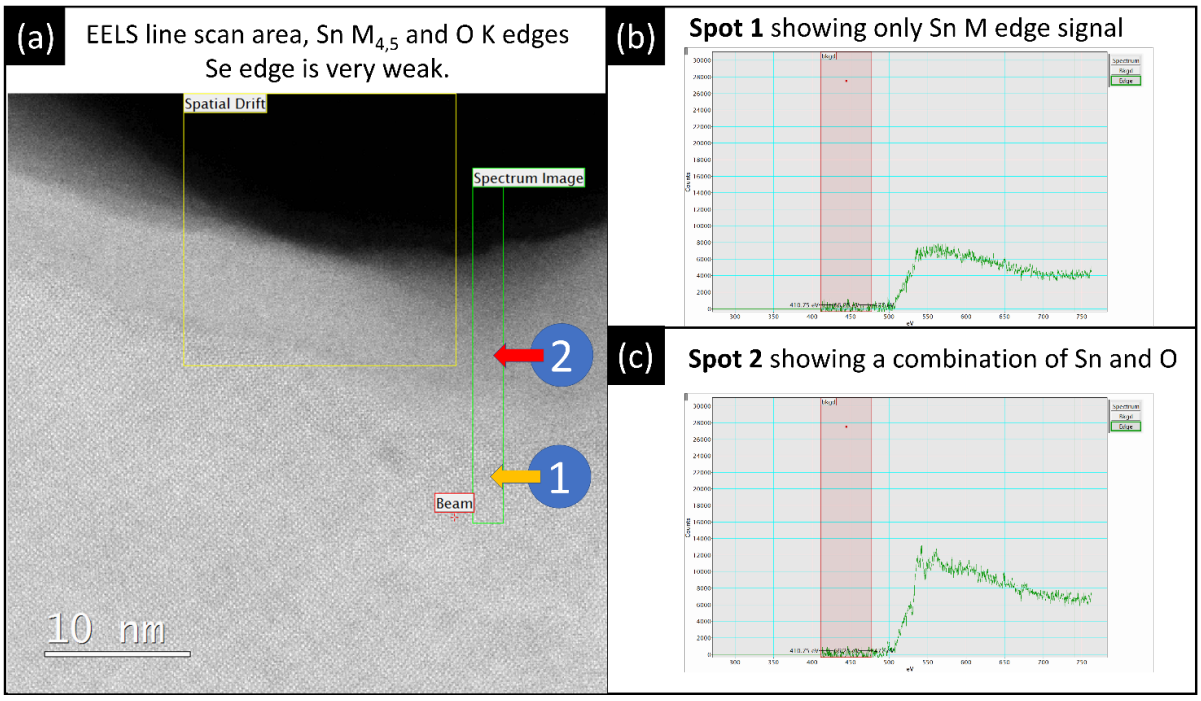


Figure A.3.3: EELS Sn and O analysis of the surface of a SnSe nanonetwork. The first 5-10 nm layer at the surface is composed of SnO_x.

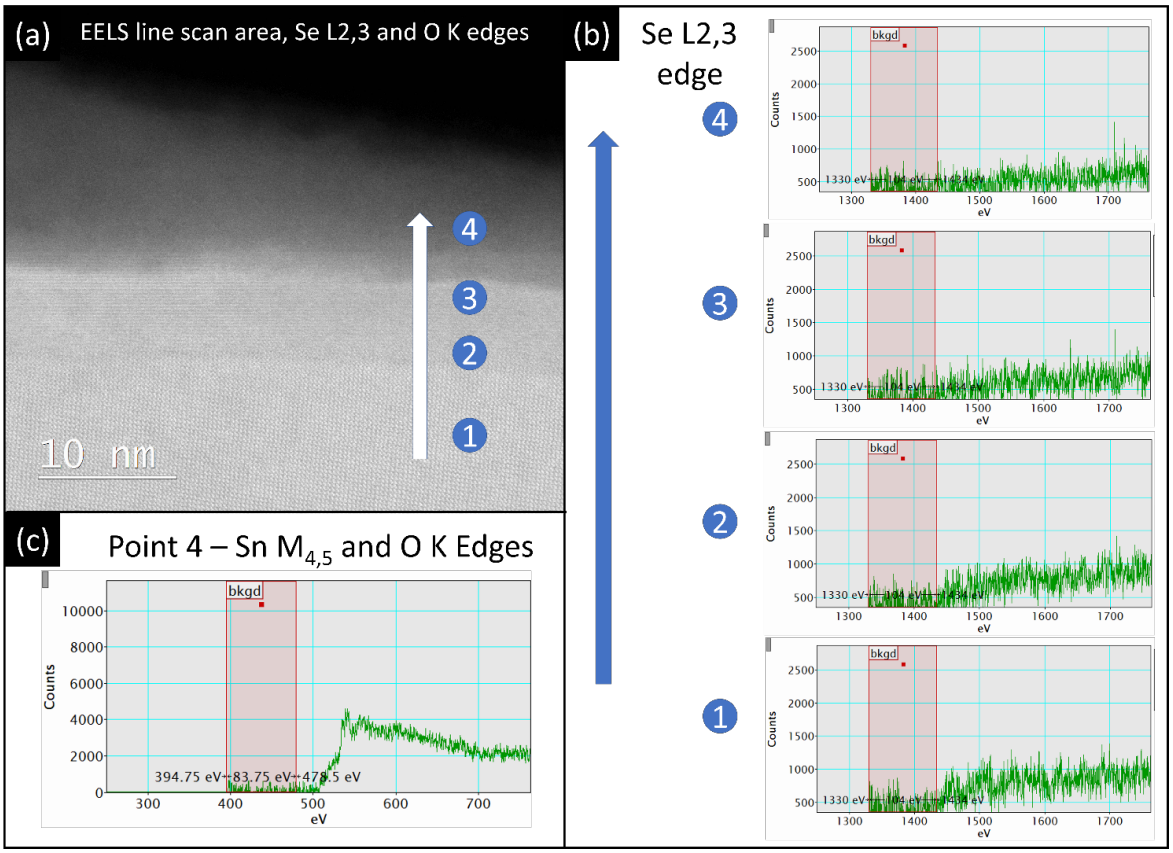


Figure A.3.4: EELS Se and O analysis of the surface of a SnSe nanonetwork. (a) shows a STEM image of a section of the SnSe nanonetwork. The spots labelled 1 to 4, indicate where the EELS measurements in (b) are taken from. A decreasing Se signal is seen moving from spot 1 to 3, which then vanishes in region 4. (c) shows that the outmost surface at region 4 shows only a SnO_x signal.

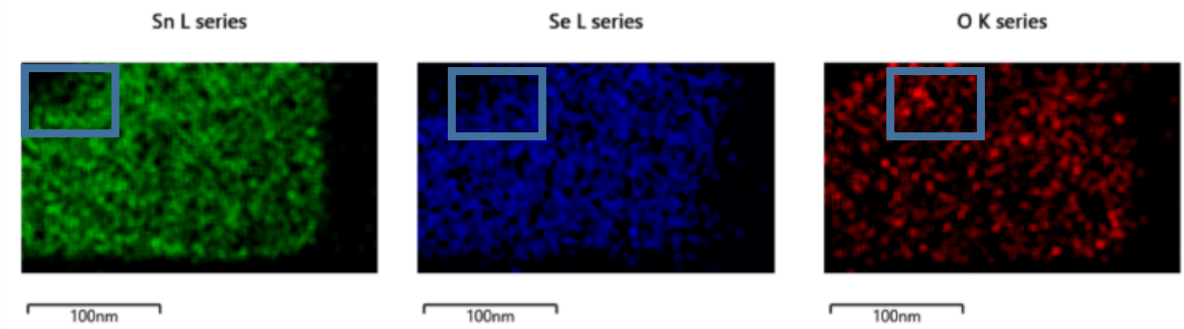


Figure A3.5: EDX mapping of a section of the SnSe network. The blue box is included as a guide for the eye, highlighting the surface region at a junction in the network. The surface is seen to consist of Sn and O, with depleted Se at the outermost surface.

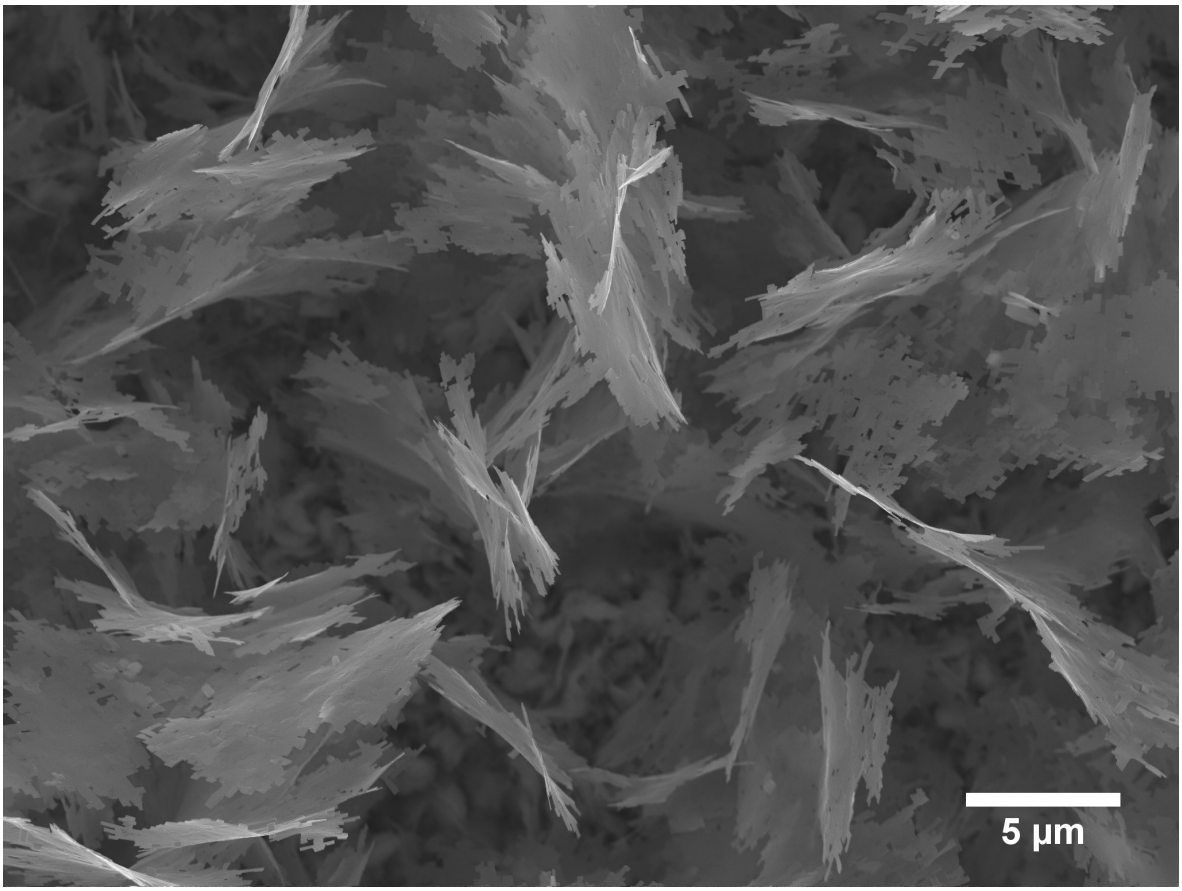


Figure A.3.6: Growth of the SnSe nanonetworks on a stainless steel substrate.

3.8.1 Appendix References

(1) Xue, M. Z.; Yao, J.; Cheng, S. C.; Fu, Z. W. Lithium Electrochemistry of a Novel SnSe Thin-Film Anode. *J. Electrochem. Soc.* **2006**, *153*, 270–274.

(2) Ning, J.; Xiao, G.; Jiang, T.; Wang, L.; Dai, Q.; Zou, B.; Liu, B.; Wei, Y.; Chen, G.; Zou, G. Shape and Size Controlled Synthesis and Properties of Colloidal IV–VI SnSe Nanocrystals. *CrystEngComm* **2011**, *13*, 4161.

(3) Kang, S. Z.; Jia, L.; Li, X.; Yin, Y.; Li, L.; Guo, Y. G.; Mu, J. Amine-Free Preparation of SnSe Nanosheets with High Crystallinity and Their Lithium Storage Properties. *Colloids Surfaces A Physicochem. Eng. Asp.* **2012**, *406*, 1–5.

(4) Wang, X.; Liu, B.; Xiang, Q.; Wang, Q.; Hou, X.; Chen, D.; Shen, G. Spray-Painted Binder-Free SnSe Electrodes for High-Performance Energy-Storage Devices. *ChemSusChem* **2014**, *7*, 308–313.

(5) Im, H. S.; Lim, Y. R.; Cho, Y. J.; Park, J.; Cha, E. H.; Kang, H. S. Germanium and Tin Selenide Nanocrystals for High-Capacity Lithium Ion Batteries: Comparative Phase Conversion of Germanium and Tin. *J. Phys. Chem. C* **2014**, *118*, 21884–21888.

(6) Zhang, Z.; Zhao, X.; Li, J. SnSe/Carbon Nanocomposite Synthesized by High Energy Ball Milling as an Anode Material for Sodium-Ion and Lithium-Ion Batteries. *Electrochim. Acta* **2015**, *176*, 1296–1301.

(7) Gurung, A.; Naderi, R.; Vaagensmith, B.; Varnekar, G.; Zhou, Z.; Elbohy, H.; Qiao, Q. Tin Selenide – Multi-Walled Carbon Nanotubes Hybrid Anodes for High Performance Lithium-Ion Batteries. *Electrochim. Acta* **2016**, *211*, 720–725.

(8) Zhang, L.; Lu, L.; Zhang, D.; Hu, W.; Wang, N.; Xu, B.; Li, Y.; Zeng, H. Dual-Buffered SnSe@CNFs as Negative Electrode with Outstanding Lithium Storage Performance.

Electrochim. Acta **2016**, *209*, 423–429.

(9) Wang, D.; Zhang, K.; Zhu, Y.; Lan, Y.; Hu, L.; Lin, N.; Zhou, J.; Qian, Y. A Novel Strategy to Prepare Graphene Oxide-Wrapped Nanocrystals Composite for High-Performance Lithium Storage. *Mater. Lett.* **2016**, *175*, 32–35.

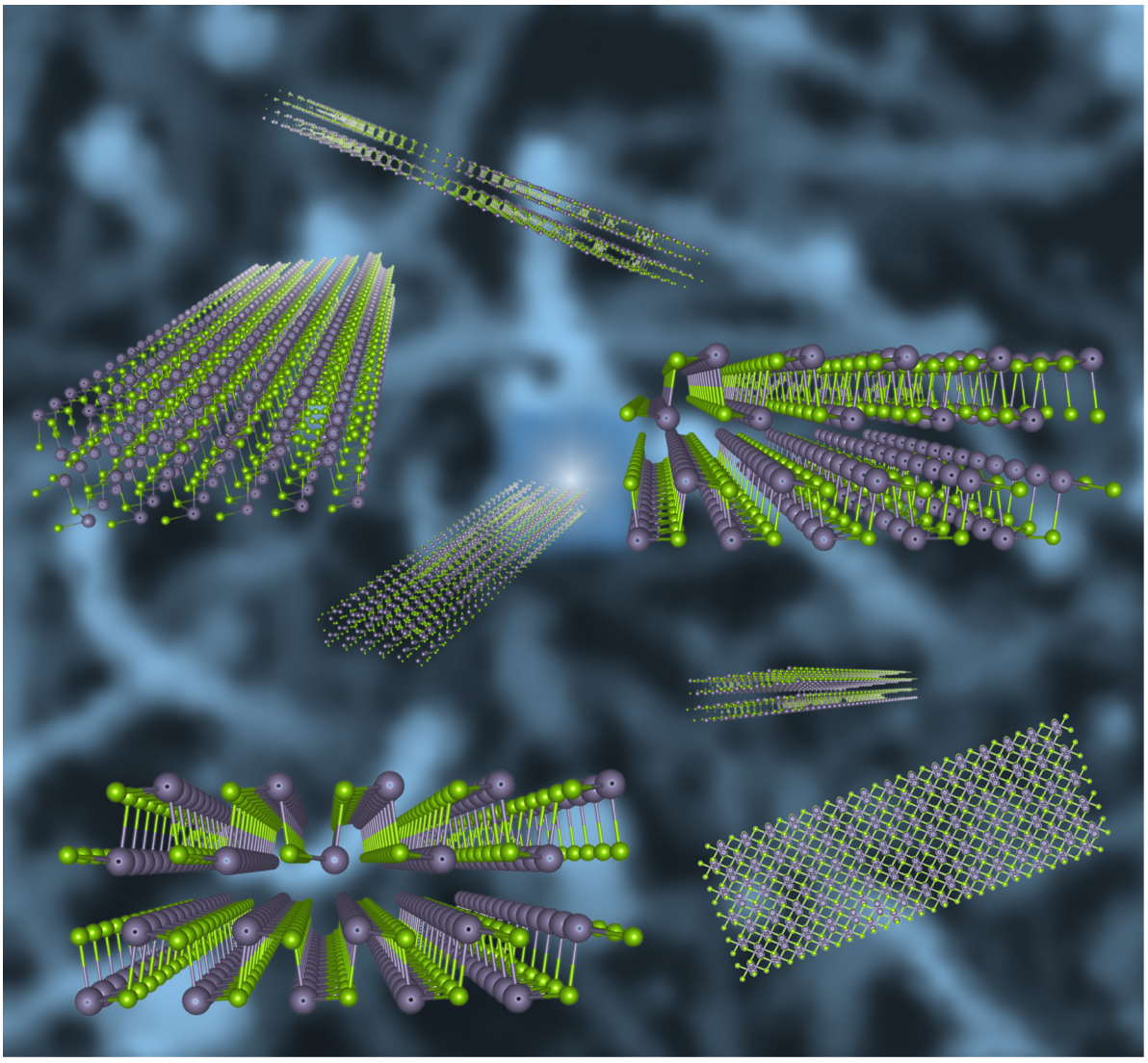
(10) Wang, W.; Li, P.; Zheng, H.; Liu, Q.; Lv, F.; Wu, J.; Wang, H.; Guo, S. Ultrathin Layered SnSe Nanoplates for Low Voltage, High-Rate, and Long-Life Alkali–Ion Batteries. *Small* **2017**, *13*, 1–7.

(11) Lee, D.-H.; Park, C.-M. Tin Selenides with Layered Crystal Structures for Li-Ion Batteries: Interesting Phase Change Mechanisms and Outstanding Electrochemical Behaviors. *ACS Appl. Mater. Interfaces* **2017**, *9*, 15439–15448.

(12) Cheng, Y.; Huang, J.; Li, J.; Cao, L.; Xu, Z.; Luo, X.; Qi, H.; Guo, P. SnSe/r-GO Composite with Enhanced Pseudocapacitance as a High-Performance Anode for Li-Ion Batteries. *ACS Sustain. Chem. Eng.* **2019**, *7*, 8637–8646.

Chapter 4

Solution Phase Growth and Characterisation of Zigzag SnSe Nanoribbons



Nanomaterial growth and analysis was performed by myself; contributing to the nanomaterial growth and performing all SEM, TEM, electron diffraction, XRD and Raman analysis.

Kamil Rahme developed the reaction protocol, and performed the initial reactions.

Manuel Roldan-Guiterrex and Shery Chang performed the EELS analysis.

Shane Garvey performed the XPS analysis.

I co-wrote this paper with Subhajit Biswas and Justin D. Holmes.

Davitt, F., Rahme, K., Roldan-Gutierrez, M., Garvey, S., Biswas, S., Chang, S. L.Y., Holmes, J. D., Solution Phase Growth and Characterisation of Zigzag SnSe Nanoribbons. (In preparation)

4.1 Abstract

Quasi-one-dimensional nanoribbon structures, formed from two dimensional (2D) layered materials, have exciting and unique physical properties compared to their conventional 2D or bulk counterparts. SnSe, a highly promising layered material, has been garnering particular interest in recent times due to its significant promise for future energy devices. Herein we report a two-step solution phase approach for growing highly crystalline (orthorhombic Pnma 62 crystal structure) layered SnSe nanoribbons employing polyvinylpyrrolidone (PVP) as a passivating agent. PVP selectively passivates the {100} and {001} facets of the nanoribbons resulting in the unique growth of nanoribbons along their b-axis, exposing the zigzag surface of SnSe along the sidewalls. The SnSe nanoribbons synthesised had thicknesses of ~11 - 13 nm, with mean widths of ~40 nm. The PVP coating was seen to offer some resistance to oxidation, with removal of the PVP seen to lead to the formation a SnSe/SnO_x core shell structure, with up to a ~3 - 4 nm thick oxide on both the top and bottom of the nanoribbon, and ~7 nm on the sides. Nanoribbons with lengths > 1 μm could be achieved, and these could be produced in relatively high quantities (>150 mg) in a single batch experiment. The use of non-toxic PVP to avoid the use of more toxic amines that are typically employed for other 1D forms of SnSe is also a significant advantage for sustainable and environmentally friendly applications.

4.2 Introduction

Engineering nanostructures into confined nanoribbon morphologies, where length > width > thickness, is especially relevant for layered materials due to the unique physical properties that are achievable in such forms.[1–3] Layered materials are formed from tightly bound atomic 2D planes, which are then separated by weakly bound Van der Waals bonds along one crystal axis. Materials which form in this layered crystal structure have been widely studied, with exciting

novel properties achievable through manipulation and exfoliation of the material layers.[4] Structuring these 2D layers into a pseudo-1D morphology gives rise to nanoribbon forms with exciting novel properties, such as the ability to tailor the bandgap and charge carrier effective mass.[2,3] Group IV-VI chalcogenides commonly form in layered forms, and are of particular interest due to the wide range of technological applications these materials are finding use in.[5] Layered SnS nanoribbons have been explored in previous reports,[6,7] but SnSe nanoribbons currently remain experimentally elusive. SnSe nanoribbons with different crystal orientations are predicted to show distinct electrical properties. Armchair SnSe nanoribbons are predicted to be semiconducting in nature and pristine zigzag SnSe nanoribbons are anticipated to be metallic.[8] Zigzag SnSe nanoribbons are theorised however to show a metal-semiconductor transition, with an opening of the bandgap if broken bonds are present.[9] A combination of crystal engineering coupled with a nanoribbon morphology thus provides great potential for further manipulating the physical properties of SnSe. To this end, new synthetic methods for morphological engineering of SnSe at the nanoscale are required.

At room temperature SnSe crystallises in an orthorhombic Pnma 62 structure, which is a highly anisotropic structure with different lattice constants along each crystal axis. Notably, SnSe forms in a layered crystal structure, with tightly bound bonds along the *b* and *c* axis and relatively weak van der Waals bonding along the *a* axis (see appendix Figure A.4.1 for a schematic of the SnSe crystal structure). Additionally, it has been shown that the anisotropic nature of SnSe results in noticeable differences in the physical properties of the material, depending on the measured orientation. In particular, Li-Dong Shao *et. al.*[10] have shown a very high thermoelectric *ZT* value of 2.62 along the *b*-axis for bulk SnSe, with lower values along the other axes. This is important as a high *ZT* material is essential for producing efficient

thermoelectric devices.[11] This anisotropic nature shows that the ability to selectively tailor the orientation of the SnSe crystals would be of significant value to this research field.

Metal chalcogenide materials have shown great promise for electronic, optoelectronic and energy device applications,[5,12] with research into these areas being a rapidly growing field of research. SnSe is a highly versatile metal chalcogenide material with applications in electronic devices,[13,14] optoelectronic devices,[15,16] and also high potential in a wide spectrum of energy technologies, *e.g.* thermoelectric devices[11] and solar cells for energy harvesting,[17,18] as well as an anode material for Li-ion batteries for energy storage.[19,20] Developing methods for the high yield and controllable synthesis of these materials is of paramount importance if they are to be successfully incorporated into future energy devices.

Many solution-based methods exist for the synthesis of metal chalcogenide materials, with advantages lying in the ease and scalability of these methods versus costly vapour deposition based methods. SnSe nanostructures have previously been synthesised in solution using directing and capping agents such as oleylamine, ethanolamine and 1,10-phenanthroline; forming nanoparticles,[21] small nanorods,[22] large nanobelts[23] and 2D like flakes.[24,25] Polyvinylpyrrolidone (PVP) is an alternative surface capping and structure-directing agent, that is commonly used for the controlled synthesis of nanoparticles[26] and nanowires,[27] due to its non-toxic nature.[28] PVP is known to offer selective shape control in solution grown crystalline materials, offering the tailored growth of nanowire structures by selective binding to different crystal planes.[29] PVP has never been used as a passivating agent to grow 1D SnSe before, but it has been shown to demonstrate biocompatibility in combination with SnSe,[30] where it was used to surface passivate SnSe nanorods in a post growth treatment. However, passivation of SnSe with PVP during growth was not studied previously, and we show that this leads to the formation of very thin SnSe nanoribbons, which have not been achieved before now. The

biocompatibility of SnSe-PVP also makes it an attractive capping agent to explore biomedical applications for SnSe further.

While SnSe nanowires have been previously explored, through both chemical vapour deposition[13,31,32] (CVD) and solution based methods,[33,34] herein we report for the first time, the simple and scalable synthesis of low dimension SnSe nanoribbons. The nanoribbons are single crystalline throughout and are synthesised using simple and readily available precursor compounds.

4.3 Experimental

SeO_2 (99.8 %), polyvinylpyrrolidone (PVP, average molecular weight = 40,000 kDa), KOH, ethylene glycol (emplura), $SnCl_2.2H_2O$ (≥ 99.99 %) and ascorbic acid (≥ 99 %) were all purchased from Sigma Aldrich.

4.3.1 Synthesis of $(Se)_m(PVP)_n$ nanoparticles

SnSe nanorods were synthesised by first preparing a solution of $(Se)_m(PVP)_n$ nanoparticle complexes. In a typical synthesis, 0.3327 g of SeO_2 (3 mmol), 3 g PVP and 0.675 g KOH were dissolved in 45 ml of ethylene glycol by heating to 80 °C under Ar while stirring, yielding a very light yellow solution. After complete dissolution the solution was heated in a Teflon lined autoclave for 18 hr at 195 °C, giving a black brown reddish solution.

4.3.2 Synthesis of SnSe nanoribbons

To synthesise SnSe nanoribbons, two additional solutions were then prepared: (1) 3 mmol $SnCl_2.2H_2O$ (0.675 g) and 0.3 g PVP were dissolved in 12 ml ethylene glycol at 80 °C under stirring and (2) 6 mmol of ascorbic acid (1.0566 g) in 4 ml ethylene glycol was prepared by

heating to 80 °C under stirring. These two solutions were then mixed and injected together into the previously prepared solution of Se-PVP nanoparticles in ethylene glycol at 80 °C under stirring. Upon addition of the $SnCl_2$-PVP-ascorbic acid mixture the solution underwent a colour change to deep red brown black; stirring was maintained for 5 min at 80 °C. This solution was then added to a Teflon lined autoclave (~7.5 ml per 20 ml cell volume) and heated at 195 °C for between 27 - 76 hr. After cooling to room temperature, the solution was washed twice with deionised water followed by centrifugation and then re-dispersed in ethanol.

4.4 Characterisation

The synthesised nanomaterials were analysed using a Helios Nanolab 600i scanning electron microscope (SEM). Raman scattering spectroscopy was performed with a Renishaw InVia Raman spectrometer equipped with a 2400 lines/mm grating using a 514 nm laser. Spectra were collected using a RenCam CCD camera, with the beam focused onto the samples using a 50 × objective lens. Measurements were undertaken at 1 % of the total 1.9 mW laser power. The crystal structure of the product was confirmed by X-ray diffraction (XRD) using a Philips X'pert Pro MPD equipped with a Panalytical Empyrean Cu X-ray tube and a Philips X'celerator detector. X-ray photoelectron spectroscopy (XPS) analysis was undertaken on an Oxford Applied Research Escabase XPS system with a base pressure of 5×10^{-10} mbar and a nonmonochromated Al K_α X-ray source at 200 W. Survey spectra were recorded between 0 - 1000 eV at a step size of 0.7 eV, a dwell time of 0.3 s and a pass energy of 100 eV. Core levels scans were acquired at a step size of 0.1 eV, a dwell time of 0.1 s and a pass energy of 20 eV. CasaXPS software was used for spectra processing with peaks corrected to a Shirley background and fitted to Voigt profiles. Charge correction was based on the C 1s peak at 285 eV. Samples were drop-cast onto a carbon coated TEM grid for detailed microscopy analysis. TEM analysis was performed on a JEOL 2100 electron microscope operating at

200 kV. EDX elemental mapping was performed at 30 kV on a Helios Nanolab 600i. High annular dark field (HAADF) and bright field (BF) STEM imaging and Electron Energy Loss Spectroscopy (EELS) was performed on a Probe Corrected JEOL ARM TEM operating at 200 kV. Vesta software was used for the illustration of crystal structures.[35]

4.5 Results and Discussion

SnSe nanoribbons were synthesised through a PVP-mediated solution phase method in a Teflon lined autoclave (see Experimental section 4.3 for a detailed explanation). In brief, SeO_2 was reduced to form a Se-PVP solution, which was then added to a $SnCl_2$-PVP-Ascorbic acid solution and was heated at 80 °C for 5 minutes, before being added to the autoclave. Before addition of this to the autoclave the solution was seen to contain very small nanoparticles (see appendix Figure A.4.2 for STEM of the dropcast Se-PVP solution, and Figure A.4.3 for the STEM of the dropcast Se-PVP + $SnCl_2$-PVP mixture). Figure 4.1 highlights how the morphology of the nanoribbons synthesised varies as a function of reaction time at a growth temperature of 195 °C in the Teflon lined autoclave reactors. After removal of the autoclave from the oven after 27 hours at 195 °C, the product obtained resembled short 1D nanostructures as seen in Figure 4.1(a) + (b). EDX analysis revealed these to consist of approximately ~ 1:1 Sn:Se (see appendix Figure A.4.4). The mean lengths and widths of these structures were found to be 216 ± 119 nm and 37 ± 13 nm respectively. A negligible amount of 2D flakes were seen in this reaction. Increasing the reaction time to 50 hr (Figure 4.1(c) + (d)) resulted in an increase in the mean lengths of the 1D structures but not their widths, *i.e.* a mean length of 358 ± 185 nm and width of 36 ± 17 nm was obtained. After a 27 hr reaction time, 90 % of the nanoribbons had lengths < 400 nm, but after 50 hr, 62 % of the nanoribbons had lengths < 400

nm, with 90 % of them below 650 nm; thus indicating that the mean length of the nanoribbons is directly proportional to the reaction time (further statistical analysis is detailed in appendix Figure A.4.5). Increasing the reaction time from 27 hrs to 50 hrs therefore resulted in an increase of the mean nanoribbon length by 189 nm. However, the nanoribbon widths remained more or less constant with the increase in the reaction time, with only a negligible increase of ~1 nm in the mean width being observed for 27 hr compared to 50 hr reaction. This increase in reaction time thus develops the nanostructures from the initial nanoparticles (appendix Figure A.4.3) to 1D like nanoribbons, which increase in length with increasing reaction time. The longest nanoribbons still maintained a mean thickness similar to the shorter nanoribbons, thus allowing the facile tuning of the aspect ratio with reaction time. Increasing the reaction time to 72 hrs yielded a further increase in nanoribbon length to 432 ± 191 nm (Figures 4.1(e) + (f)), however a wider spread in the width values was observed, corresponding to the presence of a small amount of 2D flakes. The nanoribbons were seen to have a thickness of about ~12 nm, as will be discussed in detail later in the TEM analysis section.

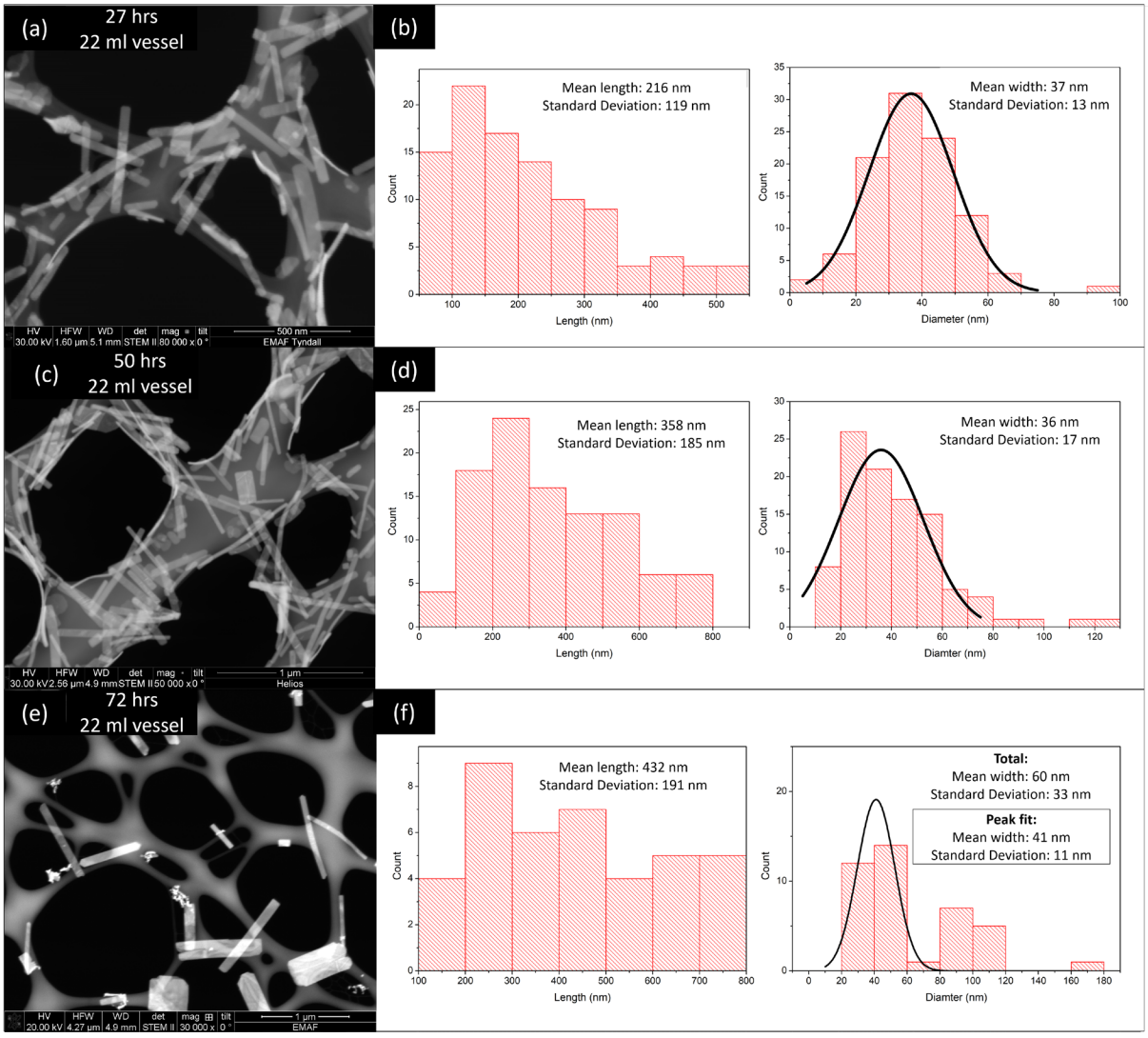


Figure 4.1. STEM images showing the evolution of the SnSe nanoribbons with respect to the growth conditions: (a) show the structures formed after a reaction time of 27 hr, with the statistical analysis of these structures detailed in (b), and (c) shows the effect of increasing the reaction time to 50 hr, with the statistical analysis shown in (d). (e) shows an SEM image after a 72 hr reaction, with the corresponding statistical analysis in (f).

To facilitate the future implementation of SnSe nanoribbons into devices, such as Li-ion batteries and thermoelectric generators, requires production of the nanomaterial in reasonable quantities. Scaling up of 1D SnSe nanorod reactions while maintaining a width : length aspect

ratio above ~5 has previously proved difficult.[36] The batch synthesis of SnSe nanoribbons produced in our approach was found readily scalable, capable of producing hundreds of mg of 1D SnSe nanoribbons with length : width aspect ratios of up to ~40 achievable (see appendix Figure A.4.6). To demonstrate the scalability of the growth process, the reaction volume was increased while keeping the reaction temperature and time constant. Figure 4.2(a) shows the morphology of the structures formed when the reaction volume was roughly doubled to a 45 ml vessel, with the reaction temperature kept at 195 °C and the reaction time set at ~3 days (76 hr). The mean length and diameter of these structures were observed to be 439 ± 211 nm and 42 ± 10 nm respectively, which were consistent with the increase in length with reaction time trend seen for the dimensions of nanoribbons obtained in smaller 22 ml reaction vessels, as seen in Figure 4.1. The nanostructures obtained upon scaling up to a 125 ml reaction vessel at 195 °C for 3 days (72 hr) are shown in Figure 4.2(c). At this higher reaction volume, a small increase in the ratio of 2D flakes to 1D nanoribbons was observed, giving an 84 % yield of nanoribbons to flakes in the 125 ml reaction vessel (see appendix Figure A.4.6), suggesting that adjustment of the reaction conditions (such as PVP to reactant ratio) may be necessary for higher reaction volumes. Figure 4.2(d) shows the statistical analysis of the nanostructures obtained in the high volume reaction, revealing a larger spread in the lengths and widths (554 ± 258 nm mean length and 118 ± 129 nm mean width) due to the 2D flakes present in the sample. A small increase in nanostructure length is also observed at the higher reaction volume. After excluding the 2D flakes while analysing the width of the nanoribbon structures, a mean width of 51 ± 18 nm was observed for the nanoribbons, relatively similar to that achieved for lower reaction volumes. A large amount of SnSe nanostructures (~ 158.7 mg) was obtained from the reaction in the 125 ml autoclave.

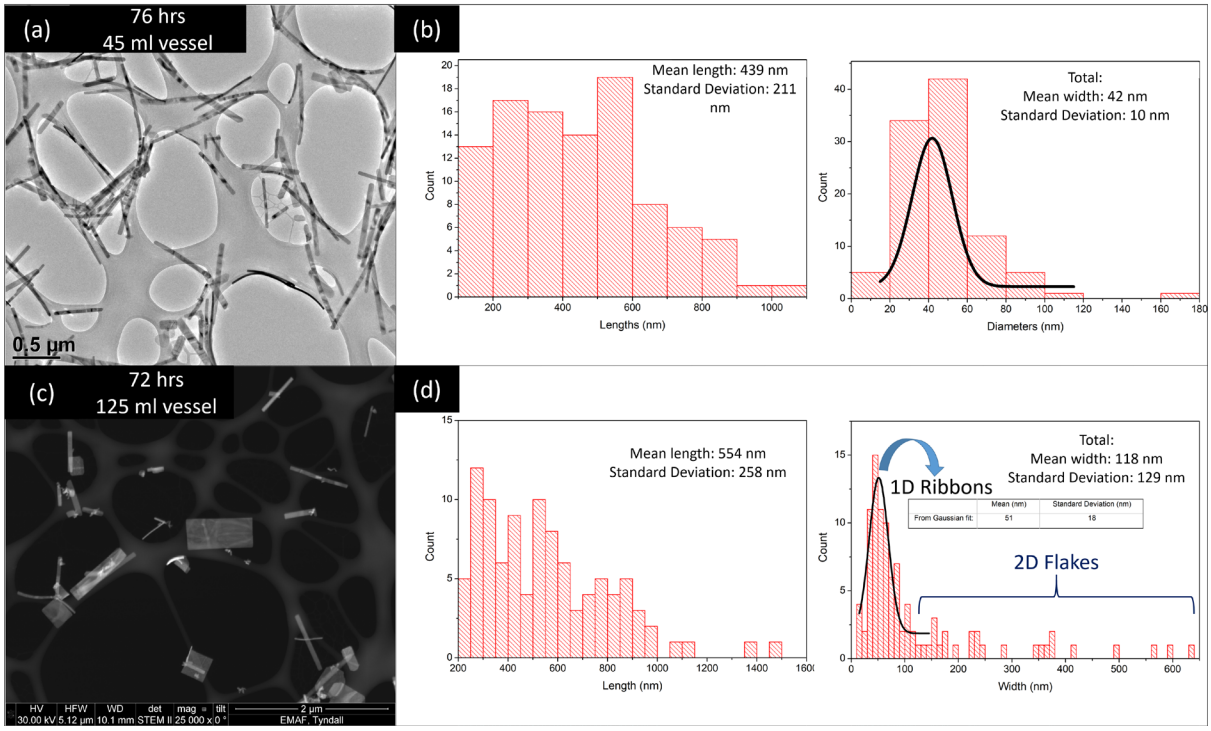


Figure 4.2: (S)TEM images showing the effect of scaling up the reaction to larger reaction vessels. (a) shows the scaled-up reaction in a 45 ml vessel for 76 hr at 195 °C, with (b) detailing the statistical analysis of the nanostructures. (c) Scaled-up reaction in a 125 ml vessel for 72 hr at 195 °C. (d) Statistical analysis of the nanostructures produced in the 125 ml vessel. All structures with widths >100 nm were seen to resemble flake like structures.

Figure 4.3(a) shows a typical XRD pattern for the SnSe nanoribbons. Phase pure orthorhombic Pnma 62 SnSe was seen, with the 200 and 400 peaks highly prominent. Figure 4.3(b) shows a Raman spectrum taken from a sample of the SnSe nanoribbons (after 76 hr in the 45 ml vessel). Clear peaks in the spectrum are seen at 106, 130 and 151 cm^{-1}, which can be assigned to the B_{3g}, A^2_g and A^3_g Raman modes of SnSe respectively. Compared to previously reported Raman analysis for SnSe flakes, the B_{3g} mode is red-shifted and the A^3_g mode is blue-shifted by about 2 cm^{-1} in both cases.[37] Compared to bulk SnSe, the values are in agreement for the A^2_g and A^3_g modes, but red-shifted by 2 cm^{-1} for the B_{3g} mode.[38] An explanation for these shifts could potentially lie in the anisotropic crystal confinement along the c-axis for the SnSe nanoribbons.

No indication of the presence of any other $SnSe_x$ phases such as $SnSe_2$ were seen in either the XRD or Raman analysis, proving the high phase purity of the SnSe nanoribbons synthesised. Figure 4.3(c) shows an EDX map of a nanoribbon (after 72 hr in the 125 ml vessel), revealing the uniform distribution of Sn and Se throughout the nanoribbons, without any elemental segregation. The SnSe nanoribbons were investigated with TEM analysis in Figure 4.3(d), however the PVP coating of the nanoribbons presented difficulty with the imaging. A SnSe nanoribbon oriented close to the [001] zone axis is presented in Figure 4.3(d), with a fast Fourier transform (FFT) pattern in the top left inset, indicating the 200 diffraction spot, which is oriented perpendicular to the nanowire growth direction. A nanoribbon thickness of ~11 nm was measured (Figure 4.3(d)), and as this is along the <100> direction, this represents the thickness of the nanoribbon. The bottom right inset of Figure 4.3(d) schematically represents how the nanoribbon is oriented in the figure, highlighting how the measured ~11 nm value corresponds to the nanoribbon thickness. A thickness of ~11 nm for this nanoribbon would indicate about ~19-20 SnSe layers in the nanoribbon structure. The exact layer number is made hard to determine by the obscuring effect of the PVP present. In general, thicknesses of between ~11 – 13 nm were observed from the TEM analysis of the SnSe nanoribbons.

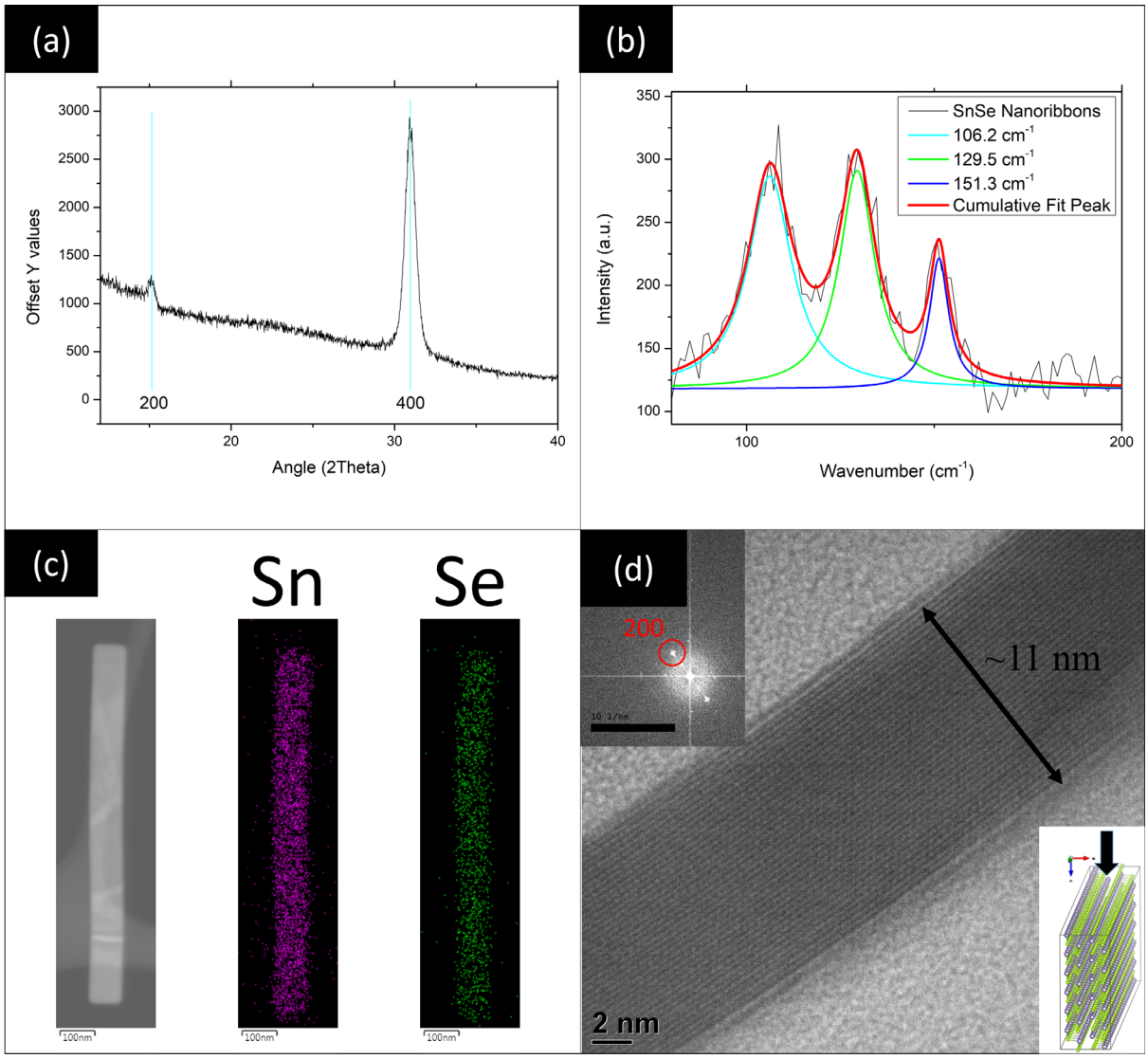


Figure 4.3: (a) XRD analysis of the SnSe nanoribbons (76 hrs, 45 ml grown sample). The two strong peaks can be indexed to phase pure orthorhombic Pnma 62 SnSe. (b) Raman analysis of the same sample as in **(a)**. Peaks at 106, 130 and 151 cm^{-1} are clearly seen, corresponding to the B_{3g}, A^2_g and A^3_g Raman modes of SnSe respectively (514 nm laser excitation, peaks fitted with a Lorentzian function). (c) EDX map of a SnSe nanoribbon (72 hr, 125ml grown sample), showing the uniform distribution of Sn and Se throughout the structure. (d) TEM image of a SnSe-PVP nanoribbon (76 hr, 45 ml grown sample) oriented close to the [001] zone axis. A nanoribbon thickness of ~11 nm is observed. The top left inset shows a fast Fourier transform (FFT), with the bottom right inset showing a schematic of the orientation of the nanoribbon (the black arrow indicates the viewing direction of the TEM image).

In order to facilitate clearer imaging of the crystal structure of the SnSe nanoribbons they were washed in ethanol to remove the majority of the PVP. Figures 4.4(a) and (b) show TEM images of ethanol washed SnSe nanoribbons grown after 76 hr in the 45 ml vessel, with indexed SAED patterns as insets, orientated along the [100] and [001] zone axes, respectively. After removing the PVP, imaging the nanoribbon becomes easier, and the zigzag structure of SnSe along the <010> direction is clearly seen in the HRTEM image in the inset of Figure 4.4(a). This is of particular interest due to the semiconductor to metallic transition that zigzag SnSe nanoribbons have previously been theorised to exhibit, when confined to sufficiently small dimensions.[8,9] However, after removing the PVP, a surface layer of a dark contrast amorphous material is apparent on the surface of the nanoribbons. This amorphous coating is darker in contrast to the previous PVP coating (Figure 4.3(d)), and is shown to consist of SnO_x by EELS analysis (see appendix Figure A.4.7). SnSe has been shown to oxidise rapidly in air, forming a SnO_x surface of ~6 nm,[13,39] which is consistent with the thickness of the amorphous layer seen in the TEM images; indicating that this layer is formed post-growth, and post removal of the PVP due to atmospheric surface oxidation. The total thickness of the SnSe nanoribbon, visible when it is viewed down the [001] zone axis in Figure 4.4(b), was seen to be ~12 nm, which is also in agreement with the nanoribbon thickness seen when the PVP was present. However, the crystalline core region is reduced to a thickness of ~6 nm, with the rest being formed of amorphous SnO_x. This indicates that the PVP appears to offer some protection to atmospheric oxidation, and removal of this PVP should be performed only directly before implementation of the SnSe nanoribbons into a device. The SnSe nanoribbons are single crystalline throughout their core, as shown in the HRTEM images and corresponding SAED patterns (Figures 4.4(a) and (b) with SAED patterns in insets). The single crystalline nature of these SnSe nanoribbons is important to note, as high yield solution phase growth methods can commonly result in the formation of nanomaterials with a polycrystalline or highly defected crystal structure.[27,40] A

growth direction along the <010> crystal direction of SnSe was observed for every nanoribbon studied (Figures 4.4(a) and (b)), demonstrating a high level of uniformity in the single crystalline nanoribbons. The crystal structure of a <010> oriented SnSe nanoribbon is illustrated in Figures 4.4(c) and (d). Most previous studies on 1D SnSe nanowires have shown growth directions along either the <011> or <100> directions,[13,32,34] but in our case, for all nanoribbons measured, the growth direction was found to be along the <010> direction. This <010> 1D growth direction of SnSe has only ever been shown for oleylamine[22] and ethanolamine[23] assisted methods, producing short nanorods and large nanobelts respectively. Nanoribbons of SnSe with a low layer number have not previously been reported. Our PVP assisted method provides many advantages in terms of its reduced toxicity and increased biocompatibility,[30] and additionally, while previous methods not only employed more toxic regents than in our synthesis, the aspect ratio of the produced 1D nanostructures was also greatly enhanced through our approach. We also demonstrate that the nanomaterials synthesised through our approach adopt a low dimension nanoribbon structure, with a thickness as low as ~11 nm (~19 - 20 SnSe layers) (Figure 4.3(d)). Growth along the <010> direction leads to the exposure of energetically unfavourable high energy surface planes for SnSe,[41] demonstrating the necessity of a suitable capping agent. In our approach PVP selectively binds to the {100} and {001} SnSe crystal surfaces, facilitating growth along the <010> direction. Of note, is that this <010> crystal direction has previously been reported to exhibit an ultralow lattice thermal conductivity, and gives rise to a very high thermoelectric figure of merit for bulk SnSe crystals along this direction.[10] Utilising these <010> SnSe nanoribbons for future thermoelectric studies would thus be of significant interest.

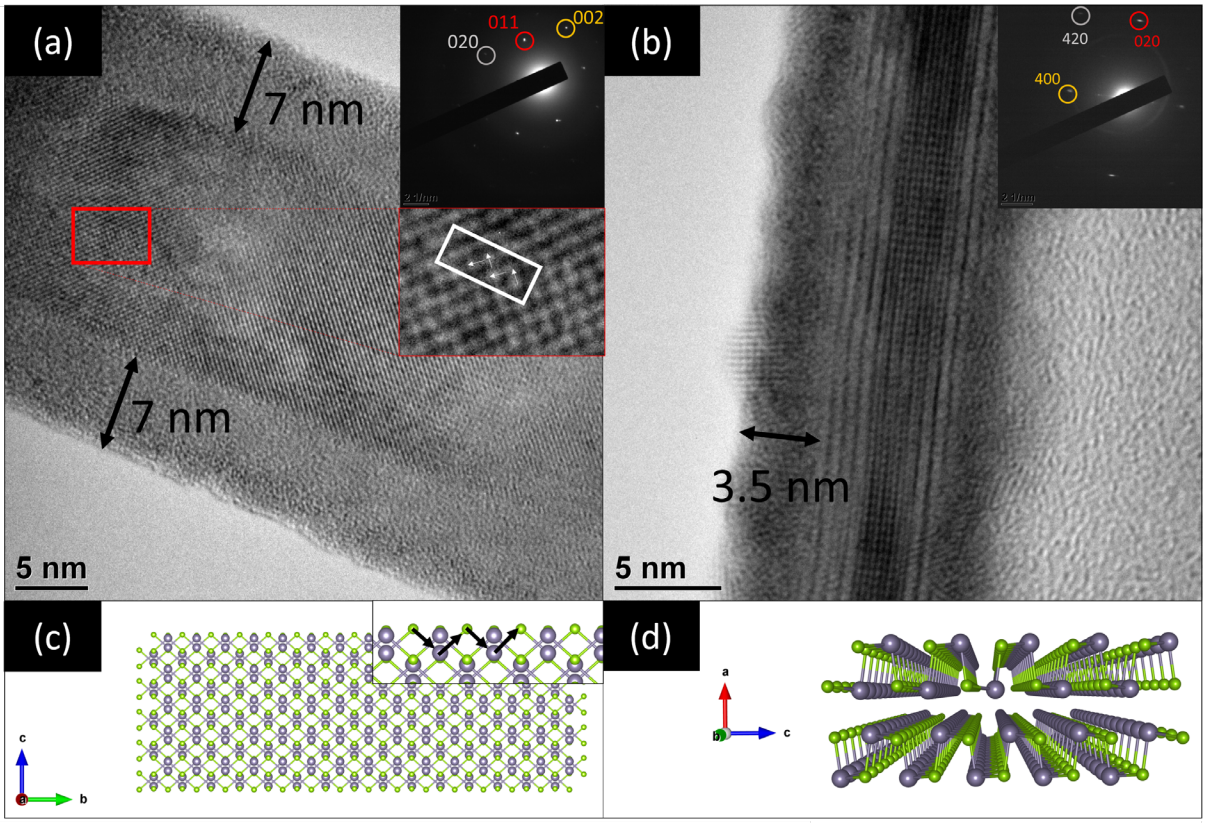


Figure 4.4: TEM analysis of the SnSe nanoribbons: (a) a SnSe nanoribbon orientated along the [100] zone axis, as confirmed from the indexed SAED pattern in the top inset. The bottom inset shows a HRTEM image of a section of the nanoribbon, revealing the zigzag structure of SnSe along the <010> direction. Amorphous regions roughly 7 nm in thickness can be seen at the edges of the nanoribbon. (b) SnSe nanoribbons orientated along the [001] zone axis, as confirmed from the indexed SAED pattern in the inset. Amorphous regions roughly 3.5 nm in thickness are seen at the edges of the nanoribbon. (c) SnSe nanoribbon structure viewed down the [100] direction. The zigzag structure is highlighted in the inset. (d) Perspective view of a SnSe nanoribbon cross-section.

Due to the layered crystal structure of SnSe, crystal growth tends to dominate along the *b* and *c* crystal axes, with minimal growth along the *a*-axis, upon which the SnSe layers are stacked. To therefore initiate growth in a 1D manner, the use of SeO_2 with a chain structure, and PVP as a passivating agent was required. SeO_2 was heated in ethylene glycol to reduce the Se^{4+} to Se^{2-},[42] which is important as tin selenides have commonly been reported to form in two phases, SnSe and $SnSe_2$, where Sn exists in both 2+ and 4+ oxidation states, respectively. The oxidation of Sn^{2+} to Sn^{4+} has been shown to be supressed by the addition of L-ascorbic acid in previous reports, aiding in the formation of phase pure SnSe.[43] The chain structure exhibited by SeO_2 is then believed to lead to the formation of a chain $(Se)_m(PVP)_n$ complex, similar to chain $(Se)_m(Oleylamine)_n$ complexes in previous 1D SnSe studies.[22] To these (Se^{2-})-PVP seeds, $SnCl_2.2H_2O$ is then added as a source of Sn^{2+}, which then diffuses into the Se-PVP to form SnSe-PVP nanoparticles. The SnSe nanoribbons then grow from the SnSe nucleation points, with the aid of PVP as a 1D directing agent. Since the nanoribbon width is not seen to increase by any significant amount with increasing length or reaction time, after the initial nanoribbon formation the growth continues only by addition along the (010) crystal facets. The growth of SnSe has commonly been reported to result in the formation of a flake morphology, without the use of any additional surfactants.[44] The growth mechanism of such a SnSe flake is illustrated at the top row of Figure 4.5(a). The growth of SnSe flakes has previously been shown to initiate as a high surface energy (010) and (001) faceted SnSe flake, with the lower surface energy (011) and (0-11) facets forming the surface planes in the later stages of growth.[41] For the formation of SnSe nanoribbons, PVP acts to confine the crystal growth in the early (010) and (001) faceted stage and restricts the growth to material addition along the (010) plane (this is illustrated in the bottom of Figure 4.5(a)).

The XPS spectrum of the ethanol washed SnSe nanoribbon sample shown in Figure 4.5(b) highlights the single oxidation state of Se^{2-}, supporting the high phase purity of the SnSe sample. Figure 4.5(c) shows the Sn XPS spectrum, revealing three oxidation states for Sn; Sn^{0}, Sn^{2+} and Sn^{4+}. This is in agreement with the EELS analysis shown previously in Figure 4.3(c), which reveals that the Sn^{4+} results from the surface oxidation of the SnSe nanoribbons, with the body of the nanoribbon remaining single crystalline SnSe. SnSe has previously been reported to oxidise rapidly in air.[13,39] PVP is expected to offer improved protection from this oxidation, but oxygen diffusion through the PVP layer will still cause small diameter nanostructures to oxidise gradually over time.[45]

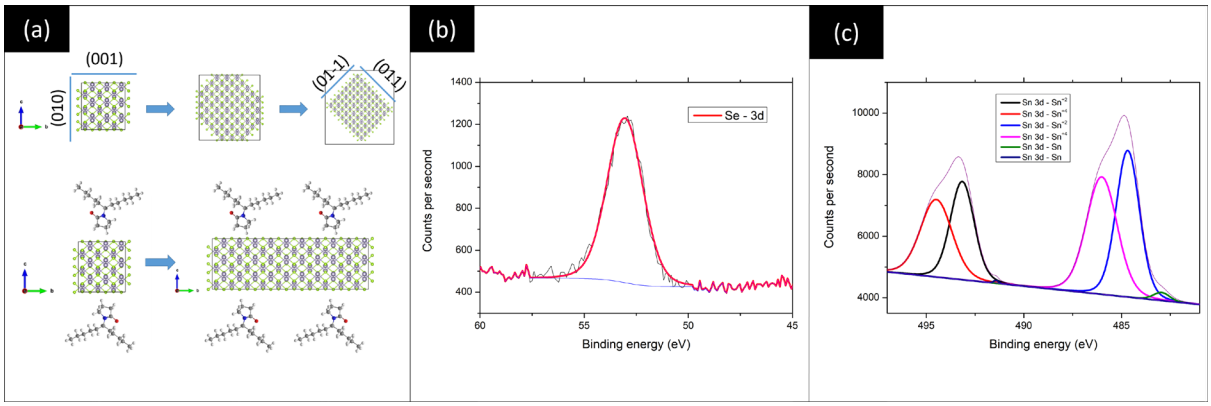


Figure 4.5: Illustration of the proposed growth of the SnSe nanoribbon crystal structure; (a) at the top is shown the growth mechanism for a 2D SnSe flake, and the bottom shows how PVP leads to the growth of SnSe nanoribbons through the passivation of the {001} facets. (b) and (c) XPS spectra of Se and Sn binding energies, respectively.

4.6 Conclusions

The synthesis of single crystalline SnSe nanoribbons has been successfully achieved through a simple solution-based method, using readily available precursors. Non-toxic PVP was used for the first time to direct the 1D growth of SnSe, and low layer number SnSe nanoribbons

were also reported for the first time. The use of non-toxic PVP could open up use of these SnSe nanoribbons for biomedical applications, as well as having potential applications in a range of applications such as batteries, solar cells, memory devices and thermoelectric generators. The synthesised nanoribbons all grow along the <010> direction, which has been previously reported to possess a remarkably low lattice thermal conductivity along this crystal orientation, highlighting the significance of these nanoribbons for potential applications in future thermoelectric devices. The growth along the <010> direction is normally hindered due to the increased exposure of high surface energy planes this induces in the structure, but is achieved in our case through the selective binding of PVP to the (100) and (001) surface planes. This increased understanding of the nature of the influence of PVP in SnSe systems could lead to increased future possibilities in material design and non-toxic growth strategies for the solution phase synthesis of SnSe. The growth of very thin <010> oriented SnSe nanoribbons has not previously been reported, and the successful synthesis of SnSe nanoribbons also enables the future exploration of the previously theorised novel properties of SnSe nanoribbons, such as an expected nanoribbon width-dependant tuneable bandgap.

4.7 References:

(1) Han, M. Y.; Özyilmaz, B.; Zhang, Y.; Kim, P. Energy Band-Gap Engineering of Graphene Nanoribbons. *Phys. Rev. Lett.* **2007**, *98*, 1–4.

(2) Xu, L. C.; Song, X. J.; Yang, Z.; Cao, L.; Liu, R. P.; Li, X. Y. Phosphorene Nanoribbons: Passivation Effect on Bandgap and Effective Mass. *Appl. Surf. Sci.* **2015**, *324*, 640–644.

(3) Cai, Y.; Zhang, G.; Zhang, Y. W. Polarity-Reversed Robust Carrier Mobility in Monolayer MoS2 Nanoribbons. *J. Am. Chem. Soc.* **2014**, *136*, 6269–6275.

(4) Nicolosi, V.; Chhowalla, M.; Kanatzidis, M. G.; Strano, M. S.; Coleman, J. N. Liquid Exfoliation of Layered Materials. *Science* **2013**, *340*, 1226419–1226419.

(5) Zhou, X.; Zhang, Q.; Gan, L.; Li, H.; Xiong, J.; Zhai, T. Booming Development of Group IV–VI Semiconductors: Fresh Blood of 2D Family. *Adv. Sci.* **2016**, *3*.

(6) Deng, Z.; Cao, D.; He, J.; Lin, S.; Lindsay, S. M.; Liu, Y. Solution Synthesis of Ultrathin Single-Crystalline SnS Nanoribbons for Photodetectors via Phase Transition and Surface Processing. *ACS Nano* **2012**, *6*, 6197–6207.

(7) Lu, J.; Nan, C.; Li, L.; Peng, Q.; Li, Y. Flexible SnS Nanobelts: Facile Synthesis, Formation Mechanism and Application in Li-Ion Batteries. *Nano Res.* **2013**, *6*, 55–64.

(8) Tyagi, K.; Waters, K.; Wang, G.; Gahtori, B.; Haranath, D.; Pandey, R. Thermoelectric Properties of SnSe Nanoribbons: A Theoretical Aspect. *Mater. Res. Express* **2016**, *3*.

(9) Huang, Y.; Ling, C.; Liu, H.; Wang, S. Edge-, Width- and Strain-Dependent Semiconductor-Metal Transition in SnSe Nanoribbons. *RSC Adv.* **2014**, *4*, 6933–6938.

(10) Zhao, L.-D.; Lo, S.-H.; Zhang, Y.; Sun, H.; Tan, G.; Uher, C.; Wolverton, C.; Dravid, V. P.; Kanatzidis, M. G. Ultralow Thermal Conductivity and High Thermoelectric Figure of Merit in SnSe Crystals. *Nature* **2014**, *508*, 373–377.

(11) Chen, Z. G.; Shi, X.; Zhao, L. D.; Zou, J. High-Performance SnSe Thermoelectric Materials: Progress and Future Challenge. *Prog. Mater. Sci.* **2018**, *97*, 283–346.

(12) Gao, M. R.; Xu, Y. F.; Jiang, J.; Yu, S. H. Nanostructured Metal Chalcogenides: Synthesis, Modification, and Applications in Energy Conversion and Storage Devices. *Chem. Soc. Rev.* **2013**, *42*, 2986–3017.

(13) Davitt, F.; Manning, H. G.; Robinson, F.; Hawken, S. L.; Biswas, S.; Petkov, N.; Druenen, M.; Boland, J. J.; Reid, G.; Holmes, J. D. Crystallographically Controlled Synthesis of SnSe Nanowires: Potential in Resistive Memory Devices. *Adv. Mater. Interfaces* **2020**, 2000474.

(14) Cho, S. H.; Cho, K.; Park, N. W.; Park, S.; Koh, J. H.; Lee, S. K. Multi-Layer SnSe Nanoflake Field-Effect Transistors with Low-Resistance Au Ohmic Contacts. *Nanoscale Res. Lett.* **2017**, *12*, 2–7.

(15) Pawbake, A. S.; Jadkar, S. R.; Late, D. J. High Performance Humidity Sensor and Photodetector Based on SnSe Nanorods. *Mater. Res. Express* **2016**, *3*.

(16) Zhao, S.; Wang, H.; Zhou, Y.; Liao, L.; Jiang, Y.; Yang, X.; Chen, G.; Lin, M.; Wang, Y.; Peng, H.; et al. Controlled Synthesis of Single-Crystal SnSe Nanoplates. *Nano Res.* **2015**, *8*, 288–295.

(17) Minnam Reddy, V. R.; Gedi, S.; Pejjai, B.; Park, C. Perspectives on SnSe-Based Thin Film Solar Cells: A Comprehensive Review. *J. Mater. Sci. Mater. Electron.* **2016**, *27*, 5491–5508.

(18) Franzman, M. A.; Schlenker, C. W.; Thompson, M. E.; Brutchey, R. L. Solution-Phase Synthesis of SnSe Nanocrystals for Use in Solar Cells. *J. Am. Chem. Soc.* **2010**, *132*, 4060–4061.

(19) Wang, W.; Li, P.; Zheng, H.; Liu, Q.; Lv, F.; Wu, J.; Wang, H.; Guo, S. Ultrathin Layered SnSe Nanoplates for Low Voltage, High-Rate, and Long-Life Alkali–Ion Batteries. *Small* **2017**, *13*, 1–7.

(20) Cheng, Y.; Huang, J.; Li, J.; Cao, L.; Xu, Z.; Luo, X.; Qi, H.; Guo, P. SnSe/r-GO

Composite with Enhanced Pseudocapacitance as a High-Performance Anode for Li-Ion Batteries. *ACS Sustain. Chem. Eng.* **2019**, *7*, 8637–8646.

(21) Baumgardner, W. J.; Choi, J. J.; Lim, Y.-F.; Hanrath, T. SnSe Nanocrystals: Synthesis, Structure, Optical Properties, and Surface Chemistry. *J. Am. Chem. Soc.* **2010**, *132*, 9519–9521.

(22) Wang, R.; Wei, M.; Jiang, G.; Liu, W.; Zhu, C. Study of the Preperation of SnSe Nanorods with Selenium Dioxide as Source. *Chem. Lett.* **2014**, *43*, 693–695.

(23) Guo, J.; Jian, J.; Liu, J.; Cao, B.; Lei, R.; Zhang, Z.; Song, B.; Zhao, H. Synthesis of SnSe Nanobelts and the Enhanced Thermoelectric Performance in Its Hot-Pressed Bulk Composite. *Nano Energy* **2017**, *38*, 569–575.

(24) Vaughn, D. D.; In, S. Il; Schaak, R. E. A Precursor-Limited Nanoparticle Coalescence Pathway for Tuning the Thickness of Laterally-Uniform Colloidal Nanosheets: The Case of SnSe. *ACS Nano* **2011**, *5*, 8852–8860.

(25) Li, L.; Chen, Z.; Hu, Y.; Wang, X.; Zhang, T.; Chen, W.; Wang, Q. Single-Layer Single-Crystalline SnSe Nanosheets. *J. Am. Chem. Soc.* **2013**, *135*, 1213–1216.

(26) Koczkur, K. M.; Mourdikoudis, S.; Polavarapu, L.; Skrabalak, S. E. Polyvinylpyrrolidone (PVP) in Nanoparticle Synthesis. *Dalt. Trans.* **2015**, *44*, 17883–17905.

(27) Jia, Y.; Ma, Y.; Lin, Y.; Tang, J.; Shi, W. Facile Synthesis of Branched MoS_2 Nanowires. *Chem. Phys.* **2018**, *513*, 209–212.

(28) Jadhav, S. V.; Nikam, D. S.; Khot, V. M.; Thorat, N. D.; Phadatare, M. R.; Ningthoujam, R. S.; Salunkhe, A. B.; Pawar, S. H. Studies on Colloidal Stability of PVP-Coated LSMO Nanoparticles for Magnetic Fluid Hyperthermia. *New J. Chem.* **2013**, *37*, 3121–3130.

(29) Sun, Y.; Mayers, B.; Herricks, T.; Xia, Y. Polyol Synthesis of Uniform Silver

Nanowires: A Plausible Growth Mechanism and the Supporting Evidence. *Nano Lett.* **2003**, *3*, 955–960.

(30) Tang, Z.; Zhao, P.; Ni, D.; Liu, Y.; Zhang, M.; Wang, H.; Zhang, H.; Gao, H.; Yao, Z.; Bu, W. Pyroelectric Nanoplatform for NIR-II-Triggered Photothermal Therapy with Simultaneous Pyroelectric Dynamic Therapy. *Mater. Horizons* **2018**, *5*, 946–952.

(31) Butt, F. K.; Mirza, M.; Cao, C.; Idrees, F.; Tahir, M.; Safdar, M.; Ali, Z.; Tanveer, M.; Aslam, I. Synthesis of Mid-Infrared SnSe Nanowires and Their Optoelectronic Properties. *CrystEngComm* **2014**, *16*, 3470.

(32) Liu, J.; Jian, J.; Yu, Z.; Zhang, Z.; Cao, B.; Du, B. Catalyst-Free Vapor Phase Growth of Ultralong SnSe Single-Crystalline Nanowires. *Cryst. Growth Des.* **2017**, *17*, 6163–6168.

(33) Shen, G.; Chen, D.; Jiang, X.; Tang, K.; Liu, Y.; Qian, Y. Rapid Synthesis of SnSe Nanowires via an Ethylenediamine-Assisted Polyol Route. *Chem. Lett.* **2003**, *32*, 426–427.

(34) Liu, S.; Guo, X.; Li, M.; Zhang, W. H.; Liu, X.; Li, C. Solution-Phase Synthesis and Characterization of Single-Crystalline SnSe Nanowires. *Angew. Chemie - Int. Ed.* **2011**, *50*, 12050–12053.

(35) Momma, K.; Izumi, F. VESTA 3 for Three-Dimensional Visualization of Crystal, Volumetric and Morphology Data. *J. Appl. Crystallogr.* **2011**, *44*, 1272–1276.

(36) Kundu, S.; Yi, S. I.; Yu, C. Gram-Scale Solution-Based Synthesis of SnSe Thermoelectric Nanomaterials. *Appl. Surf. Sci.* **2018**, *459*, 376–384.

(37) Luo, S.; Qi, X.; Yao, H.; Ren, X.; Chen, Q.; Zhong, J. Temperature-Dependent Raman Responses of the Vapor-Deposited Tin Selenide Ultrathin Flakes. *J. Phys. Chem. C* **2017**, *121*, 4674–4679.

(38) Liu, F.; Parajuli, P.; Rao, R.; Wei, P. C.; Karunarathne, A.; Bhattacharya, S.; Podila, R.;

He, J.; Maruyama, B.; Priyadarshan, G.; et al. Phonon Anharmonicity in Single-Crystalline SnSe. *Phys. Rev. B* **2018**, *98*.

(39) Tian, H.; Wang, X. F.; Mohammad, M. A.; Gou, G. Y.; Wu, F.; Yang, Y.; Ren, T. L. A Hardware Markov Chain Algorithm Realized in a Single Device for Machine Learning. *Nat. Commun.* **2018**, *9*, 1–11.

(40) Baby, B. H.; Mohan, D. B. The Formation of α-Phase SnS Nanorods by PVP Assisted Polyol Synthesis: Phase Stability, Micro Structure, Thermal Stability and Defects Induced Energy Band Transitions. *Mater. Chem. Phys.* **2017**, *192*, 317–329.

(41) Ma, X. H.; Cho, K. H.; Sung, Y. M. Growth Mechanism of Vertically Aligned SnSe Nanosheets via Physical Vapour Deposition. *CrystEngComm* **2014**, *16*, 5080–5086.

(42) Skrabalak, S. E.; Wiley, B. J.; Kim, M.; Formo, E. V.; Xia, Y. On the Polyol Synthesis of Silver Nanostructures: Glycolaldehyde as a Reducing Agent. *Nano Lett.* **2008**, *8*, 2077–2081.

(43) Pejjai, B.; Minnam Reddy, V. R.; Seku, K.; Pallavolu, M. R.; Park, C. Eco-Friendly Synthesis of SnSe Nanoparticles: Effect of Reducing Agents on the Reactivity of a Se-Precursor and Phase Formation of SnSe NPs. *New J. Chem.* **2018**, *42*, 4843–4853.

(44) Han, G.; Popuri, S. R.; Greer, H. F.; Bos, J. W. G.; Zhou, W.; Knox, A. R.; Montecucco, A.; Siviter, J.; Man, E. A.; MacAuley, M.; et al. Facile Surfactant-Free Synthesis of p-Type Snse Nanoplates with Exceptional Thermoelectric Power Factors. *Angew. Chemie - Int. Ed.* **2016**, *55*, 6433–6437.

(45) Deignan, G.; Goldthorpe, I. A. The Dependence of Silver Nanowire Stability on Network Composition and Processing Parameters. *RSC Adv.* **2017**, *7*, 35590–35597.

4.8 Appendix

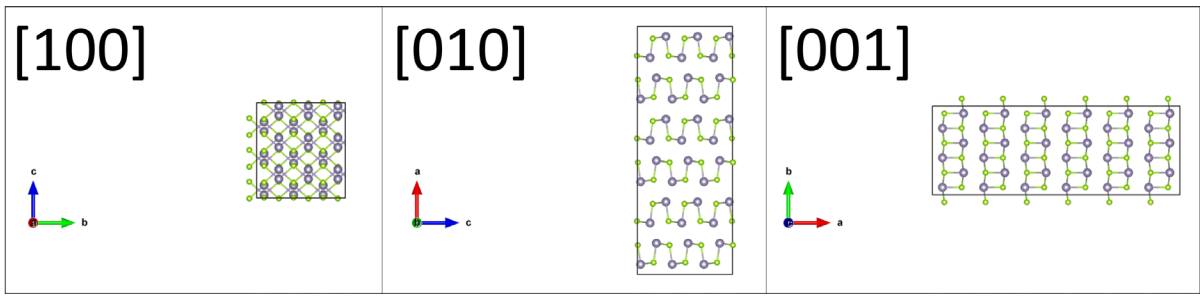


Figure A.4.1: SnSe crystal structure oriented along three major zone axes; [100], [010] and [001]. Green atoms represent Se and grey atoms Sn. The arrows in the bottom left corner indicate the directions of the *a, b* and *c* lattice directions. Red arrow: *a*-axis, green arrow: *b*-axis, blue arrow: *c*-axis.

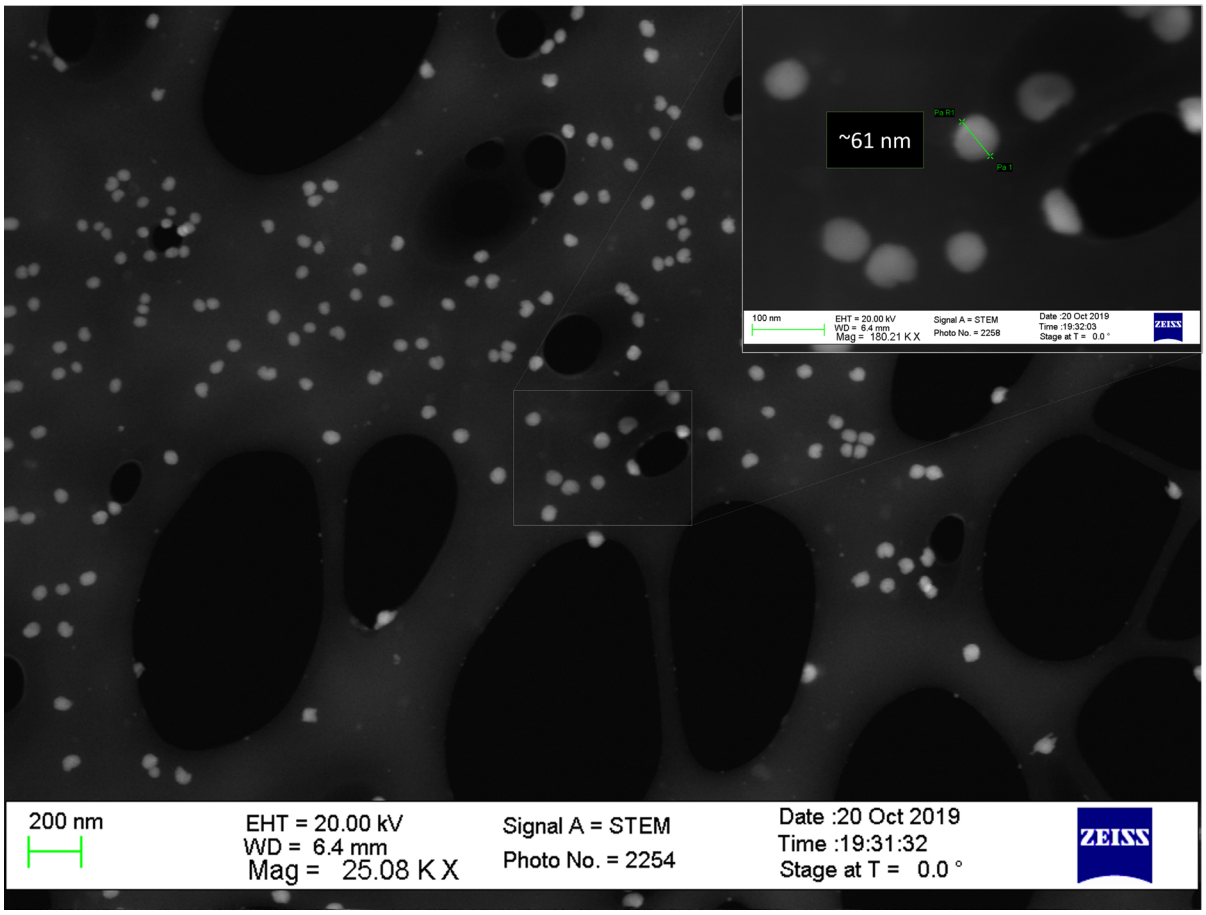


Figure A.4.2: STEM image of the Se-PVP nanoparticles produced after reduction of the SeO_2 in ethylene glycol and PVP at 195 °C for 18 hr.

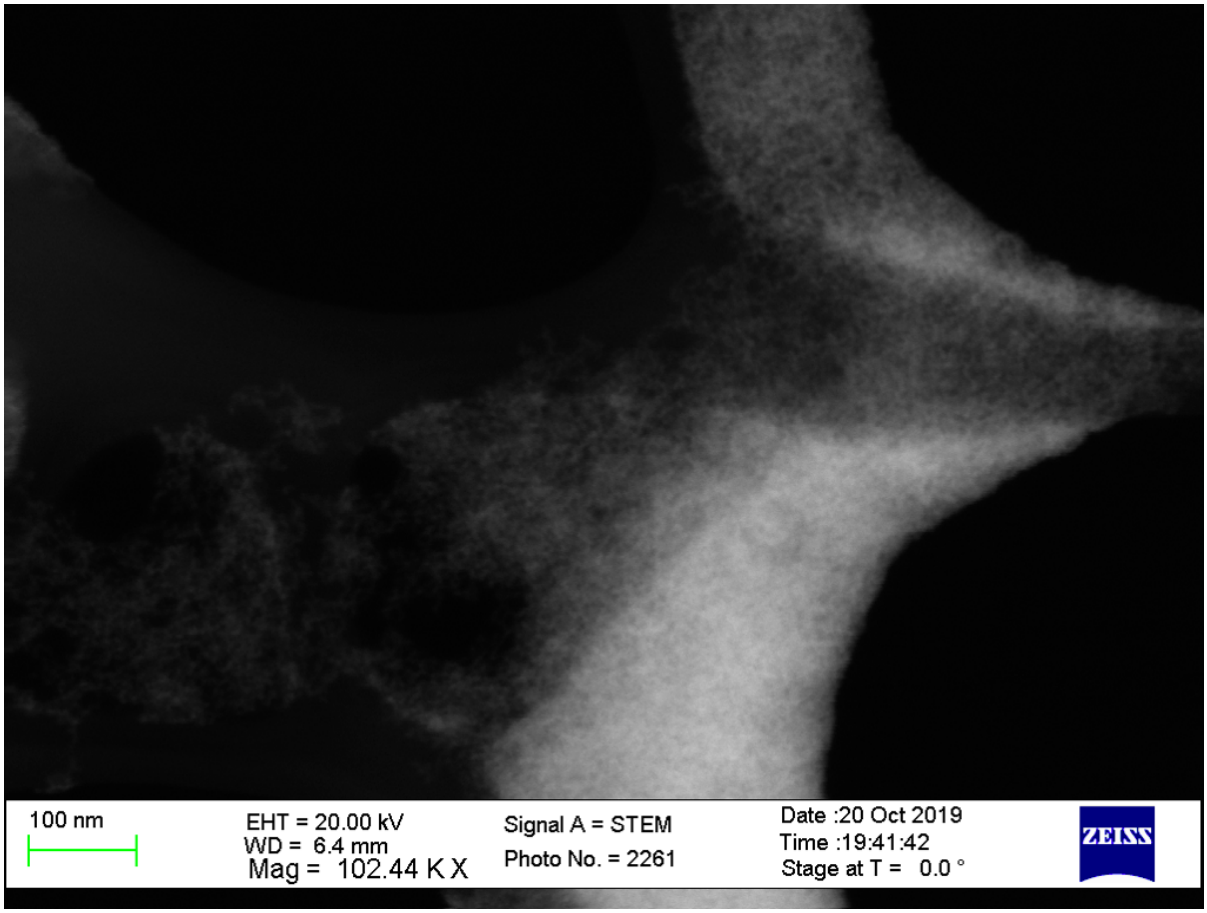


Figure A.4.3: SnSe-PVP nanoparticles formed after the addition of the $SnCl_2$ to the Se-PVP solution at 80°C.

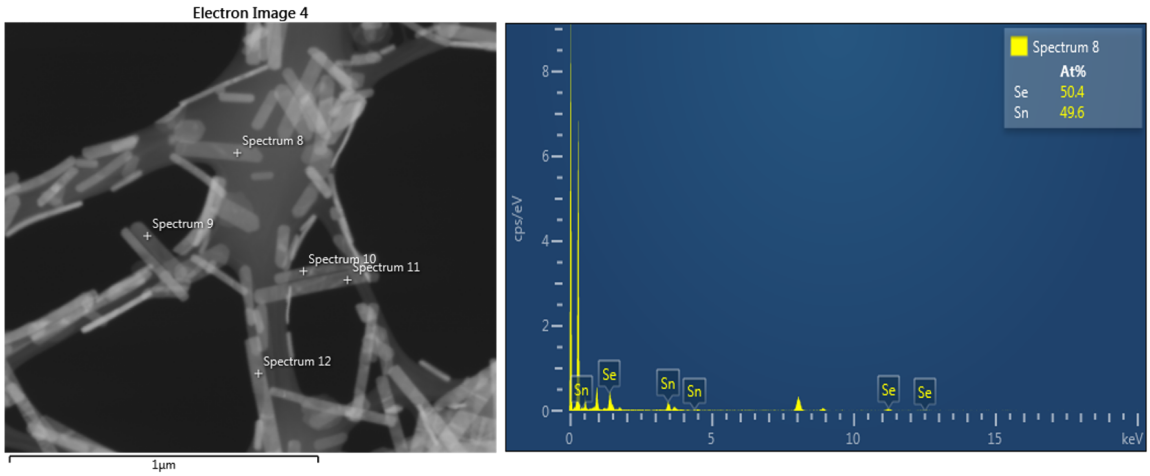


Figure A.4.4: EDX analysis of SnSe nanoribbons after 27 hr in the 22 ml vessel. A Sn : Se at% ratio of 50.04 : 49.6 is seen.

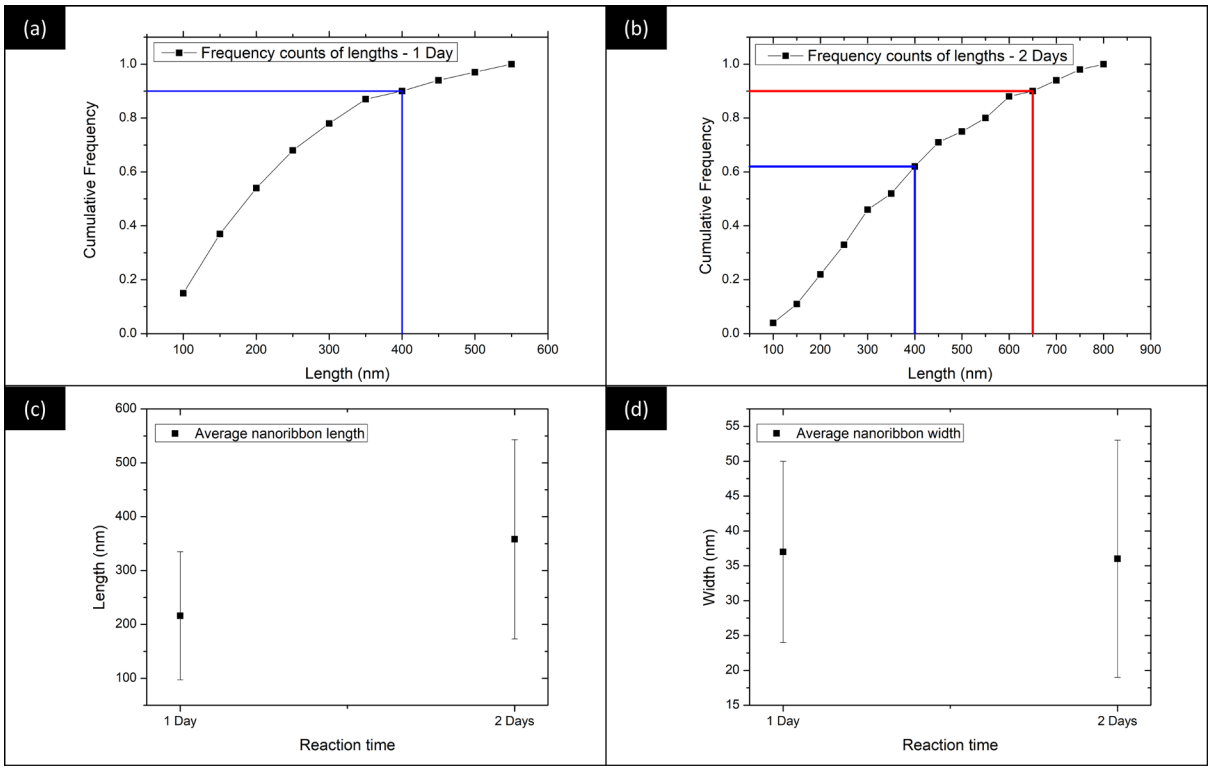


Figure A.4.5: Variation of the mean nanoribbon lengths and widths for the reactions run for 27 and 50 hr at 195 °C in a 22 ml vessel. The normalised frequency counts of the lengths of the nanoribbons produced after 27 hr are shown in (a). The blue line is a guide for the eye, indicating that 90 % of the ribbon lengths lie under 400 nm. The normalised frequency counts of the lengths of the nanoribbons produced after 50 hr are shown in (b). The blue and red lines are again guides for the eye, indicating that 62 % of the ribbon lengths lie under 400 nm, and 90 % under 650 nm. (c) and (d) compare the mean nanoribbon lengths and widths with respect to reaction time.

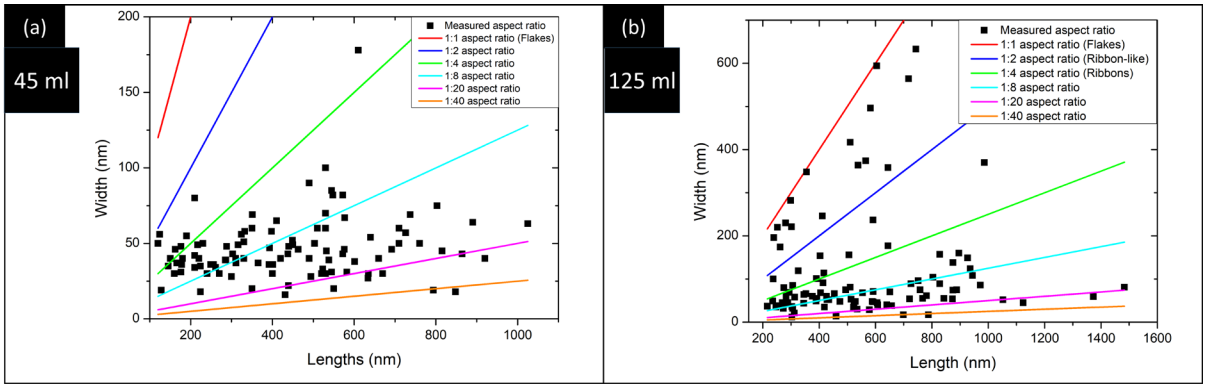


Figure A.4.6. Aspect ratios of the different nanostructures produced in (a) a 45 ml reaction vessel for 76 hr and (b) a 125 ml vessel for 72 hr. The coloured lines are guides for the eye. We define flake structures as having a width:length aspect ratio lower than 1:2 , *i.e.* all points above the blue line are flakes. In **(a)** 100 % of the data points lie below the blue line, and in **(b)** 16 % of the data points lie above the blue line, with 84 % below it; giving an 84 % yield of ribbons to flakes in the sample.

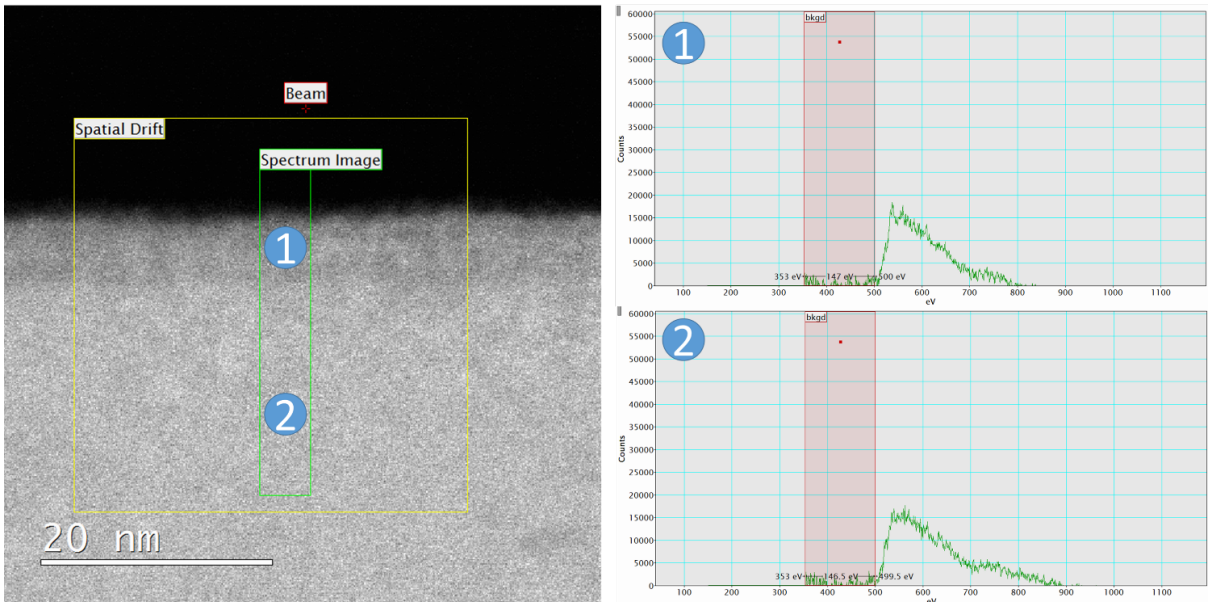


Figure A.4.7: EELS surface analysis of a SnSe nanoribbon, revealing that the amorphous surface layer is composed of SnO_x.

Chapter 5

Conclusions and Future Outlook

Research interest in SnSe materials was only just starting to garner significant interest when I began my PhD in 2015, and research into the properties of this layered chalcogenide material has been increasing in these recent years. This thesis has set out to explore, synthesise and characterise novel 1D forms of SnSe. SnSe is of significant interest for a wide range of potential applications, such as non-volatile memory devices,[1–4] field effect transistors,[5] sensors,[6,7] photodetectors,[6,8] thermoelectric devices,[9–12] solar cells[13–15] and Li-ion batteries.[16-19] These applications can be influenced by the anisotropic properties of SnSe, yielding different material behaviours along its different crystal axes.[20,21] These anisotropic properties of SnSe lend themselves particularly well to a 1D geometry, where the crystal growth direction of the 1D material can be controlled. 1D nanostructuring also offers SnSe the advantages of better scalability and reduced power requirements for the many applications to which SnSe finds use. Reports on 1D forms of SnSe were very limited in 2015, and the work reported in this thesis has contributed to the advancement of this field.

CVD grown SnSe nanowires of high quality are only a relatively recent development, and Chapter 1 of this thesis details further advancements in this area, where unparalleled control of the 1D structure of SnSe can be achieved through a liquid injection CVD method. <011> and <100> oriented SnSe nanowires could be controllably synthesised though the variation of the growth temperature. This work also advances the wide range of applications for SnSe, demonstrating the potential of SnSe nanowires for RRAM applications. <100> oriented nanowires could also offer future fundamental insight into the properties of SnSe, exhibiting cleavage of the SnSe layers when exposed to an electron beam (see appendix section 6.1).

Further control of the SnSe nanowires is detailed in Chapter 2, where interconnected nanowires are formed in a 2D nanonetwork structure. This work develops on from the work in Chapter 1, where the CVD growth conditions are further altered to yield this new SnSe morphology. The novel morphology of these SnSe nanonetworks are seen to offer improved performance as a Li-ion battery anode when compared to other SnSe forms. Of significant interest, would be to examine if similar morphologies can be achieved for the growth of materials with a similar form to SnSe, such as SnS or SnTe. Appendix section 6.2 shows some preliminarily results of the CVD synthesis of similarly layered Ge doped Sb_2Te_3 nanoribbons.

While the CVD methods reported in the previous chapters offer significant material control and novel morphologies with enhanced properties, the mass of product achievable from these methods is limited to fractions of milligrams. Solution-phase methods are typically able to overcome this limitation, and Chapter 3 details such a method which was capable of not only producing tens to hundreds of milligrams of 1D SnSe, but also a novel SnSe nanoribbon morphology with thickness values of ~11 - 13 nm, widths of ~40 nm and lengths of hundreds of nanometres. PVP was shown to result in the selective passivation of the {100} and {001} facets, leading to the crystal growth progressing primarily along the <010> direction. Very thin SnSe nanoribbons such as these have not previously been reported, and this opens the door to future work, investigating the novel theorised properties of SnSe nanoribbons such as a width dependant bandgap, yielding a predicted semiconductor to metallic transition in SnSe nanoribbons that has yet to be experimentally observed.[21,22] As such, these SnSe nanoribbons offer a platform to experimentally explore SnSe nanoribbons, which have remained only within the realm of theorists up until now.

SnSe is being widely pursued for its highly promising potential in non-volatile memory devices,[1–4] field effect transistors,[5] sensors,[6,7] photodetectors,[6,8] thermoelectric devices,[9–12] solar cells[13–15] and Li-ion batteries.[16–19] Enhancement of these devices can be achieved though

modification of the material structure in a nanomaterial form, with 2D and 1D forms being of significant interest. Due to the highly anisotropic nature of the Pnma SnSe crystal, tailoring and controlling the 1D growth of SnSe could offer significant advantages for manipulating the properties of devices formed from these 1D SnSe materials. The work demonstrated in this thesis advances the capability and knowledge of the control of 1D SnSe systems, and demonstrates the utility of these tailored nanostructures for applications such as memory and Li-ion battery devices.

5.1 References

(1) Chung, K.-M.; Wamwangi, D.; Woda, M.; Wuttig, M.; Bensch, W. Investigation of SnSe, SnSe2, and Sn2Se3 Alloys for Phase Change Memory Applications. *J. Appl. Phys.* **2008**, *103*, 083523.

(2) Chun, D.; Walser, R. M.; Bené, R. W.; Courtney, T. H. Polarity-Dependent Memory Switching in Devices with SnSe and $SnSe_2$ crystals. *Appl. Phys. Lett.* **1974**, *24*, 479–481.

(3) Davitt, F.; Manning, H. G.; Robinson, F.; Hawken, S. L.; Biswas, S.; Petkov, N.; Druenen, M.; Boland, J. J.; Reid, G.; Holmes, J. D. Crystallographically Controlled Synthesis of SnSe Nanowires: Potential in Resistive Memory Devices. *Adv. Mater. Interfaces* **2020**, 2000474.

(4) Tian, H.; Wang, X. F.; Mohammad, M. A.; Gou, G. Y.; Wu, F.; Yang, Y.; Ren, T. L. A Hardware Markov Chain Algorithm Realized in a Single Device for Machine Learning. *Nat. Commun.* **2018**, *9*, 1–11.

(5) Cho, S. H.; Cho, K.; Park, N. W.; Park, S.; Koh, J. H.; Lee, S. K. Multi-Layer SnSe Nanoflake Field-Effect Transistors with Low-Resistance Au Ohmic Contacts. *Nanoscale Res. Lett.* **2017**, *12*, 2–7.

(6) Pawbake, A. S.; Jadkar, S. R.; Late, D. J. High Performance Humidity Sensor and Photodetector Based on SnSe Nanorods. *Mater. Res. Express* **2016**, *3*.

(7) Wang, J.; Yang, G. F.; Xue, J. J.; Lei, J. M.; Chen, D. J.; Lu, H.; Zhang, R.; Zheng, Y. D. A Reusable and High Sensitivity Nitrogen Dioxide Sensor Based on Monolayer SnSe. *IEEE Electron Device Lett.* **2018**, *39*, 599–602.

(8) Zhao, S.; Wang, H.; Zhou, Y.; Liao, L.; Jiang, Y.; Yang, X.; Chen, G.; Lin, M.; Wang,

Y.; Peng, H.; Liu, Z. Controlled Synthesis of Single-Crystal SnSe Nanoplates. *Nano Res.* **2015**, *8*, 288–295.

(9) Hernandez, J. A.; Ruiz, A.; Fonseca, L. F.; Pettes, M. T.; Jose-Yacaman, M.; Benitez, A. Thermoelectric Properties of SnSe Nanowires with Different Diameters. *Sci. Rep.* **2018**, *8*, 1–8.

(10) Chen, Z. G.; Shi, X.; Zhao, L. D.; Zou, J. High-Performance SnSe Thermoelectric Materials: Progress and Future Challenge. *Prog. Mater. Sci.* **2018**, *97*, 283–346.

(11) Chandra, S.; Banik, A.; Biswas, K. N -Type Ultrathin Few-Layer Nanosheets of Bi-Doped SnSe: Synthesis and Thermoelectric Properties. *ACS Energy Lett.* **2018**, *3*, 1153–1158.

(12) Chandra, S.; Biswas, K. Realization of High Thermoelectric Figure of Merit in Solution Synthesized 2D SnSe Nanoplates via Ge Alloying. *J. Am. Chem. Soc.* **2019**, *141*, 6141–6145.

(13) Franzman, M. A.; Schlenker, C. W.; Thompson, M. E.; Brutchey, R. L. Solution-Phase Synthesis of SnSe Nanocrystals for Use in Solar Cells. *J. Am. Chem. Soc.* **2010**, *132*, 4060–4061.

(14) Liu, S.; Guo, X.; Li, M.; Zhang, W. H.; Liu, X.; Li, C. Solution-Phase Synthesis and Characterization of Single-Crystalline SnSe Nanowires. *Angew. Chemie - Int. Ed.* **2011**, *50*, 12050–12053.

(15) Minnam Reddy, V. R.; Gedi, S.; Pejjai, B.; Park, C. Perspectives on SnSe-Based Thin Film Solar Cells: A Comprehensive Review. *J. Mater. Sci. Mater. Electron.* **2016**, *27*, 5491–5508.

(16) Lee, D.-H.; Park, C.-M. Tin Selenides with Layered Crystal Structures for Li-Ion

Batteries: Interesting Phase Change Mechanisms and Outstanding Electrochemical Behaviors. *ACS Appl. Mater. Interfaces* **2017**, *9*, 15439–15448.

(17) Zhang, Z.; Zhao, X.; Li, J. SnSe/Carbon Nanocomposite Synthesized by High Energy Ball Milling as an Anode Material for Sodium-Ion and Lithium-Ion Batteries. *Electrochim. Acta* **2015**, *176*, 1296–1301.

(18) Im, H. S.; Lim, Y. R.; Cho, Y. J.; Park, J.; Cha, E. H.; Kang, H. S. Germanium and Tin Selenide Nanocrystals for High-Capacity Lithium Ion Batteries: Comparative Phase Conversion of Germanium and Tin. *J. Phys. Chem. C* **2014**, *118*, 21884–21888.

(19) Wang, W.; Li, P.; Zheng, H.; Liu, Q.; Lv, F.; Wu, J.; Wang, H.; Guo, S. Ultrathin Layered SnSe Nanoplates for Low Voltage, High-Rate, and Long-Life Alkali–Ion Batteries. *Small* **2017**, *13*, 1–7.

(20) Zhao, L.-D.; Lo, S.-H.; Zhang, Y.; Sun, H.; Tan, G.; Uher, C.; Wolverton, C.; Dravid, V. P.; Kanatzidis, M. G. Ultralow Thermal Conductivity and High Thermoelectric Figure of Merit in SnSe Crystals. *Nature* **2014**, *508*, 373–377.

(21) Xu, X.; Song, Q.; Wang, H.; Li, P.; Zhang, K.; Wang, Y.; Yuan, K.; Yang, Z.; Ye, Y.; Dai, L. In-Plane Anisotropies of Polarized Raman Response and Electrical Conductivity in Layered Tin Selenide. *ACS Appl. Mater. Interfaces* **2017**, *9*, 12601–12607.

(22) Huang, Y.; Ling, C.; Liu, H.; Wang, S. Edge-, Width- and Strain-Dependent Semiconductor-Metal Transition in SnSe Nanoribbons. *RSC Adv.* **2014**, *4*, 6933–6938.

(23) Tyagi, K.; Waters, K.; Wang, G.; Gahtori, B.; Haranath, D.; Pandey, R. Thermoelectric Properties of SnSe Nanoribbons: A Theoretical Aspect. *Mater. Res. Express* **2016**, *3*.

Appendix: Additional work

6.1 Electron beam induced exfoliation of <100> SnSe nanowires

<100> oriented SnSe nanowires were grown as reported in Chapter 1, and were seen to undergo beam induced thinning of the (100) SnSe layers when exposed to the electron beam in a TEM under general imaging conditions. A JOEL 2000 operating at 200 kV was used for these measurements. This exfoliation was seen to occur layer by layer, and is indicated in Figure 6.1.1, where three TEM images were captured at 1 second intervals, showing how the topmost SnSe layer is removed over this period of time. In Figure 6.1.2, at t = 0 s the distance from the top of the (100) faceted surface of the SnSe nanowire to the amorphous circle seen in the image is indicated by the red line, where the <100> growth direction of the SnSe nanowire is parallel to the red line. At t = 3 s the distance between the amorphous circle and the (100) SnSe surface has increased, highlighting how the (100) layer thickness has decreased after 3 seconds of exposure to the electron beam. Figure 6.1.3 shows how 500 seconds of exposure causes significant damage to the area indicated by the red circle.

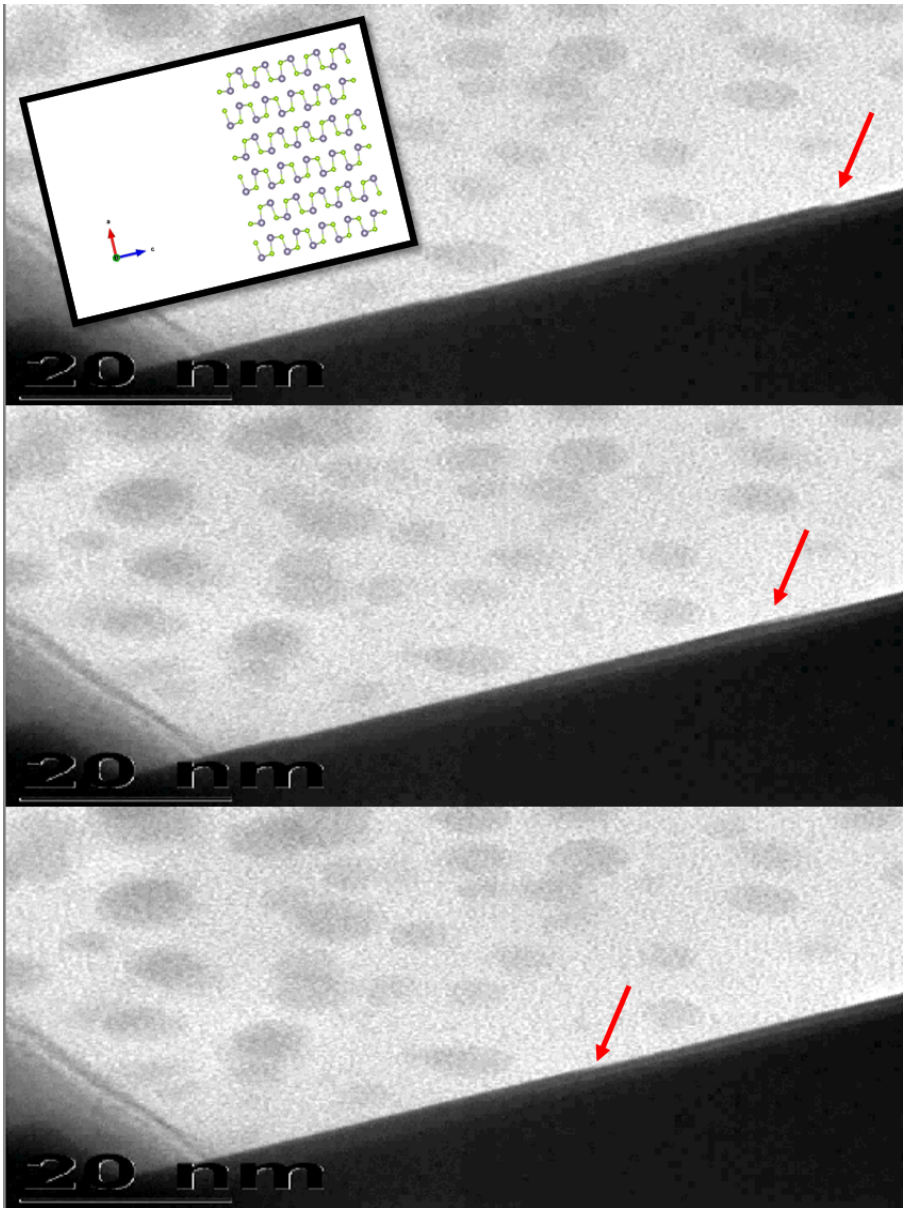


Figure 6.1.1 Beam induced exfoliation of SnSe layers in a <100> growth direction SnSe nanowire. The three images show the removal of the top surface (100) layer over the period of 3 seconds. The red arrow is a guide for the eye, indicating roughly where the edge of the top surface ends. The top inset illustrates the orientation of the *a*-axis SnSe layers in the nanowire. Red arrow: *a*-aixs, green arrow: *b*-axis and blue arrow: *c*-axis.

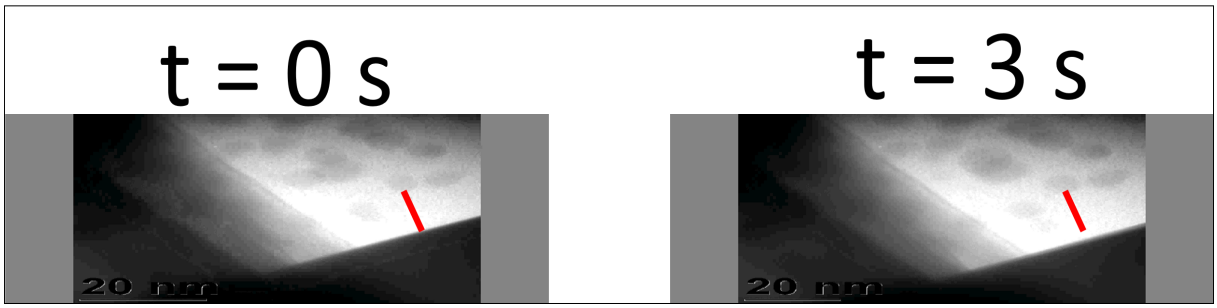


Figure 6.1.2: Beam induced exfoliation of SnSe layers in a <100> growth direction SnSe nanowire. The red line is a guide for the eye, of roughly 6.5 nm in length, indicating the increased distance between the amorphous circle at the top of the line and the top of the SnSe nanowire at the bottom of the line after 3 seconds of exposure to the electron beam.

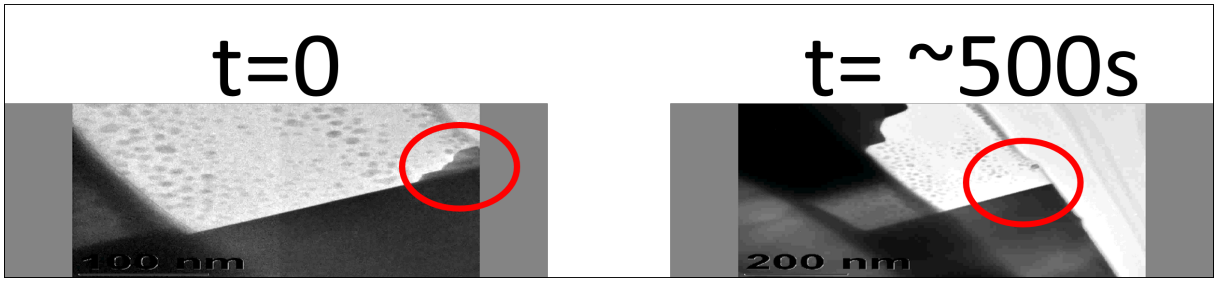
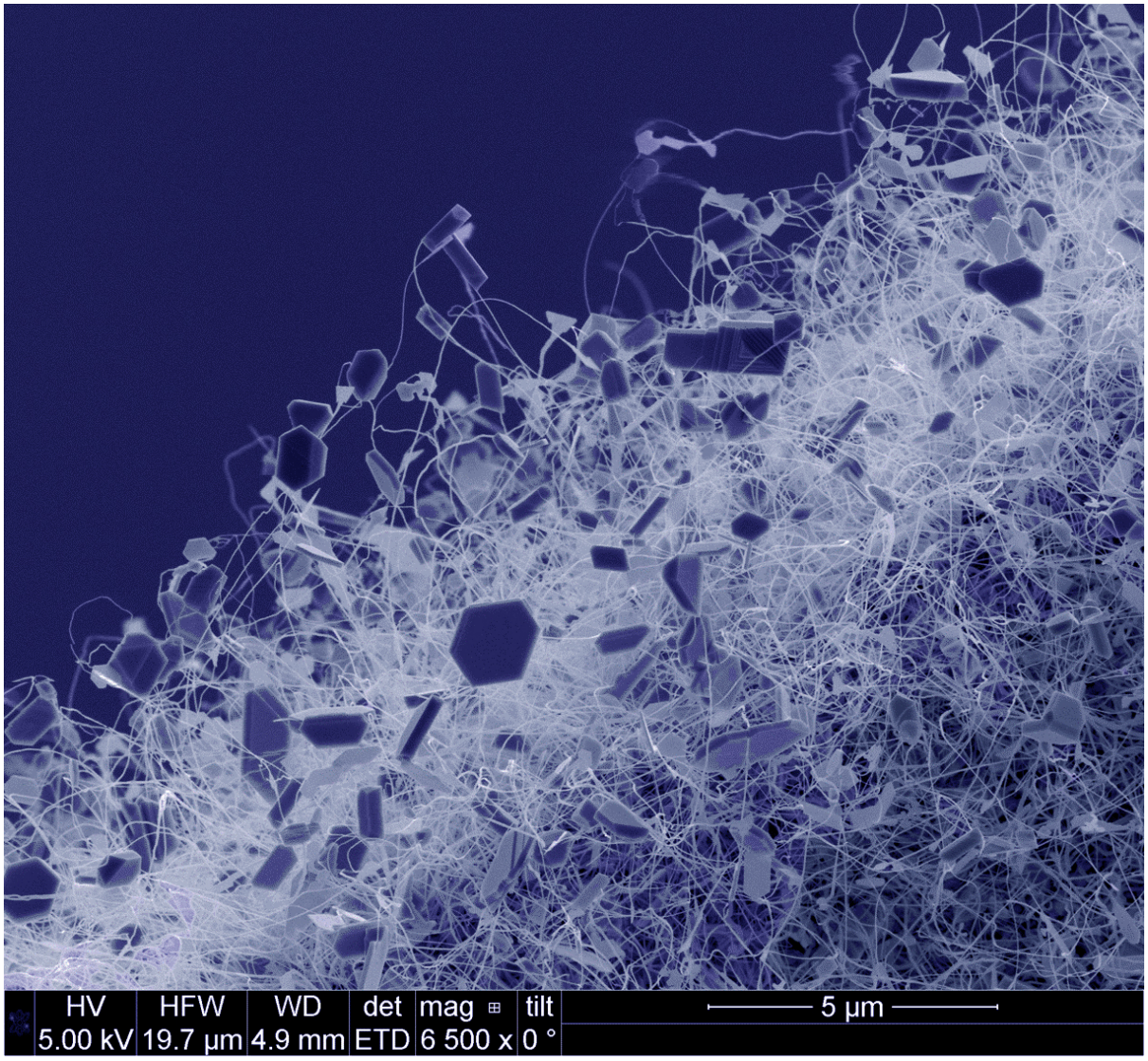


Figure 6.1.3: The beam induced exfoliation has completely removed the area highlighted by the red circle after ~500 s.

6.2 Growth and Analysis of Core-Shell Ge-Sb_2Te_3 Nanoribbons



Nanomaterial growth and analysis was performed by myself; including all CVD reactions, SEM, TEM, electron diffraction, XRD and Raman analysis.

High resolution EDX and EELS mapping was performed by myself, with assistance of the staff at the Trinity Advanced Microscopy Laboratory.

Maria Koleśnik-Gray and Vojislav Krstić performed the electrical analysis.

Tim W. Collins performed the AFM measurements.

I co-wrote this paper with Subhajit Biswas and Justin D. Holmes.

Davitt, F., Koleśnik-Gray, M., Biswas, S., Collins, T. W., Krstić, V., Holmes J. D. *Growth and Analysis of Core-Shell Ge-Sb_2Te_3 Nanoribbons.* (In preparation)

6.2.1 Abstract

Core-shell nanoribbons of Ge-Sb_2Te_3, consisting of a Ge-doped Sb_2Te_3 core and a Ge surface layer, have been grown using a low-pressure chemical vapour deposition (LPCVD) method. The nanoribbons can be grown as flexible and mechanically stable films consisting of nanoribbons several microns in length and with mean heights and widths of 12.7 ± 1.7 nm and 38.9 ± 7.2 nm, respectively. The Sb_2Te_3 core of the nanoribbons is single crystalline throughout, with an $R\bar{3}m$ (166) structure. The surface Ge layer was seen to be amorphous and was roughly ~2 - 6 nm thick. These nanoribbons had electrical properties consistent with Ge doped Sb_2Te_3, suggesting that they could be used for future applications in phase change memory or thermoelectric devices.

6.2.2 Introduction

Sb_2Te_3 is a layered chalcogenide material, with significant potential for many applications, in particular phase change random-access memory (PCRAM) devices and thermoelectric generators.[1,2] Sb_2Te_3 forms as a layered material, with strongly bound in-plane atoms and weaker Van der Waals bound layers along the <001> direction (see sub-appendix Figure A.6.1). However, in contrast to the likes of graphene, in which a single layer consists of a single atom, Sb_2Te_3 forms a quintuple layer structure, consisting of two atomic layered sheets of Sb, and three of Te.[3] Layered materials such as these display unique physical properties, such as layer dependant tuning of the material behaviour.[4,5] The cleavage of many layered materials along their weak Van der Waals planes, to form 2D flakes has been explored in depth.[6,7] However, the fabrication of pseudo-1D nanoribbon structures has not been as well explored, despite the novel properties on offer.[8–10]

Low dimension 1D nanostructures offer increased scalability and reduced power requirements for device applications.[11,12] This is of particular interest for the PCRAM devices for which Sb_2Te_3 has been explored in depth.[1] These devices rely on the inherent properties of phase change materials, in which distinct resistance states can be reversibly achieved between both their crystalline and amorphous states. This family of phase change materials encompasses a wide range of chalcogenide materials, such as GeTe,[13] Sb_2Te_3,[14,15] $G_xSb_xTe_x$ (GST),[16–20] InSbTe,[21] Bi_2Te_3[22] and $SnSe_2$[23,24] amongst many others. Sb_2Te_3 is a highly interesting form of these materials, due to its rapid resistance state switching speed.[15]

The switching properties of the material for PCRAM is also anticipated to be heavily impacted by the material composition and tailoring the composition can thus tune the device performance.[17,25,26] Sb_2Te_3 is most commonly alloyed with GeTe to form $Ge_xSb_xTe_x$ forms with differing material properties, such as better stability for PCRAM devices.[18,19,26,27] Alloying Sb_2Te_3 with various materials such as Ge,[16,28] Al[29] and Si[30] has also been studied, offering increased performance and stability for the PCRAM applications to which Sb_2Te_3 finds significant interest.

In this article we describe the synthesis and electrical characterisation of core-shell nanoribbons of Ge-Sb_2Te_3, consisting of a Ge-doped Sb_2Te_3 core and a Ge surface layer. Incorporation of Ge into Sb_2Te_3 has been shown to increase both the crystallisation temperature and the resistivity of the material, which is important for implementing Sb_2Te_3 into PCRAM devices.[28] These nanoribbons are extremely thin, with mean heights and widths of 12.7 ± 1.7 nm and 38.9 ± 7.2 nm, respectively. Whilst 1D nanowire type morphologies of Sb_2Te_3[16,31,32] and $Ge_xSb_yTe_z$[20,26,33] systems have been widely explored, nanoribbons of these materials have not been reported. Sb_2Te_3 nanobelts, without any Ge incorporation, have been reported using a hydrothermal synthesis method, but these previously reported “belts” possessed thicknesses of

the order of ~100 nm.[34] Our much lower dimension nanoribbons can potentially lead to an extremely small active device area and present the possibility of fantastic device scaling, as well as an immense possible reduction in the device power required for applications based on these nanoribbons. While at the same time, Ge incorporation is shown to exhibit a change in the conductivity of the Sb_2Te_3 nanoribbons, resulting in a shift to lower values.

6.2.3 Experimental

Experiments were performed in a homebuilt low-pressure chemical vapour deposition (CVD) system. Si (100) wafers were used as the growth substrate, and prior to the CVD reaction, these wafers were cleaned in acetone and isopropyl alcohol (IPA), and then dried overnight at 120 °C. The clean Si wafers were then coated with a 3 nm thick Au film, using a Quorum Q150R S sputter coater, before being loaded into the CVD reactor to act as a growth substrate. Powders of GeTe and Sb_2Te_3 were used as the source material for the CVD reaction. These powders were loaded into quartz boats towards the centre of the furnace, with the Si substrates located in the downstream region. Once the precursors and Si substrates were inserted, the chamber was placed under vacuum overnight, before being purged with high purity argon gas. The chamber was then heated to the reaction temperature, and the CVD reactions were then run at a constant pressure and gas flow rate. The chamber was maintained at 600 °C for 2 hours. Nanoribbon growth was seen for precursor amounts of 10 mg GeTe and 30 mg Sb_2Te_3, with a substrate temperature of ~400 °C, a chamber pressure of 150 Torr, and a carrier gas flow rate of 200 SCCM of high purity argon gas.

6.2.4 Characterisation

After growth, the nanoribbons were imaged using scanning electron microscopy (SEM) in a Helios Nanolab 600i. The crystal structure of the product was confirmed by X-ray diffraction (XRD) using a Philips X'pert Pro MPD equipped with a Panalytical Empyrean Cu X-ray tube

and a Philips X'celerator detector. The nanoribbons were then mechanically removed from the silicon growth substrate by sonication in isopropyl alcohol (IPA), and the resulting solution was then dropped onto a carbon coated copper TEM grid, for (S)TEM and EDX/EELS analysis. (S)TEM was carried out using a 30kV Helios Nanolab 600i, a 200kV JEOL 2100 TEM and a 300kV FEI Titan (S)TEM equipped with EDX and EELS.

6.2.5 Results and Discussion

Ge-Sb_2Te_3 nanoribbons were grown on Si (100) substrates using a CVD process, with Sb_2Te_3 and GeTe powders as precursors (see the Experimental section 6.2.3 for the detailed experimental and characterisation methods). The morphology of the CVD grown nanostructures is shown in Figure 6.2.1. After removal from the CVD chamber, the surface of the Si substrate was heavily coated with a black film, which was mechanically removable from the substrate with tweezers (Figure 6.2.1(a)). From SEM analysis, this film was revealed to consist of a very large network of small dimension nanoribbons (Figures 6.2.1(b) + (c)). The back side of this film, after removal from the Si wafer is shown in the top right of Figure 6.2.1(b), revealing a film of microcrystallites, which the nanoribbons are proposed to grow from (see sub-appendix Figure A.6.2 for an SEM image of nanoribbons on this film).

An individual nanoribbon, after dispersion of the nanoribbons in IPA and dropcasting onto a Si wafer is shown in the AFM image of figure 6.2.1(d). Measurements of many individual nanoribbons revealed them to have mean heights and widths of 12.7 ± 1.7 nm and 38.9 ± 7.2, respectively. Lengths of up to several microns were observed for many of the nanoribbons.

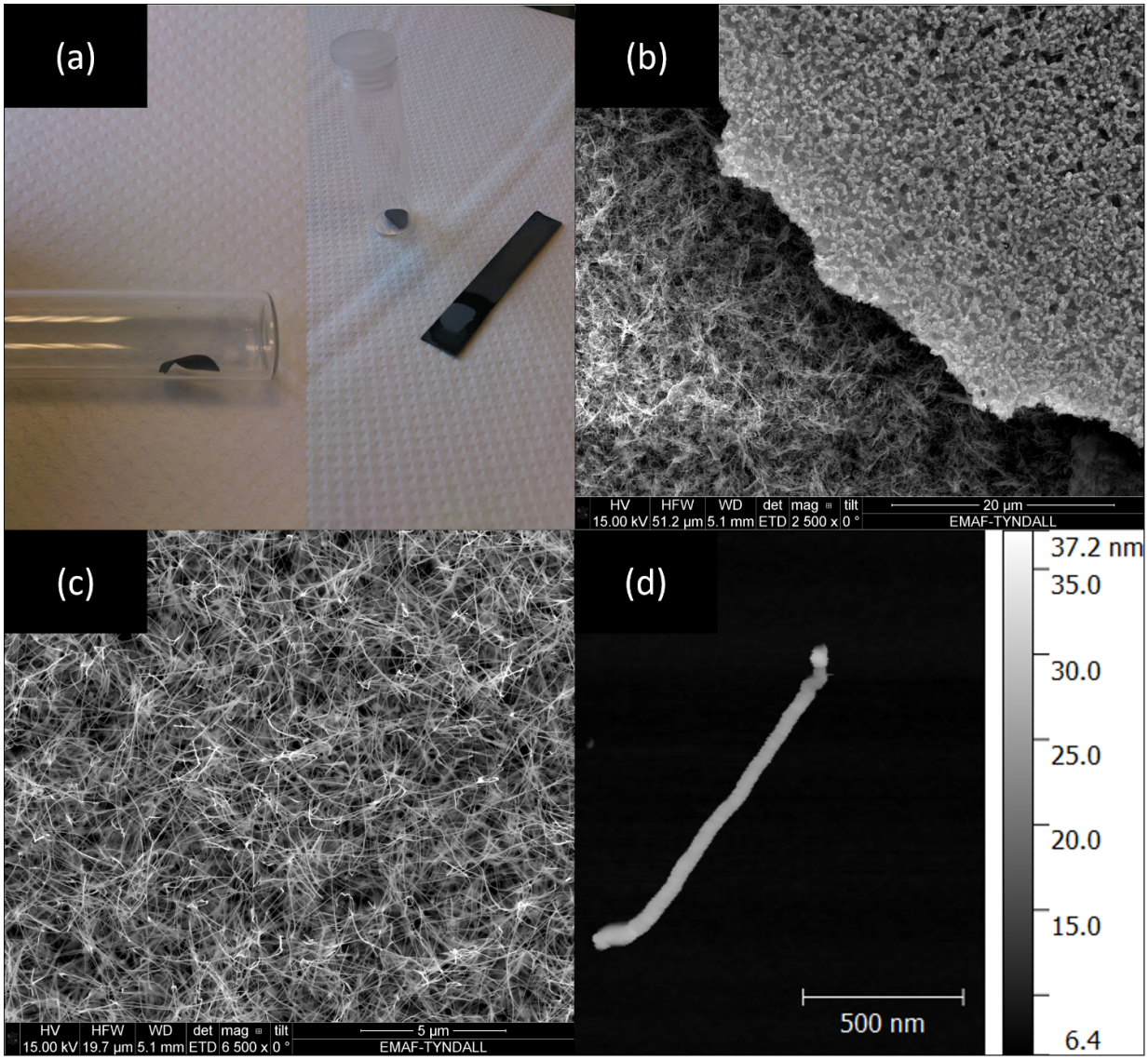


Figure 6.2.1: (a) Film formed on the Si substrate. (b) SEM image of an overlaid piece of the film, showing nanoribbons coating the top surface (bottom left) and the bottom film surface (top right). (c) SEM image showing the nanoribbon coated surface of the film in **(a)** and **(b)**. (d) AFM topography image of an individual nanoribbon.

Energy dispersive X-ray (EDX) analysis of the nanoribbons (Figure 6.2.2(a)) revealed a total core + shell composition of Ge: ~62 at.%, Sb: ~18 at.% and Te: ~20 at.%. Electron energy loss spectroscopy (EELS) mapping combined with EDX mapping (Figure 6.2.2(b)) shows the uniform nature of the Sb and Te in the body of the nanoribbon. Ge however is distributed slightly less uniformly than Sb and Te however and comparing the STEM image to the Ge EDX map shows that the amorphous surface region contains a high amount of Ge. A small amount of Sb is also seen in this surface region, but in much reduced quantity to Ge. Te is not apparent at the surface. EELS is a more sensitive technique for lighter elements such as O and using this O EELS map and the Ge EDX map, the surface of the nanoribbons is shown to consist of a germanium surface oxide. This surface oxide is thought to have grown in the time between removal from the CVD reactor and the analysis in the TEM. This presence of Ge and Sb at the surface makes it difficult to conclude the amount of Ge incorporated within the Sb_2Te_3 nanoribbon structure itself (and to a lesser extent the Sb due to the lower signal at the surface compared to Ge), and thus the composition obtained from the point EDX analysis of Figure 6.2.2(a) likely overestimates both the Ge and the Sb content of the Ge-Sb_2Te_3 nanoribbon.

No evidence of Au in the nanoribbons is seen in the EDX analysis. However, performing the CVD growth without the presence of an Au film, leads to the growth of 2D like plate structures (sub-appendix Figure A.6.3), with no long nanoribbons visible in the sample. This indicates that Au helps to promote the nanoribbon growth from the 2D flake forms, although the exact mechanism is presently unclear. Kim *et. al.* have previously reported the growth of Sb_2Te_3 nanowires using films of $Al_xGe_xSb_xTe_x$, and it is possible that our Sb_2Te_3 nanoribbons grow through a similar method, where Au is substituted for Al in our underlying film (Figure 6.2.1(b) and sub-appendix Figure A.6.2).[32]

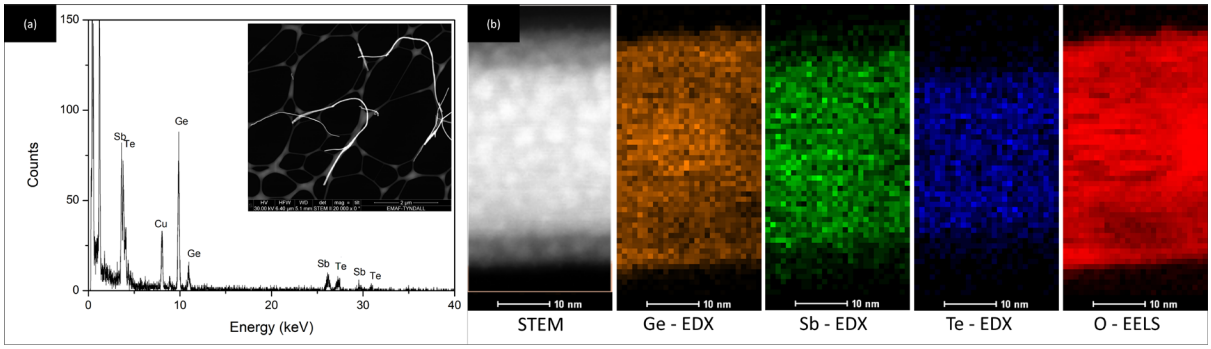


Figure 6.2.2: (a) EDX spectrum from an individual nanoribbon, showing an atomic % composition of Ge: ~62 at.%, Sb: ~18 at.% and Te: ~20 at.%. (Cu peaks from grid). Inset: STEM image of nanoribbons removed from the growth surface. (b) EDX + EELS elemental mapping of a single nanoribbon. The ribbon consists of Ge, Sb and Te throughout, with a surface oxide composed of Ge and O present.

Figure 6.2.3(a) shows an XRD spectrum recorded from the as grown nanoribbons and underlying film. The peaks present in this data correspond to values corresponding to those of R$\bar{3}$m 166 rhombohedral Sb_2Te_3 (JCPDS 15-0874). R3m 160 rhombohedral GeTe (JCPDS 47-1079) is also indicated on the figure, showing that the Ge does not form a visible amount of a GeTe phase. This indicates that whilst the presence of Ge is clearly visible from the EDX spectrum of Figure 6.2.2(a), the materials formed on the Si wafer are structured in a crystal form very close to that of rhombohedral Sb_2Te_3, with Ge potentially incorporated into the Sb_2Te_3 lattice, or else as an amorphous Ge containing phase. A small number of peaks are also seen, corresponding to the 101 peak of $P3_121$ 152 hexagonal Te (JCPDS 36-1452) [Magenta], the 102 and 201 peaks of $P4_32_12$ 96 Tetragonal Ge (JCPDS 18-0549) [Green] and the 006 peak of P$\bar{3}$m1 164 Hexagonal Sb_2Te (JCPDS 80-1722) [Grey]. Some of these peaks could potentially result from the film underlying the nanoribbons (Figure 6.2.1(b)).

TEM analysis was used to investigate the crystallographic structure of the individual nanoribbons in further depth. Figure 6.2.3(b) shows a HRTEM image of a typical nanoribbon, with a SAED pattern included in the inset. From this HRTEM image, a clear layered structure is seen, with quintuple layers of ~1 nm thick visible. This clearly reveals that the crystal structure retains the 2D layered material structure of Sb_2Te_3. This interlayer direction is assigned to the <001> direction of Sb_2Te_3. This microscopy data reveals a growth direction of the nanoribbons corresponding to a *d*-spacing value of 0.216 nm, which is assigned to the <110> direction of rhombohedral Sb_2Te_3 (Figure 6.2.3(c)). This growth direction is similar to previously reported nanowires of Sb_2Te_3.[31] A lower magnification view of the ribbon seen in Figure 6.2.3(b) is shown in the sub-appendix Figure A.6.4. Since this nanoribbon is viewed edge on, the measured diameter equates to the height of the nanoribbon, and is seen to be ~8 nm, which equates to ~8 quintuple layers of the layered Sb_2Te_3 structure.

Figure 6.2.3(d) shows a Raman spectrum, taken from as grown Ge-Sb_2Te_3 nanoribbons on the Si substrate. Peaks can be seen at ~89, ~119, ~138, ~166 and ~257 cm^{-1}. The peaks at ~119 and ~166 cm^{-1} can be ascribed to the E^2_g and A^2_{1g} modes of Sb_2Te_3 respectively.[35] The peaks at ~89 and ~138 cm^{-1} can be assigned to the $E_u(3)$ and $A_{2u}(3)$ Sb_2Te_3 infrared-active modes.[36] The low intensity peak at 257 cm^{-1} is potentially due to Ge-Te bonding[37] or GeO_2.[38] The very low intensity of the potential GeO_2 peak indicates that there is likely not a very high quantity of GeO_2 present, and combined with the absence of Ge-Ge vibrational modes is a clear indication that the high level of Ge seen from the EDX measurements is also not elemental Ge, but instead incorporated into the Sb_2Te_3 lattice in some way. This incorporation of Ge into the Sb_2Te_3 lattice has been reported before for both Sb_2Te_3 films and Sb_2Te_3 nanowires, where it was proposed that the Ge atoms substitute for Sb and Te lattice sites.[16,28] While this

incorporation yields single crystalline structures, some nanoribbons were observed to exhibit a defective crystal structure due to Ge incorporation (see sub-appendix Figure A.6.5).

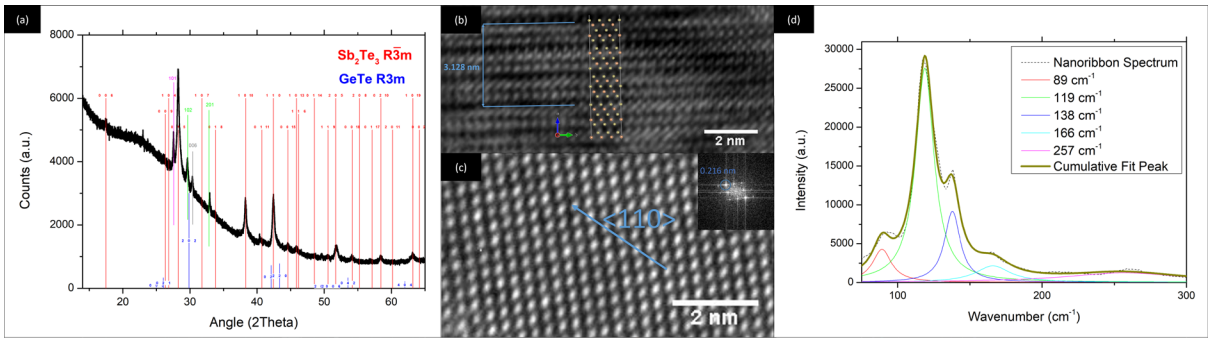


Figure 6.2.3: (a) XRD analysis of the nanoribbon coated film, showing peaks corresponding to those of R$\bar{3}$m 166 rhombohedral Sb_2Te_3 (JCPDS 15-0874) [Red] and R3m 160 rhombohedral GeTe (JCPDS 47-1079) [Blue]. Also shown is the 101 peak corresponding to $P3_121$ 152 hexagonal Te (JCPDS 36-1452) [Magenta], the 102 and 201 peaks of $P4_32_12$ 96 Tetragonal Ge (JCPDS 18-0549) [Green] and the 006 peak of P$\bar{3}$m1 164 Hexagonal Sb_2Te (JCPDS 80-1722) [Grey]. (b) HRTEM image of an individual nanoribbon viewed perpendicular to the layered *c*-axis. A visualisation of the Sb_2Te_3 crystal structure along the [100] direction is overlaid on the image. A value of 3.128 nm was measured from the TEM image, which corresponds to the d-spacing of the (001) Sb_2Te_3 plane. (c) HRTEM image of a nanoribbon, viewed down a different zone axis. From this TEM image a growth direction d-spacing of 0.216 nm is measured, assigned to the <110> direction of rhombohedral Sb_2Te_3. Inset: FFT showing a growth direction spacing in agreement with the HRTEM image. (d) Raman spectrum, taken from the nanoribbons after growth, on the Si substrate.

Electrical analysis of the nanoribbons is shown in Figure 6.2.4. This analysis was performed using both 2-probe and 4-probe measurements. A typical 2-probe I-V curve is shown in Figure 6.2.4(a), showing a non-linear symmetric form, suggesting metal contacts to a heavily doped

semiconductor material. Figure 6.2.4(b) displays the electrical conductivity values for the nanoribbons, which were calculated from the measured resistances from 4-probe measurements (a constant nanoribbon height of 10 nm was assumed for these calculations). Conductivity is plotted against nanoribbon width in Figure 6.2.4(b), and appears to show no obvious relationship to one another. These conductivity values lie between that of Sb_2Te_3 and GeTe, and present further evidence that the Ge has incorporated itself into the Sb_2Te_3 lattice. The wide span of conductivity values measured in Figure 6.2.4(b) implies however that the amount of Ge incorporated in the structures varies between different nanoribbons. The lack of uniformity in the Ge incorporation leaves room for future work, to enable the successful utilisation of these Ge-doped Sb_2Te_3 nanoribbons in applications such as PCRAM devices.

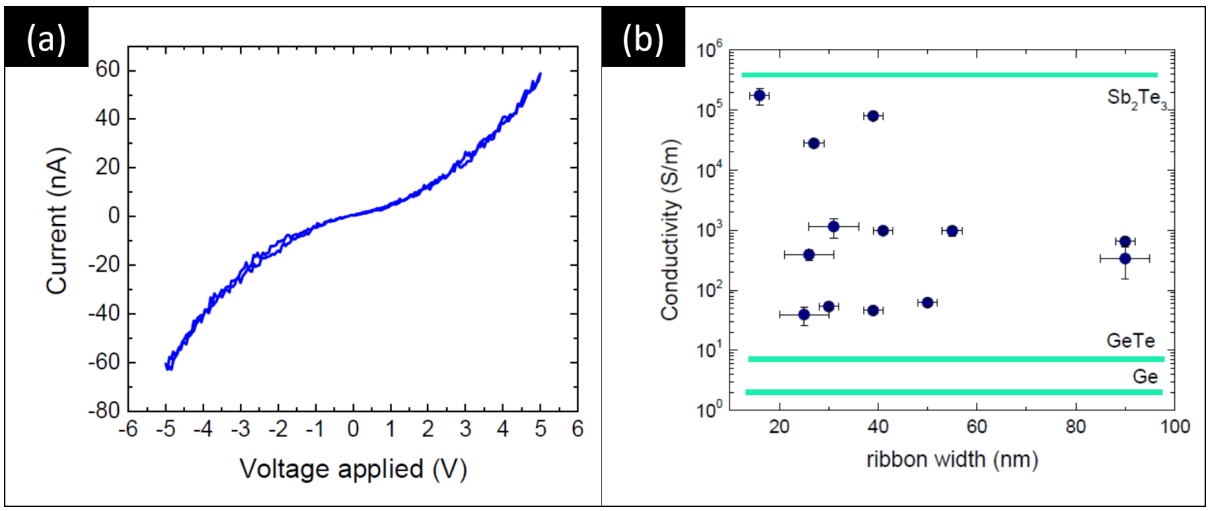


Figure 6.2.4: (a) Typical 2-point I-V curve of a Ge-Sb_2Te_3 nanoribbon device. (b) Electrical conductivity values for the nanoribbons, calculated from the measured 4-point resistances (assuming a constant ribbon height of 10 nm). Green lines show conductivity values corresponding to Sb_2Te_3, GeTe and pure Ge for comparison.

6.2.6 Conclusions

Ultra-thin Ge-Sb_2Te_3 nanoribbons with mean heights and widths of 12.7 ± 1.7 nm and 38.9 ± 7.2 nm, respectively, have been grown for the first time. These nanoribbons are up to several microns in length, and are formed in a rhombohedral Sb_2Te_3 structure, with Ge incorporation shown through EDX and 4-probe electrical analysis. These nanoribbons are grown from an underlying, and mechanically stable film of a Ge, Sb and Te alloy, with the assistance of a Au catalyst. The individual nanoribbons themselves are removable from this film for single nanoribbon analysis and applications. Electrical analysis revealed the conductively values to lie between that of GeTe and Sb_2Te_3, showing that the Ge incorporation in the Sb_2Te_3 nanoribbons offers a significant impact on the electrical properties of the material, and should offer advantageous properties for future PCRAM studies. To the best of our knowledge, these Ge doped Sb_2Te_3 nanoribbons are the smallest 1-D Sb_2Te_3 nanostructures produced to date. These low dimension Ge doped Sb_2Te_3 nanoribbons could see future potential applications in PCRAM or thermoelectric devices.

6.2.7 References

(1) Raoux, S.; Xiong, F.; Wuttig, M.; Pop, E. Phase Change Materials and Phase Change Memory. *MRS Bull.* **2014**, *39*, 703–710.

(2) Schneider, M. N.; Rosenthal, T.; Stiewe, C.; Oeckler, O. From Phase-Change Materials to Thermoelectrics? *Zeitschrift fur Krist.* **2010**, *225*, 463–470.

(3) Yang, F.; Jacobs-Gedrim, R. B.; Shanmugam, M.; Jain, N.; Murphy, M. T.; Song, E. S.; Frey, D.; Yu, B. Scalable Synthesis of Two-Dimensional Antimony Telluride Nanoplates down to a Single Quintuple Layer. *RSC Adv.* **2015**, *5*, 59320–59325.

(4) Li, L.; Kim, J.; Jin, C.; Ye, G. J.; Qiu, D. Y.; da Jornada, F. H.; Shi, Z.; Chen, L.; Zhang, Z.; Yang, F.; et al. Direct Observation of the Layer-Dependent Electronic Structure in

Phosphorene. *Nat. Nanotechnol.* **2017**, *12*, 21–25.

(5) Mak, K. F.; Lee, C.; Hone, J.; Shan, J.; Heinz, T. F. Atomically Thin MoS_2: A New Direct-Gap Semiconductor. *Phys. Rev. Lett.* **2010**, *105*, 2–5.

(6) Coleman, J. N.; Duesberg, G. S.; De, S.; O'Neill, A.; Shvets, I. V.; Kim, H.-Y.; McComb, D. W.; Hallam, T.; Arora, S. K.; Donegan, J. F.; et al. Two-Dimensional Nanosheets Produced by Liquid Exfoliation of Layered Materials. *Science* **2011**, *331*, 568–571.

(7) Nicolosi, V.; Chhowalla, M.; Kanatzidis, M. G.; Strano, M. S.; Coleman, J. N. Liquid Exfoliation of Layered Materials. *Science* **2013**, *340*, 1226419–1226419.

(8) Li, S.; Lin, Y.; Zhao, W.; Wu, J.; Wang, Z.; Hu, Z.; Shen, Y.; Tang, D.; Wang, J.; Zhang, Q.; et al. Vapour–Liquid–Solid Growth of Monolayer MoS2 Nanoribbons. *Nat. Mater.* **2018**.

(9) Kong, D.; Randel, J. C.; Peng, H.; Cha, J. J.; Meister, S.; Lai, K.; Chen, Y.; Shen, Z. X.; Manoharan, H. C.; Cui, Y. Topological Insulator Nanowires and Nanoribbons. *Nano Lett.* **2010**, *10*, 329–333.

(10) Han, M. Y.; Özyilmaz, B.; Zhang, Y.; Kim, P. Energy Band-Gap Engineering of Graphene Nanoribbons. *Phys. Rev. Lett.* **2007**, *98*, 1–4.

(11) Lee, S.-H.; Jung, Y.; Agarwal, R. Highly Scalable Non-Volatile and Ultra-Low-Power Phase-Change Nanowire Memory. *Nat. Nanotechnol.* **2007**, *2*, 626–630.

(12) Braga, S.; Cabrini, A.; Torelli, G. Impact of Technology Scaling on Phase-Change Memory Performance. In *Advances in Solid State Circuit Technologies*; InTech, 2010; p 450.

(13) Chopra, K. L.; Bahl, S. K. Amorphous versus Crystalline GeTe Films. I. Growth and Structural Behavior. *J. Appl. Phys.* **1969**, *40*, 4171–4178.

(14) Lankhorst, M. H. R.; Ketelaars, B. W. S. M. M.; Wolters, R. A. M. Low-Cost and

Nanoscale Non-Volatile Memory Concept for Future Silicon Chips. *Nat. Mater.* **2005**, *4*, 347–352.

(15) Liu, B.; Song, Z.; Feng, S.; Chen, B. Characteristics of Chalcogenide Nonvolatile Memory Nano-Cell-Element Based on Sb2Te3 Material. *Microelectron. Eng.* **2005**, *82*, 168–174.

(16) Longo, M.; Stoycheva, T.; Fallica, R.; Wiemer, C.; Lazzarini, L.; Rotunno, E. Au-Catalyzed Synthesis and Characterisation of Phase Change Ge-Doped Sb-Te Nanowires by MOCVD. *J. Cryst. Growth* **2013**, *370*, 323–327.

(17) Cheng, H. Y.; Hsu, T. H.; Raoux, S.; Wu, J. Y.; Du, P. Y.; Breitwisch, M.; Zhu, Y.; Lai, E. K.; Joseph, E.; Mittal, S.; et al. A High Performance Phase Change Memory with Fast Switching Speed and High Temperature Retention by Engineering the $Ge_xSb_yTe_z$ Phase Change Material. *IEEE Int. Electron Devices Meet.* **2011**, 3.4.1-3.4.4.

(18) Zuliani, P.; Varesi, E.; Palumbo, E.; Borghi, M.; Tortorelli, I.; Erbetta, D.; Libera, G. D.; Pessina, N.; Gandolfo, A.; Prelini, C.; et al. Overcoming Temperature Limitations in Phase Change Memories with Optimized Gex Sby Tez. *IEEE Trans. Electron Devices* **2013**, *60*, 4020–4026.

(19) Alialy, S.; Gabriel, M.; Davitt, F.; Holmes, J. D.; Boland, J. J. Switching at the Contacts in $Ge_9Sb_1Te_5$ Phase-Change Nanowire Devices. *Nanotechnology* **2019**, 30, 335706.

(20) Jung, Y.; Lee, S.-H.; Ko, D.-K.; Agarwal, R. Synthesis and Characterization of $Ge_2Sb_2Te_5$ Nanowires with Memory Switching Effect. *J. Am. Chem. Soc.* **2006**, *128*, 14026–14027.

(21) Maeda, Y.; Andoh, H.; Ikuta, I.; Minemura, H. Reversible Phase-Change Optical Data Storage in InSbTe Alloy Films. *J. Appl. Phys.* **1988**, *64*, 1715–1719.

(22) Han, N.; Kim, S. I.; Yang, J. Do; Lee, K.; Sohn, H.; So, H. M.; Ahn, C. W.; Yoo, K. H. Phase-Change Memory in Bi_2Te_3 Nanowires. *Adv. Mater.* **2011**, *23*, 1871–1875.

(23) Chung, K.-M.; Wamwangi, D.; Woda, M.; Wuttig, M.; Bensch, W. Investigation of SnSe, $SnSe_2$, and Sn_2Se_3 Alloys for Phase Change Memory Applications. *J. Appl. Phys.* **2008**, *103*, 083523.

(24) Wang, R. Y.; Caldwell, M. A.; Jeyasingh, R. G. D.; Aloni, S.; Shelby, R. M.; Wong, H. S. P.; Milliron, D. J. Electronic and Optical Switching of Solution-Phase Deposited $SnSe_2$ Phase Change Memory Material. *J. Appl. Phys.* **2011**, *109, 113506.*

(25) Boniardi, M.; Redaelli, A. Phase Change Memory: Device Scaling and Challenges for Material Engineering in the GeSbTe Compound System. *Microelectron. Eng.* **2015**, *137*, 1–4.

(26) Jung, C. S.; Kim, H. S.; Im, H. S.; Seo, Y. S.; Park, K.; Back, S. H.; Cho, Y. J.; Kim, C. H.; Park, J.; Ahn, J. P. Polymorphism of GeSbTe Superlattice Nanowires. *Nano Lett.* **2013**, *13*, 543–549.

(27) Yamada, N.; Ohno, E.; Nishiuchi, K.; Akahira, N.; Takao, M. Rapid-Phase Transitions of GeTe-Sb2Te3 Pseudobinary Amorphous Thin Films for an Optical Disk Memory. *J. Appl. Phys.* **1991**, *69*, 2849–2856.

(28) Yu, J.; Liu, B.; Zhang, T.; Song, Z.; Feng, S.; Chen, B. Effects of Ge Doping on the Properties of Sb_2Te_3 Phase-Change Thin Films. *Appl. Surf. Sci.* **2007**, *253*, 6125–6129.

(29) Peng, C.; Wu, L.; Song, Z.; Rao, F.; Zhu, M.; Li, X.; Liu, B.; Cheng, L.; Feng, S.; Yang, P.; et al. Performance Improvement of Sb_2Te_3 Phase Change Material by Al Doping. *Appl. Surf. Sci.* **2011**, *257*, 10667–10670.

(30) Zhang, Z.; Song, S.; Song, Z.; Cheng, Y.; Gu, Y.; Chen, B. Characterization of the Thermal Properties for Si-Implanted Sb_2Te_3 Phase Change Material. *Appl. Phys. Lett.* **2013**, *102*, 1–5.

(31) Jin, S. L.; Brittman, S.; Yu, D.; Park, H. Vapor-Liquid-Solid and Vapor-Solid Growth of Phase-Change Sb_2Te_3 Nanowires and Sb_2Te_3/GeTe Nanowire Heterostructures. *J.*

Am. Chem. Soc. **2008**, *130*, 6252–6258.

(32) Kim, B. G.; Kim, B. S.; Jeong, S. M.; Choi, S. M.; Whang, D.; Lee, H. L. Catalyst-Free Growth of Sb_2Te_3 Nanowires. *Mater. Lett.* **2011**, *65*, 812–814.

(33) Longo, M.; Fallica, R.; Wiemer, C.; Salicio, O.; Fanciulli, M.; Rotunno, E.; Lazzarini, L. Metal Organic Chemical Vapor Deposition of Phase Change $Ge_1Sb_2Te_4$ Nanowires. *Nano Lett.* **2012**, *12*, 1509–1515.

(34) Shi, W.; Yu, J.; Wang, H.; Zhang, H. Hydrothermal Synthesis of Single-Crystalline Antimony Telluride Nanobelts. *J. Am. Chem. Soc.* **2006**, *128*, 16490–16491.

(35) Zheng, B.; Sun, Y.; Wu, J.; Han, M.; Wu, X.; Huang, K.; Feng, S. Group IV Semiconductor Ge Integration with Topological Insulator Sb_2Te_3 for Spintronic Application. *J. Phys. D. Appl. Phys.* **2017**, *50*, aa57a0.

(36) Zhang, J.; Jalil, A. R.; Tse, P.; Kölzer, J.; Rosenbach, D.; Valencia, H.; Luysberg, M.; Mikulics, M.; Panaitov, G.; Grützmacher, D.; et al. Proximity-Effect-Induced Superconductivity in Nb/Sb_2Te_3 -Nanoribbon/Nb Junctions. ANNALEN DER PHYSIK **2020**, *532 2000273*, 1–8.

(37) Shportko, K.; Revutska, L.; Paiuk, O.; Baran, J.; Stronski, A.; Gubanova, A.; Venger, E. Compositional Dependencies in the Vibrational Properties of Amorphous Ge-As-Se and Ge-Sb-Te Chalcogenide Alloys Studied by Raman Spectroscopy. *Opt. Mater. (Amst).* **2017**, *73*, 489–496.

(38) Sato, T.; Suda, J. Lattice Dynamics and Temperature Dependence of the Linewidth of the First-Order Raman Spectra for Sintered Hexagonal GeO_2 Crystalline. *Journal of the Physical Society of Japan*. 1998, pp 3809–3815.

6.2.8 Sub-appendix: Additional figures

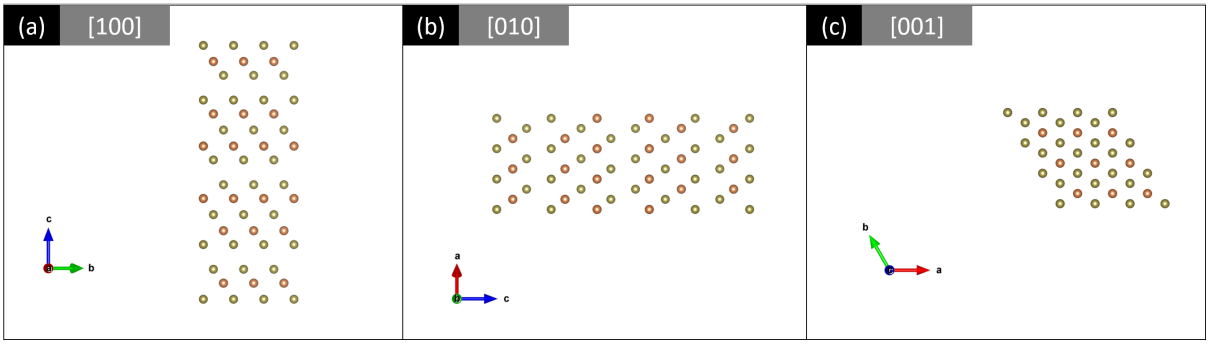


Figure A.6.1: Illustration of the Sb_2Te_3 crystal structure down three major zone axes.

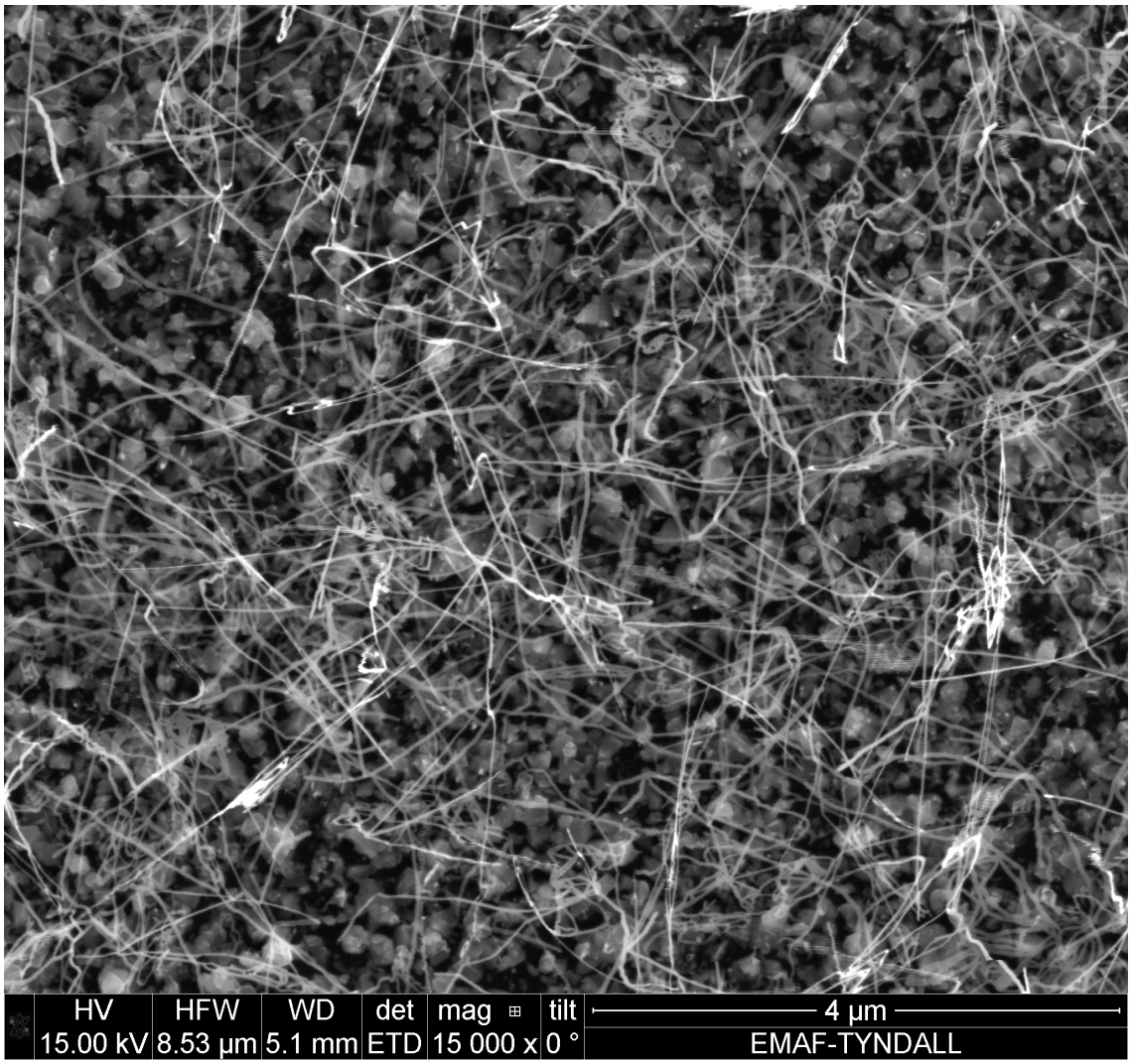


Figure A.6.2: SEM image of Ge-Sb_2Te_3 nanoribbons, with the underlying Ge, Sb and Te film visible.

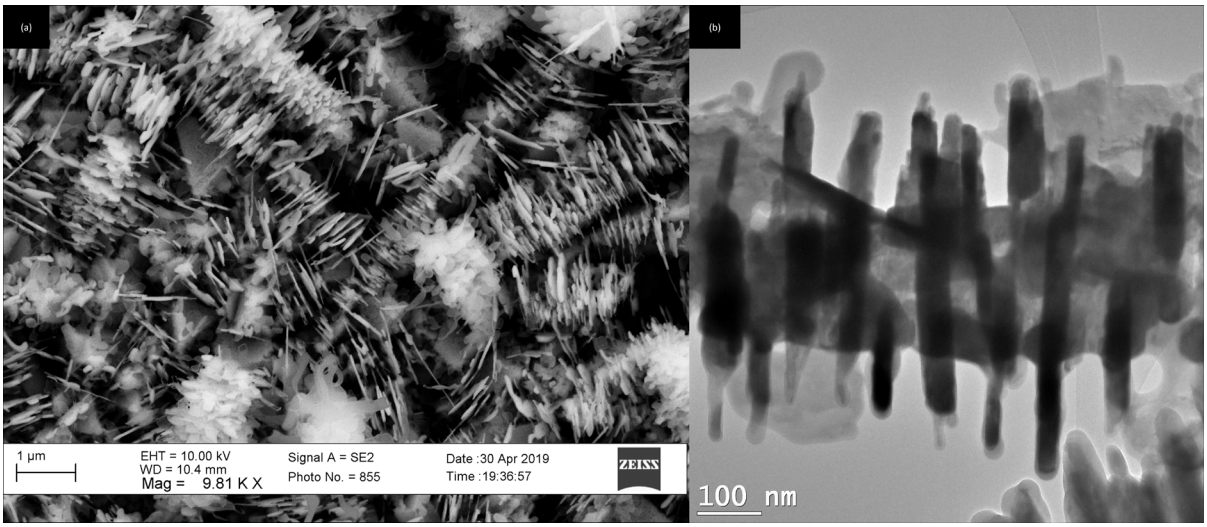


Figure A.6.3: (a) SEM + (b) TEM images of the flake structures formed when the growth is performed in the absence of Au.

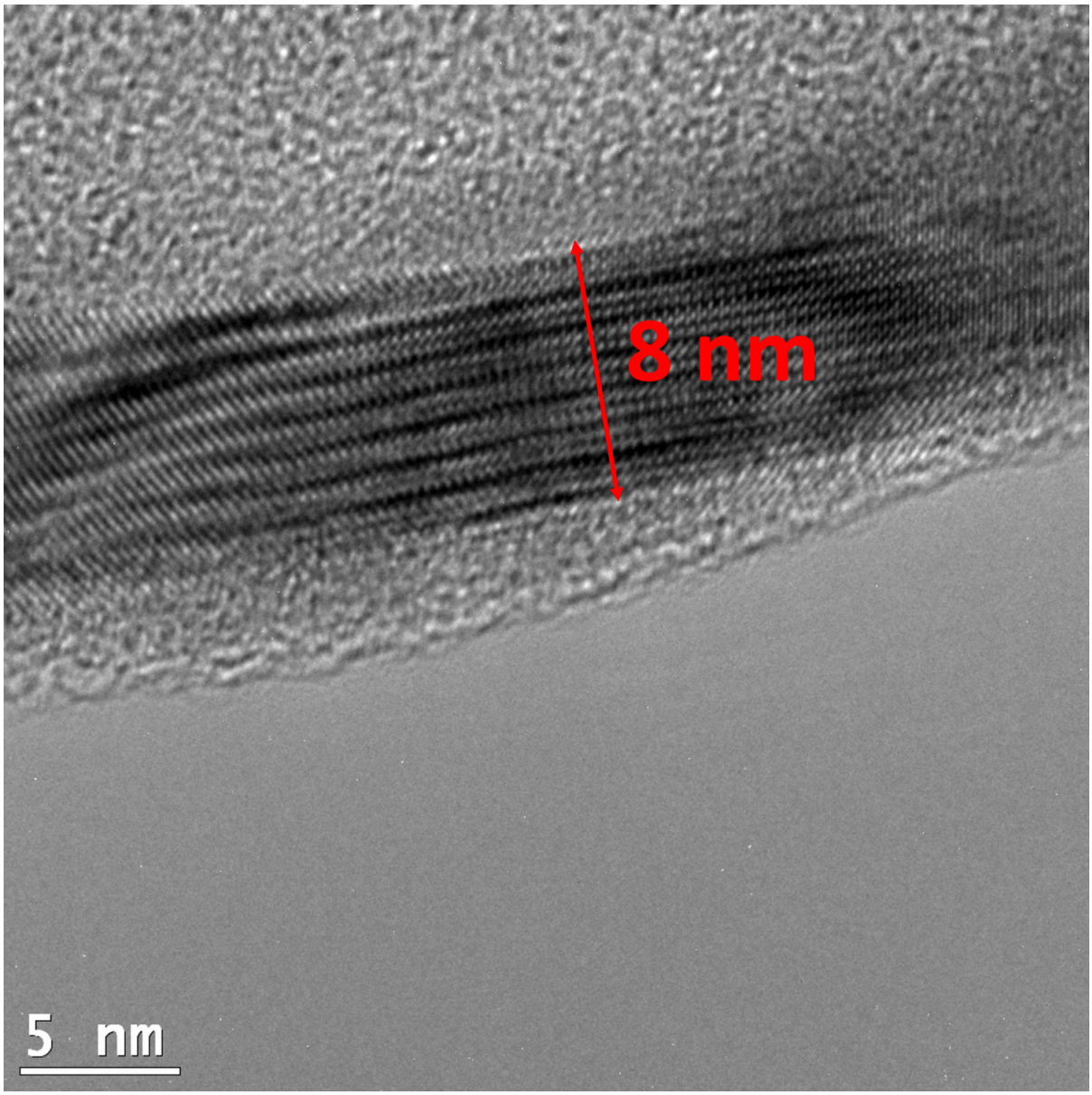


Figure A.6.4: TEM image of the side view of a Ge-Sb_2Te_3 nanoribbon.

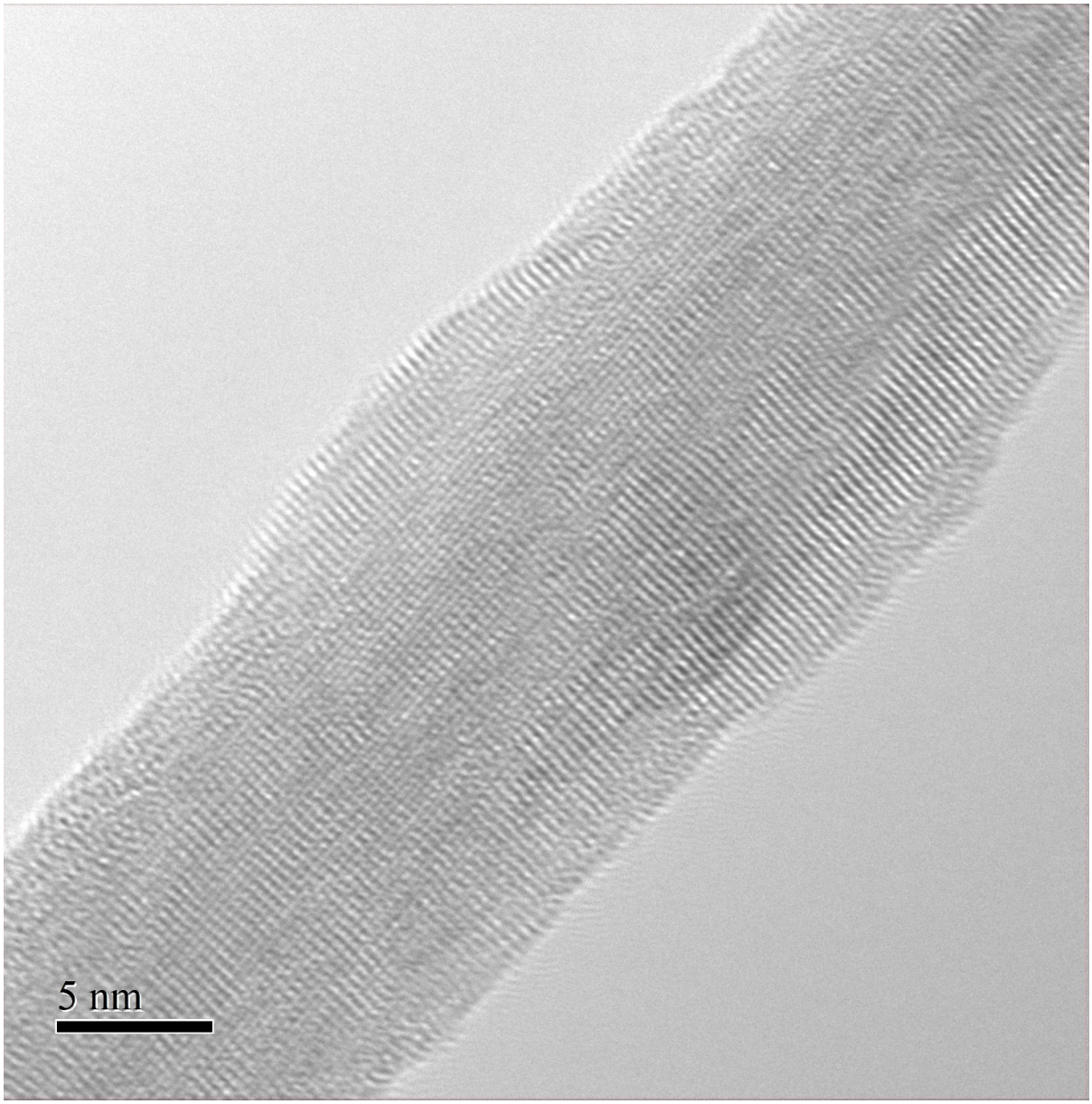


Figure A.6.5: TEM image of a Ge-Sb_2Te_3 nanoribbon with a slightly defected crystal structure. (Image provided by Dr. Colm O'Regan)

Appendix: Publications and Conference presentations

7.1 Publications arising directly from this thesis

1. Davitt, F., Manning, H. G., Robinson, F., Hawken, S. L., Biswas, S., Petkov, N., van Druenen, M., Boland, J. J., Reid, G., Holmes, J. D., *Crystallographically Controlled Synthesis of SnSe Nanowires: Potential in Resistive Memory Devices*. Adv. Mater. Interfaces 2020, 7, 2000474. https://doi.org/10.1002/admi.202000474
2. Davitt, F., Stokes, K., Collins, T. W., Roldan-Gutierrez, M., Robinson, F., Geaney, H., Biswas, S., Chang, S. L.Y., Ryan K. M., Reid, G., Holmes, J. D., *Two-Dimensional SnSe Nanonetworks: Growth and Evaluation for Li-Ion Battery Applications.* ACS Applied Energy Materials 2020, 3 (7), 6602-6610, https://doi.org/10.1021/acsaem.0c00776
3. Davitt, F., Rahme, K., Roldan-Gutierrez, M., Garvey, S., Biswas, S., Chang, S. L.Y., Holmes, J. D., *Solution Phase Growth and Characterisation of Zigzag SnSe Nanoribbons.* (In preparation)
4. Davitt, F., Koleśnik-Gray, M., Biswas, S., Collins, T. W., Krstić, V., Holmes J. D. *Growth and Analysis of Core-Shell Ge-Sb_2Te_3 Nanoribbons.* (In preparation)

7.2 Co-authored publications

5. van Druenen, M., Collins, T. W., Davitt, F., Doherty, J., Collins G., Sofer, Z., Holmes, J. D., *Stabilization of Black Phosphorus by Sonication-Assisted Simultaneous Exfoliation and Functionalization.* Chemistry – A European Journal, 2020, 26, 17581. https://doi.org/10.1002/chem.202003895
6. Alialy, S., Gabriel, M., Davitt, F., Holmes, J. D., Boland, J. J., *Switching at the contacts in $Ge_9Sb_1Te_5$ phase-change nanowire devices*. Nanotechnology, 2019, 30 (33), 335706, https://doi.org/10.1088/1361-6528/ab1cf8
7. van Druenen, M., Davitt, F., Collins, T. W., Glynn, C, O'Dwyer, C., Holmes, J. D., Collins G., *Evaluating the Surface Chemistry of Black Phosphorus during Ambient Degradation.* Langmuir, 2019, 35 (6), 2172-2178, https://doi.org/10.1021/acs.langmuir.8b04190
8. Wang, L., Pei, J., Cong, Z., Zou, Y., Sun, T., Davitt, F., Garcia-Gil, A., Holmes, J.D., O'Driscoll, C. M., Rahme, K., Guo J., *Development of anisamide-targeted PEGylated gold nanorods to deliver epirubicin for chemo-photothermal therapy in tumor-bearing mice.* International Journal of Nanomedicine, 2019, 14, 1817, https://doi.org/10.2147/IJN.S192520
9. Collins, G., Davitt, F., O'Dwyer, C., Holmes J. D., *Comparing Thermal and Chemical Removal of Nanoparticle Stabilizing Ligands: Effect on Catalytic Activity and Stability*. ACS Applied Nano Materials, 2018, 1 (12), 7129-7138, https://doi.org/10.1021/acsanm.8b02019
10. van Druenen, M., Davitt, F., Collins, T. W., Glynn, C., O'Dwyer, C., Holmes, J. D., Collins G., *Covalent Functionalization of Few-Layer Black Phosphorus Using Iodonium Salts and Comparison to Diazonium Modified Black Phosphorus*. Chemistry

of Materials, 2018, 30 (14), 4667-4674, https://doi.org/10.1021/acs.chemmater.8b01306

11. Meshgi, M. A., Biswas, S., McNulty, D., O'Dwyer, C., Verni, G. A., O'Connell, J., Davitt, F., Letofsky-Papst, I., Poelt, P., Holmes, J. D., Marschner C., *Rapid, Low-Temperature Synthesis of Germanium Nanowires from Oligosilylgermane Precursors.* Chemistry of Materials, 2017, 29 (10), 4351-4360, https://doi.org/10.1021/acs.chemmater.7b00714

7.3 Conference Presentations

1. **Davitt, F.**, Manning, H. G., Robinson, F., Hawken, S. L., Biswas, S., Collins, T. W., van Druenen, M., Boland, J. J., Reid, G., Holmes, J. D., *Morphological control of CVD grown nanostructures - 2D to 1D growth of Layered SnSe.* Materials Research Society Meeting - Boston 2018 - (Talk)
2. **Davitt, F.**, Manning, H. G., Robinson, F., Hawken, S. L., Biswas, S., Collins, T. W., van Druenen, M., Boland, J. J., Reid, G., Holmes, J. D., *Morphological control of CVD grown nanostructures - 2D to 1D growth of Layered SnSe.* International Helmholtz Research School NanoNet Annual Workshop -Dresden, Germany 2018 – (Talk)
3. **Davitt, F.**, Hawken, S. L., Biswas, S., Glynn, C., O'Connell, J., O'Dwyer, C., Reid, G., Holmes, J. D., *Chemical vapour deposition of SnSe nanowires.* Irish Chemistry Colloquium -Dublin City University, Dublin 2017 – (Poster)
4. **Davitt, F.**, Hawken, S. L., Biswas, S., Glynn, C., O'Connell, J., O'Dwyer, C., Reid, G., Holmes, J. D., *Chemical vapour deposition of SnSe nanowires.* Nanowire Week - Lund, Sweden 2017 – (Poster)